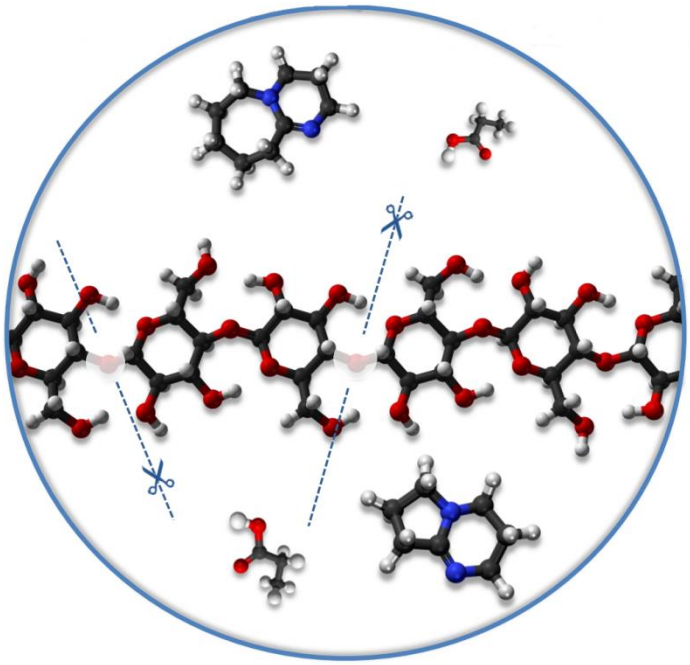

Protic Ionic Liquids for Biomass Processing

Filipe Miguel da Silva Ribeiro
Doutoramento em Química Sustentável
Departamento de Química e Bioquímica
2018

Luís Manuel das Neves Belchior Faia dos Santos
Professor Associado
Faculdade de Ciências da Universidade do Porto

Carlos Filipe Reis Alves Costa Lima
Investigador
CIQUP - Faculdade de Ciências da Universidade do Porto

Todas as correções determinadas pelo júri, e só essas, foram efetuadas.
O Presidente do Júri,

Porto, _____/_____/_____

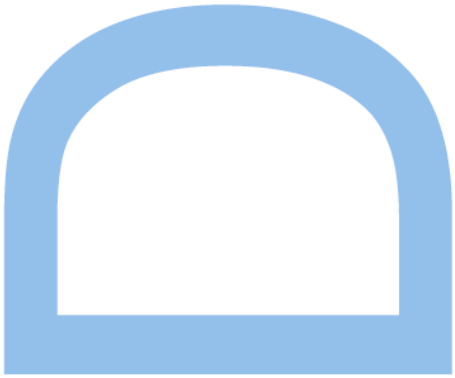

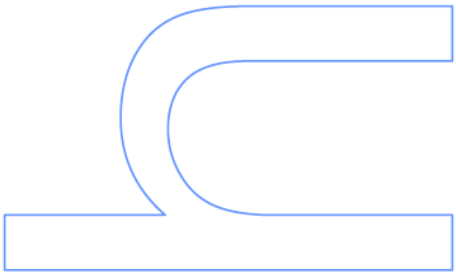

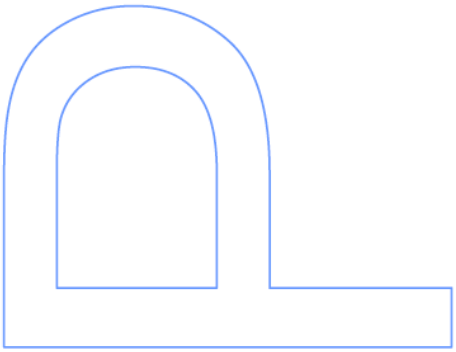

Resumo

As propriedades físico-químicas dos líquidos iónicos próticos (LIPs) são essenciais para uma interpretação robusta da sua funcionalidade como solventes/reagentes em processamento de biomassa. O trabalho e projeto de investigação que é apresentado nesta dissertação teve como objetivo o estudo das propriedades físico-químicas de LIPs, centrando-se na interpretação molecular e análise do equilíbrio de especiação. Para esse efeito, foram estudados 27 LIPs derivados da combinação de 5 superbases (1,5-diazabiciclo[4.3.0]non-5-eno (DBN), 1,8-diazabiciclo[5.4.0]undec-7-eno (DBU), triazabiciclodeceno, (TBD), 1,1,3,3-tetrametilguanidina (TMG) e 1,2-dimetil-1,4,5,6-tetrahidropirimidina (DMTHP)) com 9 ácidos carboxílicos (acético, propiónico, iso-butírico, n-butírico, n-perfluoro-butírico, n-pentanóico, n-hexanóico, n-heptanóico e n-octanóico). As propriedades estudadas foram correlacionadas com o tamanho da cadeia alquílica do ácido carboxílico, estrutura e força das superbases. O estudo foi restrito ao equilíbrio líquido-vapor, capacidades caloríficas, energias coesivas e comportamento fásico. Neste trabalho foi feita uma abordagem experimental abrangente, onde é explorada a formação e estabilidade de azeótropos em LIPs. Todos os LIPs estudados mostram pronunciados desvios negativos à Lei de Raoult, com uma diminuição significativa na pressão de vapor, indicando que a mistura é significativamente estabilizada em relação aos ácidos e bases. Concluiu-se que a acidez e basicidade dos componentes, condiciona a proporção entre espécies iónicas e neutras não sendo, no entanto, o único fator com relevância para a interpretação das propriedades destes líquidos iónicos. Quanto menor a extensão da reação ácido-base, menor a ionicidade do LIP e maior a sua tendência a desviar-se da relação molar de 0.5:0.5. Concluiu-se ainda que a composição da mistura azeotrópica é também condicionada pela capacidade de as formas neutras (ácido ou base) interatuarem com o par iónico. No caso específico de LIPs derivados da combinação de DBN, DBU, DMTHP com ácidos carboxílicos, verificou-se que o azeótropo é mais rico no ácido devido à capacidade deste, estabelecer pontes de hidrogénio com o par iónico e ainda que a sua composição azeotrópica é gradualmente mais rica para ácidos com cadeias alquílicas mais longas, existindo a indicação que a composição converge para a proporção de 0.33(3):0.66(6) (1 base para 2 ácidos).

Abstract

The physicochemical properties of protic ionic liquids (PILs) are quite essential for a robust interpretation of their functionality/applicability as solvents/reagents in biomass processing. The work and research project that is presented in this dissertation had as main goal the study of the physico-chemical properties of PILs, focusing on molecular interpretation and analysis of their speciation. For this purpose, 27 PILs derived from the combination of 5 superbases (5-diazabicyclo[4.3.0]non-5-ene (DBN), 1,8-diazabicyclo[5.4.0]undec-7-ene DBU), triazabicyclodecene (TBD), 1,1,3,3-tetramethylguanidine (TMG) and 1,2-dimethyl-1,4,5,6-tetrahydropyrimidine (DMTHP)) with 9 carboxylic acids (acetic, propionic, iso-butyric, n-butyric, n-perfluorobutyric, n-pentanoic, n -hexanoic, n-heptanoic and n-octanoic acids). The studied properties were correlated with the size of the carboxylic acid alkyl-chain, structure and strength of the superbases. The study was restricted to liquid-vapor equilibrium, heat capacities, cohesive energies and phase behavior. In this work a comprehensive experimental approach was made, where the formation and stability of azeotropes in PILs is explored. All PILs studied show pronounced negative deviations from Raoult's Law, with a significant decrease in vapor pressure, indicating that the mixture is significantly stabilized relative to neutral acids and bases. It was concluded that the acidity and basicity of the components changes the proportion between ionic and neutral species, not being, however, the only factor with relevance for the interpretation of these PILs properties. The lower the extent of the acid-base reaction, the lower the ionicity of the PIL and the greater its tendency to deviate from the molar ratio of 0.5: 0.5. It was further concluded that the composition of the azeotropic mixture is also conditioned by the ability of the neutral (acid or base) forms to interact with the ionic pair. In the specific case of PILs derived from the combination of DBN, DBU, DMTHP with carboxylic acids, it has been found that the azeotrope is richer in the acid because of its ability to establish hydrogen bonds with the ion pair and that their azeotrope composition is gradually richer for acids with longer alkyl chains, with the indication that the composition converges to the ratio of 0.33 (3): 0.66 (6) (1 base to 2 acids).

Acknowledgments

Aqui expresso a minha gratidão e apreço a todas as pessoas que de alguma forma me ajudaram a conseguir terminar esta etapa da minha vida. Foram “apenas” quatro anos que passaram, mas todas as pessoas que aqui referirei e mesmo outras que aqui possam não aparecer, agradeço tudo que me deram durante este período.

Começo por agradecer ao meu orientador, Professor Luís Belchior Santos pela oportunidade e confiança que me deu para ingressar no seu grupo, por tudo que me ensinou a todos os níveis e por saber dar independência quando ela é necessária ao nosso próprio crescimento científico. Obrigado!

Agradeço ao Dr. Carlos Lima (o “Maior”), meu coorientador e alguém que admiro muito não só pelo companheirismo, amizade e diversão como também pela aprendizagem, discussões e comentários ao longo destes anos. Que a Ciência te mantenha por muitos anos!

Ao Professor João Coutinho, Professor André Melo, Drª Ana Paula e Sr. Carlos Torres pelos “*insights*” e ajuda a vários níveis ao longo desta tese e pelo “*know-how*” em alguns dos tópicos abordados neste trabalho. Muito Obrigado!

Agradeço à Fundação para a Ciência e Tecnologia (FCT) e entidades associadas pela bolsa de PhD concedida (SFRH/BD/94211/2013).

A todos os meus colegas e amigos, sem ordem específica, incluindo pessoas como: Nana, Iuliia, Bárbara, Zé Carlos, Nuno, Rita, Bruno, Inês, Juliana, Isabel, Diogo, Ana etc. que de alguma ou outra forma me foram apoiando e ajudando ao longo destes anos.

Aos meus familiares, em especial aos meus pais, António e Aldevina, aos meus irmãos Pedro e Diogo, por todo o apoio, amor, compreensão e paciência que tiveram ao longo destes anos. Ao meu querido Avô, que já não se encontra fisicamente entre nós, mas está comigo todos os dias. Tu sabes! Sem todos vocês não estaria aqui hoje e não seria quem sou. Muito Obrigado! Um agradecimento também à Srª Maria Belen e Sr. Manuel por tudo que me deram ao longo destes anos sem sequer hesitar. Obrigado!

Por fim, o agradecimento final para a pessoa que me ajudou a despertar/acordar para este Universo e a ter uma visão, objectivos e curiosidade por Ciência e pela Vida em si. Uma das melhores pessoas que tive a sorte de conhecer. Jessica, muito obrigado pelo teu amor, sinceridade, apoio, sentido de humor e responsabilidade, motivação e carinho. Sem ti, não conseguiria chegar aqui como estou hoje, nem concluir esta etapa da minha vida. Muito Obrigado por fazeres com que todos os dias tenham sentido! A ti dedico esta tese.

Contents

List of Tables

Abstract and Table of Contents

Chapter 3 – Synthesis and Characterization

Chapter 4 – Quantum Chemical Calculations

Chapter 5 – Phase Behavior and Heat Capacities of Protic Ionic Liquids

Chapter 6 – Speciation of Protic Ionic Liquids

Chapter 7 – Cohesive Energies of Protic Ionic Liquids

Annexes

List of Figures

Chapter 2 – Introduction

Chapter 3 – Synthesis and Characterization

Chapter 4 – Quantum Chemical Calculations

Chapter 5 – Phase Behavior and Heat Capacities of Protic Ionic Liquids

Chapter 6 – Speciation of Protic Ionic Liquids

Chapter 7 –Cohesive Energies of Protic Ionic Liquids

Annexes

Nomenclature, conversion factors and dimensions

Nomenclature

The IUPAC nomenclature for inorganic and organic compounds was adopted in order to simplify the text, abbreviations for the name of compounds were adopted in some cases.

Conversion factors

In table I are presented the Unit conversion factors and their values in SI units.

Table I. Unit Names and SI unit values.

Unit name	Symbol	Value in SI units
angstrom	Å	10^{-10} m
atmosphere	atm	101.325 x 10^{3} Pa
atomic mass unit	u	1.660 540 x 10^{-27} kg
bar	bar	1 x 10^{5} Pa
calorie	cal	4.184 J
hartree	H	4.359 748 x 10^{-18} J

Dimensions

Table II. presents the symbols, dimensions and SI units of some of the physical constants used across this dissertation.

Table II. Symbols, dimensions and SI units of some physical constants.

Physical constant	Symbol	Dimensions	SI units
area	*A, S*	L^2	m^2
Avogadro constant	N_A	N^{-1}	mol^{-1}
Boltzmann constant	*k*, k_B	$L^2.M.T^{-2}.\Theta^{-1}$	$J.K^{-1}$
density	*ρ*	$L^{-3}.M$	$kg.m^{-3}$
energy	*E, U*	$L^2.M.T^{-2}$	J
energy density	*u*	$L^{-1}.M.T^{-2}$	$J.m^{-3}$
entropy	*S*	$L^2.M.T^{-2}.\Theta^{-1}$	$J.K^{-1}$
force	*F*	$L.M.T^{-2}$	N
frequency	*υ, f*	T^{-1}	Hz
gravitational constant	*G*	$L^3.M^{-1}.T^{-2}$	$m^3.kg^{-1}.s^{-2}$
hamiltonian	*H*	$L^2.M.T^{-2}$	J
heat capacity	*C*	$L^2.M.T^{-2}.\Theta^{-1}$	$J.K^{-1}$
length	*L, l*	L	m
mass	*m, M*	M	kg
molar gas constant	R	$L^2.M.T^{-2}.\Theta^{-1}.N^{-1}$	$J.mol^{-1}.K^{-1}$
Planck constant	h	$L^2.M.T^{-1}$	J.s
pressure	*p*, P	$L^{-1}.M.T^{-2}$	Pa
temperature	T	Θ	K
time	t	T	s
volume	V, υ	L^3	m^3
weight	W	$L.M.T^{-2}$	N
work	W	$L^2.M.T^{-2}$	J

Constants and units

The recommended (CODATA) [0.1] values for the physical constants used in this thesis are presented in table III.

Table III. CODATA recommended values, symbols and units for some physical constants.

Physical Constant	Symbol	Recommended Value	Unit
Speed of light in vacuum	c	299 792 458	$m \cdot s^{-1}$
Planck Constant	h	6.626 068 76(52) $x10^{-34}$	$J \cdot s$
Electron mass	m_e	9.109 381 88(72) $x10^{-31}$	kg
Proton mass	m_p	1.672 621 58(13) $x10^{-27}$	kg
Avogadro Constant *	N_A	6.022 140 76 $x10^{23}$	mol^{-1}
Molar gas Constant	R	8.314 462(15)	$J \cdot K^{-1} \cdot mol^{-1}$
Boltzmann Constant	k	1.380 650 3(24) $x10^{-23}$	$J \cdot K^{-1}$
Stefan-Boltzmann Constant	σ	5.670 400(40) $x10^{-8}$	$W \cdot m^{-2} \cdot K^{-4}$

Note: The digits in parentheses represent the 1σ uncertainty in the previous two quoted digits.
[0.1] – www.codata.org in 13rd February 2017
* - www.iupac.org in 31st January 2018.

CHAPTER 1

Aim and Organization of the Thesis

1. Aim and Organization of the Thesis

About 300 000 years ago [1.1], the anatomically modern *Homo sapiens* rise in Africa, using the remarkable fire as a source of heat and energy. Short after that, several waves of migration ventured out of Africa and populated most of the world until nowadays. This ability of our species to use, change and affect the environment to our needs is the crucial reason for our unparalleled, at least that we know of, evolutionary success. We are, step by step, shortcutting the lines of natural selection/evolution by using the resources that our planet gave and still give to us. However, if we want to secure the future of our species and future generations, and also of the species around us, we must change our behavior and learn from our past and mistakes. We have to manage better the resources that our planet has, in a more sustainable and "greener" way improving our way of thinking and of life. Modern today's life, economy and society are basically based and built around crude oil and its value. [1.2] Most of both our transportation chemicals and fuels are derived from ancient biomass that harvested solar energy millions of years ago. These resources are non-renewable! However, only if evaluated on a time-scale relevant to us, humans. When global petroleum extraction reaches its maximum it will result in an inevitable subsequent decline in the use of fuels. Regardless of when this event happens – or has happened already – we need to find sustainable alternatives to be prepare the future generations for the future. [1.2] There are, nowadays, several promising alternatives to fossil-based fuels. [1.3] Its fate, however, depends on our advances in harvesting the required energy from renewable sources. Biomass, a renewable source can be biological material from recently living organisms. Plant biomass, and especially wood biomass, is of interest due to both its availability (lots of wood biomass in our planet) and the chemistry of its three major components: cellulose, hemicellulose, and lignin.

Cellulose, the most abundant biopolymer on earth is composed of glucose monomers, and it is also the main constituent of wood. This aspect, combined with the fact that wood is renewable and non-edible for humans, it represents an alternative and still viable source of crude oil. In addition, the hexose sugar units contained in cellulose can also be fermented to yield bioethanol - that can be used as a greener fuel for transportation for example. Although wood cellulose has the potential to serve as feedstock for both biochemicals and biofuel, a far more precious asset is hidden in its molecular structure, wood cellulose contains highly crystalline regions - known as nanocrystals - with tensile properties that rival those of Kevlar® [1.4] and these nanocrystals can potentially be used to produce biocomposites with outstanding

mechanical abilities. However, an important note is that the presence of lignin (a class of complex organic polymers that form important structural materials in biomass) is a major barrier for the efficient processing of wood cellulose, and environmentally-benign methods are required to separate wood lignin from its cellulosic, viz. cellulose and hemicellulose.

1.1. Motivation

Until some years ago, the search for ILs, aprotic or protic ones, with cellulose-dissolving ability has mainly been based on trial and error. The goal of several works is to identify structural similarities among cellulose solvents in order to propose alternative ILs for enhanced cellulose dissolution. It is known that both IL cations and anions are important for the efficient dissolution of cellulose. IL ions that are found in cellulose-dissolving ILs were already identified and compared to both nondissolving ILs and traditional cellulose solvents. [1.5] Structural analysis of the native cellulose crystal lattice reveals that only one specific type of H–bond must be cleaved to achieve polymer chain separation.

It was proposed by Ken Marsh and his group [1.5] that efficient cellulose solvents are able to arrange their dipoles in a favoured geometry, allowing them to successfully compete with the strong H–bond networks of native cellulose. It is suggested that mixtures of ILs and salts, with small-sized ions such as lithium chloride, could result in highly efficient cellulose solvents that are more environmentally friendly than traditional solvents. [1.5] In general, ILs need to have the following optimal characteristics to have a more favourable cellulose dissolution:

Base/ Cation: - Ability to delocalize the positive charge;
- Aromatic heterocycle;
- Second heteroatom in an aromatic ring;
- Inherited dipolar characteristics.

Acid / Anion: - Ability to act as an H-bond acceptor;
- Substituents should not be bulky or too much hydrophobic;
- Either small in size or ability to offer several H-bond acceptor sites.

According to the current information available in literature, ILs have the potential of overtaking the conventional methods used in the biorefinery industry, as shown by

their large removal capabilities of lignin from the lignocellulosic biomass, up to 50 wt%, in combination with their ability to dissolve cellulose, up to 25 wt%. [1.6] Next to their high extraction and dissolution capacity, various studies have shown their high thermal stability, thus ensuring the use of ILs at the high temperatures needed for the extraction of lignin and dissolution of cellulose. Nevertheless, despite their advantages, ILs also have some disadvantages, which should be resolved or further investigated before scale-up or implementation in industry takes place. The biggest disadvantage is probably the production price of AILs. The combination of the low reaction yields and the use of conventional solvents leads to the need of extended purification steps increasing their price per ton. Thus, better procedures should be devised to decrease the production price. Moreover, ILs often have moderate to high viscosities, which hampers their full potential to dissolve cellulose due to a large decrease of mass transfer. PILs are promising alternatives compared to AILs. They are able to dissolve cellulose (up to 18 wt%) and to extract lignin (80 wt%) from lignocellulosic biomass. [1.6]

For some of the PILs studied in this work, the following results concerning their ability to dissolve cellulose were reported [1.7-1.8]:

PIL – Temperature / time / solubility / source of cellulose
[DBNH][MeCOO] – 80 ºC / 18 hours / 5 wt% - Eucalyptus pulp
[DBNH][EtCOO] – 80 ºC / not given / 16 wt% - Eucalyptus pulp
[DBUH][MeCOO] – 80 ºC / 18 hours / 5 wt% - Eucalyptus pulp
[DBUH][EtCOO] – 80 ºC / not given / 16 wt% - Eucalyptus pulp
[DMTHPH][EtCOO] – 80 ºC / 18 hours / 5 wt% - Eucalyptus pulp
[TBDH][EtCOO] – 80 ºC / 18 hours / 5 wt% - Eucalyptus pulp
[TMGH][EtCOO] – 100 ºC /10 min / 5 wt% - Microcrystalline cellulose (DP381)
[TMGH][nPentCOO] – 100 ºC/18 hours/0 wt%- Microcrystalline cellulose (DP381)

The major advantage of PILs over AILs is their easier and cheaper preparation. While for the AILs a complete synthesis with extended purification is needed, only mixing of the acid and base is required for the preparation of a PIL. A disadvantage of the preparation is the fact that it is exothermic, which introduces the need for cooling. At a lab scale this is a minor problem, as observed in this thesis, but heat development can cause major problems during the upscaling process. The higher volatility of PILs is often noted as a big advantage but could be explored for improving solvent recycling. Higher volatility can make applications such as distillation less energy-costly. Furthermore, only

few publications have discussed the handling of cellulose and lignocellulosic biomass with PILs.

1.2. Aim of the work and scientific context

Biocompatible composites, generated from renewable biomass feedstock, are regarded as promising materials that could replace synthetic polymers and reduce global dependence on fossil fuel sources. Wood cellulose, the most abundant biopolymer on earth, holds great potential to this purpose. [1.9] To unlock the entire scope of potential benefits of this feedstock, the wood components—namely cellulose, hemicellulose and lignin—need to be separated and processed individually. This thesis aims to increase our understanding of the interaction between protic ionic liquids and biomass, in order to develop superior biomass processing techniques. Understanding how protic ionic liquids are able to dissolve biomass should pave the way for finding new and better solutions for using biofuels.

Recently, there has been an increasing interest in the use of PILs for cost-effective and environmentally benign dissolution and processing of biomass like cellulose and wood. [1.10-1.11] The development of effective cellulose extraction methods and suitable cellulose dissolution systems is of utmost importance, but is also a great challenge for R&D in order to attain the knowledge needed for efficient process design. [1.10-1.11] In this context, ILs present particular properties, such as: large liquid temperature ranges, high thermal and chemical stabilities, high thermal conductivities, and low vapor pressures, which among their advantages allow fluid recycling in many processes. One important attribute of PILs and ILs is their enhanced ability to dissolve the most diverse compounds. [1.12-1.14] The research performed until now is mainly focused on the well-known aprotic ILs, and less effort has been invested in exploring PILs for this purpose. PILs are recently gaining interest as potential solvents in the dissolution of biomass in part, because they are relatively cheap and distillable. [1.10, 1.15] In order to make the process more economical, ionic liquids need to be recycled and separated from the product streams. Hence, for process design, it is very important to know their volatility, enthalpies of vaporization, nature of the gaseous phase, and information concerning binary mixtures of ILs with water and other solvents (solubility, excess properties, phase diagrams). Due to the large array of possible PILs, thermophysical properties for most of them are still unknown or poorly characterized, and a complete database is far from being accomplished.

Hence, the primary aims of this Ph.D. thesis were to develop a concept that explains the composition and speciation of protic ionic liquids and focus on the molecular understanding of physicochemical properties and cohesive energies of protic ionic liquids, important for their application.

The effect of different base/acid compositions and the identity of those bases and acids on the cohesive energy, volatility and speciation of PILs was explored. By speciation is meant the equilibrium proportion of all neutral species and ions that compose the PIL at given set of conditions. The present work is concerned with the thermophysical study of pure PILs having a equimolar (1:1) and non-equimolar (excess of one component) proportions of base and acid. It focuses on the molecular understanding of their physicochemical properties, chemical-reactivity and evaluation of molecular interactions in PILs that may be relevant for biomass processing. It also contributes to an increase in the experimental database of thermophysical properties of PILs, which is a valuable asset for their efficient application in biomass processing.

1.3. Organization of the Thesis

The thesis is organized in nine chapters. After the brief introduction to the aim and organization of the thesis in the present **Chapter 1 – Aim and Organization of the Thesis**, the subsequent chapters are organized as follows:

Chapter 2 - Introduction presents an introduction to the subject. In the first part of the chapter, some concepts are exposed: what are ionic liquids and what is their relation to the concepts of energy and sustainability. The differences between aprotic (AILs) and protic ionic liquids (PILs). How PILs are formed/synthesized, their unique physicochemical properties, structural organization and the most important properties and applications of each class are presented. The second part of the chapter starts with some fundamental concepts about biomass and biomass processing and after that, a discussion about biomass as a viable source of energy and the potential use of PILs for biomass processing is presented.

Chapter 3 – Synthesis and Characterization shows a summary of the compounds studied, their synthesis and purification procedures and the characterization methodologies. Additional materials (calibrants and test compounds) are also shown.

In **Chapter 4 – Quantum Chemical Calculations**, the quantum chemical calculations are presented as a complement to the energetic study and ion pair equilibria of PILs. Several calculations were made using three distinct methods and a new approach, concerning the accessible surface area, is presented. The results obtained show that the ion pair is the preferred species in all PILs.

In **Chapter 5 – Phase Behavior and Heat Capacities of Protic Ionic Liquids**, the phase behavior and heat capacities (at 298.15K and at different temperatures) are presented and discussed considering the effect of the base and acid. Some trends exploring their effects were found and the results were also used to evaluate their liquid phase structure, the possibility of nanostructuration and the PILs iconicity. Two equations to calculate the heat capacities of the same families of the studied PILs were also deducted from the obtained results.

Chapter 6 – Speciation of Protic Ionic Liquids presents the speciation issue in protic ionic liquids. How this effect influences their behavior and composition is discussed considering the vapor pressures measurements for the PILs studied. For the first time, the equilibrium proportion of acid and base was determined and correlated with the acid and base strength.

In **Chapter 7 – Cohesive Energies of Protic Ionic Liquids** the cohesive energy study is presented. The effects of different bases, acids and composition are explored in detail. The results show clearly how the composition of a protic ionic liquid affects its vaporization properties and gave insights about the iconicity and speciation of the PILs in the liquid and gas phases.

Chapter 8 – Concluding Remarks and Perspectives presents a summary of the final remarks of this thesis and some future perspectives and work that can be done in this area.

Annexes compiles all the supporting information concerning spectral (FTIR and NMR) and phase behavior data, and quantum chemical calculations results.

With the work developed in this thesis the following outputs were achieved:

Papers

I. Vaporization of protic ionic liquids derived from organic superbases and short carboxylic acids. (Published *Phys. Chem. Chem. Phys*. **2017**, 25, 16693-16701.)
II. Experimental evidence for azeotrope formation from protic ionic liquids. (Published *Chem. Phys. Chem.* **2018**, doi.org/10.1002/cphc.201800335)
III. Heat capacities of DBN and DBU based protic ionic liquids. (Submitted to *J. Mol. Liq.*)
IV. Evidence of nanostructuration in protic ionic liquids. (Manuscript in preparation)
V. Composition effect on cohesive energies of protic ionic liquids: speciation effect. (Manuscript in preparation)
VI. Vaporization and Speciation of DMTHP-based protic ionic liquids. (Manuscript in preparation)

Oral Communications

I. Speciation of Protic Ionic Liquids
ECTP21st, European Conference on Thermophysical Properties
September 2017, Graz, Austria.

Posters

I. Cohesive Energy of Protic Ionic Liquids
ILMAT IV, 4th International Conference on Ionic Liquid-based Materials
October 2017, Santiago de Compostela, Spain.

II. Thermophysical Properties of Protic Ionic Liquids
ECTP21st, European Conference on Thermophysical Properties
September 2017, Graz, Austria.

III. Cohesive energy trends in distillable protic ionic liquids
ILWS, 1st Ionic Liquids Winter School
February 2017, Porto, Portugal.

IV. Cohesive energy of protic ionic liquids
6 th EuCheMS, European Chemical Sciences.
September 2016, Sevilha, Spain.

V. Thermophysical properties of protic ionic liquids
19th Symposium on Termophysical Properties
June 2015, Boulder, United States of America.

1.4. References

[1.1] Hublin, J.; Ben-Ncer, A.; Bailey, S. E.; Freidline, S. E.; Neubauer, S.; Skinner, M. M.; Bergmann, I.; Le Cabec, A.; Benazzi, S.; Harvati, K.; Gunz, P., *Nature* **2017**, 546, 289-292.

[1.2] Hymel, M. L., *Macquarie Law Journal* **2007**, 7, 125-153.

[1.3] Wendt, H.; Gotz, M.; Linardi, M., *Quím. Nova* **2000**, 23, 538-546.

[1.4] Wallace, R., *Nanocellulose Pilot Plant to be Unveiled at Forest Products Lab*, **2012**, Lab Notes, United States Department of Agriculture.

[1.5] Pinkert, A.; Marsh, K. N.; Pang, S., *Ind. Eng. Chem. Res.* **2010**, 49, 11121.

[1.6] van Osch, D. J. G. P.; Kollau, L. J. B. M.; van den Bruinhorst, A.; Asikainen, S.; Rocha, M. A. A.; Kroon, M. C., *Phys. Chem. Chem. Phys*, **2017**, 19, 2636.

[1.7] King, A. W.; Asikkala, J.; Mutikainen, I.; Jarvi, P.; Kilpelainen, I., *Angew. Chem.* **2011**, 123, 6425.

[1.8] Parviainen, A., King, A. W.; Mutikainen, I.; Hummel, M.; Selg, C.; Hauru, L. K. J.; Sixta, H.; Kilpelainen, I., *ChemSusChem*, **2013**, 6, 2161.

[1.9] Pinkert, A.; Goeke, D. F.; Marsh, K. N.; Pang, S., *Green Chem.* **2011**, 13, 3124-3136.

[1.10] Holm, J.; Lassi, U., *Ionic Liquids: Applications and Perspectives*, ed. A. Kokorin, InTech, **2011**, 545-560.

[1.11] Pinkert, A.; Marsh, K. N.; Pang, S.; Staiger, M. P., *Chem. Rev.* **2009**, 109, 6712-6728.

[1.12] Oliveira, F. S.; Freire, M. G.; Pratas, M. J.; Pauly, J.; Daridon, J. L.; Marrucho, I. M.; Coutinho, J. A. P., *J. Chem. Eng. Data* **2009**, 55, 662–665.

[1.13] Zakrzewska, M. E.; Bogel-Lukasik, E.; Bogel-Lukasic, R., *Energy & Fuels* **2010**, 24, 737–745.

[1.14] Rosatella, A. A.; Branco, L. C.; Afonso, C. A. M., *Green Chem.* **2009**, 11, 1406–1413.

[1.15] Angell, C. A.; Byrne, N.; Belieres, J. P., *Acc. Chem. Res.* **2007**, 40, 1228-1236.

CHAPTER 2

Introduction

2. Introduction

In the past two decades the Ionic Liquids (ILs) field has grown significantly, with a strong focus on their unique properties that allow their use in specific applications. ILs are salts composed only of ions that melt at low temperatures (significantly lower when compared with other ionic salts), without decomposing or vaporizing. They have several properties (liquid range of around 300 ºC (-96 ºC to 200 ºC), excellent solvents, thermally stable under conditions up to 200 ºC, no significant vapor pressure at room temperature, etc.) that are suitable for several areas and applications. Low-temperature ionic liquids can be compared to ionic solutions, liquids that contain both ions and neutral molecules, and in particular to the so-called deep eutectic solvents, mixtures of ionic and non-ionic solid substances which have much lower melting points than the pure compounds. [2.1]

2.1. Protic ionic liquids (PILs)

Protic ionic liquids (PILs) are a subclass of ILs that are synthesized through the stoichiometric neutralization reaction of a Brønsted acid with a Brønsted base. An important feature of PILs is that they have an available proton on the cation. By convention, the other ILs can be classified as aprotic (AILs), although there are some other subsets similar to PILs that are functionalized such that they have an available proton that is typically located on the anion, the Brønsted-acidic ILs.

2.1.1. Formation of Protic ionic liquids

The simplicity of PILs synthesis through proton transfer from a Brønsted acid to a Brønsted base is an inherent characteristic of these ILs (equation 2.1). Yet, depending on the acid and base used, this proton transfer may be only partial, such that there is a portion of neutral molecular precursors remaining in the solution. Consequently, in the last few years there has been considerable effort conducted into quantifying and understanding the fundamental characteristics of these ILs, like the degree of proton transfer, ionicity, polarity and some other related properties such as conductivity. [2.2]

$$B + HA \leftrightarrow [BH][A] \qquad \textbf{(2.1)}$$

2.1.1.1. Synthesis, ionicity and proton transfer

The synthesis of PILs is generally a neutralization reaction with addition of a Brønsted acid to a Brønsted base. After that, the resulting solution is dried to remove any volatile impurity present, such as water for example. The proton transfer can be incomplete, leading to some remaining molecular neutral species within the PIL. In addition, the drying process is likely to remove more of one component than of the other, leading to a nonstoichiometric mixture enriched, usually, in the less volatile precursor species. [2.2]

A strong correlation between the extent of proton transfer and the difference in pK_a between the acid and base precursors can be found. [2.3] The effect of using a weaker or a stronger acid was already investigated using the 1-hexyl-3-methylimidazolium (C_6mim) cation paired with acids of increasing strength. The resulting stoichiometric mixtures were nearly completely ionic for strong acids such as bis(trifluoromethylsulfonyl)imide (NTf_2) and trifluoromethanesulfonate (TfO). The less acidic trifluoroacetic acid (TFA) led to a mainly ionic mixture, whereas the weaker formic and acetic acids had poor proton transfer. [2.4] Notwithstanding, they still showed proton conductive behavior, and it was proposed that they should be defined as “pseudo-protic ILs”. [2.2; 2.5]

Burrell et al. reported an alternative method for the synthesis of PILs, where the acid and base precursors were dried before their use and then added stoichiometrically to a rapidly stirred reaction vessel. [2.6] They noted that conducting the synthesis in this manner minimized the exothermic heat resulting from this reaction, and through sufficiently slow addition of the precursors enabled heat dissipation during the synthesis. [2.6] These PILs were investigated using ^{15}N NMR to show that the proton transfer had occurred as expected. An important conclusion is that the species were all ionic, however, many were in the low-ionicity region of the Walden plot, which is basically the graphical representation of $\log \Lambda = f(\log(1/\eta))$, where Λ is the equivalent conductivity of the PIL and η its viscosity. Still, it was suggested that there must be a significant proportion of electrically neutral species in the mixture, such as ion pairs. [2.6] Of the series of 48 acid−base combinations prepared by Burrell et al. from dried precursors, only 18 formed homogeneous liquids and 12 formed biphasic mixtures. [2.6] These biphasic mixtures did not occur when an additional solvent was present, and for some acid−base pairs the biphasic mixture could be converted to a homogenous product by heating above the melting point. The biphasic mixture of triethylamine or tributylamine with acetate was characterized as consisting of an acid-rich salt solution on the bottom with a predominantly unreacted amine layer on top. [2.6-2.7] It appears that the acetate anion does not always support the 1:1 stoichiometry, which is consistent with it forming biphasic mixtures with various amines

under certain synthesis conditions as stated above. The combination of N-methylpyrrolidine with acetic acid was shown to have low ionicity for the 1:1 salt and highest ionicity for the 3:1 mole ratio of acid:base, which was suggested to be similar in composition to the bottom layer of the biphasic solutions. [2.8] Based on this, the following question could be raised: These salts with acid:base ratios different from 1:1 ratio be classified as a PIL or are they only protic salts? While ILs are often described as consisting solely of ions, their ionic conductivity is often less than expected. As an alternative, a proportion of the ions may be present as ion pairs or aggregates, and for PILs there may be some neutral molecular precursors present, all of which lead to lower ionic conductivity. The ionicity of ILs has been proposed by MacFarlane et al. to be “the effective fraction of ions available to participate in conduction”. [2.9] The ILs ionicity was discussed by Watanabe et al., specifically regarding to their physicochemical properties and solvent polarity, though there was limited information concerning PILs. [2.10] The PILs lower ionicity, when compared with aprotic ILs, was suggested to be due to the stronger ion−ion interactions. [2.2; 2.11]

The difference between PILs and protic salt solutions was discussed by Canongia Lopes and Rebelo in terms of their azeotropy, where the proportion of base:acid in the vapor phase is identical to that in the liquid phase. [2.12] In particular, for “weak” PILs, it can be expected that there will be a significant proportion of neutral species, which upon drying or degasification of the PIL will lead to a liquid that is very unlikely to be stoichiometric. [2.12] The reversible proton transfer process in PILs can be exploited, and it has been shown that some PILs can be developed into ionic media buffers through addition of a non-ionic neutral species, which can be converted into the IL through exchange of the counterion, for example, through the addition of the protonated form of the anion. [2.13] A new class of PIL-like compounds was reported by Johansson et al., which were described as anion amphiprotic and involve the acid−base neutralization of methylcarbonate with trifluoromethanesulfonamide. [2.14] These compounds do not contain an acidic proton and are chemically more stable than conventional PILs, though not having a reversible reaction back to their neutral precursors. [2.2]

2.1.1.2. Intermolecular forces

Between the cations and anions in PILs, their interactions consist of a mixture of hydrogen bonding, Coulomb charge and dispersion forces. These have been investigated using a variety of spectroscopic techniques and theoretical calculations. In 2012, Dong and Zhang wrote a review on hydrogen bonds in ionic liquids and focus on aprotic ILs,

although it also includes PILs. [2.15] The hydrogen bonds that are present in PILs vary between strong linear hydrogen bonds and weaker bent ones. The hydrogen bonds angles are a consequence of the PIL nanostructure due to some alkyl chain segregation. As the proportion of linear hydrogen bonds increases, the ionic liquid becomes more “solid like”. [2.16] It was shown that hydrogen bond strength correlates well with the melting and glass transitions in PILs [2.16] and the presence of aromatic rings attached to the imidazolium ring was observed to increase the cohesive energy of these family of PILs as compared to their imidazolium counterparts. [2.17]

2.1.2. Vapor phase

Ionic liquids are often referred to as non-volatile or having a negligible vapor pressure, but this is not always true. For example, several PILs can be distilled, as reported by Angell et al. in 2003, [2.3] and many boiling points have been reported for PILs, [2.3, 2.18-2.19] Though, there is conflicting indications in the literature for whether the gas phase of PILs consists only of the molecular neutral species, or whether molecular and ionic aggregates coexist. For some aprotic ionic liquids that can be distilled under vacuum without decomposition, [2.20] the gas phase consists of neutral ion pairs. [2.21-2.22] The made investigations until now correlate well with the expected extent of proton transfer, with only PILs with particularly large pK_a differences between the precursor acids and bases leading to both molecular and ionic aggregates, and hence the suggestion that they are evaporating, at least to some extent, as ion pairs. This proposes that most PILs are like aprotic ILs, which have a vapor phase consisting of neutral ion pairs with no free ions or larger clusters detected. [2.20-2.21, 2.23]

2.1.3. Physicochemical characterization

An important parameter for PILs in many applications is their ability to conduct protons. The ΔpK_a between the acid and base precursors of the PIL has been used as an indication of the degree of proton transfer. A correlation was reported by Watanabe et al., which showed that the open circuit potential for hydrogen fuel cells increases with increasing ΔpK_a until $\Delta pK_a \approx 17$, then decreased after that. [2.24] This behavior was attributed to the PILs that have a low ΔpK_a having more neutral species present, and hence poorer electrochemical properties. The poor electrochemical behavior for the PILs with

very high ΔpK_a values was attributed to the strong hydrogen bonds between the base and the "available" hydrogen of the acid, leading to poor proton activity. [2.24] Thus, there appears to be an optimal range of ΔpK_a values for PILs to have maximum electrochemical activity. [2.2]

2.1.4. Proton activity

The pH scale is routinely used to measure the proton activity in aqueous solutions, however, the pH scale is not valid in neat ionic liquids or highly concentrated ionic liquid solutions. So, alternative measures for proton activity have been developed, although currently a standard method does not exist. Some of these techniques include the use of acid/base probe molecules that are sensitive to the proton activity present. These probes that have been used include, for example, the indicator phenol red, [2.13] the dye 4-nitroaniline [2.25] and Reichardt's dye, [2.26] all of which had their level of protonation determined previously using UV/Vis spectra. The dye 4-nitroaniline probe was used to provide a measure of the Hammett acidity functions for the addition of formic, acetic, or propionic acid into PILs that contain a carboxylate anion. The degree of acidity of the acids in the PILs was propionic > acetic > formic, which is the opposite to what is observed in water, and was attributed to the stabilization, in some degree, of the PIL cation toward the conjugate base of the acid. [2.25] A review of the Brønsted acidity of various solvents and including some considerations for the characterization of the acidity of ILs, emphasised the inherent differences from aqueous systems, and that it cannot be assumed that aqueous data is relevant for IL systems. [2.2; 2.27]

The δ(N−H) proton chemical shift, as measured using NMR, has been proposed by Angell et al. to provide a measure of the proton activity. [2.28-2.29] This technique is sensitive to water content, so it requires anhydrous conditions, with water contents less than 1000 ppm. [2.29] Another way to measure the proton activity has also been obtained from the hydrogen-redox potential for hydrogen saturated PILs by Angell et al., where the difference between the potentials required to remove a proton from the acid (cation) and to reprotonate the base (anion) correlated well with the ΔpK_a of the acid and base precursors yielding a good measure of the proton activity in the PILs. [2.30]

2.1.5. Structural organization

ILs, aprotic or protic, can possess a complicated structure in the liquid phase, like what happens with other similar molecular solvents such as alcohols, [2.31-2.33] amino-

alcohols, [2.33-2.34] and amides. [2.35] When ILs have sufficiently long alkyl chains, typically 2−4 carbons minimum, they segregate into polar and nonpolar domains. [2.36-2.38] This intermediate-range order nanostructure in the bulk liquid have previously been reviewed in studies including protic and aprotic ionic liquids, focusing on the bulk [2.39] and surface structure of ILs. [2.2; 2.40]

A good understanding of the ILs mesostructure is important for determining how they interact with other solutes such as water, [2.41-2.42] molecular solvents, [2.43] and amphiphiles. [2.39] For instance, in materials synthesis the use of silver-containing ILs to form colloidal silver could only be achieved from the strongly nanostructured Ag-(octylethylenediaminium)$_2$ TFSA and poorer results were obtained with analogous ILs with shorter alkyl chains, showing the importance of the alkyl chains and segregation in the ILs properties [2.44] Structured silica has been synthesized using the non-ionic block copolymer P123 and ethylammonium nitrate (EAN) leading to micropores and mesopores with average sizes of 1.0 and 4.5 nm, respectively. [2.45] These micropores were associated with the nanostructure of the EAN, and the mesopores from a P123−EAN lyotropic liquid crystal phase. Previously, a strong correlation has been identified between the ability of ILs to support amphiphile self-assembly and their nanostructure. [2.39] As the nonpolar domain size in the IL increases, with the increase of the alkyl chain for example, the hydrocarbon solubility increases, which leads to a lower driving force for amphiphile self-assembly. Yet, for non-structured ILs the hydrocarbon solubility is lower, and in some cases too low to enable sufficient amphiphile solubility to reach the critical aggregation concentration (CAC). [2.39]

2.1.6. Properties and applications

In the past few years, the interest in PILs and their unique properties for several applications has increased rapidly, mainly due to their unique properties in the liquid phase. [2.2] PILs can be used in:

Electrochemistry

The PILs inherent nature of having protons available for proton conduction, without the need to be acidic, makes them highly suitable as electrolytes, for fuel cells and batteries for example. [2.46] The PILs proton conductive properties can be tailored for specific applications to achieve wide electrochemical windows, high conductivity, and/or

other desirable properties. This all can be done by simply changing the structure of the cation or anion, or even through the presence of an additional solvent.

Chromatography

The PILs are being used as replacements of organic solvents as the mobile phase in liquid chromatography. Some of them were also trialed for separating proteins and showing that they are able to retain the tested proteins in their native state. [2.47-2.48]

Liquid-liquid extraction

Some reports concerning the use of aprotic ILs in the field of liquid−liquid extractions and separations have already been published. [2.49] Many of the procedures using AILs are successful due to the low solubility of the IL in water. In contrast, few studies that use PILs for liquid−liquid extraction or separation were made, maybe because of their high miscibility with water, meaning that either novel hydrophobic PILs are required or the PILs must be used in extraction from hydrophobic media. The solubility parameters of nonpolar solutes in a series of ionic liquids were reported, the ILs were mostly aprotic, but also included the protic EAN. [2.50]

In 2011, Verevkin report the activity coefficients of solvents in a protic ionic liquid. [2.51] EAN as the PIL was used and Verevkin recognised that the vapor pressure of EAN was significantly low so that it could be treated as “negligible” (similar to AILs) for activity coefficient measurements. [2.51] This work purpose was to show that activity coefficients can be measured in PILs using the same methods and assumptions as for AILs. The activity coefficients provide a quite good insight into the interactions established between ILs and solutes, with large activity coefficients corresponding to weak interactions between them. [2.51]

Gas capture

Nowadays, there is a solid need for solvents capable of absorbing efficiently CO_2 and SO_2 and also other greenhouse gases, and some ILs are promising candidates for this purpose. [2.52-2.54] Until know, predominantly aprotic ILs have been trialed, although the gas solubilities in some few PILs have also been reported. [2.55-2.60] The CO_2 solubility was determined in a series of hydroxyl-containing ammonium PILs, with the highest solubility observed in triethanolammonium lactate and tri-(2-hydroxyethoxy)ammonium acetate. [2.61] Another series of PILs with multiple amine

moieties on the cations paired with formate, acetate, or chloride anions were used for CO_2 capture and the highest CO_2 capture was obtained for the neat PILs, and one aqueous PIL solution, was ~13 w/v %, which corresponds to a mole fraction comparable to that achieved with the commonly used methylamine solution with 30 wt % water. [2.59] A nice advantage was that the amine groups present in these PILs were less basic than their molecular counterparts, leading to lower binding energies to CO_2, and producing less alkaline and less corrosive solutions, and lower energies required for the desorption of the CO_2 and consequently re-use/recycling of the PILs. [2.59]

Solvents for biological media

Summers and Flowers reported some years ago that EAN suppressed aggregation of lysozyme and improved its folding and refolding ability. [2.62-2.63] Since that work, the stability and activity of a few proteins in a wide range of PILs have been explored, and many PILs have shown to be good stabilizers. PILs have also been shown to be beneficial in biocatalysis, as additives for protein crystallization, and to a lesser extent as solvents for lignin and cellulose for biomass conversion, as can be seen at the end of the present chapter. There are numerous reviews on the use of ILs in biological applications, although these have predominantly focused on aprotic ILs. More recently, these reviews have addressed the role of ILs in biomass conversion, [2.64] the use of ILs in protein assays, [2.65] as solvents for biopolymers, [2.66] and in the stability of proteins. [2.67-2.68]

Pharmaceutics

As a new and exploratory field, there are some PILs that are being synthesized from cations and/or anions, that are known to be pharmacologically active. The pharmaceutical activity of these ions includes antiinflammatory, analgesic, antifungal, and also anti-viral properties. Potentially pharmaceutically active PILs, protic molten salts, and complexes have been developed by Mirksov et al. [2.69-2.72], and generally, their synthesis, IR, NMR, and elemental analysis have been reported. MacFarlane et al. investigated the permeation of pharmaceutically active PILs through a model membrane (simulating the skin), to further understand how some PILs may permeate the skin. [2.73] Two of the PILs investigated had pharmaceutically active cations and anions of tuammoniumheptane salicylate and bromohexinium ibuprofenate; two more conventional PILs of butylammonium acetate and heptylammonium acetate were also studied. [2.73] It must be noted that not all Brønsted acid/Brønsted base pairs will lead to protic ionic liquids, and this was shown for pharmaceutically active precursors using a theoretical DFT

method. [2.74] The investigation included the amines triethanolamine, methyldiethanolamine, dimethylethanolamine, and trimethylamine, combined with acetic acid, hydrochloric acid, and three different arylheteroacetic acids. [2.74] On the basis of the interactions and binding energies, predictions were made for whether there would be proton transfer leading to PILs, or the formation of hydrogen-bonded complexes in these systems. The obtained data suggest that protic salts or hydrogen-bonded complexes would be formed with the triethanolamine, depending on which acid it was paired with, whereas the other amines would only lead to hydrogen-bonded complexes. [2.2; 2.74]

Toxicology

Over eighty ionic liquids were studied and their in vitro cytotoxicity was evaluated using human colon cancerous cells (Caco-2). The increasing of the alkyl chain on the cation increased the toxicity, whereas the presence of a COOH or ether group decreased it for certain ILs. The toxicity was strongly dependent on the anion, although this investigation only included aprotic ILs. [2.75] The toxicology of ten PILs containing selected combinations of ethanol-, diethanol-, or triethanolammonium cations with formate, acetate, propionate, butyrate, isobutyrate, or pentanoate has been reported and compared with commonly used imidazolium and pyridinium-type aprotic ILs. [2.76-2.77] Aquatic toxicity, biodegradability, and tests on enzyme and leukemia rat cells were conducted, with the PILs having EC50 values >100 mg/L and a good biodegradability rate. [2.76] Studies of terrestrial ecotoxicity of PILs and AILs through bioassays on various plants and soil microorganisms showed no toxic effects from the PILs, with the PILs having potential biodegradation in soil. [2.77] In contrast, the aprotic ILs were generally more toxic, with EC50 values orders of magnitude lower for all of the tests, and a greater resistance to biodegradation. [2.76-2.77] In general, shorter alkyl chains and less complex structures on the ILs led to lower toxicities.

Catalysis and organic synthesis

Protic ionic liquids as solvents and/or catalysts has been extensively studied for a wide variety of organic reactions. [2.78] In order to be used in many organic reactions the IL is generally required to be a Brønsted acid, and in less extent a Lewis acid or base. The PILs are Brønsted acidic due to the fact they have an available proton. In contrast, for aprotic ionic liquids, the Brønsted acidity requires a more careful design/selection of the ions to be used, either through the presence of a Brønsted acidic group on the cation, such as $^{-}SO_3H$, or an available proton on the anion, such as HSO_4^{-}.

The ILs used in organic synthesis and other applications involving catalysis for example, are frequently referred to as “task-specific” or “functionalized” because of these requirements, even though many of the ILs can be considered as “common ILs” and are used in a broad range of applications. It is known that for many organic reactions the determining factor for the design of the “optimal PIL” is the acidity or basicity required for the reaction. For example, it was found that the HSO_4^- anion is a good source of an active proton, EAN is a good acidic PIL, and that hydroxyl-containing cations and/or the lactate anion tend to provide a good basic environment in the PIL media. Another aspect that shows why the ILs are being used in organic synthesis is their potential as greener solvents/catalysts as compared to the existing molecular solvents. Several reviews of the green chemistry aspects in organic synthesis have discussed the role of ILs, there potential benefits, if the ILs are recoverable and reusable, etc. [2.79-2.83] The wide range of solvent properties within PILs (and aprotic ILs) enables a good solvent optimization for each reaction.

2.2. Biomass processing

2.2.1. Fundamental concepts

The basis of biomass are lignocellulosic materials, complex composite materials composed mainly of cellulose, hemicellulose, and lignin, even though some extractives like waxes and proteins are also present in smaller quantities. [2.84-2.86] The chemical composition of plants differs considerably and is influenced by both genetic and environmental factors. [2.87] The three main fractions of lignocellulosic materials exhibit different physical and chemical structures and are schematic shown in figure 2.1.

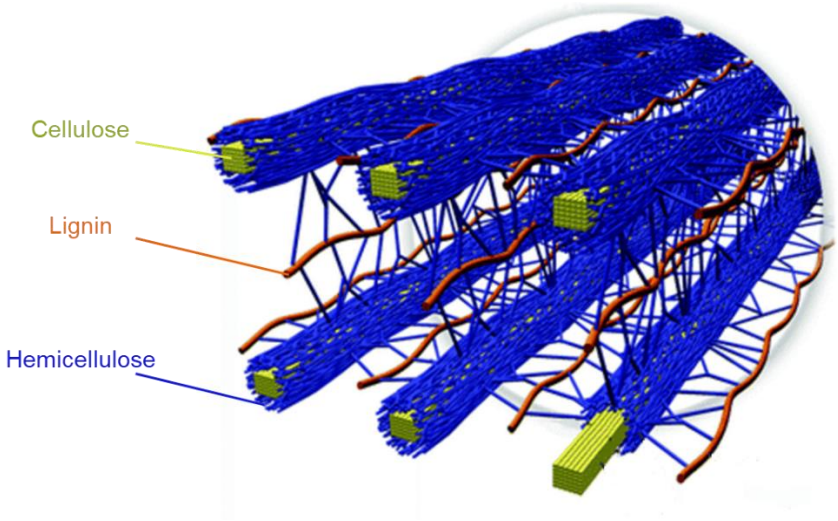

Figure 2.1. Scheme of the spatial arrangement of cellulose, hemicellulose, and lignin in the cell wall. Adapted from source [2.88].

Cellulose

Cellulose, the most common organic polymer, is considered an almost endless source of raw material for the increasing demand for environmentally friendly and biocompatible products. Common wood consists of up to 47 % m/m of cellulose, which is the main structural component of the primary cell walls of plants. [2.89] Although wood pulp remains the most important raw material source for cellulose, this biopolymer can also be extracted from algae, bacteria, and even annual crops. [2.90]

Cellulose is a linear polymer of cellobiose, which is composed of two glucose sugar units linked by glycosidic linkages (C-O-C) at the C1 and C4 positions (figure 2.2). The cellulose polymer chain length depends on the degree of polymerization (DP), which is the

number of repeating units of glucose. The DP can vary considerably from about twenty, in the case of laboratory-synthesized cellulose, to ten thousand or more for bacterial cellulose. [2.90-2.91] Each unit of glucose is rotated by 180º with respect to its neighbors, so that the structure repeats itself every cellobiose unit (represented in figure 2.2). The cellulose prevenient from wood contains approximately ten thousand units, and the polymer can reach a length of about 5 μm in the highly crystalline regions. [2.89] One of the chain end has a hemiacetal group at the C1 position, known as the reducing-end, while in the other side there is an alcoholic hydroxy (OH–) group on the C4 carbon position, referred to as nonreducing end.

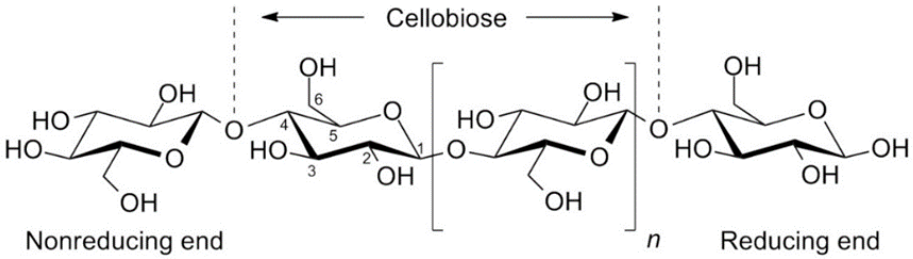

Figure 2.2. Schematic figure of a cellulose polymer chain. Adapted from source [2.92].

There are known at least seven different crystal structures of cellulose: I_α, I_β, II, III_I, III_{II}, IV_I, and IV_{II}. These differ mainly in their unit-cell dimensions, chain-packing, and H–bond interactions. Cellulose I and II are the most common forms and cellulose I (native) consists of parallel aligned chains, while cellulose II (regenerated), has antiparallel alignment. Although being thermodynamically more stable than cellulose I at standard conditions, the conformation of the hydroxymethyl group in cellulose II is not suitable for intermolecular H–bonding (example in figure 2.3), resulting in this allomorph being more susceptible to be attacked by a solvent. [2.93] Native cellulose is a linear but semicrystalline polymer, consisting of highly structured crystalline regions, known as microfibrils, and amorphous parts. The other components, such as lignin or hemicellulose, have branched structures. [2.94]

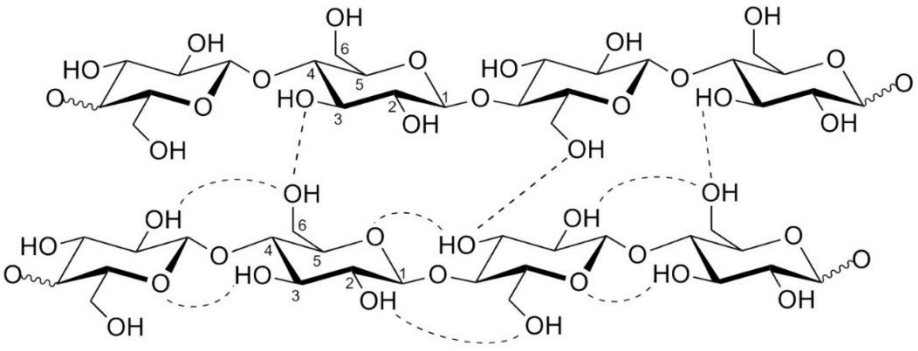

Figure 2.3. Schematic representation of the intra- and intermolecular hydrogen bonds in cellulose. Adapted from source [2.92].

In their natural state, about 40 to 70 cellulose chains are interconnected by H–bonds, between the hydroxymethyl at position C6 and the OH–group at position C3 of the adjacent chain, to form a microfibril. [2.95] These microfibrils are extremely stiff, with an elastic modulus of approximately 220 GPa in fiber direction and about 15 GPa perpendicular to it. [2.96] Both the strong glycosidic bonds and the large degree of intra- and intermolecular H–bonding in cellulose are responsible for its great chemical and mechanical stability and the hydrophilic character of cellulose is due to its numerous OH–groups. [2.91]

Lignin

Lignin is a natural, highly branched and amorphous polymer of high molecular weight, acting as the essential “glue” that gives plants their structural integrity and representing the second most abundant natural polymer on earth, after cellulose. [2.97] As an integral part of the secondary cell wall of plants, and due to its hydrophobic character, it plays a very important role in transporting water into the plant stems. Lignin lacks a clearly defined secondary or tertiary order and its variable composition depends on the plant source. [2.98-2.99] In a simplified way, lignin can be regarded as the polymerized product of three fundamental phenylpropane units, commonly known as monolignols: *p*-coumaryl alcohol, coniferyl alcohol and sinapyl alcohol. In the lignin macromolecule, these monolignols are incorporated in the form of phenylpropanoids: *p*-hydroxyphenyl (H), guaiacyl (G) and syringyl (S). [2.98] These monomeric units differin their number of substituted methoxy groups and, although representing most of repeating units in the lignin macropolymer, other lignols may be present in smaller quantities.

The composition of lignin varies depending on wood species and plant type. Harder woods tend to have slightly higher lignin contents than the soft ones. Softwood lignin, predominantly found in coniferous trees, consists primarily of coniferyl alcohol units, while hardwood lignin contains both coniferyl and large amounts of sinapyl units. The least substituted monolignol, *p*-coumaryl alcohol, is scarcely present in wood and is more common in grasses. [2.98] The classification of lignin is important to industrial applications and it goes into two different types: acid-soluble lignin and acid-insoluble lignin. [2.98] It is still under debate whether covalent bonds between lignin and wood carbohydrates exist, but many studies indicate the presence of such a lignin–carbohydrate complex (LCC). [2.97, 2.100-2.101]

2.2.2. Biomass processing with ILs

Ionic liquids are highly polar due to their ionic character, resulting in their enhanced biopolymer dissolving capacity. [2.102] Several factors influence the ILs ability to dissolve cellulose. Low-viscosity ILs promote the dissolution process, mainly due to their higher ions mobility, and it was shown that longer dissolution times (> 12 h) do not always lead to better results, especially at higher temperatures. [2.102-2.105] There is a risk of partial degradation at elevated temperatures and these needs to be taken into account for the fact that the favoured dissolution temperature is very often 10 K above the melting temperature of the IL. [2.102; 2.106-2.107]

Great results have been obtained when (3 to 5) s microwave pulses were used instead of thermal heating. As an example, the solubility of cellulose with a DP of 1000 was increased by 150 % using this method. [2.108] Microwave heating is characterized by an internal heating process, due to the direct absorption of energy by polar molecules and differs significantly from conventional heating methods that are based on heat transfer. This internal heating may be responsible for a more effective breakdown of the H–bond network between the microfibrils, although care must be taken because heating occurs very rapidly and can easily lead to pyrolysis of the biopolymer. [2.109] The sonication-assisted IL treatment of cellulose does not seem to significantly influence the dissolution process. [2.108] Other additional factors influencing the dissolution are the DP of the biopolymer and maybe the most important, the solvent's structure. [2.104] Several cations have already been studied and the most successful cations for cellulose dissolution are based on methylimidazolium and methylpyridinium core structures, with allyl-, ethyl-, or butyl- side chains (the short-ones). Even numbers of carbon atoms in the side chain are

more favorable for cellulose dissolution than odd numbers. [2.110] The maximum dissolution power is reached with the butyl side chain, and it was reported that OH–groups in the side chain can enhance cellulose solubility. [2.109] This can be explained by the additional polarity in the heteroatomic substituents on the imidazolium ring. Imidazolium ILs with side chains containing double bonds can show reduced viscosity. The same effect is observed if one of the alkyl chain carbon atom is replaced by an oxygen atom, although those ILs do not tend to dissolve cellulose. [2.111-2.112] The most promising IL anions for cellulose dissolution are chloride, acetate, and formate. ^{13}C and $^{35/37}Cl$ NMR relaxation studies indicate that there is a stoichiometric interaction between the chloride anions and the cellulose OH–groups. [2.113] It is thought that both anions and cations are involved in the dissolution process and figure 2.4 shows the proposed interaction between PIL ions and cellulose during dissolution. [2.109] The oxygen and hydrogen atoms of the cellulose form electron donor–electron acceptor complexes. It has been suggested that this occurs primarily in the OH–groups at positions C3 and C6 of neighboring cellulose chains, resulting in chain separation and subsequent the dissolution of the biopolymer. [2.102; 2.109, 2.114-2.115]

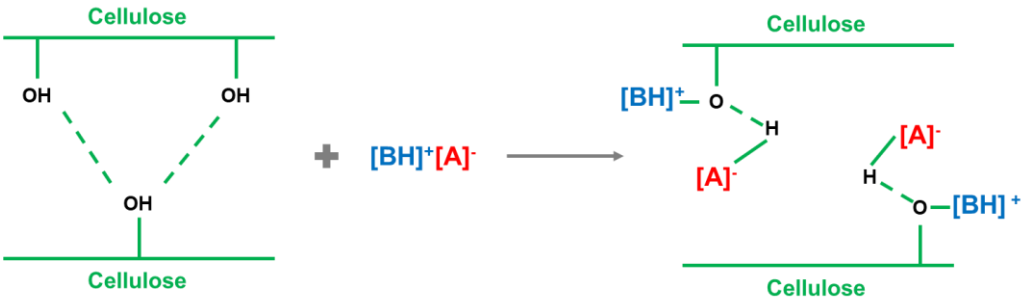

Figure 2.4. Proposed interaction between a PIL [BH][A] and cellulose chains during the dissolution of the biopolymer.

It was already investigated the interactions of IL cations using low DP cellooligomers as simplified cellulose model systems. [2.116] It was proposed that [EMIM]Ac forms a covalent bond between the C1 carbon of the glucose unit and the C2 carbon of the imidazolium core, because NMR studies showed previously that the C1 carbon signal of the glucose unit disappeared after dissolution in [C_2mim]Ac. Ebner et al. verified this hypothesis by means of labeling experiments with ^{13}C isotopes or fluorescence markers, suggesting the formation of a covalent bond between the C2 carbon of 1-alkyl-3-methyl-imidazolium ILs and the reducing end of cellulose. [2.117] Unexpectedly, this was not the case when the oligomer was dissolved in [C_2mim]Cl. [2.116] Considering that the suggested bond formation between the IL and cellulose is base-catalysed, the

presence of residual imidazolium impurities in the IL could be a possible explanation for this observation. Another reason for this phenomenon might be the proposed H–bond network within [C_2mim]Cl, as this would result in a saturated coordination sphere of the cation. [2.116-2.117] Leipner et al. studied the dissolution of cellulose in molten salt hydrates and concluded that an unsaturated coordination sphere of the cation is necessary to interact successfully with the cellulose. [2.118] Though, the similar dissolution power for cellulose of both ILs, [C_4mim]Cl and [C_2mim]Cl, does not agree with those conclusions. It has been suggested that dissolved cellulose can exist in many different states, depending on the solvent and some other factors. [2.90, 2.114] Varying dissolution states of cellulose are another possible reason for the differing reactivity of IL cations with regard to cellulose. [2.102]

Figure 2.5. presents the structure of an analogous IL, but with a different anion, binding covalently to the oligomer.

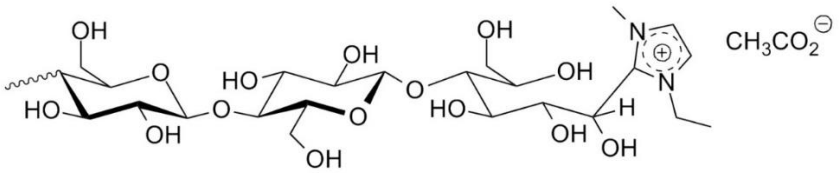

Figure 2.5. Structure proposed for the covalent binding of [EMIM]Ac to cellooligomer. Adapted from source [2.92].

Impurities and other sort of contaminations can also influence the cellulose dissolution ability of an IL. It has been shown that a mass fraction (*w*) of water of 0.01 in [C_4mim]Cl is sufficient to prevent and alter the dissolution of the biopolymer. [2.108] High pressures of (0.2 to 0.9) MPa can help the dissolution process and adding co-solvents can either reduce the dissolution rate (e.g. with carbon disulfide) or decrease the viscosity of the mixture (e.g. with DMSO, $CHCl_3$, or DMF). [2.102, 2.119-2.122]

2.2.3. Biomass conversion

The conversion of cellulose and lignin into useable biomass requires the dissolution and hydrolysis of the biopolymers into smaller fragments. ILs have been shown to be capable of dissolving cellulose, and some general characteristics of the cation and anion likely to lead to dissolution have been identified. Specifically, good cation characteristics are “an aromatic heterocycle with delocalized positive charge” and a second heterocycle atom in the aromatic ring that results in a dipolar character of the cation. [2.123] For the anion, the promising characteristics are “small-sized H-bond acceptors, substituents that should neither be bulky nor hydrophobic, and the ability to offer several H-bond acceptor sites.” [2.123] The use of ILs in the pre-treatment of lignocellulosic biomass was reviewed in 2013, [2.124] and while there were many ILs that were useful, some factors, like: the cost, difficulty to recycle, and viscosity were identified as challenges to the use of ILs at an industrial scale. [2.124] Protic ILs have the key benefit, as compared to their aprotic counterparts, of being simple to synthesize and generally much cheaper. In particular, the PIL [C_4im] HSO_4 was compared to the effective lignocellulose dissolving aprotic IL [C_4mim] HSO_4.. [2.125] Nonstoichiometric proportions of the [C_4im] HSO_4 between acid-rich and base-rich compositions modified the final products whereas slightly acid-rich compositions led to increased glucose yields, highly acid-rich compositions were detrimental to the overall process. The presence of water was essential for a good digestion of the cellulose. [2.125]

Few other PILs have been reported which are capable of dissolving these biopolymers. The PIL of [CH_3im] Cl dissolved cellulose and was also able to support cellulase enzymes with good hydrolysis rates, although not as good as the aprotic IL of tris(2-hydroxyethyl)methylammonium methylsulfate (HEMA). [2.126] PILs consisting of the CH_3im cation paired with the anions of Cl, Br, hydrogen sulfate, and BF_4 were able to degrade lignin through hydrolysis of the β-O_4 ether linkage. [2.127] The IL [CH_3im] Cl was found to be a better solvent for corn straw and soybean straw lignocellulosic materials than the PILs consisting of [CH_3im] with acetate, $H_2PO_4^-$, or HSO_4^-. [2.128] [CH_3im] HSO_4 was used in an optimization study to isolate cellulose and other components from the lignocellulosic feedstock of sugarcane bagasse. [2.129] The PIL was used as a catalyst to hydrolyze the filtrate obtained after the cellulose had been removed, resulting in the synthesis of furfural. [2.129] There was no correlation identified between the acidity of the PILs and their ability to catalyse the hydrolysis. However, the anions that were more capable of forming stronger hydrogen bonds had a greater ability to dissolve the biomass and to degrade the lignin. [2.127] Triethylammonium methanesulfonate was selected as a

low viscosity, high conductivity solvent for dissolving lignocellulosic biomass. [2.130] Electro-oxidative cleavage of this solution resulted in a wide range of aromatic fragments. The ability of this PIL to dissolve the lignin was attributed to the sulfate component of the anion. PILs containing the cations of pyridinium, or pyrrolidinium paired with acetate were able to dissolve the lignin to levels greater than 50 wt %, although they were poor solvents for cellulose. Though, they are promising solvents for lignin extraction and furthermore these PILs can be recycled. [2.131]

Protic ionic liquids containing the alkanolammonium cations ethanolammonium, diethanolammonium, triethanolammonium, propan-1-olammonium, and diallylammonium paired with the anions formate, acetate, malonate, and citrate did not dissolve cellulose. [2.132] But, ethanolammonium formate and ethanolammonium acetate were both reported to be good solvents for dissolving the protein polymer from corn processing, known as *zein*, which is water insoluble. [2.133] Both PILs performed similarly, with up to 20 % *zein* being dissolved at 95 °C, or higher, using microwave radiation. These PILs were proposed as economical and environmental alternatives to organic solvents, or to aprotic ILs, such as [C_4mim] Cl. [2.133] The best dissolution was obtained at 150 °C, although it was observed that both PILs boiled at this temperature. Previously, differential scanning calorimetry, *DSC*, studies (with peaks at 192 and 210 °C) were attributed as the boiling points of ethanolammonium formate and ethanolammonium acetate, [2.18] so it is interesting that the addition of *zein* significantly lowered the boiling point to less than 150 °C for these PILs. Both of these PILs, especially ethanolammonium formate, readily form an amide through a condensation reaction, and the rate is increased on heating. [2.18] Depending on the reaction time used in these experiments, it could be expected that there will be an appreciable amount of amide present. Some solvation properties of monosaccharides D(+)glucose and D(−)ribose dissolved in an aqueous solution of 3-hydroxypropylammonium formate were investigated, as part of an understanding of cellulose dissolution in ILs. Overall, the solvation was found to predominantly have ionic interactions, which were stronger for the glucose. Parameters related to the taste quality of massic volume and apparent massic isentropic compressibility indicated that the sweet taste of these two monosaccharides is maintained within this PIL solution. [2.134]

2.3. References

[2.1] Seddon, K. *Everything You always wanted to Know about Ionic Liquids, but were Afraid to Ask*, Presentation ILWS 2017, Porto, Portugal.

[2.2] Greaves, T. L.; Drummond, C. J., *Chem. Rev.* **2015**, 115, 11379-11448.

[2.3] Yoshizawa, M.; Xu, W.; Angell, C. A., *J. Am. Chem. Soc.* **2003**, 125, 15411−15419.

[2.4] Kanzaki, R.; Doi, H.; Song, X. D.; Hara, S.; Ishiguro, S.; Umebayashi, Y., *J. Phys. Chem. B* **2012**, 116, 14146−14152.

[2.5] Doi, H.; Song, X.; Minofar, B.; Kanzaki, R.; Takamuku, T.; Umebayashi, Y., *Chem. - Eur. J.* **2013**, 19, 11522−11526.

[2.6] Burrell, G. L.; Burgar, I. M.; Separovic, F.; Dunlop, N. F., *Phys. Chem. Chem. Phys.* **2010**, 12, 1571−1577.

[2.7] Lv, Y. Q.; Guo, Y.; Luo, X. Y.; Li, H. R., *Sci. China: Chem.* **2012**, 55, 1688−1694.

[2.8] Johansson, K. M.; Izgorodina, E. I.; Forsyth, M.; MacFarlane, D. R.; Seddon, K. R. *Phys. Chem. Chem. Phys.* **2008**, 10, 2972−2978.

[2.9] MacFarlane, D. R.; Forsyth, M.; Izgorodina, E. I.; Abbott, A. P.; Annat, G.; Fraser, K. *Phys. Chem. Chem. Phys.* **2009**, 11, 4962−4967.

[2.10] Ueno, K.; Tokuda, H.; Watanabe, M., *Phys. Chem. Chem. Phys.* **2010**, 12, 1649−1658.

[2.11] Yaghini, N.; Nordstierna, L.; Martinelli, A., *Phys. Chem. Chem. Phys.* **2014**, 16, 9266−9275.

[2.12] Canongia Lopes, J. N.; Rebelo, L. P. N., *Phys. Chem. Chem. Phys.* **2010**, 12, 1948−1952.

[2.13] MacFarlane, D. R.; Vijayaraghavan, R.; Ha, H. N.; Izgorodin, A.; Weaver, K.; Elliott, G. D., *Chem. Commun.* **2010**, 46, 7703−7705.

[2.14] Treskow, M.; Pitawala, J.; Arenz, S.; Matic, A.; Johansson, P., J. *Phys. Chem. Lett.* **2012**, 3, 2114−2119.

[2.15] (26) Dong, K.; Zhang, S. J., *Chem. - Eur. J.* **2012**, 18, 2748−2761.

[2.16] Hayes, R.; Imberti, S.; Warr, G. G.; Atkin, R., *Angew. Chem., Int. Ed.* **2013**, 52, 4623−4627.

[2.17] Nazari, S.; Cameron, S.; Johnson, M. B.; Ghandi, K., *J. Mater. Chem. A* **2013**, 1, 11570−11579.

[2.18] Greaves, T. L.; Weerawardena, A.; Fong, C.; Krodkiewska, I.; Drummond, C. J., *J. Phys. Chem. B* **2006**, 110, 22479−22487

[2.19] Greaves, T. L.; Weerawardena, A.; Krodkiewska, I.; Drummond, C. J., *J. Phys. Chem. B* **2008**, 112, 896−905.

[2.20] Earle, M. J.; Esperanca, J. M. S. S.; Gilea, M. A.; Canongia Lopes, J. N.; Rebelo, L. P. N.; Magee, J. W.; Seddon, K. R.; Widegren, J. A., *Nature* **2006**, 439, 831−834.

[2.21] Lovelock, K. R. J.; Deyko, A.; Licence, P.; Jones, R. G., *Phys. Chem. Chem. Phys.* **2010**, 12, 8893−8901.

[2.22] Deyko, A.; Lovelock, K. R. J.; Licence, P.; Jones, R. G. *Phys. Chem. Chem. Phys.* **2011**, 13, 16841−16850.

[2.23] Leal, J. P.; Esperanca, J.; da Piedade, M. E. M.; Lopes, J. N. C.; Rebelo, L. P. N.; Seddon, K. R. *J. Phys. Chem. A* **2007**, 111, 6176−6182.

[2.24] Miran, M. S.; Yasuda, T.; Susan, M. A.; Dokko, K.; Watanabe, M. *RSC Adv.* **2013**, 3, 4141−4144.

[2.25] Shukla, S. K.; Kumar, A. *J. Phys. Chem. B* **2013**, 117, 2456−2465.

[2.26] Adam, C.; Bravo, M. V.; Mancini, P. M. E. *Tetrahedron Lett.* **2014**, 55, 148−150.

[2.27] Mihichuk, L. M.; Driver, G. W.; Johnson, K. E. *ChemPhysChem* **2011**, 12, 1622−1632.

[2.28] Byrne, N.; Angell, C. A. *J. Mol. Biol.* **2008**, 378, 707−714

[2.29] Byrne, N.; Belieres, J. P.; Angell, C. A. *Aust. J. Chem.* **2009**, 62, 328−333.

[2.30] Bautista-Martinez, J. A.; Tang, L.; Belieres, J. P.; Zeller, R.; Angell, C. A.; Friesen, C*. J. Phys. Chem. C* **2009**, 113, 12586−12593.

[2.31] Zoranic, L.; Sokolic, F.; Perera, *J. Chem. Phys.* **2007**, 127, 24502.

[2.32] Tomsic, M.; Jamnik, A.; Fritz-Popovski, G.; Glatter, O.; Vlcek, L. *J. Phys. Chem. B* **2007**, 111, 1738−1751.

[2.33] Wijaya, E. C.; Greaves, T. L.; Drummond, C. J. *Faraday Discuss*. **2014**, 167, 191.

[2.34] Haufa, K. Z.; Czarnecki, M. *Appl. Spectrosc*. **2010**, 64, 351−358.

[2.35] Greaves, T. L.; Weerawardena, A.; Drummond, C. *J. Chem. Chem. Phys.* **2011**, 13, 9180−9186.

[2.36] Canongia Lopes, J. N.; Padua, A. A. H. *J. Phys. Chem. B* **2006**, 110, 3330−3335.

[2.37] Triolo, A.; Russina, O.; Bleif, H. J.; Di Cola, E. *J. Phys. Chem. B* **2007**, 111, 4641−4644.

[2.38] Atkin, R.; Warr, G. G. *J. Phys. Chem. B* **2008**, 112, 4164−4166.

[2.39] Greaves, T. L.; Drummond, C. J. *Chem. Soc. Rev.* **2013**, 42, 1096−1120.

[2.40] Hayes, R.; Warr, G. G.; Atkin, R*. Phys. Chem. Chem. Phys*. **2010**, 12, 1709−1723.

[2.41] Greaves, T. L.; Kennedy, D. F.; Weerawardena, A.; Tse, N. M. K.; Kirby, N.; Drummond, C. J*. J. Phys. Chem. B* **2011**, 115, 2055−2066.

[2.42] Hayes, R.; Imberti, S.; Warr, G. G.; Atkin, R. *Angew. Chem., Int. Ed.* **2012**, 51, 7468−7471.

[2.43] Greaves, T. L.; Kennedy, D. F.; Kirby, N.; Drummond, C. J. *Phys. Chem. Chem. Phys.* **2011**, 13, 13501−13509.

[2.44] Iida, M.; Kawakami, S.; Syouno, E.; Er, H.; Taguchi, E. *J. Colloid Interface Sci.* **2011**, 356, 630−638.

[2.45] Chen, Z.; Greaves, T. L.; Caruso, R. A.; Drummond, C. J. *J. Mater. Chem.* **2012**, 22, 10069−10076.

[2.46] MacFarlane, D. R.; Tachikawa, N.; Forsyth, M.; Pringle, J. M.; Howlett, P. C.; Elliott, G. D.; Davis, J. H., Jr.; Watanabe, M.; Simon, P.; Angell, C. A. *Energy Environ. Sci.* **2014**, 7, 232−250.

[2.47] Collins, M. P.; Zhou, L.; Camp, S. E.; Danielson, N. D. *J. Chromatogr. Sci.* **2012**, 50, 869−876.

[2.48] Grossman, S.; Danielson, N. D. *J. Chromatogr. A* **2009**, 1216, 3578−3586.

[2.49] Elshwishin, A.; Koeser, J.; Schroeer, W.; Qiao, B*. J. Mol. Liq.* **2014**, 192, 127−136.

[2.50] Yoo, B.; Afzal, W.; Prausnitz, J. M*. Ind. Eng. Chem. Res.* **2012**, 51, 9913−9917.

[2.51] Verevkin, S. P.; Zaitsau, D. H.; Tong, B.; Welz-Biermann, U. *Phys. Chem. Chem. Phys.* **2011**, 13, 12708−12711.

[2.52] Yu, C.-H.; Huang, C.-H.; Tan, C.-S. *Aerosol Air Qual. Res.* **2012**, 12, 745−769.

[2.53] Pollet, P.; Davey, E. A.; Urena-Benavides, E. E.; Eckert, C. A.; Liotta, C. L. *Green Chem.* **2014**, 16, 1034−1055.

[2.54] Ramdin, M.; de Loos, T. W.; Vlugt, T. J. H. *Ind. Eng. Chem. Res.* **2012**, 51, 8149−8177.

[2.55] Mendez-Morales, T.; Carrete, J.; Cabeza, O.; Russina, O.; Triolo, A.; Gallego, L. J.; Varela, L. M*. J. Phys. Chem. B* **2014**, 118, 761−770.

[2.56] Smith, J. A.; Webber, G. B.; Warr, G. G.; Zimmer, A.; Atkin, R.; Werzer, O., *J. Colloid Interface Sci.* **2014**, 430, 56−60.

[2.57] Afzal, W.; Yoo, B.; Prausnitz, J. M. *Ind. Eng. Chem. Res*. **2012,** 51, 4433−4439.

[2.58] Shiflett, M. B.; Niehaus, A. M. S.; Elliott, B. A.; Yokozeki, A. *Int. J. Thermophys.* **2012,** 33, 412−436.

[2.59] Vijayraghavan, R.; Pas, S. J.; Izgorodina, E. I.; MacFarlane, D. R. *Phys. Chem. Chem. Phys.* **2013**, 15, 19994−19999.

[2.60] Zhang, S.; Dokko, K.; Watanabe, M. *Chem. Mater.* **2014**, 26, 2915−2926.

[2.61] Yuan, X.; Zhang, S.; Liu, J.; Lu, X. *Fluid Phase Equilib*. **2007**, 257, 195−200.

[2.62] Summers, C. A.; Flowers, R. A*. Biochemistry* **2000**, 39, 161.

[2.63] Summers, C. A.; Flowers, R. A. *Protein Sci.* **2000**, 9, 2001−2008.

[2.64] Mood, S. H.; Golfeshan, A. H.; Tabatabaei, M.; Jouzani, G. S.; Najafi, G. H.; Gholami, M.; Ardjmand, M., *Renewable Sustainable Energy Rev*. **2013**, 27, 77−93.

[2.65] Chen, X. W.; Liu, J. W.; Wang, J. H. *Anal. Methods* **2010**, 2, 1222−1226.

[2.66] Kohno, Y.; Ohno, H. *Chem. Commun*. **2012**, 48, 7119−7130.

[2.67] Kumar, A.; Venkatesu, P. *Chem. Rev*. **2012,** 112, 4283−4307.

[2.68] Kumar, A.; Venkatesu, P. *Int. J. Biol. Macromol.* **2014**, 63, 244−253.

[2.69] Adamovich, S. N.; Mirskov, R. G.; Mirskova, A. N.; Voronkov, M. G. *Russ. J. Gen. Chem.* **2012**, 82, 1455−1456.

[2.70] Adamovich, S. N.; Mirskova, A. N.; Mirskov, R. G.; Lopyrev, V. A. *Mendeleev Commun.* **2012**, *22*, 330−331.

[2.71] Adamovich, S. N.; Mirskova, A. N.; Mirskov, R. G.; Voronkov, M. G. *Russ. Chem. Bull.* **2012**, 61, 2192−2193.

[2.72] Adamovich, S. N.; Mirskov, R. G.; Mirskova, A. N.; Voronkov, M. G., *Russ. Chem. Bull.* **2012**, 61, 1262−1263.

[2.73] Stoimenovski, J.; MacFarlane, D. R. *Chem. Commun.* **2011**, 47, 11429−11431.

[2.74] Chipanina, N. N.; Aksamentova, T. N.; Adamovich, S. N.; Albanov, A. I.; Mirskova, A.; Mirskov, R. G.; Voronkov, M. G. *Comput. Theor. Chem.* **2012**, 985, 36−45.

[2.75] Frade, R. F. M.; Rosatella, A. A.; Marques, C. S.; Branco, L. C.; Kulkarni, P. S.; Mateus, N. M. M.; Afonso, C. A. M.; Duarte, C. M. M. *Green Chem*. **2009**, 11, 1660−1665.

[2.76] Peric, B.; Sierra, J.; Marti, E.; Cruanas, R.; Antonia Garau, M.; Arning, J.; Bottin-Weber, U.; Stolte, S. *J. Hazard. Mater.* **2013**, 261, 99−105.

[2.77] Peric, B.; Sierra, J.; Marti, E.; Cruanas, R.; Garau, M. A. *Chemosphere* **2014**, 108, 418−425.

[2.78] Hallett, J. P.; Welton, T. *Chem. Rev.* **2011**, 111, 3508−3576.

[2.79] Clark, J. H.; Deswarte, F. E. I.; Farmer, T. *J. Bioprod. Biorefin*. **2009**, 3, 72−90.

[2.80] Gupta, M.; Paul, S.; Gupta, R. *Curr. Sci*. **2010**, 99, 1341−1360.

[2.81] Russ, C.; Koenig, B. *Green Chem*. **2012**, 14, 2969−2982.

[2.82] Suresh; Sandhu, J. S. *Green Chem. Lett. Rev*. **2011**, 4, 289−310.

[2.83] Gu, Y. L.; Jerome, F*., Green Chem.* **2010**, 12, 1127−1138.

[2.84] Clark, J. H. *J. Chem. Technol. Biotechnol.* **2007**, *82*, 603.

[2.85] Tan, S. S. Y.; MacFarlane, D. R.; Upfal, J.; Edye, L. A.; Doherty, W. O. S.; Patti, A. F.; Pringle, J. M.; Scott, J. L. *Green Chem.* **2009**, *11*, 339.

[2.86] Malherbe, S.; Cloete, T. E. *Rev. Environ. Sci. Biotechnol.* **2002**, *1*, 105.

[2.87] Leonowicz, A.; Matuszewska, A.; Luterek, J.; Ziegenhagen, D.; Wojtas-Wasilewska, M.; Cho, N. S.; Hofrichter, M.; Rogalski, J. *Fungal Genet. Biol.* **1999**, *27*, 175.

[2.88] A. Brandt, J. Gräsvik, J.P. Hallett, T. Welton, Green Chem. 15 (2013) 550.

[2.89] Walker, J. *Primary Wood Processing: Principles and Pratice,* 1st ed.; Chapman and Hall: London, 1993.

[2.90] Klemm, D.; Heublein, B.; Fink, H.-P. et al. *Angew. Chem.* **2005**, *44*, 3358–3398.

[2.91] Kraessig, H.; Schurz, J.; Steadman, R. et al. *Ullmann's Encyclopedia of Industrial Chemistry*, 5th ed.; Wiley: Weinheim, Germany, 2002.

[2.92] Pinkert, A., PhD thesis, *Investigations on the use of ionic liquids for superior biomass processing*, University of Canterbury, **2011**.

[2.93] Van de Vyver, S.; Geboers, J.; Jacobs, P. A. et al. *ChemCatChem* **2011**, *3*, 82–94.

[2.94] Young, R. A., Rowell, R. M., Eds. *Cellulose: Structure, Modification, and Hydrolysis*, 1st ed.; Wiley-Interscience: New York, 1986.

[2.95] Gardner, K. H.; Blackwell, J. *Biopolymers* **1974**, *13*, 1975–2001.

[2.96] Diddens, I.; Murphy, B.; Krisch, M. et al. *Macromolecules* **2008**, *41*, 9755–9759.

[2.97] Guerra, A.; Filpponen, I.; Lucia, L. A. et al. *J. Agric. Food Chem.* **2006**, *54*, 5939–5947.

[2.98] Notley, S. M.; Norgren, M. *Lignin: Functional Biomaterial with Potential in Surface Chemistry and Nanoscience*; The Nanoscience and Technology of Renewable Biomaterials; John Wiley & Sons, Ltd, 2009.

[2.99] Stärk, K.; Taccardi, N.; Bösmann, A. et al. *ChemSusChem* **2010**, *3*, 719–723.

[2.100] Iversen, T. *Wood Sci. Technol.* **1985**, *19*, 243–251.

[2.101] Lawoko, M.; Henriksson, G.; Gellerstedt, G. *Biomacromolecules* **2005**, *6*, 3467–3473.

[2.102] Pinkert, A.; Marsh, K. N.; Pang, S.; Staiger, M. P., *Chem. Rev.* **2009**, *109*, 6712–6728.

[2.103] Fort, D. A.; Remsing, R. C.; Swatloski, R. P. et al. *Green Chem.* **2007**, *9*, 63–69.

[2.104] Kilpelainen, I.; Xie, H.; King, A. et al. *J. Agric. Food Chem.* **2007**, *55*, 9142–9148.

[2.105] Aaltonen, O.; Jauhiainen, O. *Carbohydr. Polym.* **2009**, *75*, 125–129.

[2.106] Heinze, T.; Schwikal, K.; Barthel, S. *Macromol. Biosci.* **2005**, *5*, 520–525.

[2.107] Barthel, S.; Heinze, T. *Green Chem.* **2006**, *8*, 301–306.

[2.108] Swatloski, R. P.; Spear, S. K.; Holbrey, J. D. et al. *J. Am. Chem. Soc.* **2002**, *124*, 4974–4975.

[2.109] Feng, L.; Chen, Z.-l. *J. Mol. Liq.* **2008**, *142*, 1–5.

[2.110] Erdmenger, T.; Haensch, C.; Hoogenboom, R. et al. *Macromol. Biosci.* **2007**, *7*, 440–445.

[2.111] Wasserscheid, P.; van Hal, R.; Bosmann, A. et al. ACS Symposium Series; American Chemical Society: Washington, DC, 2003; Vol. 856; pp 57–69.

[2.112] Laus, G.; Bentivoglio, G.; Schottenberger, H. et al. *Lenzinger Berichte* **2005**, *84*, 71–85.

[2.113] Remsing, R. C.; Swatloski, R. P.; Rogers, R. D. et al. *Chem. Commun.* **2006**, 1271–1273.

[2.114] Kosan, B.; Michels, C.; Meister, F. *Cellulose* **2008**, *15*, 59–66.

[2.115] Zhang, H.; Wu, J.; Zhang, J. et al. *Macromolecules* **2005**, *38*, 8272–8277.

[2.116] Heinze, T.; Dorn, S.; Schoebitz, M. et al. *Macromol. Symp.* **2008**, *262*, 8–22.

[2.117] Ebner, G.; Schiehser, S.; Potthast, A. et al. *Tetrahedron Lett.* **2008**, *49*, 7322–7324.

[2.118] Leipner, H.; Fischer, S.; Brendler, E. et al. *Macromol. Chem. Phys.* **2000**, *201*, 2041–2049.

[2.119] Myllymaeki, V.; Aksela, R. World Patent, WO 2005/017001 A1; 2005.

[2.120] Cuissinat, C.; Navard, P.; Heinze, T. *Cellulose* **2008**, *15*, 75–80.

[2.121] Koehler, S.; Liebert, T.; Heinze, T. *J. Polym. Sci., Part A: Polym. Chem.* **2008**, *46*, 4070–4080.

[2.122] Gericke, M.; Liebert, T.; Heinze, T. *Macromol. Biosci.* **2009**, *9*, 343–353.

[2.123] Pinkert, A.; Marsh, K. N.; Pang, S. *Ind. Eng. Chem. Res.* **2010**, 49, 11121−11130.

[2.124] Mood, S. H.; Golfeshan, A. H.; Tabatabaei, M.; Jouzani, G. S.; Najafi, G. H.; Gholami, M.; Ardjmand, M. *Renewable Sustainable Energy Rev.* **2013**, 27, 77−93.

[2.125] Verdia, P.; Brandt, A.; Hallett, J. P.; Ray, M. J.; Welton, T. *Green Chem.* **2014**, 16, 1617−1627.

[2.126] Bose, S.; Armstrong, D. W.; Petrich, J. W. *J. Phys. Chem. B* **2010**, 114, 8221−8227.

[2.127] Cox, B. J.; Jia, S. Y.; Zhang, Z. C.; Ekerdt, J. G*. Polym. Degrad. Stab*. **2011**, 96, 426−431.

[2.128] Hu, X.; Xiao, Y.; Niu, K.; Zhao, Y.; Zhang, B.; Hu, B. *Carbohydr. Polym*. **2013**, 97, 172−176.

[2.129] Wang, Y.; Song, H.; Hou, J.-P.; Jia, C.-M.; Yao, S. *Sep. Sci. Technol*. **2013**, 48, 2217−2224.

[2.130] Reichert, E.; Wintringer, R.; Volmer, D. A.; Hempelmann, R. *Phys. Chem. Chem. Phys.* **2012**, 14, 5214−5221.

[2.131] Achinivu, E. C.; Howard, R. M.; Li, G.; Gracz, H.; Henderson, W. A. *Green Chem*. **2014**, 16, 1114−1119.

[2.132] Pinkert, A.; Ang, K. L.; Marsh, K. N.; Pang, S. *Phys. Chem. Chem. Phys*. **2011**, 13, 5136−5143.

[2.133] Choi, H. M.; Kwon, I. *Ind. Eng. Chem. Res*. **2011**, 50, 2452−2454.

[2.134] Singh, V.; Chhotaray, P. K.; Gardas, R. L. *J. Chem. Thermodyn*. **2014**, 71, 37−49.

CHAPTER 3

Synthesis and Characterization

3. Synthesis and Characterization

This chapter summarizes the compounds studied in this research project, the synthesis and purification procedures, the posterior characterization by Nuclear magnetic resonance (NMR), Fourier-transformed infrared spectroscopy (FTIR) and Differential scanning calorimetry (DSC) and the list of the studies performed for each compound.

3.1. Compounds studied

The compounds studied in this work cover some bases, carboxylic acids, and their representative PILs families, figure 3.1. Different combinations of bases and carboxylic acids were used to evaluate the effects of structural changes (length of the acid's alkyl chain, symmetry, identity of base and acid, etc.) on the thermophysical properties of PILs and their ability for biomass processing.

The following PIL families were explored: 1,5-diazabicyclo(4.3.0)non-5-ene, $[DBNH^+][A^-]$; 1,8-diazabicyclo(5.4.0)undec-7-ene, $[DBUH^+][A^-]$; triazabicyclodecene, $[TBDH^+][A^-]$; 1,1,3,3-tetramethylguanidine, $[TMGH^+][A^-]$ and 1,2-dimethyl-1,4,5,6-tetrahydropyrimidine, $[DMTHPH^+][A^-]$, where$[A^-]$ is a carboxylate anion.

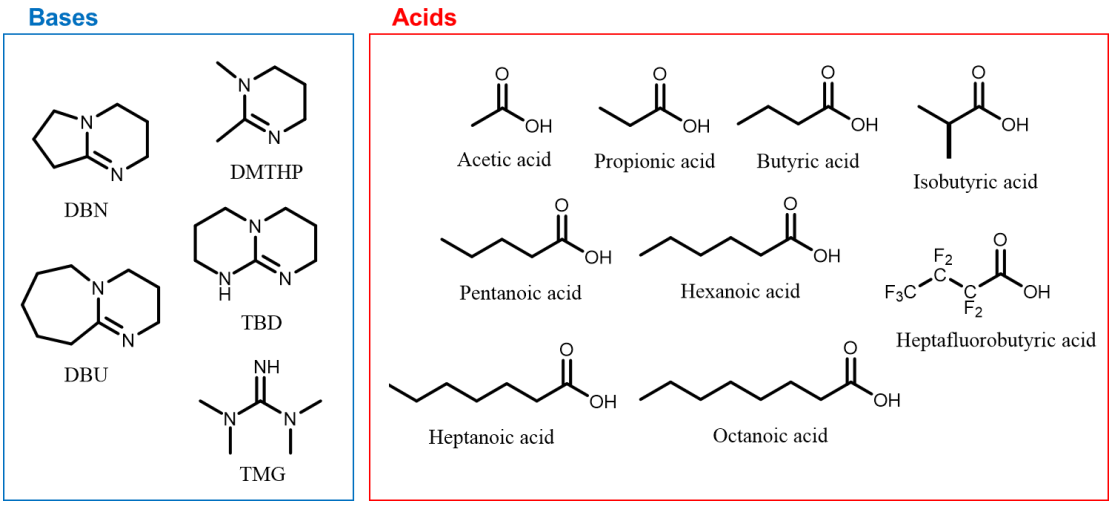

Figure 3.1. Molecular structure of the studied superbases and carboxylic acids.

Table 3.1 presents a summary of the combinations of bases and carboxylic acids studied in this work and tables 3.2. to 3.10. present the compounds studied, their structural and schematic formula, abbreviation used, molar mass, purity, supplier, and the types of studies performed in this work for each of them.

Table 3.1. Summary of the combinations of superbases and carboxylic acids studied in this thesis.

Acid / **Base**	Acetic CH_3COOH	Propionic CH_3CH_2COOH	Butyric $CH_3(CH_2)_2COOH$	Iso-butyric $(CH_3)_2CHCOOH$	Fluoro-Butyric $CF_3(CF_2)_2COOH$	Pentanoic $CH_3(CH_2)_3COOH$	Hexanoic $CH_3(CH_2)_4COOH$	Heptanoic $CH_3(CH_2)_5COOH$	Octanoic $CH_3(CH_2)_6COOH$
DBN 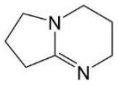	●	●	●	●	●	●	●	●	●
DBU 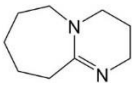	●	●	●	●		●	●	●	●
TBD 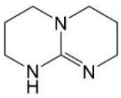		●					●		
TMG 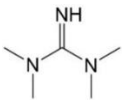		●					●		
DMTHP 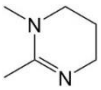		●	●			●	●	●	●

● – compounds studied in this work.

Table 3.2. Summary of the bases studied in this work.

Base	Abbreviation	Structural formula	Molar Mass / g·mol^{-1}	Purity / %*	Source CAS number	Studies performed [a]
1,5-diazabicyclo(4.3.0)non-5-ene	DBN	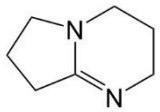	124.18	99.9	Sigma-Aldrich 3001-72-7	CM; PB; QCC C_p (298.15 K, *T*)
1,8-diazabicyclo(5.4.0)undec-7-ene	DBU	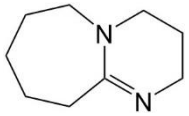	152.24	99.3	Sigma-Aldrich 6674-22-2	CM; PB; QCC C_p (298.15 K, *T*)
triazabicyclodecene	TBD	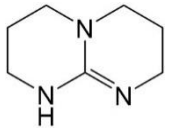	139.20	99.6	Sigma-Aldrich 5807-14-7	QCC
1,1,3,3-tetramethylguanidine	TMG	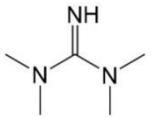	115.18	99.5	Sigma-Aldrich 80-70-6	QCC
1,2-dimethyl-1,4,5,6-tetrahydropyrimidine	DMTHP	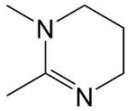	112.17	98.0	Fluorochem 4271-96-9	CM; QCC C_p (298.15 K, *T*)

[a] CM – Calvet microcalorimetry; PB – Phase Behavior; QCC – Quantum Chemical Calculations; C_p (298.15 K, *T*) – Heat capacities at 298.15 K and at different temperatures.

*-as specified by the supplier.

Table 3.3. Summary of the acids studied in this work. (Part I of II)

Acid	Abbreviation	Structural formula	Molar Mass / g·mol^{-1}	Purity / %*	Source CAS number	Studies performed [a]
Acetic acid	MeCOOH		60.05	100.0	VWR Chemicals 64-19-7	PB; QCC
Propionic acid	EtCOOH	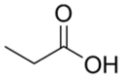	74.08	99.8	TCI 79-09-4	PB; QCC
Butyric acid	nPrCOOH	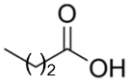	88.11	99.8	Sigma-Aldrich 107-92-6	PB; QCC
Pentanoic acid	nButCOOH	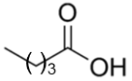	102.13	99.9	Sigma-Aldrich 109-52-4	QCC
Hexanoic acid	nPentCOOH	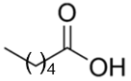	116.16	99.8	Sigma-Aldrich 142-62-1	QCC
Heptanoic acid	nHexCOOH	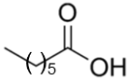	130.19	99.9	Sigma-Aldrich 111-14-8	QCC

[a] PB – Phase Behavior; QCC – Quantum Chemical Calculations.

*-as specified by the supplier.

Table 3.4. Summary of the acids studied in this work. (Part II of II)

Acid	Abbreviation	Structural formula	Molar Mass / g·mol^{-1}	Purity / %*	Source CAS number	Studies performed [a]
Octanoic acid	nHeptCOOH	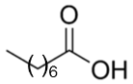	144.21	99.5	Sigma-Aldrich 124-07-2	QCC
Isobutyric acid	IPrCOOH	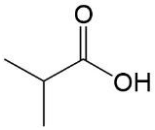	88.11	99.7	Sigma-Aldrich 79-31-2	QCC
Heptafluorobutyric acid	FPrCOOH	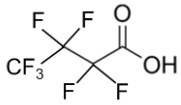	214.04	98.8	Sigma-Aldrich 375-22-4	QCC

[a] QCC – Quantum Chemical Calculations.

*-as specified by the supplier.

Table 3.5. Summary of the protic ionic liquids studied in this work. (Part I of V)

Protic Ionic Liquid	Abbreviation	Structural formula	Molar Mass / g·mol^{-1}	Purity / %	Source CAS number	Studies performed [a]
1,5-diazabicyclo(4.3.0)non-5-enium acetate	[DBNH][MeCOO]	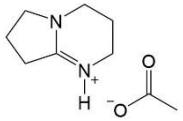	184.23	>99	Synthesized	CM; PB; QCC
1,5-diazabicyclo(4.3.0)non-5-enium propanoate	[DBNH][EtCOO]	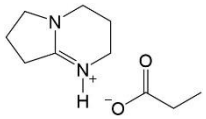	198.26	>99	Synthesized	CM; PB; QCC; KNQ C_p (298.15 K, T)
1,5-diazabicyclo(4.3.0)non-5-enium butanoate	[DBNH][nPrCOO]	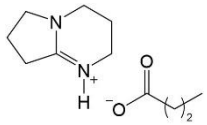	212.29	>99	Synthesized	CM; PB; QCC; KNQ C_p (298.15 K, T)
1,5-diazabicyclo(4.3.0)non-5-enium pentanoate	[DBNH][nButCOO]	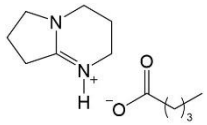	226.32	>99	Synthesized	CM; QCC; KNQ
1,5-diazabicyclo(4.3.0)non-5-enium hexanoate	[DBNH][nPentCOO]	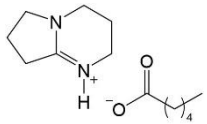	240.35	>99	Synthesized	CM; PB; QCC; KNQ C_p (298.15 K, T)
1,5-diazabicyclo(4.3.0)non-5-enium heptanoate	[DBNH][nHexCOO]	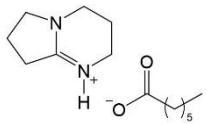	254.37	>99	Synthesized	CM; QCC; KNQ

[a] CM – Calvet microcalorimetry; PB – Phase Behavior; QCC – Quantum Chemical Calculations KNQ – Knudsen experiment; C_p (298.15 K, T) – Heat capacities at different temperatures and at 298.15 K.
Molar masses of the protic ionic liquids calculated as the sum of the molar masses of the acid and base.

Table 3.6. Summary of the protic ionic liquids studied in this work. (Part II of V)

Protic Ionic Liquid	Abbreviation	Structural formula	Molar Mass / g·mol^{-1}	Purity / %	Source CAS number	Studies performed [a]
1,5-diazabicyclo(4.3.0)non-5-enium octanoate	[DBNH][nHeptCOO]	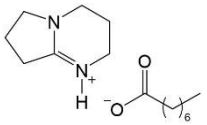	268.40	>99	Synthesized	CM; PB; QCC; KNQ C_p (298.15 K, *T*)
1,8-diazabicyclo(5.4.0)undec-7-enium acetate	[DBUH][MeCOO]	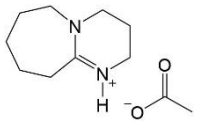	212.29	>99	Synthesized	CM; PB; QCC
1,8-diazabicyclo(5.4.0)undec-7-enium propanoate	[DBUH][EtCOO]	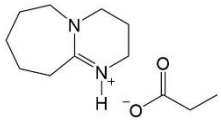	226.32	>99	Synthesized	CM; PB; QCC; KNQ C_p (298.15 K, *T*)
1,8-diazabicyclo(5.4.0)undec-7-enium butanoate	[DBUH][nPrCOO]	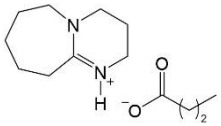	240.35	>99	Synthesized	CM; PB; QCC; KNQ C_p (298.15 K, *T*)
1,8-diazabicyclo(5.4.0)undec-7-enium pentanoate	[DBUH][nButCOO]	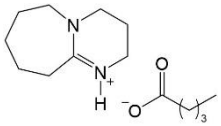	254.37	>99	Synthesized	CM; QCC; KNQ
1,8-diazabicyclo(5.4.0)undec-7-enium hexanoate	[DBUH][nPentCOO]	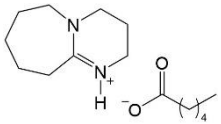	268.40	>99	Synthesized	CM; PB; QCC; KNQ C_p (298.15 K, *T*)

[a] CM – Calvet microcalorimetry; PB – Phase Behavior; QCC – Quantum Chemical Calculations KNQ – Knudsen experiment; C_p (298.15 K, *T*) – Heat capacities at different temperatures and at 298.15 K. Molar masses of the protic ionic liquids calculated as the sum of the molar masses of the acid and base.

Table 3.7. Summary of the protic ionic liquids studied in this work. (Part III of V)

Protic Ionic Liquid	Abbreviation	Structural formula	Molar Mass / g·mol^{-1}	Purity / %	Source CAS number	Studies performed [a]
1,8-diazabicyclo(5.4.0)undec-7-enium heptanoate	[DBUH][nHexCOO]	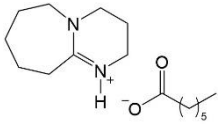	282.43	>99	Synthesized	CM; QCC; KNQ
1,8-diazabicyclo(5.4.0)undec-7-enium octanoate	[DBUH][nHeptCOO]	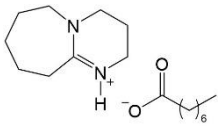	296.45	>99	Synthesized	CM; PB; QCC; KNQ C_p (298.15 K, *T*)
1,8 diazabicyclo(4.3.0)non-5-enium isobutanoate	[DBNH][IPrCOO]	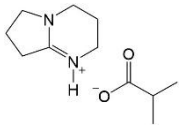	212.29	>99	Synthesized	PB; QCC
1,5-diazabicyclo(4.3.0)non-5-enium heptafluorobutanoate	[DBNH][FPrCOO]	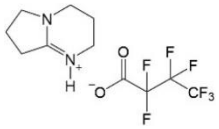	338.22	>99	Synthesized	QCC; KNQ
1,8-diazabicyclo(5.4.0)undec-7-enium isobutanoate	[DBUH][IPrCOO]	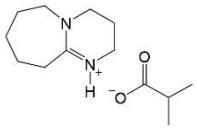	240.35	>99	Synthesized	PB; QCC

[a] CM – Calvet microcalorimetry; PB – Phase Behavior; QCC – Quantum Chemical Calculations KNQ – Knudsen experiment; C_p (298.15 K, *T)* – Heat capacities at different temperatures and at 298.15 K.

Molar masses of the protic ionic liquids calculated as the sum of the molar masses of the acid and base.

Table 3.8. Summary of the protic ionic liquids studied in this work. (Part IV of V)

Protic Ionic Liquid	Abbreviation	Structural formula	Molar Mass / g·mol^{-1}	Purity / %	Source CAS number	Studies performed [a]
Triazabicyclodecenium propanoate	[TBDH][EtCOO]	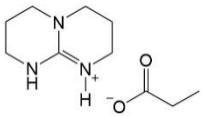	213.28	>99	Synthesized	QCC
Triazabicyclodecenium hexanoate	[TBDH][nPentCOO]	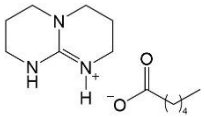	255.36	>99	Synthesized	PB; QCC
1,1,3,3-tetramethylguanidinenium propanoate	[TMGH][EtCOO]	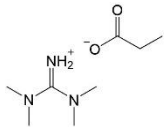	189.26	>99	Synthesized	PB; QCC
1,1,3,3-tetramethylguanidinenium hexanoate	[TMGH][nPentCOO]	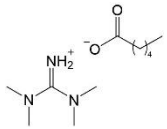	231.34	>99	Synthesized	PB; QCC

[a] CM – Calvet microcalorimetry; PB – Phase Behavior; QCC – Quantum Chemical Calculations KNQ – Knudsen experiment; C_p (298.15 K, *T)* – Heat capacities at different temperatures and at 298.15 K.

Molar masses of the protic ionic liquids calculated as the sum of the molar masses of the acid and base.

Table 3.9. Summary of the protic ionic liquids studied in this work. (Part V of V)

Protic Ionic Liquid	Abbreviation	Structural formula	Molar Mass / g·mol^{-1}	Purity / %	Source CAS number	Studies performed [a]
1,2-dimethyl-1,4,5,6-tetrahydropyrimidinenium propanoate	[DMTHPH][EtCOO]	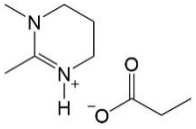	186.25	>99	Synthesized	CM; QCC; KNQ
1,2-dimethyl-1,4,5,6-tetrahydropyrimidinenium butanoate	[DMTHPH][nPrCOO]	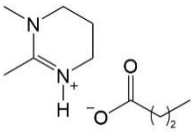	200.28	>99	Synthesized	CM; QCC
1,2-dimethyl-1,4,5,6-tetrahydropyrimidinenium pentanoate	[DMTHPH][nButCOO]	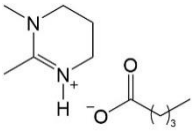	214.31	>99	Synthesized	CM; QCC
1,2-dimethyl-1,4,5,6-tetrahydropyrimidinenium hexanoate	[DMTHPH][nPentCOO]	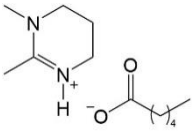	228.33	>99	Synthesized	CM; QCC; KNQ C_p (298.15 K, *T*)
1,2-dimethyl-1,4,5,6-tetrahydropyrimidinenium heptanoate	[DMTHPH][nHexCOO]	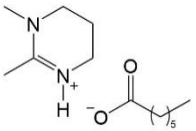	242.35	>99	Synthesized	CM; QCC
1,2-dimethyl-1,4,5,6-tetrahydropyrimidinenium octanoate	[DMTHPH][nHeptCOO]	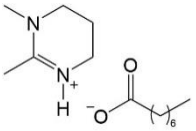	256.38	>99	Synthesized	CM; QCC

[a] CM – Calvet microcalorimetry; PB – Phase Behavior; QCC – Quantum Chemical Calculations KNQ – Knudsen experiment; C_p (298.15 K, *T)* – Heat capacities at different temperatures and at 298.15 K.

Molar masses of the protic ionic liquids calculated as the sum of the molar masses of the acid and base.

Table 3.10. Summary of the protic ionic liquids with different proportions of base and acid studied in this work.

Protic Ionic Liquid	Base : Acid Proportion	Molar Mass / g·mol^{-1}	Purity / %	Source	Studies performed [a]
[DBNH][nPrCOO] 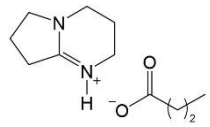	3:1	115.88	>99	Synthesized	CM
	2:1	111.66	>99	Synthesized	CM
	eq (1:1.38)	103.62	>99	Synthesized	CM
	1:3	97.49	>99	Synthesized	CM
[DBNH][nHeptCOO] 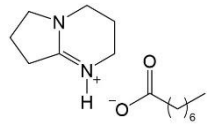	3:1	129.59	>99	Synthesized	CM
	2:1	130.99	>99	Synthesized	CM
	eq (1:1.78)	137.20	>99	Synthesized	CM
	1:3	139.00	>99	Synthesized	CM
[DBUH][nPrCOO] 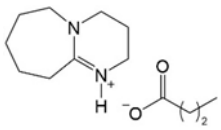	3:1	137.49	>99	Synthesized	CM
	2:1	130.76	>99	Synthesized	CM
	eq (1:1.27)	116.97	>99	Synthesized	CM
	1:3	104.78	>99	Synthesized	CM
[DBUH][nHeptCOO] 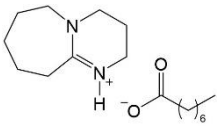	3:1	150.23	>99	Synthesized	CM
	2:1	149.51	>99	Synthesized	CM
	eq (1:1.56)	147.34	>99	Synthesized	CM
	1:3	146.22	>99	Synthesized	CM

[a] CM – Calvet microcalorimetry.
Molar masses of the protic ionic liquids (proportions) calculated as the proportion of the molar masses of the acid and base.

Table 3.10 presents a summary of the studied PILs with different base:acid proportions and the studies performed. The molar masses were calculated as the sum of the proportions of the molar masses of the acid and the base.

3.2. Synthesis and purification

3.2.1. Synthesis procedure

The general synthetic procedure involves the exothermic neutralization of base with a stoichiometric amount of different acids. The neutralization reaction is given by the following equation:

$$B + HA \leftrightarrow [BH][A] \qquad \textbf{(3.1)}$$

The synthesis of [DBUH][MeCOO] is described here and a similar procedure has been used for the other PILs. 15 mL (0.10 mol) of DBU was taken into a 500 mL triple necked round bottomed flask, fitted with a pressure equalizing dropping funnel in a water bath. An equimolar amount (stoichiometric quantity) 5.9 mL (0.10 mol) of acetic acid was added dropwise through a dropping funnel under a nitrogen atmosphere N_2 (g) and under constant stirring. After completion of acid addition, the mixture was stirred for 24 h under nitrogen atmosphere. All the compounds were used as purchased and were kept under nitrogen atmosphere to avoid the contamination with CO_2 and H_2O.

Figure 3.2 shows the typical experimental assembly, adopted in the synthesis of the PILs studied.

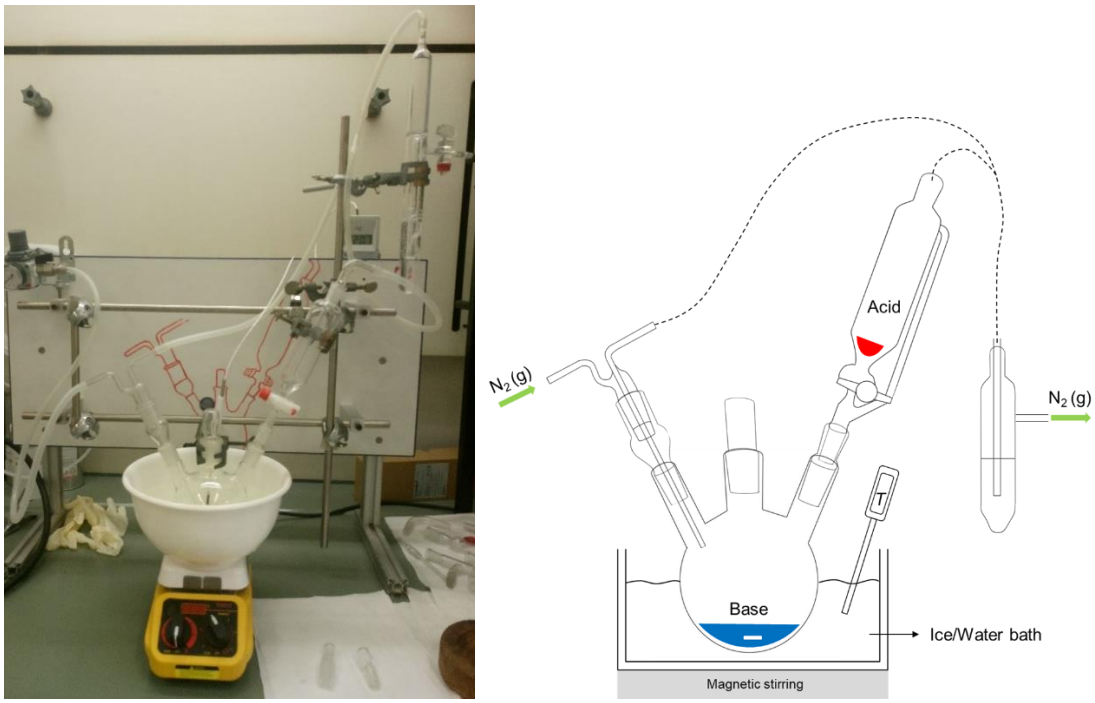

Figure 3.2. Image and schematic representation of the synthesis assembly.

In order to remove the unreacted reactants (if any) and moisture from the PIL, high vacuum was applied for about 24 h. A dried pale-yellow color and viscous liquid was obtained, which was characterized by ^{1}H and ^{13}C NMR spectroscopic techniques. The non-stoichiometric PIL mixtures were prepared in an analogous way, by mixing the respective quantities of acid and base.

Table 3.11 summarizes the yields (%) obtained for the compounds synthesized.

Table 3.11. Summary of the yield (%) of the relevant synthesized compounds.

Compound	Yield (%) *	Compound	Yield (%) *
[DBNH][MeCOO] (1:1)	94	[DBUH][nPrCOO] (eq)	64
[DBNH][EtCOO] (1:1)	93	[DBUH][nPrCOO] (1:3)	81
[DBNH][nPrCOO] (1:1)	93	[DBUH][nButCOO] (1:1)	67
[DBNH][nPrCOO] (3:1)	92	[DBUH][nPentCOO] (1:1)	81
[DBNH][nPrCOO] (2:1)	94	[DBUH][nHexCOO] (1:1)	76
[DBNH][nPrCOO] (eq)	81	[DBUH][nHeptCOO] (1:1)	79
[DBNH][nPrCOO] (1:3)	91	[DBUH][nHeptCOO] (3:1)	86
[DBNH][nButCOO] (1:1)	91	[DBUH][nHeptCOO] (2:1)	82
[DBNH][nPentCOO] (1:1)	93	[DBUH][nHeptCOO] (eq)	65
[DBNH][nHexCOO] (1:1)	94	[DBUH][nHeptCOO] (1:3)	71
[DBNH][nHeptCOO] (1:1)	92	[DBUH][iPrCOO] (1:1)	83
[DBNH][nHeptCOO] (3:1)	93	[TBDH][EtCOO] (1:1)	91
[DBNH][nHeptCOO] (2:1)	92	[TBDH][nPentCOO] (1:1)	85
[DBNH][nHeptCOO] (eq)	83	[TMGH][EtCOO] (1:1)	93
[DBNH][nHeptCOO] (1:3)	85	[TMGH][nPentCOO] (1:1)	64
[DBNH][iPrCOO] (1:1)	91	[DMTHPH][EtCOO] (1:1)	83
[DBNH][FPrCOO] (1:1)	87	[DMTHPH][nPrCOO] (1:1)	90
[DBUH][MeCOO] (1:1)	77	[DMTHPH][nButCOO] (1:1)	86
[DBUH][EtCOO] (1:1)	87	[DMTHPH][nPentCOO] (1:1)	87
[DBUH][nPrCOO] (1:1)	89	[DMTHPH][nHexCOO] (1:1)	86
[DBUH][nPrCOO] (3:1)	89	[DMTHPH][nHeptCOO] (1:1)	82
[DBUH][nPrCOO] (2:1)	86		

* Isolated yield, corrected for sample purity.

3.2.2. Purification

Purification procedures

The laboratory was equipped with a drying installation suitable for the small-scale routine purification of protic ionic liquids. It was used in the course of this thesis. This apparatus has the possibility of simultaneous by drying four different protic ionic liquid samples. The system consists of customized *schlenk*, a specific temperature in an aluminum block. The customized *Schlenk* flasks are based on a tube shape (external diameter 17 mm, internal diameter 13 mm) fitted with a vacuum greaseless valve (J. Young Right Angel Taps) and a male joint (B 19/26, diameter = 19 mm and height = 26 mm), allowing easier sample manipulation and avoiding contamination with grease. The *Schlenk* flask is covered with a female glass cap and was designed for small-scale purification/drying of samples (3 cm^3), with sufficient free space to avoid bumping of the sample to the glass cap and the vacuum valve. The image and the schematic representation of the *Schlenk* flask are presented in figure 3.3.

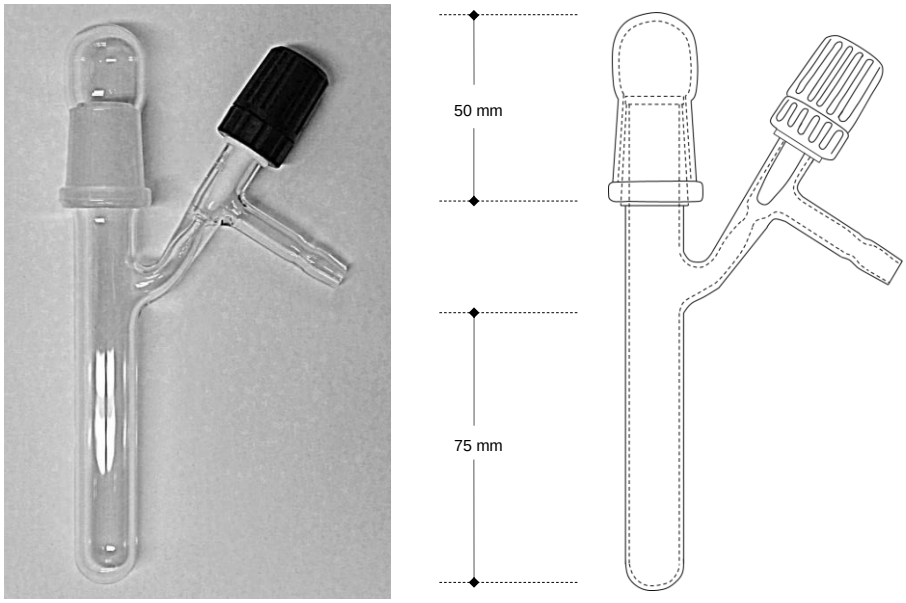

Figure 3.3. Image and schematic representation of the *Schlenk* flask. (adapted from source [3.1])

The cylindrical aluminum block (diameter = 100 mm and height = 100 mm) is heated by a customized electrical heater (100 watts at 230 VAC, "Resisterma", 8 mm external diameter, 50 mm heating length), placed in the center of the block. The temperature of the block is kept constant by an ON/OFF temperature controller that

receives information of a thermistor, located near to the electrical heater, as presented schematically in figure 3.4.

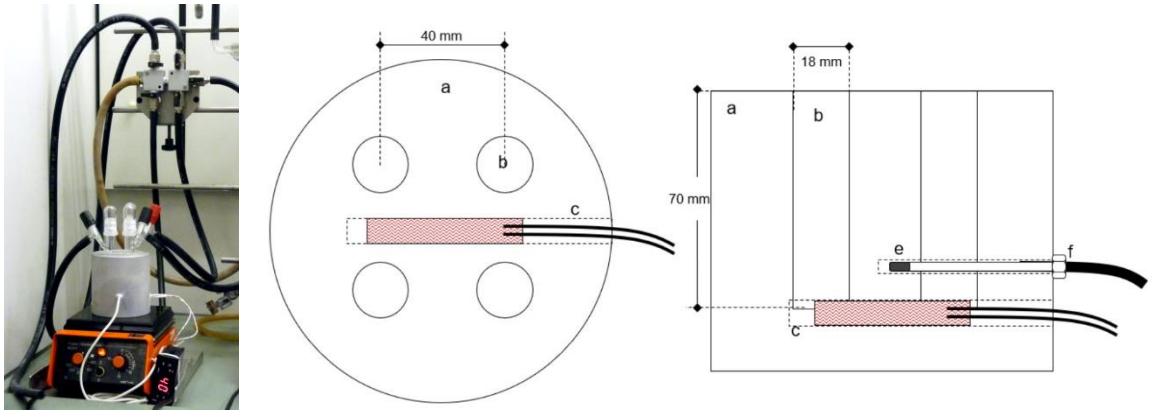

Figure 3.4. Figure and schematic representation of the temperature-controlled aluminum block of the drying apparatus. a - aluminum block; b - *Schlenk* flask cavity; c - electrical heater cavity; d - electrical heater; e - temperature sensor cavity; f - thermistor for temperature monitoring and control. (adapted from source [3.1])

The aluminum block is on top of a magnetic stirring plate, which enables constant stirring (Teflon coated spherical magnetic stirring ball, the diameter of 8 mm) of the protic ionic liquid during the drying process. The system is connected to a glass/aluminum vacuum line already assembled in our laboratory. The vacuum pumping system is based on a dual stage rotary vane vacuum pump (Edwards model E2M8), reaching a final pressure of purification lower than 100 Pa.

All protic ionic liquids were dried under vacuum at a moderate temperature (≈298 K) and constant stirring, and with molecular sieves (3 Å) in order to reduce the presence of water, gases or other volatile impurities. This process was performed systematically before and during the thermophysical measurements. The purity of each ionic liquid after drying was evaluated by FTIR, and ^{1}H, ^{13}C, and ^{19}F NMR. No impurities were detected for all ionic liquids, and the mole fraction purity was considered to be at least the purity of the components (acid and/or base), meaning, higher than 0.99.

3.3. Characterization

3.3.1. Fourier transform infrared spectroscopy - FTIR

Fourier Transform Infrared Spectroscopy is a spectroscopic technique used to obtain an infrared spectrum of absorption, emission, photoconductivity or Raman scattering of a solid, liquid or gas. [3.2] A FTIR spectrometer simultaneously collects spectral data in a wide spectral range. This confers a significant advantage over a dispersive spectrometer, which measures intensity over a narrow range of wavelengths at a time. FTIR has made dispersive infrared spectrometers obsolete (except for some particular methodologies in the near infrared), opening up new applications of infrared spectroscopy.

Experimental

The FTIR measurements were performed using a Perkin-Elmer FTIR Spectrum BX II spectrometer (figure 3.5), equipped with a GladiATR diamond crystal ATR sampling accessory with temperature control (from 298 K to 470 K). A total of 30 scans were taken for several protic ionic liquids studied in this work. The spectrum resolution was 4 cm^{-1} and all the FTIR spectra were recorded at T = 298 K. The software package Spectrum v5.3.1 from Perkin Elmer was used in the data acquisition and spectral analysis. The results are presented as supporting information in Annexes. As an example, figure 3.6. presents the FTIR spectrum obtained for liquid DBN at 298 K.

Figure 3.5. View of the FTIR instrument used in this work (Perkin-Elmer FTIR, model Spectrum BX II-FTIR).

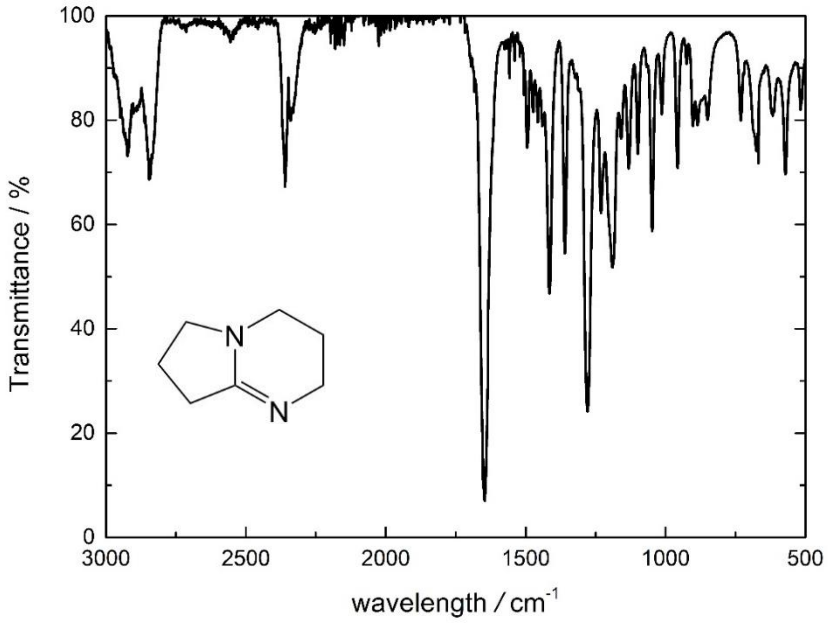

Figure 3.6. Example of a FTIR spectrum obtained for DBN superbase, at *T* = 298 K.

The FTIR measurements were useful to structurally characterize the PILs and understand how much and how easily they absorb and release H_2O and CO_2. The obtained results, presented in Annex A, were mostly used to check for the presence of impurities in the PILs studied (e.g. H_2O and CO_2).

3.3.2. Nuclear magnetic resonance – NMR

NMR spectroscopy is a useful technique to structurally characterize organic and inorganic compounds. It is a very powerful tool for the characterization of the PILs studied and has a special place among the most important characterization techniques in Chemistry. [3.5] The principle behind NMR is that many nuclei have spin and all nuclei are electrically charged. If an external magnetic field is applied, an energy transition is possible from the fundamental to a higher energy level (generally a single energy gap). The transition takes place at a wavelength that corresponds to radio frequencies and when the spin returns to its ground-state, energy is emitted at the same frequency. The signal that matches this transition is measured and processed in order to yield an NMR spectrum for the nuclei under study. This technique was used to study the speciation in PILs (Chapter 6), namely to determine the molar composition of these compounds at various stages.

Experimental

Unless otherwise noted, the ^{1}H and ^{13}C NMR spectra of the pure samples and of the samples dissolved in $CDCl_3$ were recorded on a Bruker Avance 300 [operating at 300.13 MHz (^{1}H), 75.47 MHz (^{13}C)] spectrometer, at T = 298 K, using TMS as an internal reference. The results confirm the ionic character of the PILs; their base:acid compositions, and show no detectable amount of impurities. The detailed experimental results are presented in Annexes.

3.4. Additional materials

The experimental measurement techniques used in this work were calibrated and tested against recommended standards. The summary of the standards and test compounds is listed in table 3.12.

Table 3.12. Standards and test compounds, apparatus, and purpose.

Compound	Supplier	Technique	Purpose
1,3,5-triphenylbenzene	Sigma-Aldrich	KNQ	Test
Sapphire (α-aluminum oxide)	NBS standard sample, SRM 720	Drop Calorimeter µDSC	Calibration
Benzoic Acid	NIST Standard Reference Material 39j	Drop Calorimeter µDSC	Test
Ferrocene	Sigma-Aldrich	Calvet	Calibration
Undecane	Sigma-Aldrich	Calvet	Calibration

KNQ - Knudsen effusion quartz crystal microbalance.

The Knudsen effusion method combined with a quartz crystal microbalance apparatus was tested using 1,3,5 - triphenylbenzene (Sigma–Aldrich). The compound was purified by vacuum sublimation. The heat capacity drop calorimeter was calibrated with the reference materials [3.7], water and α-aluminum oxide. The sample of α-aluminum oxide was dried at T = 423 K. The calorimeter was tested with benzoic acid - a primary reference material (NIST Standard Reference Material 39j), was used after drying under reduced pressure (at 300 K; p < 10 Pa; 24 h). The calvet calibration was made using ferrocene (Sigma-Aldrich) and undecane (Sigma-Aldrich). The purity of all compounds was checked by gas chromatography, using an HP 4890 apparatus equipped with an HP-5 column, cross-linked, 5% diphenyl and 95% dimethylpolysiloxane. All compounds showed a mass fraction purity greater than 0.998.

3.5. References

[3.1] Rocha, M. A. A., *Thermodynamic Properties of Ionic Liquids* **2013**, PhD Thesis, Porto, Portugal.

[3.2] Ribeiro da Silva, M. A. V.; Ferrão, M. L. C. C. H.; Lopes, A. J. M., *J. Chem. Thermodyn*. **1993**, 25, 229.

[3.3] Kirshna, G. M. et al, *Int. J. Pharm.* **2013***,* 3, 396-402.

[3.4] Saraswathi, M. et al, *Int. J. ChemTech* **2012***,* 4, 1343-1349.

[3.5] Shen, M.; Zhang, Y.; Chen, K.; Che, S.; Yao, J.; Li, H.; *J. Phys. Chem. B* **2017**, 121, 6, 1372-1376.

[3.6] Meija, J.; Coplen, T. B.; Berglund, M.; Brand, W. A.; De Bie`vre, P.; Groning, M.; Holden, N. E.; Irrgeher, J.; Loss, R. D.; Walczyk T. and Prohaska, T., *Pure Appl. Chem*. **2016**, 88, 265–291.

[3.7] Sabbah, R.; Xu-wu, A.; Chickos, J. S.; Leitão, M. L. P.; Roux, M. V.; Torres, L. A. *Thermochim. Acta* **1999***,* 331, 93–204.

CHAPTER 4

Quantum Chemical Calculations

4. Quantum Chemical Calculations

Chapter 4 was designed and organized to support the experimental work presented in the next chapters to complement the energetic study of several PILs. For that purpose, several computational calculations based on quantum chemistry were carried out.

4.1. Methodologies

Computational chemistry is a branch of chemistry that uses the principles of computer science in the determination of some properties to aid in the resolution of chemical problems. Some examples of properties determined through quantum chemistry calculations include molecular and atomic structure, absolute and relative energies, charge distribution, vibrational frequencies, spectroscopic properties, among others. In this work, several properties were determined, and, in this chapter, the results will be presented and discussed. There are different methodologies that can be used in quantum chemical calculations. The three most known are *ab initio*, semi-empirical or empirical, and the one based on density functional theory. The *ab initio* (meaning "from the beginning") methodology is based on quantum mechanics, does not include empirical parameters, is mathematically rigorous and it's based on wave functions. This method has some important advantages: can be used on every type of system, does not depend on experimental data, and allows the calculation of transition and excited states. But, it also has a great disadvantage: it's computationally demanding.

Density functional theory (DFT) is a computational quantum mechanical modeling method used in physics, chemistry, and materials science to investigate the electronic structure (principally the ground state) of many-body systems, in particular atoms, molecules, and condensed phases. Using this theory, the properties of a many-electron system can be determined by using functionals, i.e. functions of another function, which in this case is the spatially dependent electron density. Hence the name density functional theory comes from the use of functionals of the electron density. The main advantages of DFT are: it includes an approximate treatment of electronic correlation; less computationally demanding when compared to *ab initio*, and the "quality" is similar; allows the calculation of transition states. Some disadvantages are: less rigorous than most *ab initio* methods; does not allow to systematically improve the results and poorly

describes dispersive interactions. Nowadays, some improved DFT methods are able to calculate excited states and describe satisfactorily dispersive interactions.

The semi-empirical and empirical methodology is the less computationally demanding of the three and allows the calculation of transition and excited states but requires the input of experimental data or data from previous *ab initio* or DFT calculations. It is also less rigorous than the other two methodologies and it is based on several approximations in various stages of the calculations. The present work uses not only the DFT methodology to study the different bases, acids and protic ionic liquids, but also one method derived from *ab initio*, the Moller-Plesset perturbation theory of second order (MP2).

4.1.1. Basis functions, sets, and functionals

Three different computational methods were employed in this work; for each of them the limitations with more relevance to this work are [4.1]:

- B3LYP – it is not a pure *ab initio* method; the exchange/correlation functionals cannot describe dispersive interactions, which derive from electron correlation at long range;
- M06-2X – it is a highly nonlocal functional that's parametrized only for nonmetals;
- MP2 – it is not variational; correlation energy is accounted for by only one corrective term; relatively computationally expensive.

However, knowing in advance the limitations of a given computational method can sometimes furnish good indications about the factors affecting energetics. For instance, if an Hartree-Fock or B3LYP result points to molecular destabilization relative to an experimental result, the cause for that error may well be related with the existence of a significant dispersive interaction and/or extensive electronic delocalization. Since DFT needs functionals to calculate the properties, several approaches have been designed to improve the results obtained with this method. The two most popular functionals are known as BLYP (from the name Becke for the exchange part and Lee, Yang and Parr for the correlation part) and B3LYP, which are hybrid functionals in which the exchange energy, in this case from Becke's exchange functional, is combined with the exact energy from Hartree–Fock theory. In B3LYP, along with the component exchange and correlation functionals, three parameters define the hybrid functional, specifying how much of the exact exchange is "mixed in". Unfortunately, although the

results obtained with these functionals are usually sufficiently accurate for most applications, there is no systematic way of improving them. Hence in the current DFT approach, it is not possible to estimate the error of the calculations without comparing them to other methods or experiments. [4.2] Møller–Plesset perturbation theory (MP) is one of several quantum chemistry post-Hartree–Fock *ab initio* methods in the field of computational chemistry. It improves on the Hartree–Fock method by adding electron correlation effects by means of Rayleigh–Schrödinger perturbation theory (RS-PT), usually to the second (MP2), third (MP3) or fourth (MP4) order. Its main idea was published as early as 1934 by Christian Møller and Milton S. Plesset. [4.3]

A basis set is a group of functions that are combined in linear combinations to create atomic and molecular orbitals. For convenience these functions are typically atomic orbitals centered on atoms but can be any combination of functions that produce a good description of a molecular orbital; plane waves are frequently used in bulk materials calculations. [4.4-4.6]

In quantum chemistry, calculations using finite basis sets are susceptible to basis set superposition error (BSSE). As the atoms of interacting molecules (or of different parts of the same molecule - intramolecular BSSE) [4.7-4.8] approach one another, their basis functions overlap. Each interacting fragment "borrows" functions from the other, effectively increasing its basis set and impacting on the calculation of derived properties such as energy. If the total energy is minimised as a function of the system geometry, the short-range energies from the mixed basis sets must be compared with the long-range energies from the unmixed sets, and this comparison introduces an error. Other than using infinite basis sets, two methods exist to eliminate the BSSE. In the Chemical Hamiltonian Approach (CHA), [4.9-4.10] basis set mixing is prevented *à priori*, by replacing the conventional Hamiltonian with one in which all the projector-containing terms that would allow mixing have been removed. In the counterpoise method (CP), [4.11-4.13] the BSSE is calculated by re-performing all the calculations using the mixed basis sets, and the error is then subtracted *à posterior* from the uncorrected energy. The mixed basis sets are realised by introducing "ghost orbitals", basis set functions that have no electrons nor protons. [4.8] Though conceptually very different, the two methods tend to give similar results. [4.14] It has, however, been shown that the error is often larger when using the CP method since the central atoms in the system have much greater freedom to mix with all of the available functions compared to the outer atoms. In the CHA model, those orbitals have no greater intrinsic freedom and therefore the correction treats all fragments equally. [4.15] The errors inherent to either BSSE

correction disappear more rapidly than the total value of BSSE with the increase in basis sets. [4.16]

4.1.2. Geometry optimization and frequency calculations

For the compounds included in the computational study, full geometry optimizations, with no symmetry restrictions, were performed at the MP2/cc-pVDZ, M06-2X/6-311++G(d,p) and B3LYP/6-311++G(d,p) levels of theory. The optimization of each compound was made independently from the others. After the geometry optimization, the vibrational frequencies were calculated using the levels of theory previously described. These values were then corrected using the scaling factors proposed by Radom et al. [4.17-4.19]

Table 4.1. Applied anharmonicity scaling factors for the correction of the vibrational frequencies for the calculation of the selected parameters considering different quantum chemical models.

Model/basis set	**ZPE**	$H^0(T)$	$S^0(T)$	$C_p^0(T)$
B3LYP/6-311++G(d,p)	0.9887	1.0102	1.0161	0.9688
M06-2X/6-331++G(d,p)	0.9700	0.9440	0.9440	0.9830
MP2/cc-pVDZ	0.9784	0.9796	0.9379	0.9543

4.1.3. Accessible Surface Area – ASA

The accessible surface area (ASA) or solvent-accessible surface area (SASA) is the surface area of a molecule or biomolecule that is accessible to a solvent. Measurements of ASA are usually described in units of square Angstroms, $Å^2$.

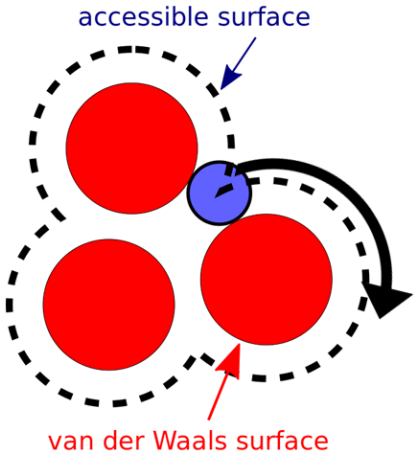

Figure 4.1. Illustration of the solvent accessible surface in comparison to the van der Waals surface. The van der Waals surface as given by the atomic radii is shown in red. The accessible surface is drawn with dashed lines and is measured by tracing the center of the probe sphere (in blue) as it rolls along the van der Waals surface.

ASA was first described by Lee & Richards in 1971 and is sometimes called the Lee-Richards molecular surface. [4.20] ASA is typically calculated using the 'rolling ball' algorithm developed by Shrake & Rupley in 1973. [4.21] This algorithm uses a sphere (of solvent) of a particular radius to 'probe' the surface of the molecule, as illustrated in figure 4.1.

Figure 4.2. presents an example of the obtained ASA for the optimized geometry of [DBNH][EtCOO]:

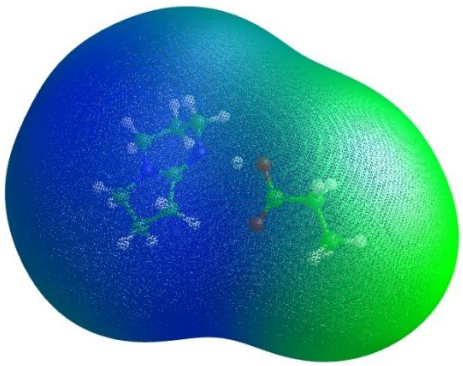

Figure 4.2. Accessible surface area, *ASA*, for the optimized geometry of [DBNH][EtCOO], at the B3LYP/6-311++G(d,p) level of theory, probe radius = 1.4 Å.

Shrake-Rupley algorithm

The Shrake-Rupley algorithm is a numerical method that draws a mesh of points equidistant from each atom of the molecule and uses the number of these points that are solvent accessible to determine the surface area. [4.21] The points are drawn at a water molecule's estimated radius beyond the van der Waals radius, which is effectively similar to ‘rolling a ball’ along the surface. All points are checked against the surface of neighbouring atoms to determine whether they are buried or accessible. The number of points accessible is multiplied by the portion of surface area each point represents to calculate the ASA. The choice of the 'probe radius' does have an effect on the observed surface area, as using a smaller probe radius detects more surface details and therefore reports a larger surface. A typical value is 1.4 Å, which approximates the radius of a water molecule. Another factor that affects the results is the definition of the VDW radii of the atoms in the molecule under study. For example, the molecule may often lack hydrogen atoms which are implicit in the structure. The hydrogen atoms may be implicitly included in the atomic radii of the 'heavy' atoms, with a measure called the 'group radii'. In addition, the number of points created on the van der Waals surface of each atom determines another aspect of discretization, where more points provide an increased level of detail.

4.2. Results and discussion

The proton affinity of an anion or of a neutral atom or molecule is the negative of the enthalpy change in the reaction between the following species in the gas phase:

$$A^- + H^+ \rightarrow HA$$
$$B + H^+ \rightarrow BH^+$$

These reactions are always exothermic in the gas phase, i.e. energy is released when the reaction advances in the direction shown and enthalpy is negative, while the proton affinity is positive.

Table 4.2. Proton affinities for the bases considered in this work, at the B3LYP/6-311++G(d,p), M06-2X/6-311++G(d,p) and the MP2/cc-pVDZ levels of theory.

Compound	Proton affinity / kJ·mol^{-1}		
	B3LYP	**M06-2X**	**MP2**
DBN + $H^+ \leftrightarrow$ $DBNH^+$	1039	1029	1035
DBU + $H^+ \leftrightarrow$ $DBUH^+$	1047	1034	1038
TBD + $H^+ \leftrightarrow$ $TBDH^+$	1058	1050	1057
TMG + $H^+ \leftrightarrow$ $TMGH^+$	898	888	907
DMTHP + $H^+ \leftrightarrow$ $DMTHPH^+$	1037	1029	1037

The proton affinities for the optimized geometries of the superbases studied in this work are calculated using the equation 4.1:

$$\text{Proton affinity} = (H_{298.15}(\text{DBN}) + H_{298.15}(H^+)) - H_{298.15}(DBNH^+) \quad \textbf{(4.1)}$$

The results are presented in table 4.2. As can be seen the proton affinity of TBD is the highest and TMG the lowest the order, being: TBD > DBU > DBN ≥ DMTHP > TMG. Although DBN is also considered an organic superbase, it is not clear if DMTHP is a weaker base. To clarify this, the relative basicity of DMTHP, DBN and DBU was also studied by recording the ^{1}H NMR spectra of the DBN:DBU:EtCOOH (1:1:1) and DMTHP:DBN:FEtCOOH (1:1:1) mixtures in $CDCl_3$. According to the literature, DBU is the strongest base in acetonitrile and gas phase. [4.22]

For these three bases both experiment and theory indicate the following order of base strength: DBU > DBN ≈ DMTHP.

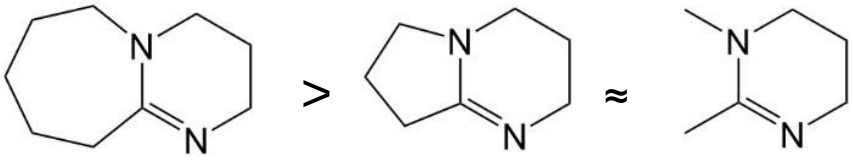

Figure 4.3. Base strength of the studied superbases: DBU > DBN ≈ DMTHP.

The electronic energies concerning the trimers were calculated in this work in order to explore the interactions that the neutral acid or base can establish with the ion pair. (see figure 4.4)

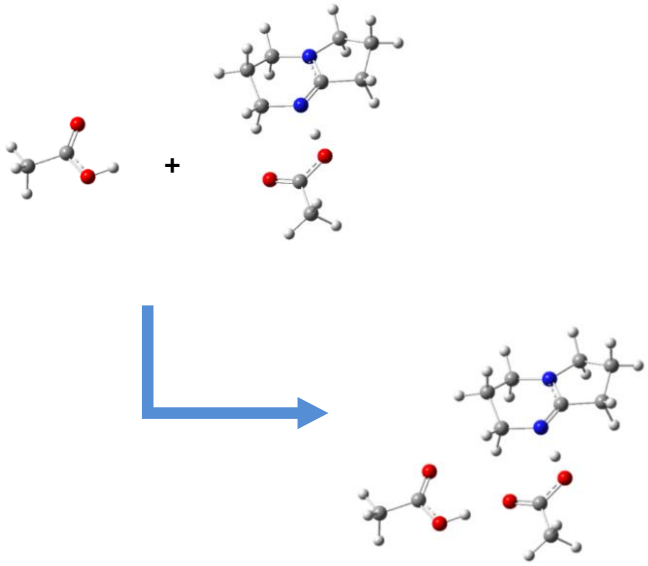

Figure 4.4. Schematic representation of the interaction between the PIL ion pair and a neutral molecule of acid.

Table 4.3 presents the electronic energies, E_{int}, uncorrected and corrected for BSSE by the counterpoise method. Not only for the gas phase complexes formed between the PIL ion pair and a neutral molecule of acid or base.

Table 4.3. Electronic energies, E_{int}, uncorrected and corrected for BSSE by the counterpoise method, for the gas phase complexes formed between the PIL ion pair and a neutral molecule of acid or base, calculated at the M06-2X/6-311++G(d,p) level of theory. Values in Hartrees.

Species	E_{el} (uncorrected)	E_{el} (BSSE corrected)
[DBNH][CH_3COO]···CH_3COOH	−841.57260	−841.57146
[DBNH][CH_3COO]···DBN	−995.90485	−995.90277
[DBNH][CF_3COO]···CF_3COOH	−1437.04506	−1437.04316
[DBNH][CF_3COO]···DBN	−1293.64514	−1293.64284

Note: 1 Hartree = 2625.5 kJ·mol^{-1}

It can be said that to some preferred interaction the neutral carboxylic acids establish with the PIL ion pairs, arising from their ability as hydrogen bond donors. This hypothesis was evaluated by calculating the interaction energies at T = 0 K, ΔE_{int}, (corrected for BSSE by the counterpoise method) [4.23-4.24] for the M06-2X/6-311++G(d,p) [4.25] optimized intermolecular complexes formed between the PIL ion pairs [DBNH][CH_3COO] and [DBNH][CF_3COO] with an additional molecule of neutral acid or base (tables 4.3 and 4.4). This model was considered because it is the simplest for which the derived ΔE_{int} is expected to capture the major energetic contributions for the interactions between the neutral form of the acid or the base and the ion pair.

Table 4.4. Interaction energies, ΔE_{int}, corrected for BSSE by the counterpoise method, [4.23-4.24] between the PIL ion pair and a neutral molecule of acid or base, calculated at the M06-2X/6-311++G(d,p) level of theory.[a]

Species	ΔE_{int} / kJ·mol^{-1}
[DBNH][CH_3COO]···CH_3COOH	−44
[DBNH][CH_3COO]···DBN	−35
[DBNH][CF_3COO]···CF_3COOH	−77
[DBNH][CF_3COO]···DBN	−49

[a] ΔE_{int} includes the geometry distortion energy of the interacting fragments associated with the formation of the trimers.

The computational results confirm the stronger interaction between the ion pair and the neutral acid, which is explained by the establishment of a hydrogen bond between the two carboxylic moieties, as can be seen in figure 4.4. This explains the excess of acid observed at the azeotrope of most PILs. In the case of the PILs with fluorinated acids, although the interaction of the acid with the ion pair is stronger, the extent of the acid-base equilibrium is higher and reduces the fraction of neutral species to negligible amounts.

The distance between the acid and the superbase, in the optimized geometry, was evaluated. According to figure 4.6, the carboxylic acids prefer DBU when compared to DBN and DMTHP superbases. This is expected if taking into account the strength of the superbases. For DBN and DBU-based PILs, smaller acids are closer to the superbase, but for DMTHP-based PILs, the size of the acid seems quite irrelevant.

Figures 4.5 and 4.6 presents the distances between the -OH and =O group of the different acids and the superbases and how they were calculated at the B3LYP/6-311++G(d,p) level of theory. The other results concerning the distances between acids and superbases are presented in Annex B.

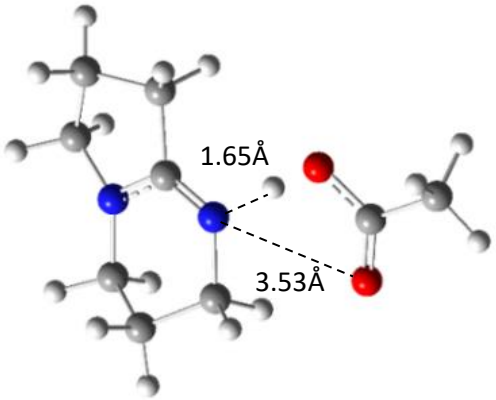

Figure 4.5. The distances between the -OH and =O group of propionic acid to the superbase DBN as calculated at the B3LYP/6-311++G(d,p) level of theory.

As can be seen in figure 4.6, the distance between the -OH group of the carboxylic acid to the N atom of the superbase varies with the different families of PILs. As expected, for stronger superbases the distance is shorter. The observed variation/trendshift with the carboxylic acid chain length in *n* = 4 and 5 must be seen with precaution. These calculations were made with care but all the possible geometries and configurations between the acid and base were not explored, so further and extensive work needs to be done to reach such a higher conclusion – trendshift exists.

The ASA was calculated for all PILs and increases linearly with the increase of the size of the acid, see figure 4.7. DBU-based PILs are the PILs with larger ASA and so, it is suggested, also taking into account the stronger basicity of this base, that solvents will interact more with DBU-based PILs than with the others.

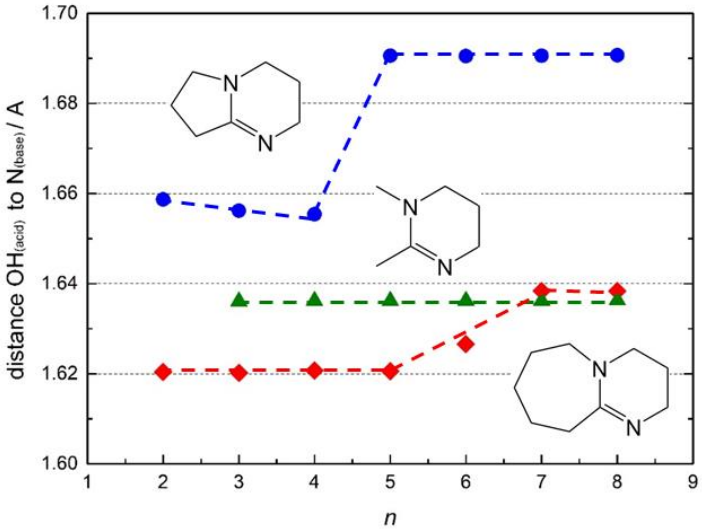

Figure 4.6. The distance between the -OH group of the carboxylic acid to the N atom of the superbase as a function of the chain length of the acid (*n* is the total number of carbon atoms in the acid) in each protic ionic liquid. (calculated at the B3LYP/6-311++G(d,p) level of theory). DBN-based protic ionic liquids – blue circles, DBU-based protic ionic liquids – red diamonds and DMTHP-based protic ionic liquids – green triangles.

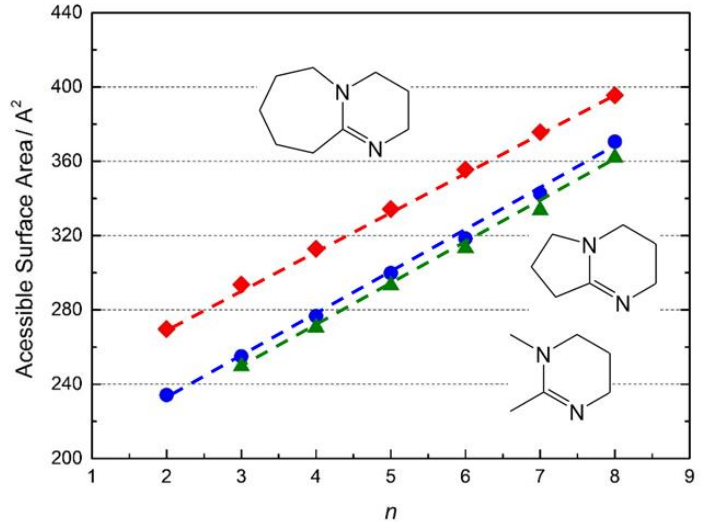

Figure 4.7. Accessible surface area, ASA for the optimized geometries as a function of the chain length of the acid (*n* is the total number of carbon atoms in the acid) in each protic ionic liquid. (calculated at the B3LYP/6-311++G(d,p) level of theory with probe radius = 1.4 Å). DBN-based protic ionic liquids – blue circles, DBU-based protic ionic liquids – red diamonds and DMTHP-based protic ionic liquids – green triangles.

The acid-base and ion pair equilibria in the gas phase of the PILs studied were evaluated by quantum chemical calculations. The speciation of these PILs in the gas phase may comprise the ion pair, isolated charged species and isolated

neutral species in varying proportions, as depicted in figure 4.8. All theoretical methods agree on the relative magnitude of the three gas phase reactions (R1, R2 and R3), and their dependence with the base and the acid. The results are presented in Annex B.

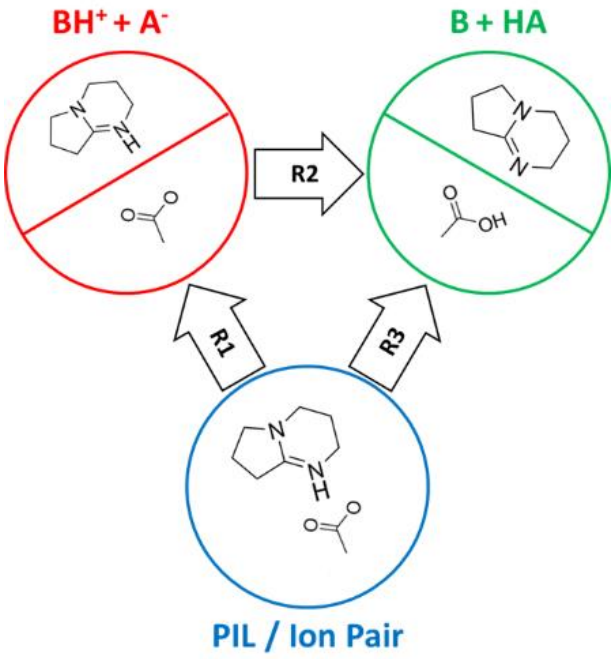

Figure 4.8. Schematic representation of reactions and species that may exist in the gas phase of PILs and their participation in acid-base and ion pair equilibria; the PIL [DBNH][MeCOO] is shown as an example.

According to the obtained results, the ion pair is the enthalpically preferred species in all PILs. It can also be observed that, as expected, the isolated ions are significantly less stable, see table B.8 in Annex B. Hence, it can be concluded that, in the gas phase, the PILs exist mostly as a distribution of ion pair and isolated neutral species (R3 equilibrium). However, depending on the conditions of temperature and pressure, $-T \cdot \Delta S$ can be high enough to overcome ΔH and shift the R3 equilibrium in the direction of the separated neutral species. The results suggest that, as indicated by the calculated ΔH_r for R1, $[DBNH]^+$ has a slightly stronger intermolecular interaction with the acids in the ion pair than $[DBUH]^+$. However, this is somewhat compensated by the stronger basicity of DBU, which makes R2 less exothermic for DBU than for DBN. The combination of these effects results in an ion pair equilibrium, as translated by R3, which, in enthalpic terms, has virtually no dependence with the acid and shows a slightly higher tendency of the DBN PILs to be as ion pairs.

4.3. References

[4.1] Roy, D.; Marianski, M.; Maitra, N. T.; Dannenberg, J. J., *J. Chem. Phys*. **2012**, 137, 134109.

[4.2] Dunning, T. H., *J. Chem. Phys*. **1989**, 90, 1007–1023.

[4.3] Møller, C., Plesset, M. S. *Phys. Rev*. **1934**, 46 (7), 618–622.

[4.4] http://www.cfs.dl.ac.uk/docs/html/part3/node14.html

[4.5] http://www.wavefun.com/support/sp_compfaq/BasisSetFAQ.html

[4.6] Frank Jensen, *Introduction to Computational Chemistry* **1999**.

[4.7] Balabin, R. M., *J. Chem. Phys.* **2008**, 129 (16), 164101.

[4.8] Hobza, P., Müller-Dethlefs, K., *Non-covalent Interactions: Theory and Experiment* **2010**.

[4.9] Mayer, I., Valiron, P. *J. Chem. Phys.* **1998**, 109 (9), 3360–3373.

[4.10] Bende, A., *The Chemical Hamiltonian Approach* **2010**.

[4.11] Van Duijneveldt, F. B.; van Duijneveldt-van de Rijdt, J. G. C. M.; van Lenthe, J. H., *Chem. Rev.* **1994**, 94 (7), 1873–1885.

[4.12] Rösch, N., *Counterpoise Correction* **2003**.

[4.13] Sedano, P. S., *Counterpoise Corrected Potential Energy Surfaces* **2000**.

[4.14] Paizs, B., Suhai, S., *J. Comput. Chem.* **1998**, 19 (6), 575–584.

[4.15] Mentel, L.; Baerends, E. J., *J. Comput. Chem.* **2013**, 10 (1), 252–267.

[4.16] Mayer, I., *Int. J. Quantum Chem.* **2004**, 100 (4), 559–566.

[4.17] Merrik, J. P.; Moran, D.; Radom, L., *J. Phys. Chem. A* **2007**, 111, 11683-11700.

[4.18] Santos, L. M. N. B. F.; Rocha, M. A. A.; Gomes, L. R.; Schröder, B.; Coutinho, J. A. P., *J. Chem. Eng. Data* **2010**, 55, 2799–2808.

[4.19] Dorofeeva O.V., *Thermochim. Acta* **1986**, 102, 59-66.

[4.20] Lee, B.; Richards, F. M., *J. Mol. Biol.* **1971**, 55 (3), 379–400.

[4.21] Shrake, A.; Rupley, J. A., *J. Mol. Biol.* **1973**, 79 (2), 351-371.

[4.22] Ishikawa, T., *Superbases for Organic Synthesis: Guanidines, Amidines, Phosphazenes and Related Organocatalysts*, John Wiley & Sons, **2009**.

[4.23] Boys, S. F.; Bernardi, F. *Mol. Phys.*, **1970**, 19, 553−566.

[4.24] van Duijneveldt, F. B.; van Duijneveldt-van de Rijdt, J. G. C. M.; van Lenthe, J. H. *Chem. Rev.* **1984**, 94, 1873−1885.

[4.25] Zhao, Y.; Truhlar, D. G. *Theor. Chem. Acc.* **2008**, 120, 215–241.

CHAPTER 5

Phase Behavior and Heat capacities of Protic Ionic Liquids

5. Phase Behavior and Heat capacities of Protic Ionic Liquids

In this chapter, the phase behavior and heat capacities (at 298.15K and at different temperatures) of several PILs are presented and discussed considering the effect of the base and acid. The main purpose of this study was to find some trends exploring the effect of the superbase and the acid. Another goal was to evaluate the liquid phase structure of the PILs, the possibility of nanostructuration and the PILs ionicity.

5.1. Fundamentals

Calorimetric differential analysis allows the direct determination of transition temperatures in condensed phases and respective enthalpies, the measurement of temperature-dependent properties such as heat capacities, detection of thermal decomposition processes, identification of different polymorphic forms, etc, on a vast diversity of materials/compounds such as liquid crystals, drugs, biological materials, metals polymers, glass and ceramics, ionic liquids, etc. [5.1] In differential measuring systems, the calorimeter signal depends on the difference between the responses of a reference and a sample to a temperature variation. The most important advantage of the differential principle is that disturbances to the system, except for those occurring in the sample, affect both the sample and the reference and are compensated by the difference between the individual signals. Differential calorimeters are also easy to work with, the experiments are quite fast, require small amounts of sample (about 5-10 mg), can be performed at temperatures significantly above ambient and allow the study of “slow” reactions, which are outside the normal operating range of most adiabatic calorimeters. These advantages, however, have some costs in terms of accuracy, yielding results usually less accurate than the corresponding measurements by adiabatic calorimetry. [5.2]

There are two types of differential calorimeters that must be distinguished, according to their operation principle: [5.3-5.4]

The power compensation calorimeters, where the output signal of the calorimeter is proportional to the difference between the heat flow rates supplied to the sample and the reference in separate furnaces, and the **heat flux** calorimeters, where the temperature gradient between the sample and reference, in the same furnace, is directly converted to a potential difference which is proportional to the difference in the heat flow rate applied to the sample and to the reference. Differential calorimeters can be operated in a dynamic (non-isothermal) mode, where the sample is subjected to heating and/or cooling, or in an isothermal mode, in which the temperature is maintained constant. As can be seen in figure 5.1, a power compensation calorimeter, consists of two identical microfurnaces, thermally decoupled, one containing the sample (S) and other the reference (R), each associated to a temperature sensor (1) and a heating resistance (2) controlled by independent electrical circuits.

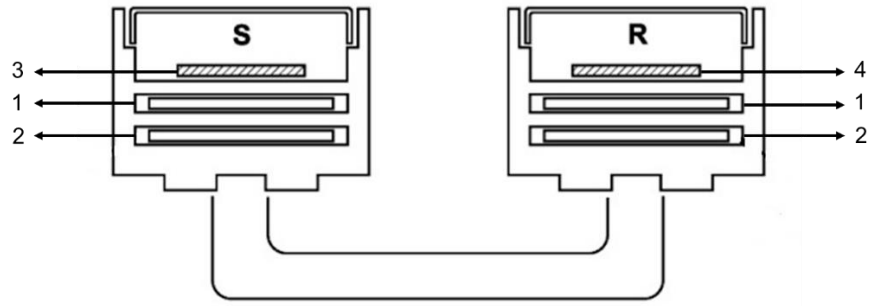

Figure 5.1. General schematic representation of a power compensation calorimeter (S. sample furnace; R. reference furnace; 1. temperature sensors; 2. heating resistances; 3. sample crucible; 4. reference crucible).

The samples are enclosed in crucibles (3), made of high thermal conductivity materials (e.g., aluminum, copper), which may or may not be hermetically sealed, depending on the type of application/experiment. The selection of the appropriate crucibles depends on the characteristics of the sample to be analysed and the properties to be determined. The reference crucible generally consists of an empty one (4) with a mass as similar as possible to that of the sample crucible. During the experiments, a purging gas (e.g., helium, argon, nitrogen) is flowed through the furnaces at a constant rate to ensure that the ambient conditions are as uniform as possible in all experiments. During a thermal characterization study, the same heating power is supplied to both furnaces to change their temperature in accordance with a

pre-set heating rate. If there is ideal thermal symmetry between both furnaces, their temperature should be/is the same. When thermal asymmetry occurs, after the release or consumption of heat due to a certain physical or chemical process/phase change in the sample, the system compensates the temperature gradient by adjusting the heat flow rate by Joule heating (in the mW range) through a heating resistance.

Phase transition measurements

All known substances can exist in different phases and these phases are the result of different atomic or molecular arrangements and dynamics having characteristic properties. Transitions between these different states of matter are known as phase transitions. [5.5] Phase transitions can be observed by thermal analysis techniques and their different behaviors interpreted and associated to different transitions. Different peak shapes can be due to different heating\cooling temperature rates. A quick heating rate can lead to a sharp and longer peak when compared to a lower cooling rate. When a phase transition is detected, a procedure must be performed, so that the corresponding phase transition temperature (the onset temperature, T_{onset}) can be reported in a rigorous way. The onset temperature in this work was defined as the intersection of the baseline with the peak slope. For the PILs studied, three typical phase transitions can be highlighted:

- Glass transition temperature, T_g, is the midpoint of a small heat capacity change on heating from the amorphous glass state to a liquid state.
- Cold crystallization temperature, T_{cc}, is the onset of an exothermic peak on heating from a subcooled liquid state to a crystalline solid state.
- Melting point, T_m, was considered as the onset of the endothermic melting peak on heating.

Crystallization

Crystallization occurs when there is formation of solid crystals from a primary liquid phase (when cooling the sample). The crystallization process can be divided in two more elementary steps: nucleation and nuclei growth. Another form of crystallization occurs when the sample is slowly heated above T_g, forming crystalline structures – defined as cold crystallization, T_{cc} [5.6]. Both processes occur from a less organized structure, amorphous solid or liquid, to a more organized crystalline structure.

An amorphous solid state does not have a characteristic crystal shape. Such samples are difficult to crystallize in one step and, in a general way, those compounds possess long alkylic side chains that tend to crystallize by steps, due to C-C (carbon-carbon) bond rotation. These solid-solid phase transitions occurring before the melting point are often referred to as rotator phases, which generally possess plastic properties. [5.7]

Different peak shapes and areas can be due to different crystallization degrees. This can be detected by not having a cold crystallization peak in the first measurement and different peak sizes in the following measurements. In the first measurement, since the compound is totally crystalline, the heat released/absorved is higher and there is no cold crystallization peak. In the second measurement, due to fast cooling, some of the sample didn't have time to crystallize and thus there is a smaller crystallization peak and a smal cold crystallization peak from the amorphous crystal fraction. In the last measurement, the sample is totally amorphous, and the heat flow signal is characterized by only a large cold-crystallization peak. The use of a fast cooling rate can result in a sample with many amorphous zones, whereas slow cooling leads to higher degrees of crystallization.

Glass transition

A glass transition or liquid-glass transition, T_g, is the reversible transition in amorphous materials from a molten or rubber-like liquid state into a hard and relatively brittle state and vice-versa. [5.8] This characteristic is important since some ILs only show a crystallization peak – cold crystallization - upon heating from low temperatures. Usually, the cold crystallization peak can be seen from 20 to 30 temperature degrees after the glass transition. Also, some ILs do not crystallize, until the glass transition temperature is reached, staying in a supercooled liquid state. [5.9] The transition kinetics, mainly governed by the cooling rate (rapid or slow cooling), plays an important role, so, in order to obtain reliable thermal phase behavior data, long equilibration times and small samples are required. Usually, the T_g can be difficult to determine because it can take place over a wide temperature range and is highly dependent on conditions such as the measurement method and pressure [5.10]. For 1-alkyl-3-methylimidazolium salts, T_g are typically in the region between 203 K and 183 K. [5.11] The T_g can also be related with the melting temperature as shown in equation 5.1 (temperature values are presented in K):

$$T_g/T_m = 2/3 \quad [5.12] \qquad \textbf{(5.1)}$$

The value presented in equation 5.1 is the most common value found in literature for AILs families. For most of the PILs studied in this work the value can change and approach the value of equation 5.2:

$$T_g/T_m = 3/4 \qquad \textbf{(5.2)}$$

This difference arrives from the structure of the IL and their phase transition differences. For PILs, generally, the glass transition temperatures are closer to the melting temperatures.

Melting point

The melting point is the temperature at which, a given pressure, there is a phase transition from solid to isotropic liquid. At this temperature, the sample is in solid-liquid equilibrium and remains isothermal, until the whole sample is melted. [5.13] In PILs, just like in aprotic ILs the melting point is deeply influenced by many factors: [5.14]

- charge and molecular shape of the anions and cations;
- dissimilar anion and cation sizes can lead to lower fusion temperatures (weaker electrostatic interactions in the crystal lattice);
- symmetrical components lead to higher fusion temperatures (better crystal packing);
- greater charge delocalization leads to lower fusion temperature.

Heat capacities

Heat capacity is one of the most important thermophysical properties that can be used to characterize a substance. It is intimately related to the temperature dependence of fundamental thermodynamic functions and consequently essential for figuring and interpreting how they change with temperature. Heat capacities are widely used in several areas, such as thermodynamics for obtaining entropy and enthalpy values, thermochemistry for calculating changes in enthalpies of reaction , and in chemical engineering for establishing energy balances. [5.15-5.16]

The heat capacity, *C*, is defined by the following differential relation:

$$C = \left(\frac{\partial Q}{\partial T}\right)_x , \qquad \textbf{(5.3)}$$

where ∂Q is the heat exchanged between the system and the surroundings and ∂T is the change in temperature of the system under the specified conditions, *x*. Different thermodynamic functions for the heat capacity can be found; according to the specified conditions:

1. heat capacity at constant volume (or isochoric heat capacity), C_V

$$C_V = \left(\frac{\partial U}{\partial T}\right)_V = T \cdot \left(\frac{\partial S}{\partial T}\right)_V = -T \cdot \left(\frac{\partial^2 A}{\partial T^2}\right)_V \qquad \textbf{(5.4)}$$

2. heat capacity at constant pressure (or isobaric heat capacity), C_p

$$C_p = \left(\frac{\partial H}{\partial T}\right)_p = T \cdot \left(\frac{\partial S}{\partial T}\right)_p = -T \cdot \left(\frac{\partial^2 G}{\partial T^2}\right)_p \qquad \textbf{(5.5)}$$

3. heat capacity at the saturation vapor pressure of the liquid, C_{sat}

$$C_{sat} = T \cdot \left(\frac{\partial S}{\partial T}\right)_{sat} \qquad \textbf{(5.6)}$$

The thermodynamic functions *U*, *H*, *S*, *A*, and *G* represent the internal energy, enthalpy, entropy, Helmholtz, and Gibbs functions, respectively.

The heat capacity of a sample can be measured in a calorimeter that is able to measure simultaneously the amount of heat input or output and the temperature change in the sample. [5.16-5.19] The measurements can be performed by continuously scanning temperature or by stepwise measurements. For the case of continuous scanning measurements, the heat capacity is derived as the ratio $\left(\frac{\partial Q}{\partial t}\right)/\left(\frac{\partial T}{\partial t}\right)$, and, depending on the conditions, a correction for the instrument response may be applied. If the calorimeter response can be expressed by a first-order exponential in time, the Tian equation can be used [5.16]:

$$\left(\frac{\partial Q}{\partial t}\right)_{\mathrm{c}} = \left(\frac{\partial Q}{\partial t}\right)_{\mathrm{m}} + \tau \cdot \left[\frac{\partial}{\partial t}\left[\left(\partial Q / \partial t\right)_{\mathrm{m}}\right]\right] \qquad \textbf{(5.7)}$$

Where $\left(\partial Q / \partial t\right)_{\mathrm{c}}$ is the corrected heat rate, $\left(\partial Q / \partial t\right)_{\mathrm{m}}$ is the heat rate measured, and τ is the time constant for the response of the calorimeter and sample to a temperature change. In the case of stepwise measurements, a correction for the time response is not necessary; however, ΔT must be small, in order to assure the differential definition of heat capacity.

Differential scanning calorimetry, *DSC*, is the most common calorimetric technique used for heat capacity measurements. Typically, sample volumes of <0.1 cm^3 are used in the DSC. Taking into account that ΔQ is proportional to the sample size, larger sample volumes are useful to decrease the relative error in the ΔQ measurements. [5.16-5.19] Therefore, DSCs with sample volumes higher than 1 cm^3 and better heat detection limits present advantages. [5.16-5.19] In this method, two types of ampoules can be used: sealed ampoules with some vapor space that measure the C_{sat} and overflow ampoules that measures the C_p. Obviously, the sealed ampoules require a hermetic seal, in order to avoid loss of the sample during the experiment and taking into account that the vapor pressure of the sample varies with temperature (the measurements give C_{sat}). The overflow ampoule consists of a cylindrical ampoule with a filling tube extending outside the calorimeter. [5.16, 5.20] In order to obtain high accuracy in the heat capacity measurements using a DSC, a correction for the thermal expansion of the ampoule might be required.

Another accurate method for heat capacity measurement is based on the isoperibol temperature-change calorimetry. Despite not having the temperature range or pressure range of the DSC, isoperibol calorimetry works with larger volumes (≥ 25

cm^3) and allows a very accurate determination of ΔT. [5.16, 5.21] The isoperibol temperature-change calorimeter typically consists of a Dewar vessel flask, in which the temperature changes are measured with a thermistor (micro-degree resolution), and ΔQ is given by an electrical heater submerged in the liquid. [5.16, 5.21] This method requires the correction for the heat exchange with the surroundings. This is a complex procedure because as the physical size of the reaction vessel decreases, the rate of the heat exchange with the surroundings and the reaction time increase. This method is not recommended for volatile liquids. [5.15, 5.21] Isothermal flow calorimetry is considered the best alternative for measuring the heat capacity at constant pressure over a wide temperature range. In this method, no correction for vapor-liquid equilibrium is required. Temperature control, careful calibration, and maintenance of the pumps is crucial to achieve good accuracy on the measurements. Since viscous liquids present difficulties when pumped through the tubing and viscous flow will generate sufficient heat to obstruct the measurements, this method is limited to low viscous liquids. For measurements of C_p, two methods can be used:

- the temperature of the input flow is controlled, heat is added to the liquid at a constant rate, and the temperature of the output flow is measured;
- the temperature of the input flow is controlled at a different temperature of the isothermal calorimeter, as a result, the output flow is at the calorimeter's temperature.

Drop calorimetry is the simplest method for measuring heat capacities over a wide range of temperatures and is used not only for heat capacity measurements but also for studies of enthalpies of phase transitions. [5.16, 5.22-5.25] In this method, an ampoule containing the sample is moved from an initial temperature to a calorimeter at a different final temperature. The applicable temperature range depends on the type of heat flow sensors. For high-temperature calorimeters reaching 1300 K, platinum-platinum/rhodium thermocouples in series are frequently used, whereas for temperatures under 420 K, high sensitive heat flow plates (usually semiconductor Peltier plates) are used. Drop calorimeters of the heat conduction type have the advantage of improved sensitivity, due to the isothermal working mode of the heat flow sensors. The twin design has proven to be suitable for very long reaction periods, as the surrounding disturbances are significantly reduced. These characteristics (sensitivity and long-term stability) are very important when the calorimeters are used in solution chemistry, in particular for biological and pharmaceutical applications. [5.16, 5.26-5.28]

5.2. Experimental methodologies

5.2.1. Differential scanning calorimetry *DSC*

Apparatus and methodology

The differential scanning calorimeter used in this work was a PerkinElmer Diamond Pyris 1 calorimeter. The detailed description and mode of operation of the apparatus can be found in the respective manual provided with the device. [5.29]

Figure 5.2. View of the Perkin Elmer Pyris Diamond, a *DSC* power compensation calorimeter.

DSC studies were carried out using hermetically sealed aluminum crucibles (30 or 50 μL capacity) and a flow of nitrogen used as purging gas. The calibration of the calorimeter was made by using high purity reference materials and test substances and the same heating rate and aluminum crucibles used in the sample study. The power and temperature scales of the calorimeter were calibrated simultaneously, at 2, 5 and 10 $K \cdot min^{-1}$ heating rates, by measuring the melting temperature and enthalpies of the following substances [5.30]: naphthalene, benzoic acid, diphenylacetic acid, triphenylene, perylene, o-terphenyl 1,3,5-triphenylbenzene, 4- methoxybenzoic acid and anthracene.

Typical results

DSC results are usually displayed as thermal analysis curves, or thermograms, in which the instrument signal, heat flow rate, is plotted as a function of time and temperature. In the absence of any changes in the sample, the sample and reference

furnaces are at the same temperature and the heat flow rate is approximately constant, establishing the baseline. The baseline is related to the heat capacity of the sample in the absence of phase transitions or chemical transformations, and its good definition is crucial for the reproducibility and accuracy of experimental results. Prior to heating, the sample is generally subjected to an isothermal period to ensure thermal equilibrium with the furnace conditions. The sample is then heated, according to a preset heating rate, and when a physical or chemical transformation occurs, the resulting change in heat flow rate causes a deviation from the baseline in the form of a peak. In the *DSC* experiments performed in the present work, a negative deviation corresponds to an endothermic process (e.g., melting), whereas a positive deviation corresponds to an exothermic process (e.g., crystallization).

Figure 5.3 represents a typical thermogram of an endothermic process based on a dynamic method, showing the temperature ramp (blue line) and the heat flow rate. associated with the occurring transitions (green line). To characterize the transition associated to the peak, it is necessary to define the onset temperature and the area of the peak, which are respectively related to the temperature and enthalpy of transition. The transition temperature is the onset temperature defined by the intersection between the tangent that follows the downslope of the peak and the extrapolated baseline. The heat associated with the process is proportional to the area of the peak, defined from the interpolation of the baseline connecting the beginning and end of the transition. Assuming that the experiment occurs at constant pressure, the measured heat corresponds to the change in enthalpy during the process. The difference between the baseline before and after the transition reflects the different heat capacities of the two phases of the sample.

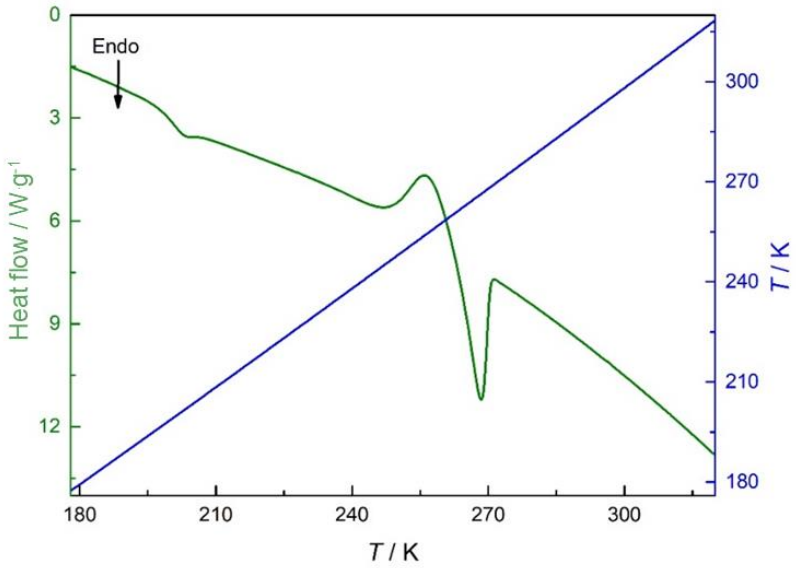

Figure 5.3. Typical thermogram obtained using a power compensation calorimeter.

Calibration

The calorimeter's signal does not depend solely on the occurring thermal process but also on several factors inherent to the calorimeter, namely heating rate, the thermal conductivity of the crucible material, nature and flow of the purge gas, etc. To account for thermal gradients between the crucibles (of sample and reference), it's crucial to carefully calibrate the apparatus. [5.31] To achieve reproducibility and accuracy of the results, it is necessary to perform the calibration in terms of temperature and in terms of heat flow. The calibration constants determined are factors of proportionality between quantities measured by the device and the actual values. Because the calibration constants are complex and generally unknown functions of various parameters, the calibration experiments should be carried under the same experimental conditions used for the sample experiments.The recommended calibration method for a dynamic operated *DSC* involves the determination of the temperature and enthalpy of fusion of several standard substances for thermal analysis, as some of those recommended by Sabbah et al. [5.32], over the temperature range of the equipment and using various heating rates. A number of the recommended temperature standards have well-established enthalpies of transition, allowing both temperature and enthalpy calibration to be performed simultaneously.

Experimental

The thermal analysis and phase behavior of the PILs studied were explored in the temperature range from 173 K to 373 K, on a *DSC*, PerkinElmer, model Pyris Diamond using a heating rate of 5 $K \cdot min^{-1}$, an N_2(g) flow of 50 $mL \cdot min^{-1}$ and sealed aluminum crucibles. The crucibles were weighted using a Mettler Toledo XS105 dual range analytical balance (sensitivity of 1 x 10^{-5} g and repeatability of 8 x 10^{-6} g), the typical sample load was of about 10 mg.

5.2.2. High-precision drop calorimetry

Apparatus

The heat capacities, at T = 298.15 K, for some PILs studied in this thesis were measured by the high-precision heat capacity drop calorimeter previously described in the literature. [5.23-5.24, 5.33-5.34]

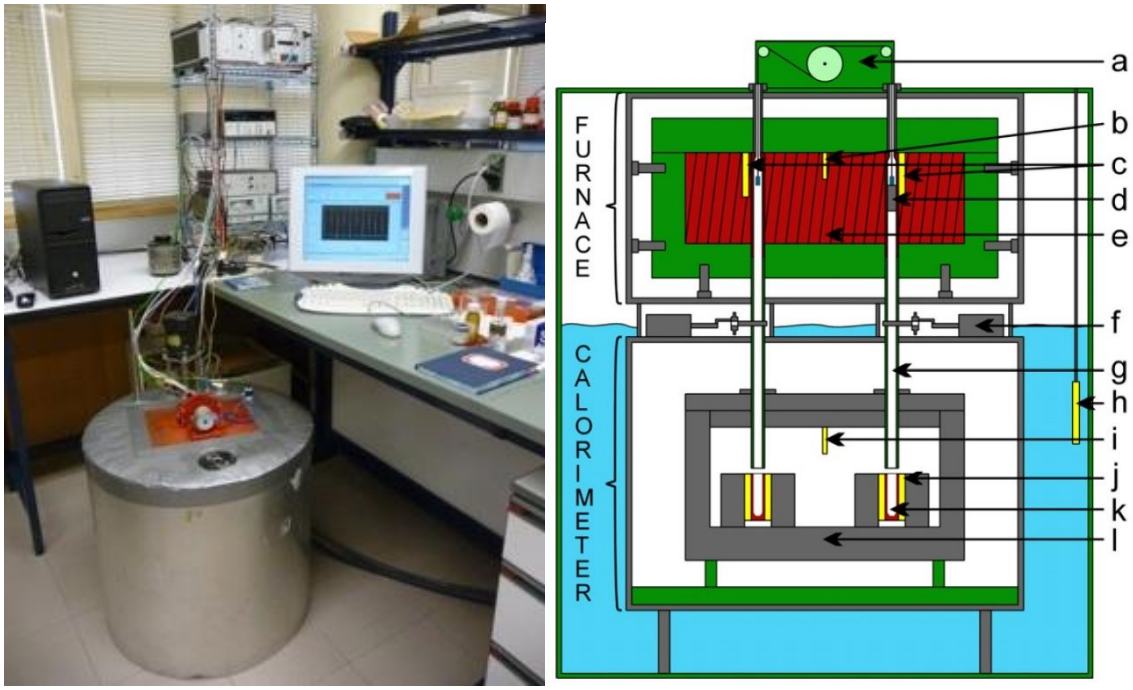

Figure 5.4. Photograph and schematic representation of the twin high-precision drop calorimeter used in this thesis. Materials: (■): water; (■): PVC; (■): metal; (■): copper; (■): measuring elements; a: automatic lift; b: thermistor for temperature control; c: Pt100, temperature sensors; d: magnet holding ampoule; e: copper block (T_i) with manganin heater wound; f: electromechanical shutter; g: tube for the ampoule (top copper, bottom plastic); h: thermistor; i: Pt100, temperature sensor located in wall of block; j: Peltier plates; k: ampoule receiver; l: aluminum calorimeter block (T_f). Adapted from source [5.15].

The apparatus is shown in figure 5.4 and comprises two main parts: a furnace block made of copper with manganin heater wound in which Pt100 temperature sensors are coupled, and the receiving calorimeter made of aluminum. The receiving calorimeter consists of a twin heat conduction calorimeter assembled with Peltier plates. The furnace and receiving calorimeter are kept at constant temperatures, 303.15 ± 0.01 K and 293.15 ± 0.01 K, respectively. The twin calorimeter measures the heat exchange resulting from the ampoule cooling from the initial temperature (T_i = 303.15 K) to the final temperature (T_f = 293.15 K), which results in a change in voltage

signal, $\emptyset/\mu V$, across the thermopiles. A software application in Agilent VEE, v9.0 [5.35] was developed for data acquisition and data treatment. This application allows to collect and monitor data in real-time and to define the experimental setup (e.g. control the time interval between each drop, define the number of drop repeats per run).

Typical results

The heat exchange resulting from the ampoule cooling is recorded as the change in voltage signal (U) with time. Figure 5.5 depicts the typical data acquired by the software application.

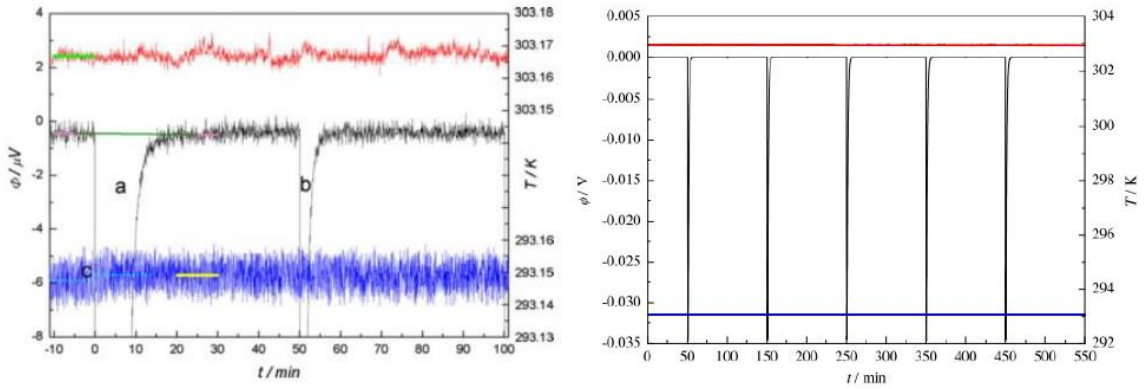

Figure 5.5. Typical experimental data recorded in a five drops experiment. (─) furnace temperature; (─) heat flow; (─) calorimeter temperature. Adapted from the reference [5.33].

The integrated heat flow is normalized to the temperature difference between the furnace and the calorimeter, according to equation (5.6), determined from the software application.

$$A_{\text{ampoule/sample}} = \frac{\int U \mathrm{d}t}{(T_i - T_f)} \qquad \textbf{(5.8)}$$

Calibration

The calibration constant is determined from chemical calibration, which allows canceling systematic errors inherent to the drop methodology. The calibration constant is calculated by equation (5.7).

$$\varepsilon = \frac{(C^0_{p,m} \cdot m_{sample})}{(A_{ampoule+sample} - A_{ampoule}) \cdot M} \qquad \textbf{(5.9)}$$

The $C^0_{p,m}$ is the available heat capacity of the reference material (primary) used in the calibration, m_{sample} is the mass of sample and $A_{ampoule+sample}$ and $A_{ampoule}$ are the normalized integrated areas of the filled ampoule and the empty ampoule (blank), respectively, M is the molar mass of the compound. The calorimeter was calibrated with sapphire (α-Al_2O_3 NBS standard sample, SRM7 20) using the heat capacity value of $C^0_{p,m}$ (sapphire) = (79.03±0.08) $J \cdot K^{-1} \cdot mol^{-1}$, at T = 298.15 K. [5.36] The determined calibration constant was ε = (6.6040 ± 0.0036) $W \cdot V^{-1}$. The heat capacity ($J \cdot K^{-1} \cdot mol^{-1}$) of a compound is calculated by equation (5.8) taking into account the chemical calibration.

$$C^0_{p,m} = \frac{\varepsilon \cdot (A_{ampoule+sample} - A_{ampoule}) \cdot M}{m_{sample}} \qquad \textbf{(5.10)}$$

The accuracy of the apparatus for measurements of heat capacities of liquids and solids was tested using benzoic acid, hexafluorobenzene, p-terphenyl, 1,3,5 - triphenylbenzene and [$^1C_6{}^3C_1$im][NTf_2]. [5.33,5.37] All the uncertainties are given as twice of the standard deviation of the mean and include the calibration uncertainty. The buoyancy effect correction was considered.

Experimental

The heat capacities at T = 298.15 K were measured by the drop method and the ampoules were weighted using a Mettler Toledo XS105 dual range analytical balance (sensitivity of 1 x 10^{-5} g and repeatability of 8 x 10^{-6} g), the typical sample load was of about 300 to 500 mg.

5.2.3. Micro-differential scanning calorimetry *μ*DSC

The apparatus was repaired as a part of this work. The calibration and methodology applied were made thinking in the heat capacity measurements of ILs and particularly of PILs.

Apparatus

The heat capacities of the liquid PILs were also measured using a Setaram μDSC III (figure 5.6), in the range from 283 to 363 K and using the incremental temperature mode with the step method. Each 5 K step at a heating rate of 0.3 K min^{-1} was spaced between two isothermal runs of 2600 s. The typical mass of samples was of about 0.5 g to 1.0 g.

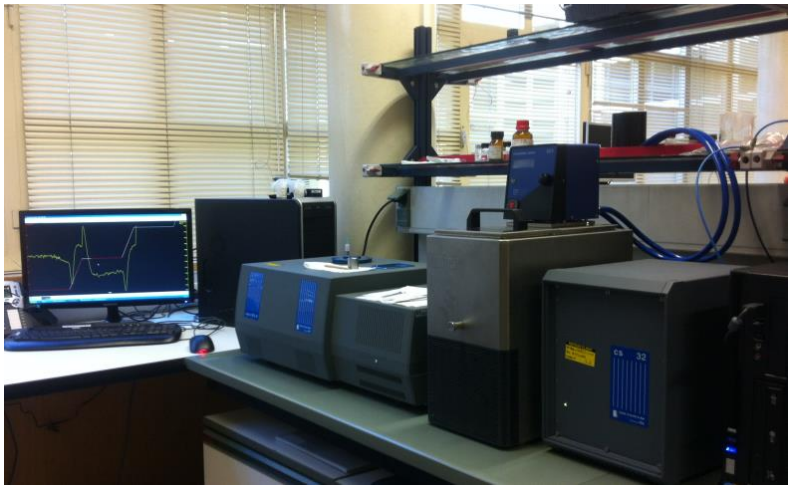

Figure 5.6. The Setaram μDSC III used in this work for the heat capacity measurements at different temperatures.

The combined expanded uncertainty of the heat capacity measurements using this method is estimated as $U_c(C^0_{p,m}) = 0.01 \cdot C^0_{p,m}$. [5.38] Figure 5.7. presents the type of vessels used in this apparatus: a closed Hastelloy C (mostly made of Nickel, Chromium, and Molybdenum) vessel, with a volume of 1 cm^3.

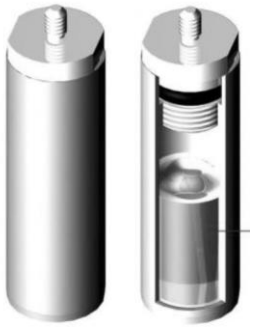

Figure 5.7. The μDSC vessels used in the Setaram μDSC III. Adapted from [5.39]

The calorimeter's temperature is controlled by an external water circulating system that removes the excess heat.

Some of the Setaram μDSC III characteristics are:

- Temperature range: 273 K to 393 K;
- Scanning rate from 0.01 K min^{-1} to 1.2 K·min^{-1} in the whole temperature range;
- Detection limit from 0.2 to 2 μW;
- Resolution of 40 *n*W.

Typical results

The heat capacities at different temperatures between 283 and 363 K obtained using the μDSC were measured by the step method (increase and decrease of temperature – step = 5 K) described previously and the ampoules were weighted using Mettler Toledo XS105 dual range analytical balance (sensitivity of 1 x 10^{-5} g and repeatability of 8 x 10^{-6} g), the typical sample load was of about 600 to 700 mg.

Heat capacity measurements can be performed in two different ways: using the step method or the continuous method.

- **Step method** (figure 5.8) is an intercalary method between temperature stabilizations and temperature increments;
- The **continuous method** (figure 5.9) uses a linear dependence of temperature with the heat flow.

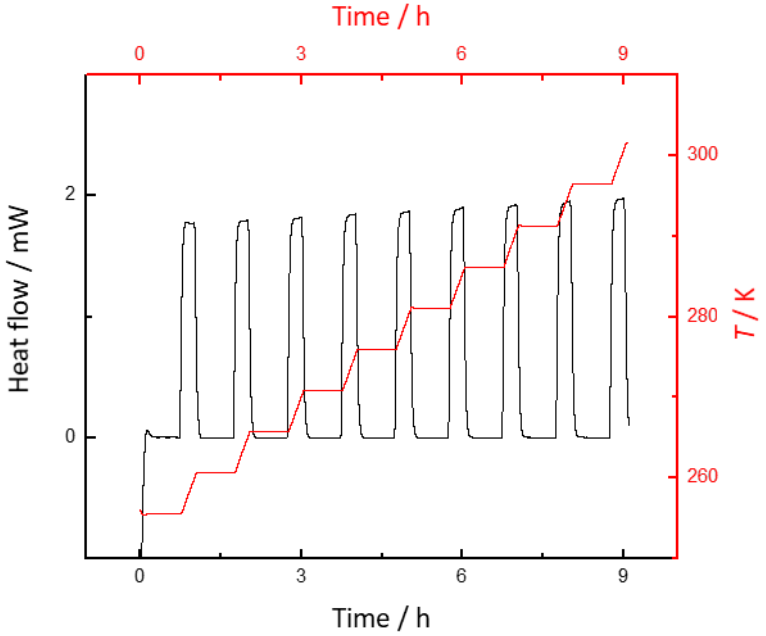

Figure 5.8. Representation of the step method. Adapted from reference [5.39].

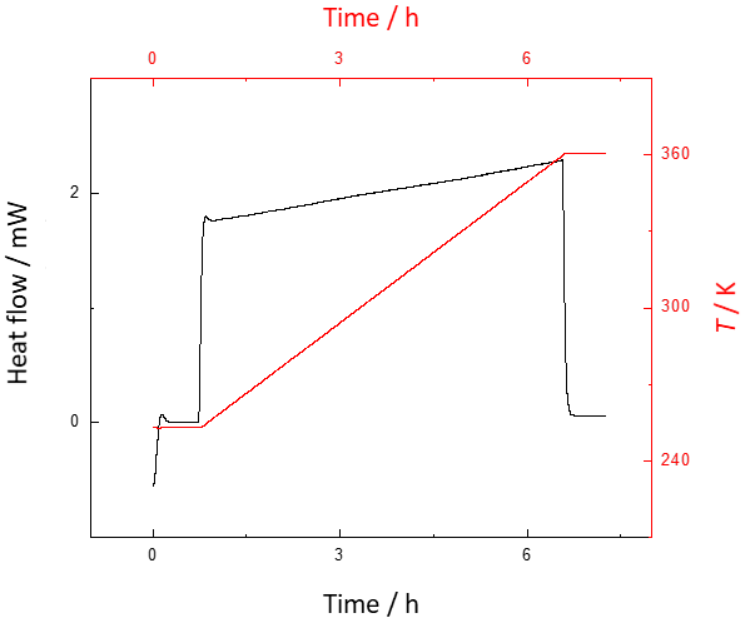

Figure 5.9. Representation of the continuous method. Adapted from reference [5.39].

The step method fits temperature stages between temperature increments, as shown in figures 5.8 and 5.9. Those steps are repeated over a temperature range until the desired temperature is reached. This method was performed with a sample and reference (an empty pan) simultaneously, in identical experimental conditions. The result is the difference between the sample and the reference and, hence, the signal measured is directly proportional to the sample's heat capacity.

Figure 5.10 presents a typical result of an experiment obtained from the μDSC III using the step method. The software used in this apparatus was adapted from the one created for the Drop calorimeter in order to integrate the peaks faster and with accuracy. [5.33]

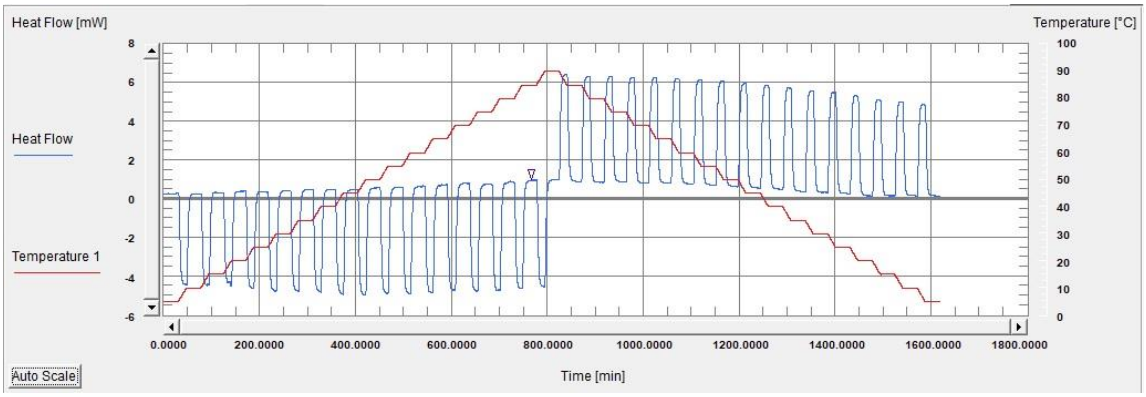

Figure 5.10. Typical results obtained from μDSC III with step method. The measurement was performed for superbase DBN at 0.3 K·min^{-1} in the temperature range of 283 to 363 K.

To compute the sample's heat capacity at a given temperature, equation 5.11. can be used:

$$C_{p,s}(T) = \frac{m_{sapp} \cdot C_{p,sapp}(T) \cdot \left(\frac{A_s(T)}{\Delta T} - \frac{A_B(T)}{\Delta T}\right)}{m_s \cdot \left(\frac{A_{sapp}(T)}{\Delta T} - \frac{A_B(T)}{\Delta T}\right)} \qquad \textbf{(5.11)}$$

Where $C_{p,\mathrm{sapp}}$ is the sapphire molar heat capacity and m_{sapp} its mass, m_{s} is the sample's mass, A_{s} is the sample peak area, A_{B} is the blank peak area, A_{sapp} is the sapphire peak area and ΔT is the peak temperature interval. Each area meaning the integration of the heat flow overtime. The step method procedure is considered more reliable than the continuous one for heat capacity measurements since it minimizes errors caused by kinetic processes (such as lack of rapid thermal transmittance and stability of the sample). On the other hand, this method is much more time consuming, since the various steps need several minutes for the isotherms to stabilize and it is more difficult to analyse possible phase transitions.

Calibration

The calibration made in this methodology was similar to the one made in the drop calorimeter. The calibration constant was determined from chemical calibration, which allowed canceling systematic errors inherent to the methodology. The calibration constant was calculated by equation (5.7). The calorimeter was also calibrated with sapphire (α-Al_2O_3 NBS standard sample, SRM7 20) using the heat molar capacity value of $C^0_{p,m}$ (sapphire) = (79.03±0.08) $J \cdot K^{-1} \cdot mol^{-1}$, at T = 298.15 K. [5.36] The mass of sapphire was taken into account in order to the value of A_{sapp} is similar to A_s in equation 5.11. The accuracy of the apparatus for measurements of heat capacities of PILs was tested using benzoic acid. All the uncertainties are given as twice of the standard deviation of the mean and include the calibration uncertainty (calibration constant K). The buoyancy effect correction was also considered, and the value of the calibration constant K varies less than 5% in the temperature range studied. Where K is the calibration constant, m_{sapp} the sapphire mass, M_{sapp} the sapphire molar mass, A_B is the blank peak area, A_{sapp} is the sapphire peak area and $C_{p,sapp}$ is the sapphire heat capacity value of reference. [5.22] Figure 5.11 and table 5.1 show the dependence of the K values with temperature:

$$K\ (T) = \frac{C_{p,sapp}(T) \cdot \dfrac{m_{sapp}}{M_{sapp}}}{\dfrac{A_{sapp}(T)}{\Delta T} - \dfrac{A_B(T)}{\Delta T}} \qquad \textbf{(5.12)}$$

With the calibration constant calculated, the heat capacity can be obtained by equation 5.13:

$$C_{p,s}(T) = \frac{K\ (T) \cdot \left(\dfrac{A_s(T)}{\Delta T} - \dfrac{A_B(T)}{\Delta T}\right)}{m_s} \cdot M_s \qquad \textbf{(5.13)}$$

Where K is the calibration constant, m_s the sample mass, M_s the sample molar mass, A_B is the blank peak area, A_s is the sample peak area and $C_{p,s}(T)$ is the sample heat capacity at T.

Table 5.1. Experimental results (average) obtained for the calibration constant *K* (*T*) using μDSC as a function of *T* and values of Δ***T*** for each step. Three independent experiments were made.

T / K	***K*** (***T***)	Δ***T*** / K
283.15	0.0013285	4.9927
288.15	0.0013155	4.9964
293.15	0.0013047	5.0010
298.15	0.0012960	5.0012
303.15	0.0012891	5.0004
308.15	0.0012839	5.0008
313.15	0.0012805	5.0010
318.15	0.0012785	5.0007
323.15	0.0012781	5.0010
328.15	0.0012792	5.0006
333.15	0.0012816	5.0007
338.15	0.0012855	5.0006
343.15	0.0012908	5.0012
348.15	0.0012975	5.0006
353.15	0.0013057	5.0010
358.15	0.0013153	5.0009
363.15	0.0013264	5.0015

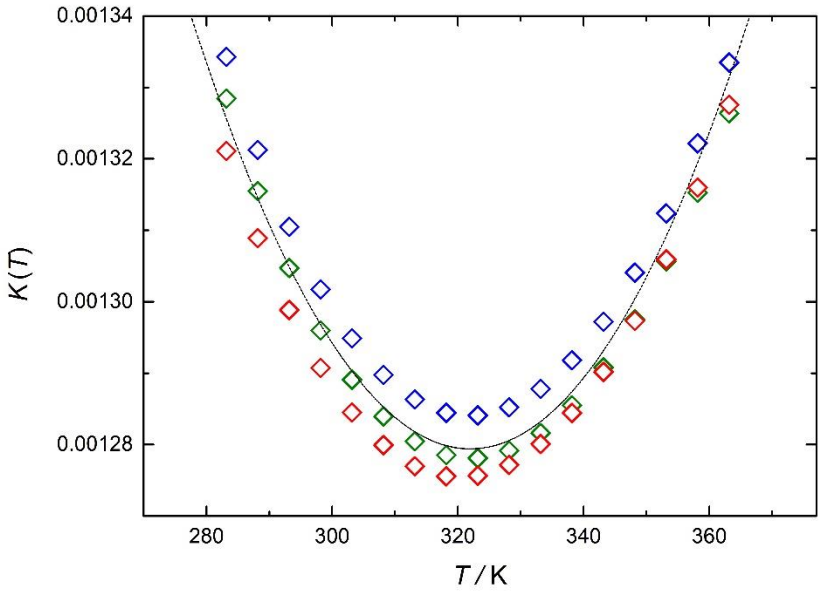

Figure 5.11. Experimental results obtained for the calibration constant *K* (*T*) using μDSC (three independent experiments). ━ (green line) values for *K* (*T*) at different temperatures using the polynomial equation: $K(T) = 0.001354 - 0.000003068 \cdot T + 0.00000003072 \cdot T^2$.

Blanks

Blanks were made before each experiment and in figure 5.12 an example of a typical blank is presented.

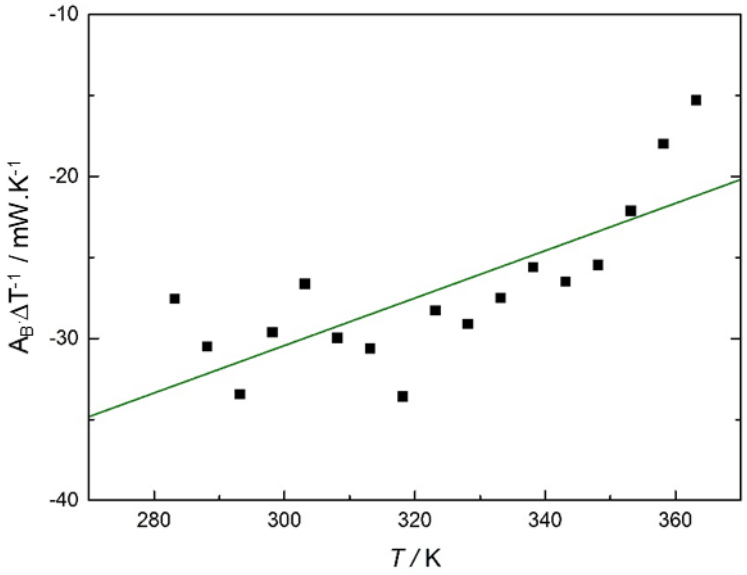

Figure 5.12. Experimental results obtained for the blank using μDSC. ━ (green line) values obtained at different temperatures using the linear equation: $A_B \cdot \Delta T^{-1} = 0.1465 \cdot T - 34.01$.

5.3. Results and discussion

5.3.1. Phase behavior

Table 5.2 presents the experimental results obtained by DSC for each compound studied in this thesis.

Table 5.2. Experimental results obtained by DSC for the compounds studied; T_c is the crystallization temperature, T_m is the melting temperature, T_g the glass transition temperature and T_{cc} the cold-crystallization temperature.

Compound	*T* / K
DBN	185.5 ± 0.5 (T_g)
DBU	185.8 ± 0.5 (T_g)
[DBNH][MeCOO]	202.2 ± 0.5 (T_g) 257.8 ± 0.5 (T_{cc}) 277.9 ± 0.5 (T_m) T_g / T_m = (0.73)
[DBNH][EtCOO]	200.5 ± 0.5 (T_g) 245.3 ± 0.5 (T_c) 274.2 ± 0.5 (T_m) T_g / T_m = (0.73)
[DBNH][nPrCOO]	200.7 ± 0.5 (T_g)
[DBNH][iPrCOO]	206.3 ± 0.5 (T_g)
[DBNH][nPentCOO]	201.3 ± 0.5 (T_g)
[DBNH][nHeptCOO]	194.1 ± 0.5 (T_g) 243.7 ± 0.5 (T_c) 259.1± 0.5 (T_m) T_g / T_m = (0.75)
[DBUH][MeCOO]	222.7 ± 0.5 (T_g)
[DBUH][EtCOO]	220.0 ± 0.5 (T_g)
[DBUH][nPrCOO]	226.6 ± 0.5 (T_g)
[DBUH][iPrCOO]	230.4 ± 0.5 (T_g)
[DBUH][nPentCOO]	217.0 ± 0.5 (T_g)
[DBUH][nHeptCOO]	216.3 ± 0.5 (T_g)
[TBDH][nPentCOO]	208.1 ± 0.5 (T_g) 226.2 ± 0.5 (T_c) 264.3 ± 0.5 (T_m) T_g / T_m = (0.79)
[TMGH][EtCOO]	213.5 ± 0.5 (T_g)
[TMGH][nPentCOO]	206.5 ± 0.5 (T_g) 243.8 ± 0.5 (T_c) 257.8 ± 0.5 (T_m) T_g / T_m = (0.80)

Figure 5.13 presents the graphic representation of T_g, T_c, T_{cc}, and T_m values as a function of the number of carbon atoms in the PIL. As can be seen, for the PILs with acids of intermediate chain length no T_m, T_{cc} or T_c could be determined. This result is quite similar to previous work dealing with aprotic ILs [5.40], in which this zone is a consequence of the weakening of the electrostatic interactions and decrease of the symmetry of the IL-cation. In this case, the explanation can be similar, and this zone with only T_g can mark the beginning of a different structuration in the PIL.

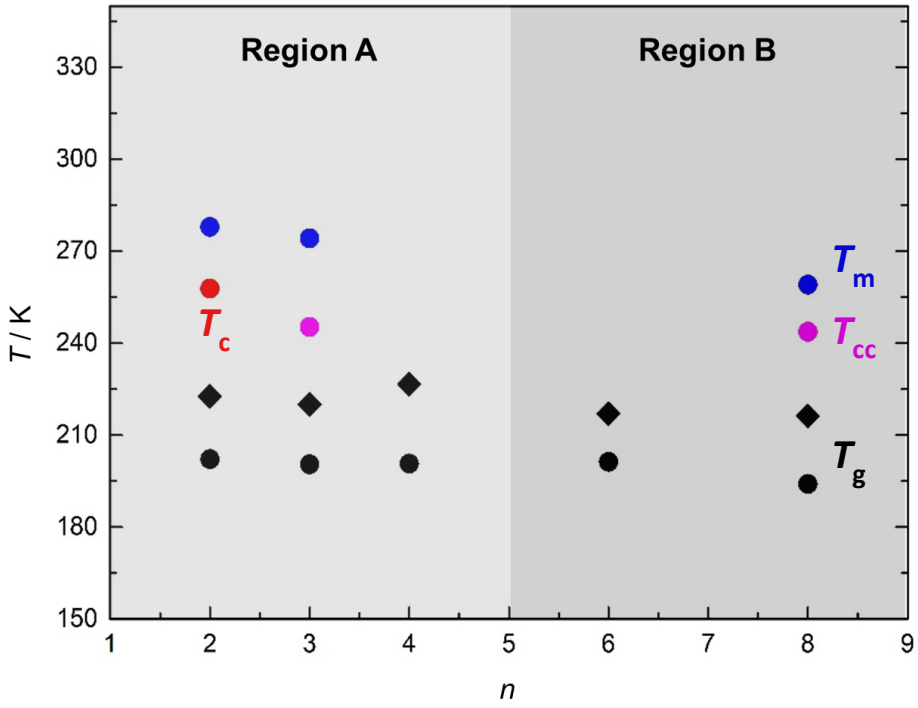

Figure 5.13. Phase behavior results for the PILs studied. DBN-based PILs (●) and DBU-based PILs (♦). *n* – number of C atoms in the acid.

The higher T_g of DBU PILs compared to the DBN analogues, can be explained by their higher ionicity. Since the DBU PILs are more ionic, and assuming that the composition of the PILs in the glass resembles that of the liquid, the T_g increases because strong intermolecular interactions generally increase the stability of the glass relative to the undercooled liquid.

5.3.2. Heat capacities at T = 298.15 K

The heat capacities at T = 298.15 K were measured using two different apparatus. In this sub-chapter the results obtained using the Drop calorimeter are presented. Before each measurement a blank was made in order to calibrate the apparatus. Table 5.3. presents the experimental results obtained for the blanks using the three different ampoules.

Table 5.3. Experimental results obtained by Drop calorimetry with empty ampoules (blanks), using three different ampoules, the results are presented as the average of N experiments for each compound, each experiment with independent number of drops, N_{drop}.

m_{amp} / g	Compound	$\langle T_{furnace} \rangle$ / K	$\langle T_{calorimeter} \rangle$ / K	$\langle A_{amp} \rangle$ / V·s·K^{-1}	N	N_{drop}
2.96201	DBN	293.19	303.31	0.21930	1	25
2.93192	DBU	293.19	303.33	0.21415	1	17
2.96204	[DBNH][nEtCOO]	293.19	303.31	0.21930	1	21
2.96207	[DBNH][nPrCOO]	293.19	303.31	0.21930	3	62
2.96206	[DBNH][nPentCOO]	293.19	303.31	0.21930	2	54
2.96207	[DBNH][nHeptCOO]	293.19	303.31	0.21930	2	46
2.93206	[DBUH][nEtCOO]	293.19	303.33	0.21415	2	35
2.93199	[DBUH][nPrCOO]	293.19	303.33	0.21415	2	34
2.93198	[DBUH][nPentCOO]	293.19	303.33	0.21415	1	23
2.93205	[DBUH][nHeptCOO]	293.19	303.33	0.21415	2	35

Tables 5.4 to 5.20 present the experimental results obtained for the PILs studied: number of drops for each studied compound, N_{drop}, (each experiment has several drops), the corrected normalized areas of the peaks, A_{corr} and the obtained C_p at T = 298.15K are presented. Figures 5.14 to 5.30 illustrate the variance of these measurements across the various drop experiments. The results of C_p are shown as the mean and the standard deviation of the mean. In all experiments the $\langle T \rangle$ is around 298.3 K, that is ≈ 298.15 K, but, with rigor, the obtained C_p should be considered for the $\langle T \rangle$ of each experiment. The errors in the heat capacity values were calculated by applying propagation of uncertainty to equation 5.10.

Table 5.4. Experimental results obtained by Drop calorimetry for DBN (M = 124.18 g·mol^{-1}; m = 0.49664 g; ε = 6.6040 W·V^{-1}).

N_{drop}	$T_{furnace}$ / K	$T_{calorimeter}$ / K	ΔT / K	A_{corr} / V·s·K^{-1}	C_p (298.15 K) / J·K^{-1}·mol^{-1}
1	303.38	293.19	10.19	0.127735	210.93
2	303.38	293.19	10.19	0.127530	210.59
3	303.38	293.19	10.19	0.127735	210.93
4	303.36	293.20	10.16	0.127405	210.39
5	303.39	293.19	10.20	0.127834	211.10
6	303.39	293.19	10.20	0.127849	211.12
7	303.40	293.18	10.22	0.127485	210.52
8	303.39	293.19	10.20	0.127810	211.06
9	303.41	293.18	10.23	0.127457	210.47
10	303.39	293.19	10.21	0.127089	210.38
11	303.38	293.20	10.17	0.126904	210.37
12	303.38	293.19	10.18	0.127395	210.70
C_p (298.15 K) / J·K^{-1}·mol^{-1}= (210.75 ± 0.21)					

A_{corr} = ($A_{ampoule+sample}$ – $A_{ampoule}$). $A_{ampoule}$ is presented in table 5.3.

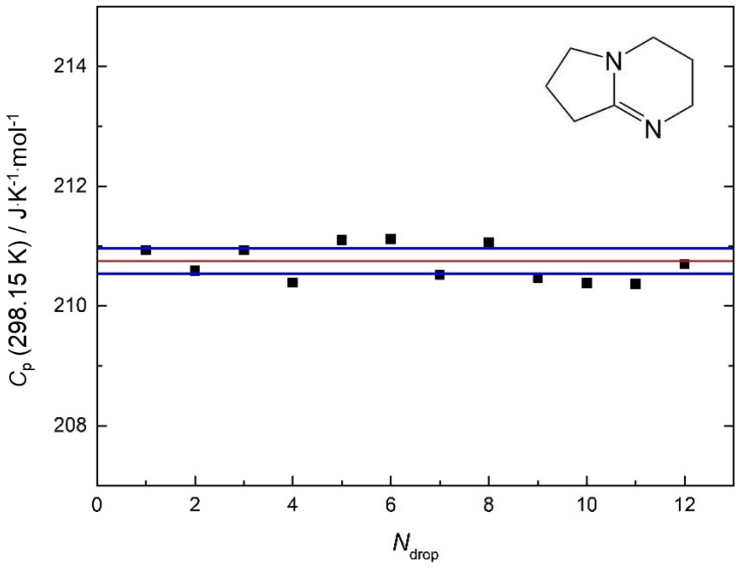

Figure 5.14. Experimental results obtained by Drop calorimetry for DBN. ━ (red line) value obtained for C_p at 298.15 K. ━ (blue lines) error lines obtained for C_p at 298.15 K.

Table 5.5. Experimental results obtained by Drop calorimetry for DBU (M = 152.24 g·mol^{-1}; m = 0.49449 g; ε = 6.6040 W·V^{-1}).

N_{drop}	$T_{furnace}$ / K	$T_{calorimeter}$ / K	ΔT / K	A_{corr} / V·s·K^{-1}	C_p (298.15 K) / J·K^{-1}·mol^{-1}
1	303.38	293.20	10.17	0.129902	264.11
2	303.42	293.20	10.22	0.130088	264.49
3	303.43	293.20	10.23	0.130115	264.54
4	303.41	293.20	10.22	0.129841	263.99
5	303.38	293.18	10.20	0.129841	263.83
6	303.37	293.20	10.18	0.129948	264.21
7	303.40	293.19	10.21	0.129752	263.81
8	303.40	293.18	10.21	0.129797	263.90
9	303.40	293.18	10.21	0.129745	263.79
10	303.38	293.17	10.22	0.130053	264.42
C_p (298.15 K) / J·K^{-1}·mol^{-1}= (264.11 ± 0.23)					

A_{corr} = ($A_{ampoule+sample}$ – $A_{ampoule}$). $A_{ampoule}$ is presented in table 5.3.

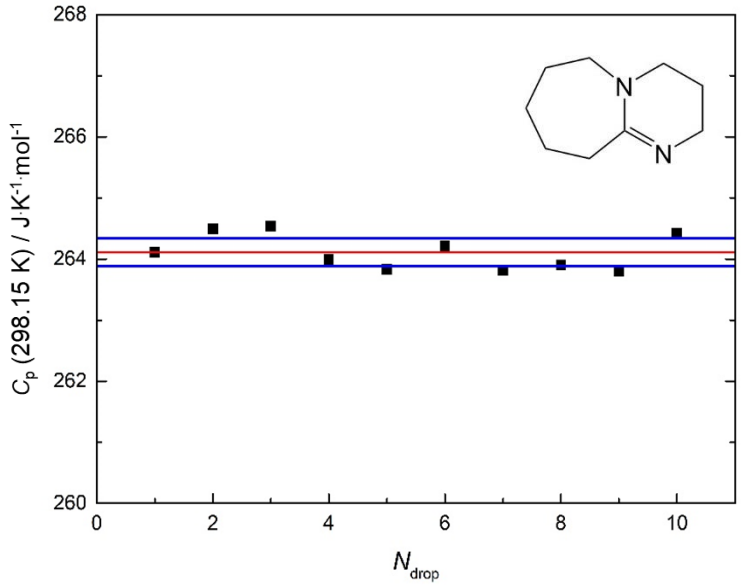

Figure 5.15. Experimental results obtained by Drop calorimetry for DBU. ━ (red line) value obtained for C_p at 298.15 K. ━ (blue lines) error lines obtained for C_p at 298.15 K.

Table 5.6. Experimental results obtained by Drop calorimetry for [DBNH][EtCOO] (M = 198.26 g·mol^{-1}; m = 0.45349 g; ε = 6.6040 W·V^{-1}).

N_{drop}	$T_{furnace}$ / K	$T_{calorimeter}$ / K	ΔT / K	A_{corr} / V·s·K^{-1}	C_p (298.15 K) / J·K^{-1}·mol^{-1}
1	303.24	293.43	9.81	0.129431	373.70
2	303.25	293.46	9.78	0.129793	374.74
3	303.24	293.46	9.78	0.129825	374.84
4	303.21	293.47	9.74	0.129502	373.90
5	303.19	293.48	9.71	0.129481	373.84
6	303.19	293.51	9.69	0.129682	374.42
7	303.21	293.52	9.69	0.129645	374.32
8	303.24	293.53	9.71	0.129788	374.73
9	303.23	293.53	9.70	0.129481	373.84
10	303.25	293.52	9.73	0.129733	374.57
11	303.26	293.52	9.74	0.129794	374.75
12	303.19	293.57	9.63	0.129417	373.66
13	303.22	293.60	9.62	0.129641	374.30
14	303.23	293.60	9.63	0.129760	374.65
15	303.24	293.59	9.65	0.129800	374.76
16	303.25	293.57	9.68	0.129726	374.55
17	303.21	293.54	9.67	0.129595	374.17
18	303.21	293.54	9.67	0.129486	373.86
19	303.22	293.54	9.68	0.129633	374.28
20	303.21	293.54	9.68	0.129445	373.74
21	303.20	293.54	9.66	0.129426	373.68
22	303.23	293.55	9.68	0.129810	374.79
23	303.25	293.54	9.70	0.129749	374.61
24	303.25	293.54	9.72	0.129518	373.95
25	303.26	293.51	9.75	0.129730	374.56
26	303.26	293.48	9.78	0.129579	374.12
27	303.25	293.47	9.78	0.129597	374.18
28	303.23	293.47	9.76	0.129543	374.02
29	303.24	293.47	9.77	0.129453	373.76
30	303.24	293.47	9.77	0.129748	374.61
C_p (298.15 K) / J·K^{-1}·mol^{-1}= (374.26 ± 0.25)					

A_{corr} = ($A_{ampoule+sample}$ – $A_{ampoule}$). $A_{ampoule}$ is presented in table 5.3.

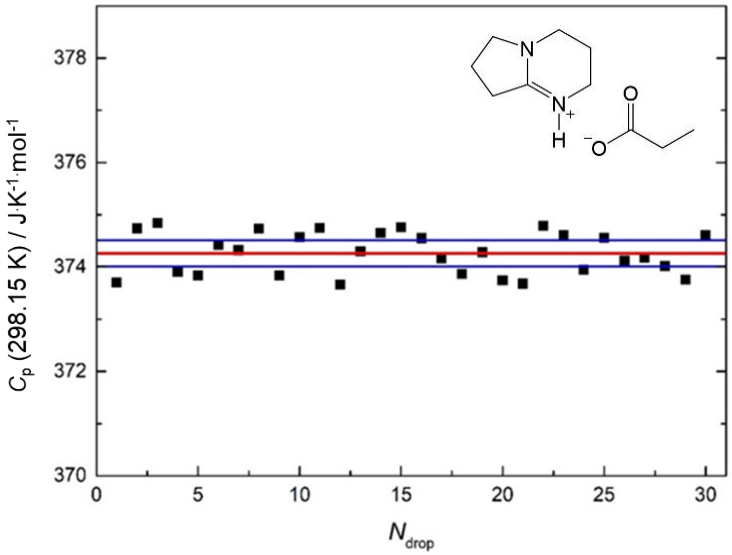

Figure 5.16. Experimental results obtained by Drop calorimetry for [DBNH][EtCOO]. ━ (red line) value obtained for C_p at 298.15 K. ━ (blue lines) error lines obtained for C_p at 298.15 K.

Table 5.7. Experimental results obtained by Drop calorimetry for [DBNH][nPrCOO], experiment 1 (M = 212.29 g·mol^{-1}; m = 0.49827 g; ε = 6.6040 W·V^{-1}).

N_{drop}	$T_{furnace}$ / K	$T_{calorimeter}$ / K	ΔT / K	A_{corr} / V·s·K^{-1}	C_p (298.15 K) / J·K^{-1}·mol^{-1}
1	303.15	293.73	9.41	0.144688	407.10
2	294.15	293.75	9.40	0.144706	407.15
3	303.16	293.76	9.40	0.144626	406.93
4	303.16	293.76	9.40	0.144526	406.65
5	303.17	293.76	9.41	0.144657	407.02
6	303.14	293.73	9.41	0.144453	406.44
7	303.08	293.79	9.29	0.144571	406.77
8	303.09	293.80	9.29	0.144656	407.01
9	303.10	293.82	9.29	0.144675	407.07
C_p (298.15 K) / J·K^{-1}·mol^{-1}= (406.90 ± 0.27)					

A_{corr} = ($A_{ampoule+sample}$ – $A_{ampoule}$). $A_{ampoule}$ is presented in table 5.3.

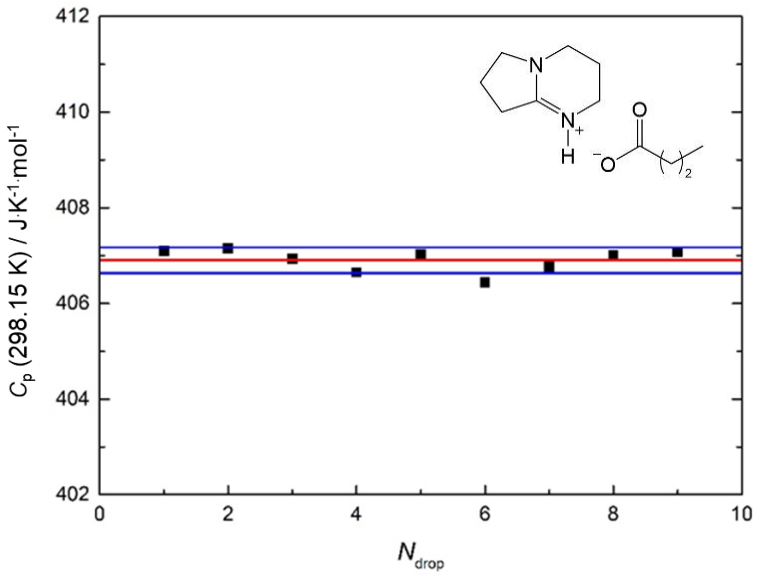

Figure 5.17. Experimental results obtained by Drop calorimetry for [DBNH][nPrCOO], experiment 1. ━ (red line) value obtained for C_p at 298.15 K. ━ (blue lines) error lines obtained for C_p at 298.15 K.

Table 5.8. Experimental results obtained by Drop calorimetry for [DBNH][nPrCOO], experiment 2 (M = 212.29 g·mol^{-1}; m = 0.49860 g; ε = 6.6040 W·V^{-1}).

N_{drop}	$T_{furnace}$ / K	$T_{calorimeter}$ / K	ΔT / K	A_{corr} / V·s·K^{-1}	C_p (298.15 K) / J·K^{-1}·mol^{-1}
1	303.16	293.83	9.34	0.145337	408.66
2	303.17	293.73	9.45	0.145233	408.37
3	303.19	293.69	9.51	0.145294	408.54
4	303.21	293.64	9.56	0.145446	408.96
5	303.21	293.62	9.59	0.145395	408.82
6	303.21	293.60	9.61	0.145425	408.91
7	303.22	293.58	9.64	0.145298	408.55
8	303.22	293.56	9.65	0.145266	408.46
9	303.21	293.55	9.67	0145258	408.44
10	303.22	293.52	9.70	0.145395	408.82
11	303.22	293.51	9.71	0.145358	408.72
12	303.21	293.50	9.71	0.145363	408.73
13	303.22	293.49	9.72	0.145390	408.81
14	303.22	293.49	9.74	0.145405	408.85
15	303.23	293.48	9.75	0.145558	409.28
16	303.24	293.47	9.77	0.145338	408.66
17	303.24	293.46	9.78	0.145488	409.08
C_p (298.15 K) / J·K^{-1}·mol^{-1}= (408.74 ± 0.25)					

A_{corr} = ($A_{ampoule+sample}$ – $A_{ampoule}$). $A_{ampoule}$ is presented in table 5.3.

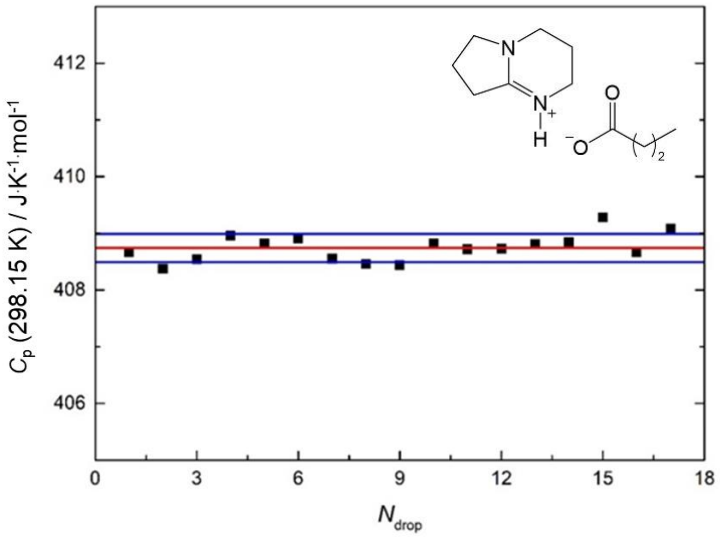

Figure 5.18. Experimental results obtained by Drop calorimetry for [DBNH][nPrCOO], experiment 2. ━ (red line) value obtained for C_p at 298.15 K. ━ (blue lines) error lines obtained for C_p at 298.15 K.

Table 5.9. Experimental results obtained by Drop calorimetry for [DBNH][nPrCOO], experiment 3 (M = 212.29 g·mol^{-1}; m = 0.49794 g; ε = 6.6040 W·V^{-1}).

N_{drop}	$T_{furnace}$ / K	$T_{calorimeter}$ / K	ΔT / K	A_{corr} / V·s·K^{-1}	C_p (298.15 K) / J·K^{-1}·mol^{-1}
1	303.24	293.40	9.84	0.145568	409.85
2	303.23	293.39	9.83	0.145356	409.25
3	303.22	293.39	9.83	0.145486	409.62
4	303.23	293.40	9.84	0.145358	409.26
5	303.24	293.39	9.85	0.145484	409.61
6	303.25	293.39	9.86	0.145480	409.60
7	303.25	293.35	9.89	0.145570	409.85
8	303.24	293.36	9.88	0.145568	409.85
9	303.22	293.36	9.86	0.145398	409.37
10	303.22	293.38	9.84	0.145492	409.64
11	303.22	293.38	9.84	0.145529	409.74
12	303.23	293.39	9.84	0.145480	409.60
13	303.23	293.39	9.84	0.145465	409.56
14	303.24	293.39	9.84	0.145545	409.79
15	303.24	293.39	9.85	0.145492	409.63
16	303.24	293.39	9.86	0.145407	409.40
17	303.23	293.38	9.85	0.145524	409.73
18	303.24	293.40	9.84	0.145431	409.85
C_p (298.15 K) / J·K^{-1}·mol^{-1}= (409.60 ± 0.24)					

A_{corr} = ($A_{ampoule+sample}$ – $A_{ampoule}$). $A_{ampoule}$ is presented in table 5.3.

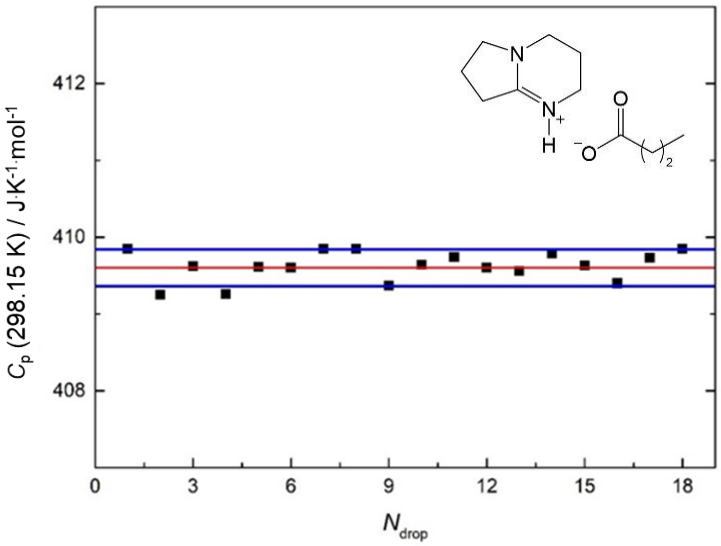

Figure 5.19. Experimental results obtained by Drop calorimetry for [DBNH][nPrCOO], experiment 3. ━ (red line) value obtained for C_p at 298.15 K. ━ (blue lines) error lines obtained for C_p at 298.15 K.

Table 5.10. Experimental results obtained by Drop calorimetry for [DBNH][nPentCOO], experiment 1 (M = 240.34 g·mol^{-1}; m = 0.45586 g; ε = 6.6040 W·V^{-1}).

N_{drop}	$T_{furnace}$ / K	$T_{calorimeter}$ / K	ΔT / K	A_{corr} / V·s·K^{-1}	C_p (298.15 K) / J·K^{-1}·mol^{-1}
1	303.30	293.22	10.08	0.136544	475.42
2	303.33	293.24	10.08	0.136641	475.76
3	303.33	293.24	10.09	0.136509	475.30
4	303.35	293.23	10.12	0.136428	475.02
5	303.29	293.26	10.04	0.136406	474.94
6	303.33	293.27	10.06	0.136635	475.74
7	303.33	293.27	10.06	0.136616	475.67
8	303.33	293.22	10.10	0.136450	475.10
9	303.33	293.23	10.10	0.136562	475.49
10	303.34	293.23	10.11	0.136601	475.62
11	303.34	293.23	10.11	0.136423	475.00
12	303.34	293.22	10.11	0.136482	475.21
13	303.32	293.23	10.09	0.136685	475.91
C_p (298.15 K) / J·K^{-1}·mol^{-1}= (475.40 ± 0.36)					

A_{corr} = ($A_{ampoule+sample}$ – $A_{ampoule}$). $A_{ampoule}$ is presented in table 5.3.

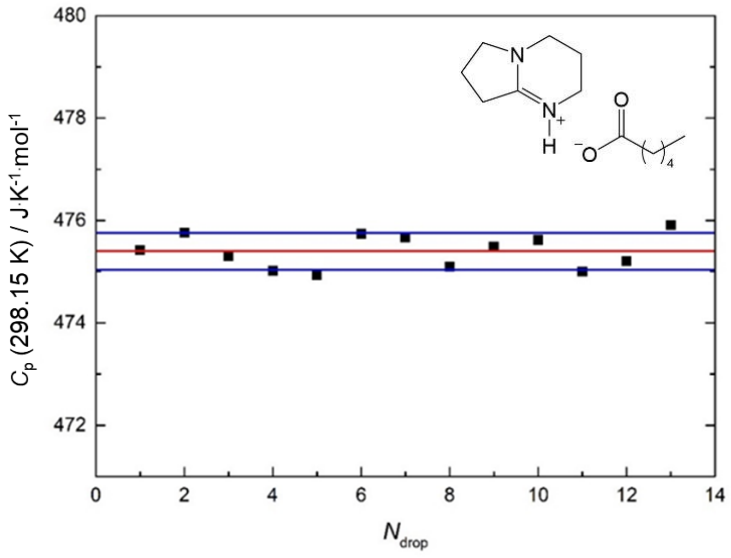

Figure 5.20. Experimental results obtained by Drop calorimetry for [DBNH][nPentCOO], experiment 1. ━ (red line) value obtained for C_p at 298.15 K. ━ (blue lines) error lines obtained for C_p at 298.15 K.

Table 5.11. Experimental results obtained by Drop calorimetry for [DBNH][nPentCOO], experiment 2 (M = 240.34 g·mol^{-1}; m = 0.45629 g; ε = 6.6040 W·V^{-1}).

N_{drop}	$T_{furnace}$ / K	$T_{calorimeter}$ / K	ΔT / K	A_{corr} / V·s·K^{-1}	C_p (298.15 K) / J·K^{-1}·mol^{-1}
1	303.30	293.23	10.07	0.136387	474.43
2	303.28	293.25	10.03	0.136351	474.30
3	303.26	293.28	9.98	0.136455	474.66
4	303.32	293.31	10.01	0.136404	474.49
5	303.33	293.30	10.03	0.136366	474.36
6	303.31	293.26	10.05	0.136411	474.51
7	303.30	293.25	10.05	0.136482	474.76
8	303.28	293.27	10.01	0.136198	473.77
C_p (298.15 K) / J·K^{-1}·mol^{-1}= (474.41 ± 0.33)					

A_{corr} = ($A_{ampoule+sample}$ – $A_{ampoule}$). $A_{ampoule}$ is presented in table 5.3.

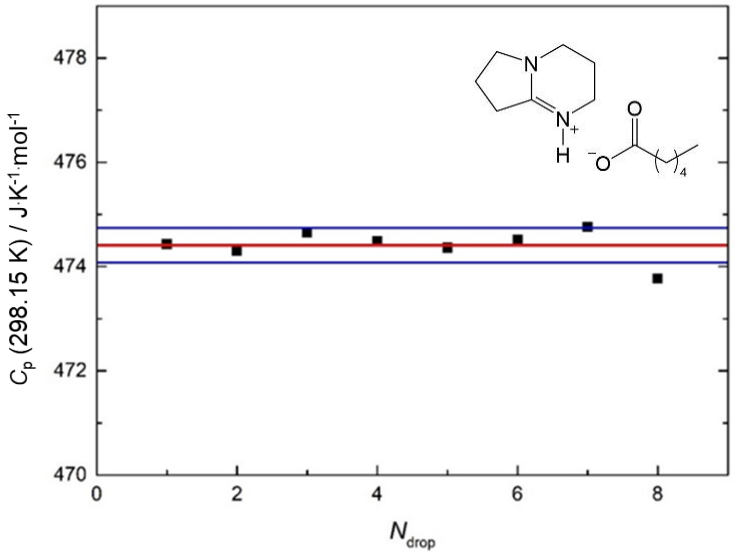

Figure 5.21. Experimental results obtained by Drop calorimetry for [DBNH][nPentCOO], experiment 2. ━ (red line) value obtained for C_p at 298.15 K. ━ (blue lines) error lines obtained for C_p at 298.15 K.

Table 5.12. Experimental results obtained by Drop calorimetry for [DBNH][nHeptCOO], experiment 1 (M = 268.40 g·mol^{-1}; m = 0.41717 g; ε = 6.6040 W·V^{-1}).

N_{drop}	$T_{furnace}$ / K	$T_{calorimeter}$ / K	ΔT / K	A_{corr} / V·s·K^{-1}	C_p (298.15 K) / J·K^{-1}·mol^{-1}
1	303.33	293.26	10.07	0.128028	543.97
2	303.34	293.26	10.09	0.128068	544.14
3	303.36	293.22	10.14	0.128033	543.99
4	303.37	293.22	10.15	0.128040	544.02
5	303.37	293.21	10.17	0.128069	544.15
6	303.38	293.21	10.17	0.128186	544.64
7	303.38	293.21	10.17	0.128168	544.57
8	303.35	293.21	10.15	0.128202	544.71
9	303.38	293.21	10.17	0.128151	544.50
10	303.39	293.21	10.19	0.128141	544.45
11	303.39	293.20	10.19	0.128098	544.27
12	303.39	293.21	10.18	0.128249	544.91
13	303.39	293.21	10.19	0.128194	544.68
14	303.38	293.20	10.17	0.128035	544.00
15	303.38	293.20	10.18	0.128213	544.76
16	303.38	293.20	10.17	0.128229	544.83
17	303.37	293.20	10.17	0.128213	544.76
18	303.38	293.20	10.18	0.128093	544.25
19	303.38	293.20	10.18	0.128398	545.54
20	303.39	293.20	10.18	0.128072	544.16
21	303.39	293.20	10.19	0.128057	544.09
22	303.38	293.21	10.17	0.128174	544.59
23	303.38	293.20	10.18	0.128128	544.40
C_p (298.15 K) / J·K^{-1}·mol^{-1}= (544.45 ± 0.34)					

A_{corr} = ($A_{ampoule+sample}$ – $A_{ampoule}$). $A_{ampoule}$ is presented in table 5.3.

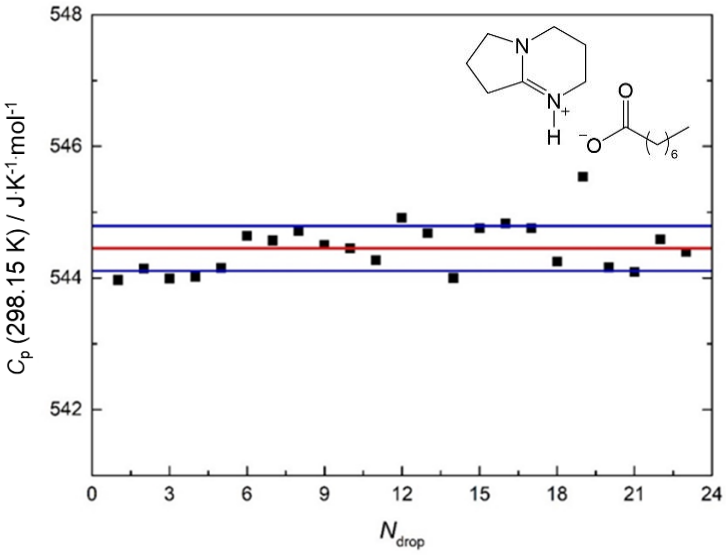

Figure 5.22. Experimental results obtained by Drop calorimetry for [DBNH][nHeptCOO], experiment 1. ━ (red line) value obtained for C_p at 298.15 K. ━ (blue lines) error lines obtained for C_p at 298.15 K.

Table 5.13. Experimental results obtained by Drop calorimetry for [DBNH][nHeptCOO], experiment 2 (M = 268.40 g·mol^{-1}; m = 0.41737 g; ε = 6.6040 W·V^{-1}).

N_{drop}	$T_{furnace}$ / K	$T_{calorimeter}$ / K	ΔT / K	A_{corr} / V·s·K^{-1}	C_p (298.15 K) / J·K^{-1}·mol^{-1}
1	303.40	293.20	10.20	0.128630	546.27
2	303.37	293.20	10.17	0.128502	545.72
3	303.37	293.20	10.17	0.128446	545.49
4	303.40	293.20	10.20	0.128555	545.95
5	303.40	293.20	10.20	0.128472	545.59
6	303.40	293.20	10.20	0.128530	545.84
7	303.40	293.20	10.20	0.128463	545.56
8	303.40	293.20	10.20	0.128591	546.10
9	303.38	293.20	10.18	0.128487	545.66
10	303.39	293.20	10.19	0.128584	546.07
11	303.40	293.20	10.20	0.128609	546.18
12	303.40	293.20	10.20	0.128631	546.27
C_p (298.15 K) / J·K^{-1}·mol^{-1}= (545.89 ± 0.34)					

A_{corr} = ($A_{ampoule+sample}$ – $A_{ampoule}$). $A_{ampoule}$ is presented in table 5.3.

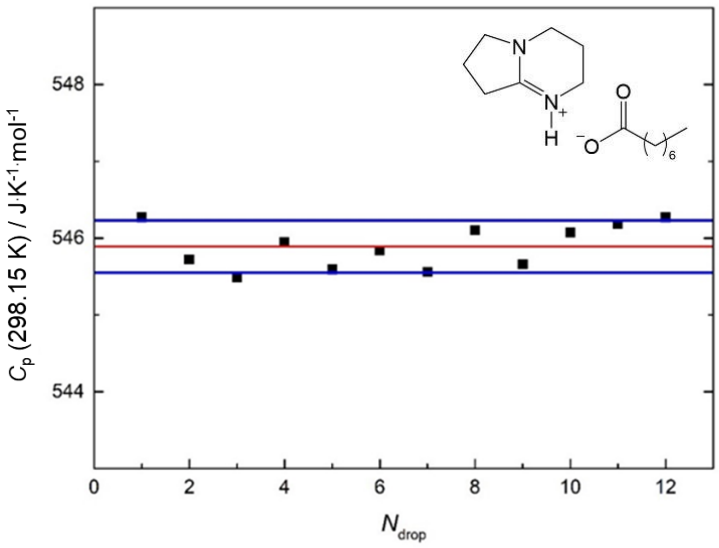

Figure 5.23. Experimental results obtained by Drop calorimetry for [DBNH][nHeptCOO], experiment 2. ━ (red line) value obtained for C_p at 298.15 K. ━ (blue lines) error lines obtained for C_p at 298.15 K.

Table 5.14. Experimental results obtained by Drop calorimetry for [DBUH][EtCOO], experiment 1 (M = 226.32 g·mol^{-1}; m = 0.50405 g; ε = 6.6040 W·V^{-1}).

N_{drop}	$T_{furnace}$ / K	$T_{calorimeter}$ / K	ΔT / K	A_{corr} / V·s·K^{-1}	C_p (298.15 K) / J·K^{-1}·mol^{-1}
1	303.31	293.34	9.98	0.152457	452.06
2	303.34	293.32	10.01	0.152268	451.50
3	303.33	293.31	10.02	0.152313	451.63
4	303.34	293.31	10.03	0.152346	451.73
5	303.29	293.30	9.99	0.152300	451.60
6	303.30	293.31	9.99	0.152290	451.57
7	303.32	293.32	10.00	0.152390	451.86
8	303.33	293.29	10.04	0.152210	451.33
9	303.34	293.28	10.06	0.152364	451.79
10	303.33	293.26	10.07	0.152326	451.67
11	303.33	293.26	10.07	0.152441	452.01
12	303.29	293.29	10.00	0.152433	451.99
13	303.31	293.30	10.01	0.152420	451.95
14	303.32	293.30	10.02	0.152355	451.76
15	303.34	293.30	10.03	0.152278	451.53
16	303.33	293.25	10.08	0.152224	451.37
17	303.29	293.29	10.01	0.152412	451.93
18	303.31	293.30	10.01	0.152334	451.70
19	303.33	293.30	10.03	0.152207	451.32
C_p (298.15 K) / J·K^{-1}·mol^{-1}= (451.70 ± 0.27)					

A_{corr} = ($A_{ampoule+sample}$ – $A_{ampoule}$). $A_{ampoule}$ is presented in table 5.3.

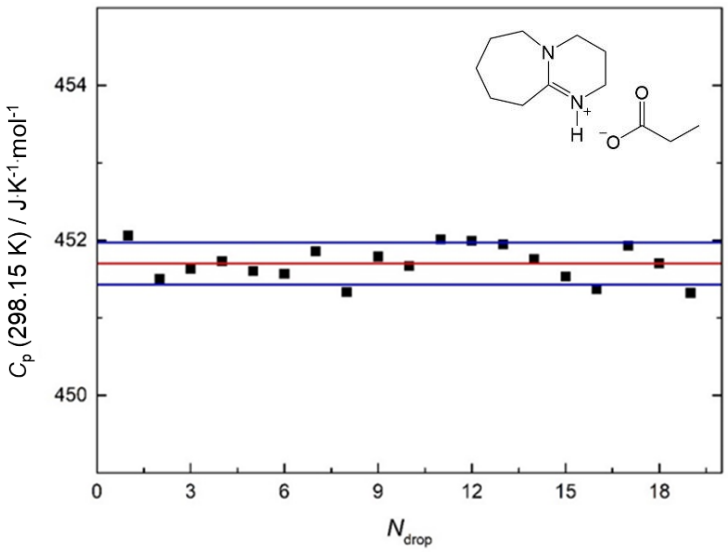

Figure 5.24. Experimental results obtained by Drop calorimetry for [DBUH][EtCOO], experiment 1. ━ (red line) value obtained for C_p at 298.15 K. ━ (blue lines) error lines obtained for C_p at 298.15 K.

Table 5.15. Experimental results obtained by Drop calorimetry for [DBUH][EtCOO], experiment 2 (M = 226.32 g·mol^{-1}; m = 0.33658 g; ε = 6.6040 W·V^{-1}).

N_{drop}	$T_{furnace}$ / K	$T_{calorimeter}$ / K	ΔT / K	A_{corr} / V·s·K^{-1}	C_p (298.15 K) / J·K^{-1}·mol^{-1}
1	303.30	293.29	10.00	0.101852	452.27
2	303.32	293.32	9.99	0.102074	453.26
3	303.36	293.33	10.03	0.102014	453.00
4	303.33	293.30	10.03	0.102109	453.42
5	303.31	293.39	9.91	0.101831	452.18
6	303.33	293.40	9.93	0.102114	453.44
7	303.37	293.36	10.00	0.102046	453.14
8	303.34	293.35	10.00	0.102995	452.91
9	303.33	293.33	10.00	0.101869	452.35
10	303.33	293.33	10.00	0.101900	452.49
11	303.30	293.36	9.94	0.102080	453.29
12	303.31	293.36	9.96	0.101864	452.33
13	303.33	293.36	9.96	0.101946	452.69
14	303.35	293.35	10.00	0.102984	452.86
C_p (298.15 K) / J·K^{-1}·mol^{-1}= (452.83 ± 0.34)					

A_{corr} = ($A_{ampoule+sample}$ – $A_{ampoule}$). $A_{ampoule}$ is presented in table 5.3.

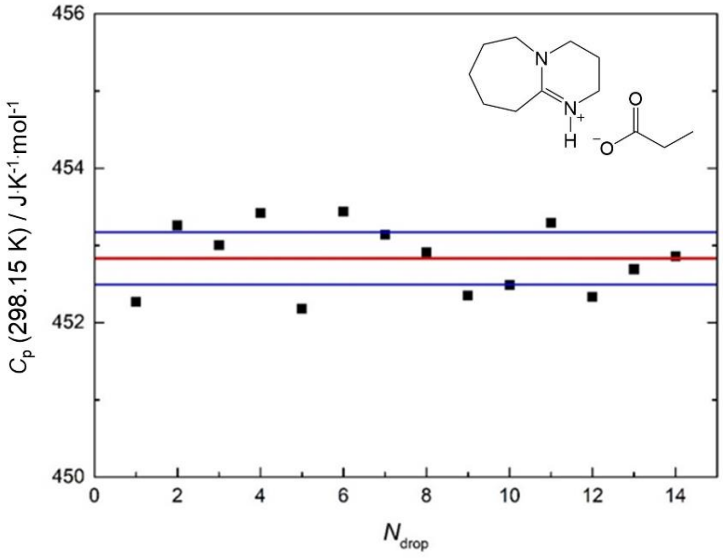

Figure 5.25. Experimental results obtained by Drop calorimetry for [DBUH][EtCOO], experiment 2. ━ (red line) value obtained for C_p at 298.15 K. ━ (blue lines) error lines obtained for C_p at 298.15 K.

Table 5.16. Experimental results obtained by Drop calorimetry for [DBUH][nPrCOO], experiment 1 (M = 240.34 g·mol^{-1}; m = 0.51639 g; ε = 6.6040 W·V^{-1}).

N_{drop}	$T_{furnace}$ / K	$T_{calorimeter}$ / K	ΔT / K	A_{corr} / V·s·K^{-1}	C_p (298.15 K) / J·K^{-1}·mol^{-1}
1	303.28	293.25	10.03	0.159106	489.04
2	303.28	293.28	10.00	0.159262	489.52
3	303.29	293.30	9.99	0.159210	489.36
4	303.30	293.31	9.99	0.159391	489.92
5	303.31	293.33	9.97	0.159407	489.97
6	303.31	293.33	9.98	0.159362	489.83
7	303.33	293.34	9.99	0.159108	489.05
8	303.33	293.34	9.99	0.159179	489.27
9	303.31	293.34	9.97	0.159271	489.55
10	303.30	293.34	9.97	0.159211	489.37
11	303.28	293.34	9.95	0.159402	489.95
12	303.28	293.35	9.93	0.159232	489.43
13	303.28	293.37	9.91	0.159060	488.90
14	303.29	293.38	9.91	0.159382	489.89
15	303.31	293.39	9.93	0.159261	489.52
16	303.32	293.38	9.94	0.159216	489.38
17	303.32	293.38	9.95	0.159002	488.73
18	303.31	293.37	9.94	0.159220	489.40
19	303.28	293.38	9.90	0.159096	489.01
C_p (298.15 K) / J·K^{-1}·mol^{-1}= (489.43 ± 0.32)					

A_{corr} = ($A_{ampoule+sample}$ – $A_{ampoule}$). $A_{ampoule}$ is presented in table 5.3.

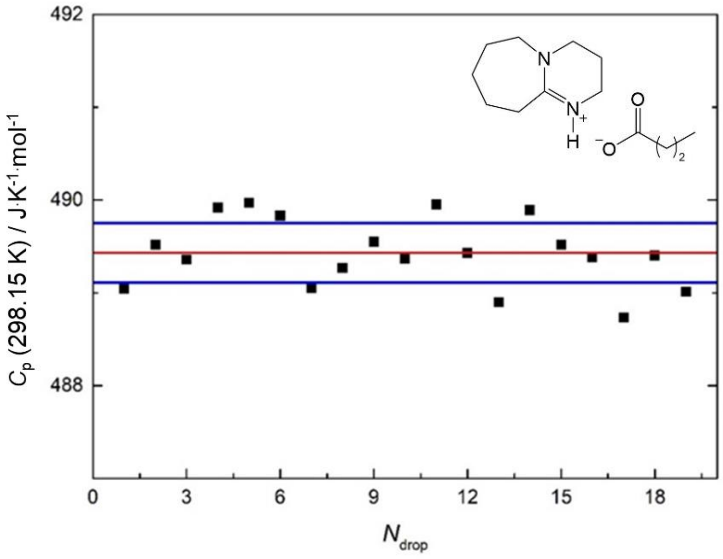

Figure 5.26. Experimental results obtained by Drop calorimetry for [DBUH][nPrCOO], experiment 1. ━ (red line) value obtained for C_p at 298.15 K. ━ (blue lines) error lines obtained for C_p at 298.15 K.

Table 5.17. Experimental results obtained by Drop calorimetry for [DBUH][nPrCOO], experiment 2 (M = 240.34 g·mol^{-1}; m = 0.51677 g; ε = 6.6040 W·V^{-1}).

N_{drop}	$T_{furnace}$ / K	$T_{calorimeter}$ / K	ΔT / K	A_{corr} / V·s·K^{-1}	C_p (298.15 K) / J·K^{-1}·mol^{-1}
1	303.28	293.39	9.88	0.159315	489.32
2	303.28	293.41	9.88	0.159270	489.19
3	303.32	293.40	9.92	0.159359	489.46
4	303.33	293.39	9.94	0.159133	488.77
5	303.33	293.38	9.95	0.159127	488.75
6	303.32	293.34	9.98	0.159212	489.01
7	303.31	293.33	9.98	0.159526	489.97
8	303.33	293.32	10.01	0.159483	489.84
9	303.34	293.31	10.03	0.159421	489.65
10	303.34	293.30	10.05	0.159347	489.42
11	303.34	293.29	10.05	0.159130	488.76
12	303.36	293.25	10.11	0.159351	489.44
13	303.36	293.24	10.12	0.159371	489.50
14	303.35	293.24	10.11	0.159528	489.98
15	303.34	293.23	10.11	0.159127	488.75
C_p (298.15 K) / J·K^{-1}·mol^{-1}= (489.32 ± 0.35)					

A_{corr} = ($A_{ampoule+sample}$ – $A_{ampoule}$). $A_{ampoule}$ is presented in table 5.3.

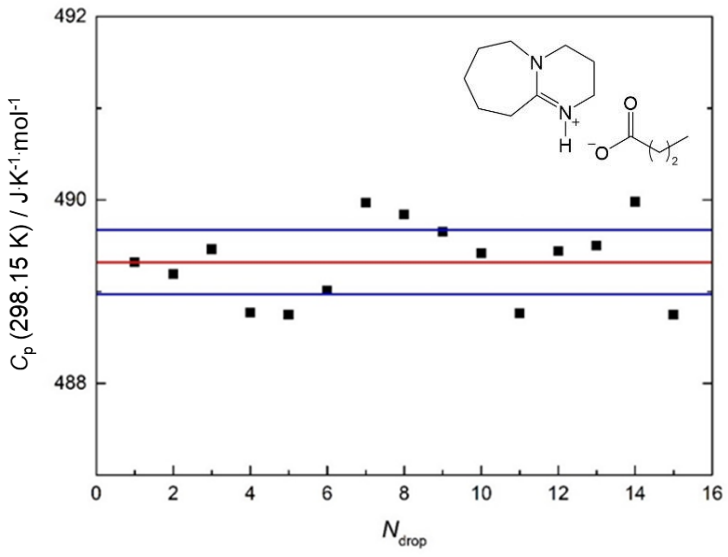

Figure 5.27. Experimental results obtained by Drop calorimetry for [DBUH][nPrCOO], experiment 2. ━ (red line) value obtained for C_p at 298.15 K. ━ (blue lines) error lines obtained for C_p at 298.15 K.

Table 5.18. Experimental results obtained by Drop calorimetry for [DBUH][nPentCOO] (M = 268.40 g·mol^{-1}; m = 0.44772 g; ε = 6.6040 W·V^{-1}).

N_{drop}	$T_{furnace}$ / K	$T_{calorimeter}$ / K	ΔT / K	A_{corr} / V·s·K^{-1}	C_p (298.15 K) / J·K^{-1}·mol^{-1}
1	303.31	293.20	10.11	0.139731	553.19
2	303.36	293.20	10.16	0139914	553.91
3	303.35	293.20	10.15	0.139772	553.35
4	303.33	293.19	10.14	0.139947	554.04
5	303.33	293.20	10.13	0.139847	553.64
6	303.32	293.20	10.12	0.139872	553.74
7	303.33	293.20	10.12	0.140987	554.20
8	303.33	293.20	10.13	0.139828	553.57
9	303.32	293.20	10.12	0.139699	553.06
10	303.28	293.29	9.99	0.139899	553.85
11	303.29	293.32	9.97	0.139829	553.57
12	303.28	293.44	9.84	0.139845	553.64
13	303.29	293.44	9.85	0.139767	553.33
14	303.28	293.43	9.85	0.139767	553.33
15	303.25	293.43	9.83	0.139674	552.96
16	303.27	293.44	9.84	0.139743	553.23
17	303.28	293.44	9.84	0.139692	553.03
18	303.29	293.44	9.84	0.139725	553.16
C_p (298.15 K) / J·K^{-1}·mol^{-1}= (553.49 ± 0.35)					

A_{corr} = ($A_{ampoule+sample}$ – $A_{ampoule}$). $A_{ampoule}$ is presented in table 5.3.

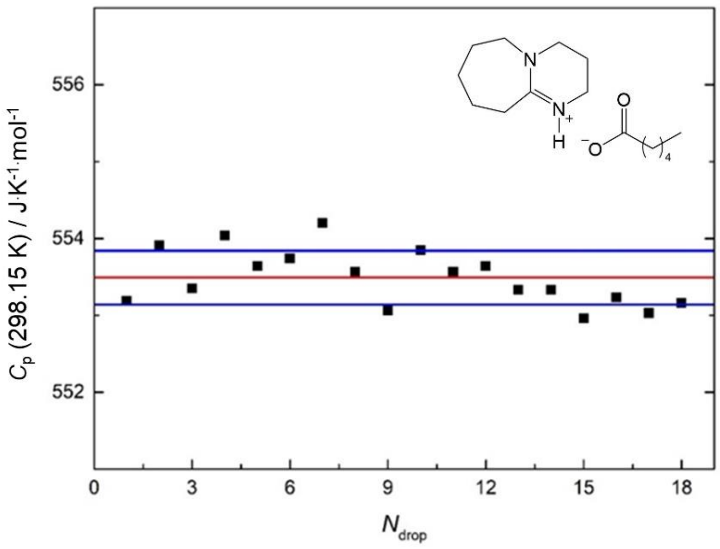

Figure 5.28. Experimental results obtained by Drop calorimetry for [DBUH][nPentCOO]. ━ (red line) value obtained for C_p at 298.15 K. ━ (blue lines) error lines obtained for C_p at 298.15 K.

Table 5.19. Experimental results obtained by Drop calorimetry for [DBUH][nHeptCOO], experiment 1 (M = 296.44 g·mol^{-1}; m = 0.53223 g; ε = 6.6040 W·V^{-1}).

N_{drop}	$T_{furnace}$ / K	$T_{calorimeter}$ / K	ΔT / K	A_{corr} / V·s·K^{-1}	C_p (298.15 K) / J·K^{-1}·mol^{-1}
1	303.44	293.19	10.25	0.169282	622.69
2	303.41	293.22	10.19	0.169589	623.82
3	303.43	293.21	10.22	0.169238	622.53
4	303.43	293.19	10.24	0.169436	623.25
5	303.44	293.20	10.24	0.169583	623.79
6	303.43	293.20	10.24	0.169372	623.02
7	303.43	293.21	10.21	0.169081	621.95
8	303.41	293.20	10.21	0.169017	621.71
9	303.42	293.21	10.21	0.169230	622.50
10	303.44	293.20	10.24	0.169579	623.78
11	303.41	293.20	10.21	0.169140	622.16
12	303.44	293.20	10.25	0.169441	623.27
13	303.40	293.21	10.19	0.169478	623.41
14	303.40	293.21	10.19	0.169153	622.21
15	303.43	293.22	10.21	0.169322	622.84
16	303.43	293.21	10.22	0.169286	622.70
17	303.46	293.22	10.24	0.169420	623.19
C_p (298.15 K) / J·K^{-1}·mol^{-1}= (622.87 ± 0.46)					

A_{corr} = ($A_{ampoule+sample}$ – $A_{ampoule}$). $A_{ampoule}$ is presented in table 5.3.

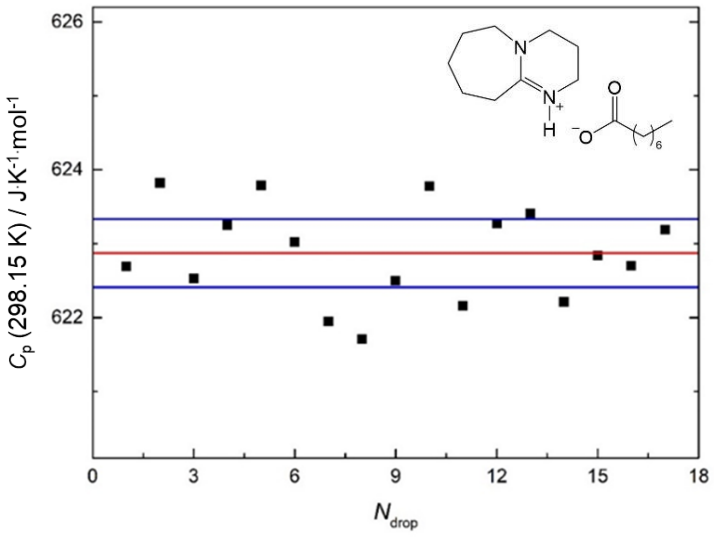

Figure 5.29. Experimental results obtained by Drop calorimetry for [DBUH][nHeptCOO], experiment 1. ━ (red line) value obtained for C_p at 298.15 K. ━ (blue lines) error lines obtained for C_p at 298.15 K.

Table 5.20. Experimental results obtained by Drop calorimetry for [DBUH][nHeptCOO], experiment 2 (M = 296.44 g·mol^{-1}; m = 0.53123 g; ε = 6.6040 W·V^{-1}).

N_{drop}	$T_{furnace}$ / K	$T_{calorimeter}$ / K	ΔT / K	A_{corr} / V·s·K^{-1}	C_p (298.15 K) / J·K^{-1}·mol^{-1}
1	303.47	293.21	10.26	0.168872	622.35
2	303.47	293.20	10.27	0.168935	622.58
3	303.45	293.19	10.26	0.168912	622.50
4	303.42	293.19	10.23	0.168864	622.32
5	303.42	293.19	10.23	0.168596	621.33
6	303.37	293.19	10.18	0.168814	622.14
7	303.36	293.19	10.17	0.168289	620.20
8	303.34	293.20	10.14	0.168310	620.28
9	303.37	293.21	10.16	0.168694	621.69
10	303.37	293.19	10.18	0.168125	619.59
11	303.38	293.20	10.18	0.168710	621.75
12	303.38	293.20	10.18	0.168353	620.43
13	303.38	293.20	10.18	0.168499	620.97
14	303.34	293.20	10.14	0.168478	620.90
15	303.34	293.20	10.14	0.168108	619.53
16	303.33	293.19	10.13	0.168409	620.64
17	303.34	293.19	10.14	0.168018	619.20
C_p (298.15 K) / J·K^{-1}·mol^{-1}= (621.08 ± 0.64)					

A_{corr} = ($A_{ampoule+sample}$ – $A_{ampoule}$). $A_{ampoule}$ is presented in table 5.3.

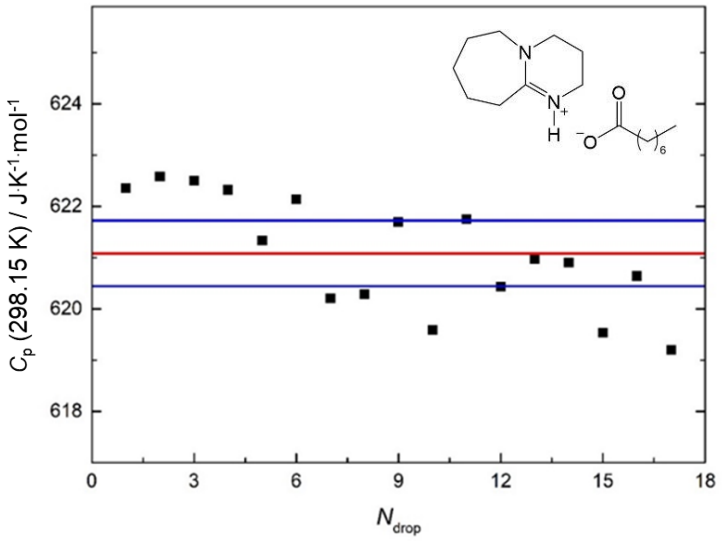

Figure 5.30. Experimental results obtained by Drop calorimetry for [DBUH][nHeptCOO], experiment 2. ━ (red line) value obtained for C_p at 298.15 K. ━ (blue lines) error lines obtained for C_p at 298.15 K.

Table 5.21. Experimental results obtained with by Drop calorimetry for each compound, at T = 298.15 K.

Compound	N_{drop}	M / g·mol^{-1}	C_p (298.15 K) / J·K^{-1}·mol^{-1}
DBN	12	124.18	210.75 ± 0.21
DBU	10	152.24	264.11 ± 0.23
[DBNH][EtCOO]	30	198.26	374.26 ± 0.25
[DBNH][nPrCOO]	44	212.29	406.39 ± 0.29
[DBNH][nPentCOO]	21	240.34	474.91 ± 0.35
[DBNH][nHeptCOO]	35	268.40	545.17 ± 0.34
[DBUH][EtCOO]	33	226.32	452.27 ± 0.31
[DBUH][nPrCOO]	34	240.34	489.38 ± 0.34
[DBUH][nPentCOO]	18	268.40	553.49 ± 0.35
[DBUH][nHeptCOO]	34	296.44	621.98 ± 0.55

N_{drop} – number of drops. For all compounds, the presented value is the average value of all experiments.

Table 5.21 presents the obtained heat capacities at T = 298.15 K results for each compound. Figure 5.31 shows the plots of C_p at T = 298.15 K as a function of the chain length of the carboxylic acid for the DBN and DBU PILs and figure 5.32 their deviation.

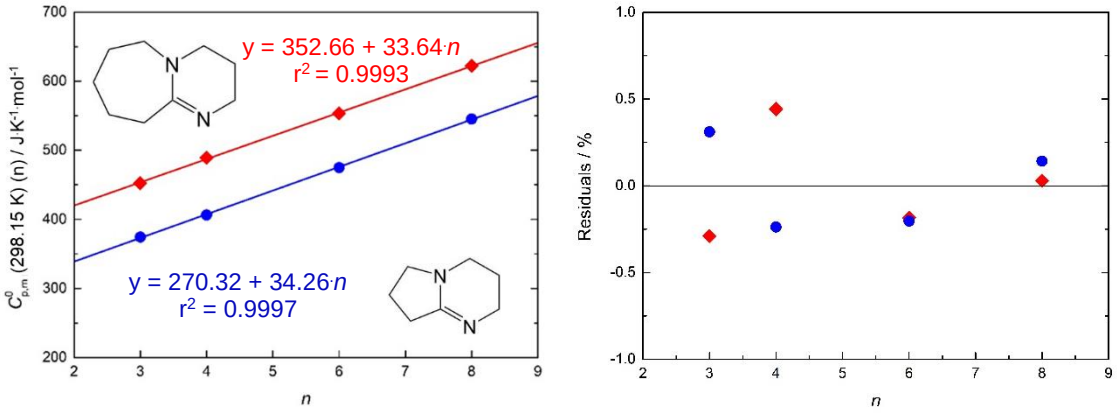

Figure 5.31. Molar heat capacities, at T = 298.15 K, for DBN-based protic ionic liquids (●) and DBU-based protic ionic liquids (♦), as a function of the alkyl chain length of the acid, n. **Figure 5.32.** Obtained residuals, for DBN-based protic ionic liquids (●) and DBU-based protic ionic liquids (♦), as a function of the alkyl chain length of the acid, n.

At T = 298.15 K, the molar heat capacities of the DBN-based protic ionic liquids are around 80 J·K^{-1}·mol^{-1} lower than those of the DBU-based protic ionic liquids, which reflects the lower molar heat capacity contribution of the DBN base when compared to DBU. The higher heat capacity contribution of the DBU base is partially due to the higher number of atoms when compared to DBN. The value per -CH_2- increase in the

acid (for DBN-based PILs is 34.26 ± 0.36 $J{\cdot}K^{-1}{\cdot}mol^{-1}$ and for DBU-based is 33.64 ± 0.50 $J{\cdot}K^{-1}{\cdot}mol^{-1}$) is quite similar to AILs and alkanes (around 33 $J{\cdot}K^{-1}{\cdot}mol^{-1}$). [5.15] With the obtained results and the $C^0_{p,m}$ literature values for the carboxylic acids (C_p (298.15 K) propionic acid: 158.60 $J{\cdot}K^{-1}{\cdot}mol^{-1}$ [5.41]; C_p (298.15 K) butyric acid: 177.70 $J{\cdot}K^{-1}{\cdot}mol^{-1}$ [5.42]; C_p (298.15 K) pentanoic acid: 197.00 $J{\cdot}K^{-1}{\cdot}mol^{-1}$ [5.43]; C_p (298.15 K) hexanoic acid: 225.10 $J{\cdot}K^{-1}{\cdot}mol^{-1}$ [5.44]; C_p (298.15 K) heptanoic acid: 267.31 $J{\cdot}K^{-1}{\cdot}mol^{-1}$ [5.45]; C_p (298.15 K) octanoic acid: 297.92 $J{\cdot}K^{-1}{\cdot}mol^{-1}$ [5.46]), the excess molar heat capacities, $C^0_{p,m}$ (excess), were calculated and discussed. Figure 5.33 shows the calculated $C^0_{p,m}$ as a function of the size of the acid (region A for shorter acids and region B for longer acids). There is a trend shift for longer acids (region B), which is related not only with some structural change in the PIL at the supramolecular level, but also with the trend shift that also occurs in the heat capacity values of the carboxylic acids (figure 5.34). The $C^0_{p,m}$ (excess) for the mixtures with 1:1 proportion, was calculated as:

$$C^0_{p,m}\,(\text{excess}) = C^0_{p,m}\,(\text{PIL}) - (C^0_{p,m}\,(\text{Base}) + C^0_{p,m}\,(\text{Acid})) \qquad \textbf{(5.17)}$$

After n = 5, the $C^0_{p,m}$ (excess) seems to stabilize or, at least, decrease very slowly.

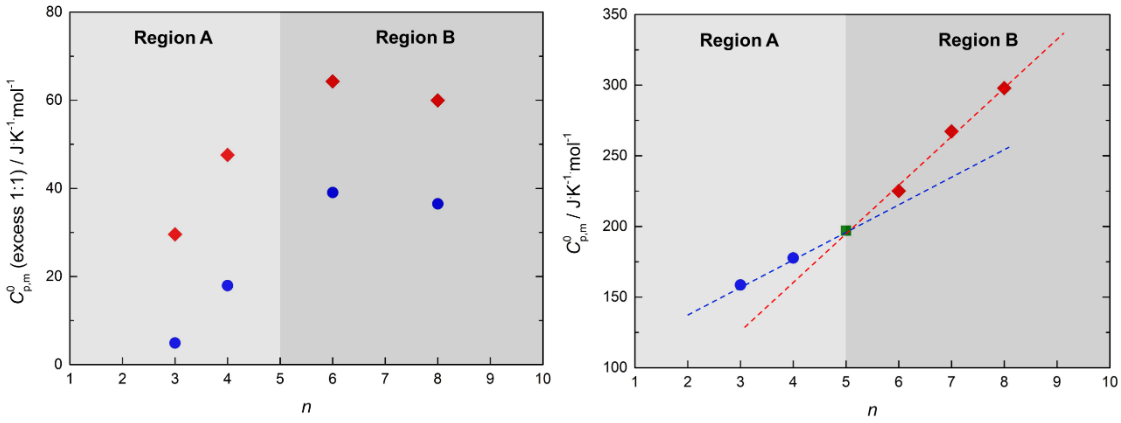

Figure 5.33. Excess molar heat capacities at T = 298.15 K, for the 1:1 PIL mixtures of DBN-based protic ionic liquids (●) and DBU-based protic ionic liquids (♦). **Figure 5.34.** Molar heat capacities at T = 298.15 K, for the shorter carboxylic acids (●), pentanoic acid (■) and longer carboxylic acids (♦).

5.3.3. Temperature dependency of heat capacities

After the measurement of the heat capacity values of PILs and respective superbases at T = 298.15 K, the temperature dependence of the heat capacities was studied. This sub-chapter presents the obtained results for the superbases and PILs at different temperatures, between 283 and 363 K, obtained using the μDSC apparatus. The method used was the step method, previously described in this chapter. Tables 5.22 to 5.31 present the experimental results obtained for the compounds studied, and figures 5.36 to 5.55 show the results and the deviation between the calculated and the experimental C_p (T).

In all measurements the same methodology was used. This method consists in the combination of three different measurements (in all steps, an empty reference cell is measured simultaneously):

i) A blank measurement with an empty sample cell (the obtained peak area is A_B);
ii) A measurement where the sample cell is filled with the reference material, in this case, sapphire (the obtained peak area A_{sapp}), with known heat capacity ($C_{p,sapp}$);
iii) And a final measurement where the sample cell is filled with the sample (the obtained peak area - A_s). For each studied compound, three concordant experiments were made.

A graphical representation of this methodology can be seen in figure 5.35:

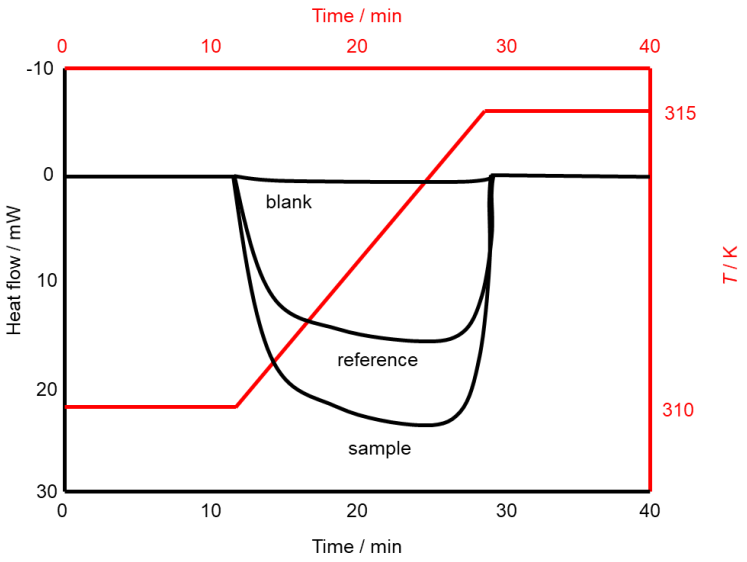

Figure 5.35. Graphical representation of the three-step method used in the measurements.

Table 5.22. Experimental results obtained by μDSC for DBN. The presented values of C_p (T) and ΔT are the average value of all three independent series of experiments made for this compound.

T/ K	C_p (T) / J·K^{-1}·mol^{-1}	ΔT
283.15	198.9	4.9942
288.15	203.0	4.9973
293.15	207.0	5.0010
298.15	**210.9**	**5.0011**
303.15	214.7	5.0011
308.15	218.5	5.0007
313.15	222.2	5.0007
318.15	225.9	4.9999
323.15	229.4	4.9997
328.15	232.9	4.9991
333.15	236.3	5.0019
338.15	239.3	4.9991
343.15	242.9	5.0004
348.15	246.2	5.0008
353.15	249.3	5.0061
358.15	252.4	5.0001
363.15	255.5	5.0009

,

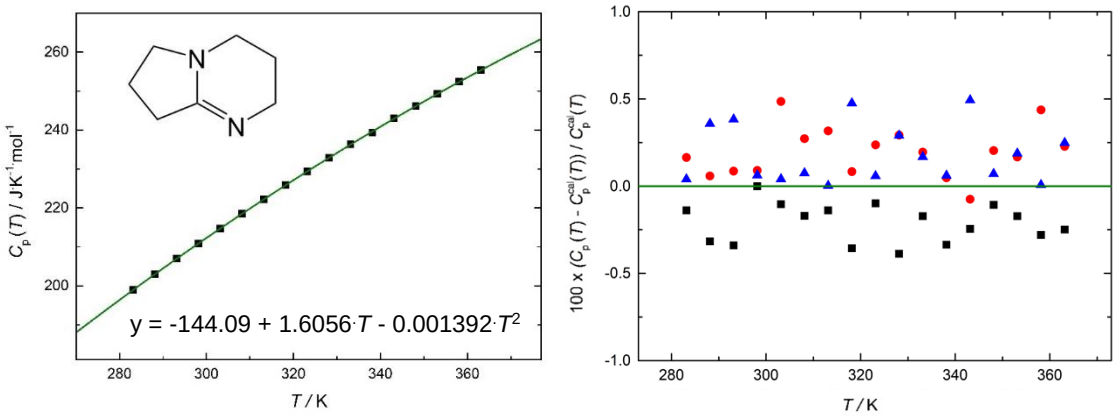

Figure 5.36. Experimental results obtained for DBN using μDSC. ─ (green line) values for C_p at different temperatures using the polynomial equation presented above. **Figure 5.37.** Deviation between the polynomial fitting of C_p (T) and the individual values obtained experimentally (three independent series of experiments) for DBN.

Table 5.23. Experimental results obtained by μDSC for DBU. The presented values of C_p (T) and ΔT are the average value of all three independent series of experiments made for this compound.

T/ K	C_p (T) / J·K^{-1}·mol^{-1}	ΔT
283.15	252.7	5.0014
288.15	256.5	5.0012
293.15	260.3	5.0012
298.15	**264.0**	**5.0012**
303.15	267.6	5.0015
308.15	271.1	5.0016
313.15	274.6	5.0017
318.15	277.9	5.0018
323.15	281.3	5.0019
328.15	284.4	5.0028
333.15	287.6	5.0027
338.15	290.6	5.0034
343.15	293.6	5.0038
348.15	296.5	5.0039
353.15	299.3	5.0041
358.15	302.0	5.0040
363.15	304.7	5.0049

,

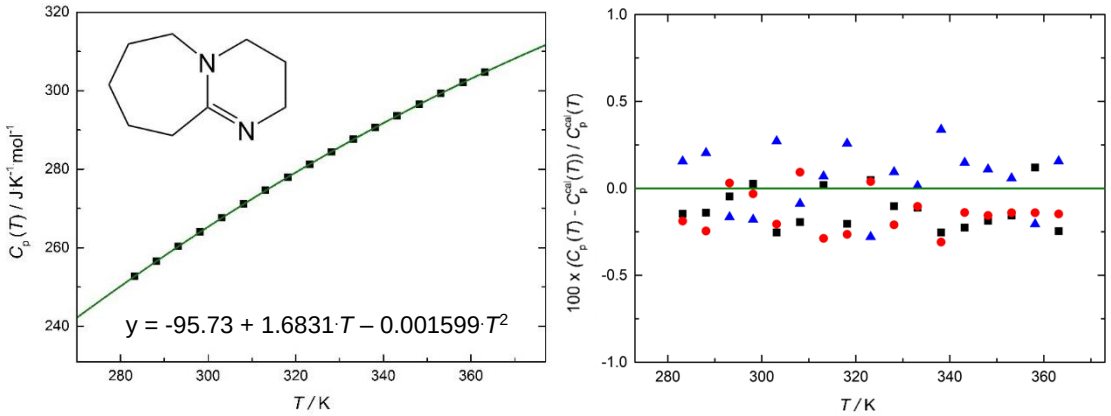

Figure 5.38. Experimental results obtained for DBU using μDSC. ━ (green line) values for C_p at different temperatures using the polynomial equation presented above. **Figure 5.39.** Deviation between the polynomial fitting of C_p (T) and the individual values obtained experimentally (three independent series of experiments) for DBU.

Table 5.24. Experimental results obtained by μDSC for [DBNH][EtCOO]. The presented values of C_p (T) and ΔT are the average value of all three independent series of experiments made for this compound.

T/ K	C_p (T) / J·K^{-1}·mol^{-1}	ΔT
283.15	354.9	5.0008
288.15	360.9	5.0009
293.15	366.9	4.9983
298.15	**372.7**	**5.0014**
303.15	378.4	5.0013
308.15	384.0	5.0019
313.15	389.6	5.0015
318.15	395.0	5.0013
323.15	400.4	5.0017
328.15	405.7	5.0020
333.15	411.0	5.0018
338.15	416.2	5.0023
343.15	421.4	5.0023
348.15	426.5	5.0024
353.15	431.6	5.0028
358.15	436.6	5.0029
363.15	441.6	5.0034

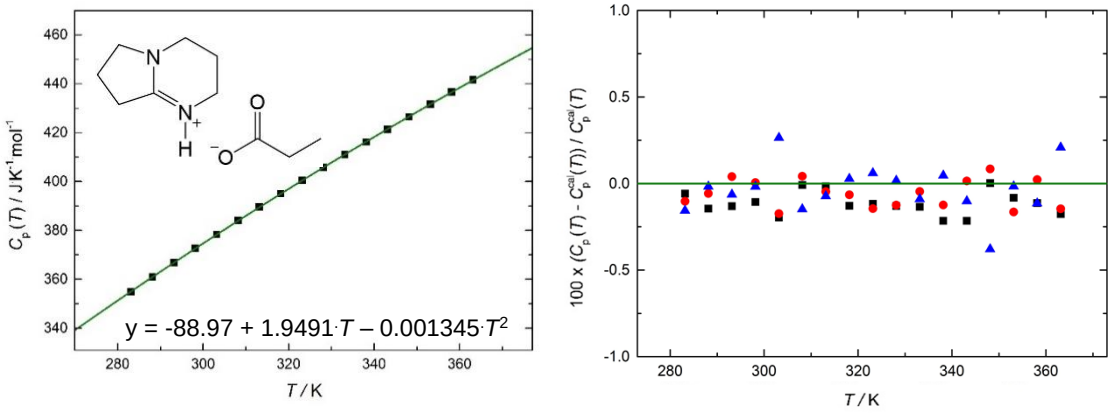

Figure 5.40. Experimental results obtained for [DBNH][EtCOO] using μDSC. ━ (green line) values for C_p at different temperatures using the polynomial equation presented above. **Figure 5.41.** Deviation between the polynomial fitting of C_p (T) and the individual values obtained experimentally (three independent series of experiments) for [DBNH][EtCOO].

Table 5.25. Experimental results obtained by μDSC for [DBNH][nPrCOO]. The presented values of C_p (T) and ΔT are the average value of all three independent series of experiments made for this compound.

T/ K	C_p (T) / J·K^{-1}·mol^{-1}	ΔT
283.15	390.8	4.9934
288.15	396.3	4.9985
293.15	401.7	5.0007
298.15	**407.0**	**5.0016**
303.15	412.3	5.0011
308.15	417.4	5.0011
313.15	422.5	5.0006
318.15	427.5	5.0005
323.15	432.5	5.0007
328.15	437.3	5.0000
333.15	442.1	5.0007
338.15	446.9	5.0008
343.15	451.6	5.0010
348.15	456.2	5.0010
353.15	460.8	5.0003
358.15	465.4	5.0008
363.15	470.0	5.0003

,.

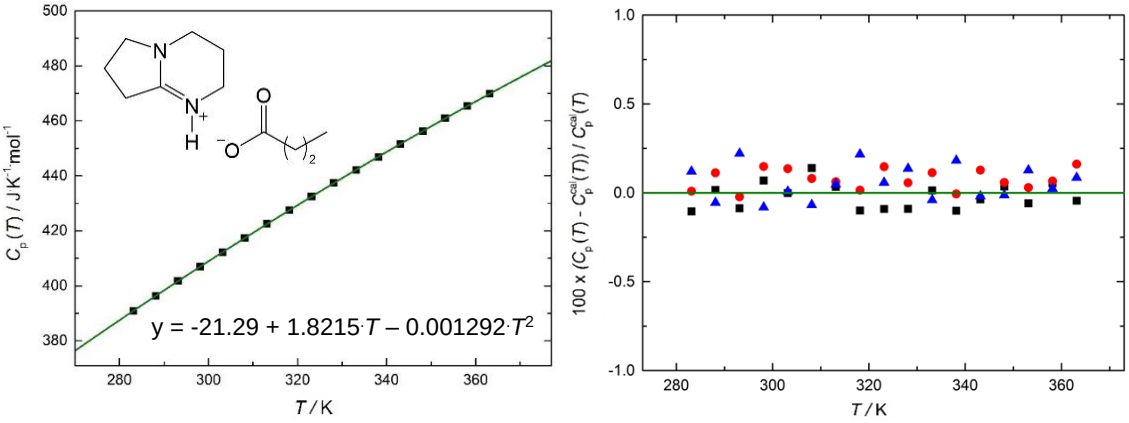

Figure 5.42. Experimental results obtained for [DBNH][nPrCOO] using μDSC. ━ (green line) values for C_p at different temperatures using the polynomial equation presented above. **Figure 5.43.** Deviation between the polynomial fitting of C_p (T) and the individual values obtained experimentally (three independent series of experiments) for [DBNH][nPrCOO].

Table 5.26. Experimental results obtained by μDSC for [DBNH][nPentCOO]. The presented values of C_p (T) and ΔT are the average value of all three independent series of experiments made for this compound.

T/ K	C_p (T) / J·K^{-1}·mol^{-1}	ΔT
283.15	459.5	5.0015
288.15	464.5	5.0012
293.15	469.4	5.0012
298.15	**474.3**	**5.0010**
303.15	479.0	5.0012
308.15	483.6	5.0010
313.15	488.2	5.0013
318.15	492.7	5.0011
323.15	497.2	5.0016
328.15	501.5	5.0017
333.15	505.8	5.0022
338.15	510.0	5.0022
343.15	514.1	5.0026
348.15	518.2	5.0029
353.15	522.1	5.0036
358.15	526.0	5.0033
363.15	529.9	5.0047

,

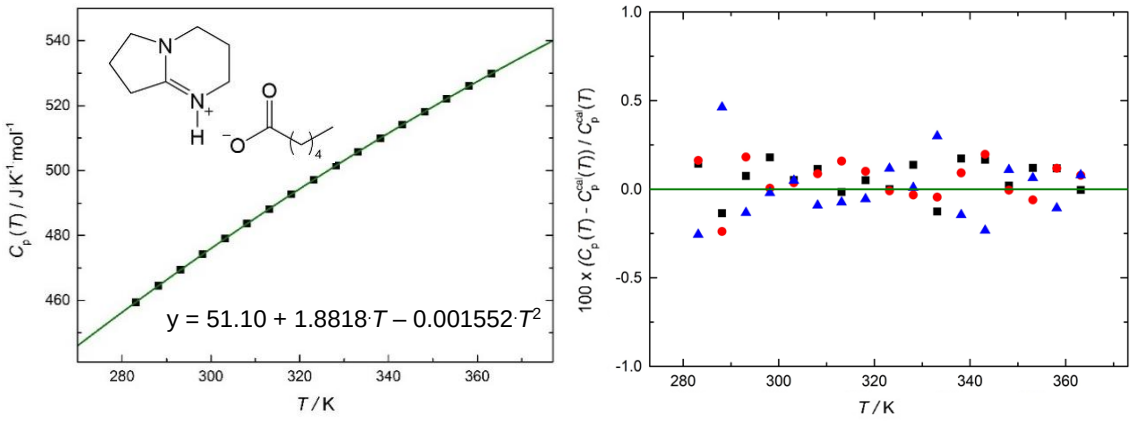

Figure 5.44. Experimental results obtained for [DBNH][nPentCOO] using μDSC. ━ (green line) values for C_p at different temperatures using the polynomial equation presented above. **Figure 5.45.** Deviation between the polynomial fitting of C_p (T) and the individual values obtained experimentally (three independent series of experiments) for [DBNH][nPentCOO].

Table 5.27. Experimental results obtained by μDSC for [DBNH][nHeptCOO]. The presented values of C_p (T) and ΔT are the average value of all three independent series of experiments made for this compound.

T/ K	C_p (T) / J·K^{-1}·mol^{-1}	ΔT
283.15	529.0	5.0048
288.15	533.8	5.0022
293.15	538.6	5.0032
298.15	**543.2**	**5.0005**
303.15	547.7	5.0014
308.15	552.2	5.0023
313.15	556.5	5.0009
318.15	560.8	5.0013
323.15	564.9	5.0014
328.15	569.0	5.0012
333.15	573.0	5.0015
338.15	576.9	5.0016
343.15	580.8	5.0045
348.15	584.6	5.0008
353.15	588.4	5.0012
358.15	592.0	5.0013
363.15	595.6	5.0012

,

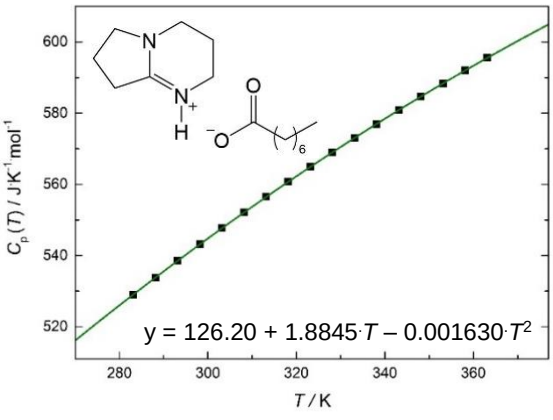

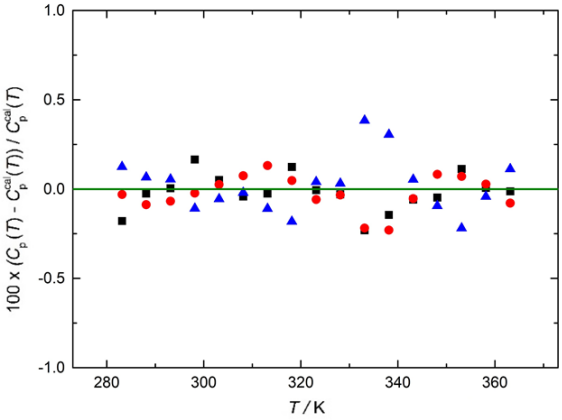

Figure 5.46. Experimental results obtained for [DBNH][nHeptCOO] using μDSC. ━ (green line) values for C_p at different temperatures using the polynomial equation presented above. **Figure 5.47.** Deviation between the polynomial fitting of C_p (T) and the individual values obtained experimentally (three independent series of experiments) for [DBNH][nHeptCOO].

Table 5.28. Experimental results obtained by μDSC for [DBUH][EtCOO]. The presented values of C_p (T) and ΔT are the average value of all three independent series of experiments made for this compound.

T/ K	C_p (T) / J·K^{-1}·mol^{-1}	ΔT
283.15	437.1	4.9879
288.15	442.1	4.9950
293.15	447.1	4.9999
298.15	**451.9**	**5.0012**
303.15	456.6	5.0005
308.15	461.2	5.0004
313.15	465.8	5.0008
318.15	470.2	5.0008
323.15	474.6	5.0006
328.15	478.9	5.0010
333.15	483.2	5.0010
338.15	487.4	5.0005
343.15	491.6	5.0007
348.15	495.7	5.0007
353.15	499.7	5.0012
358.15	503.8	5.0009
363.15	507.8	5.0009

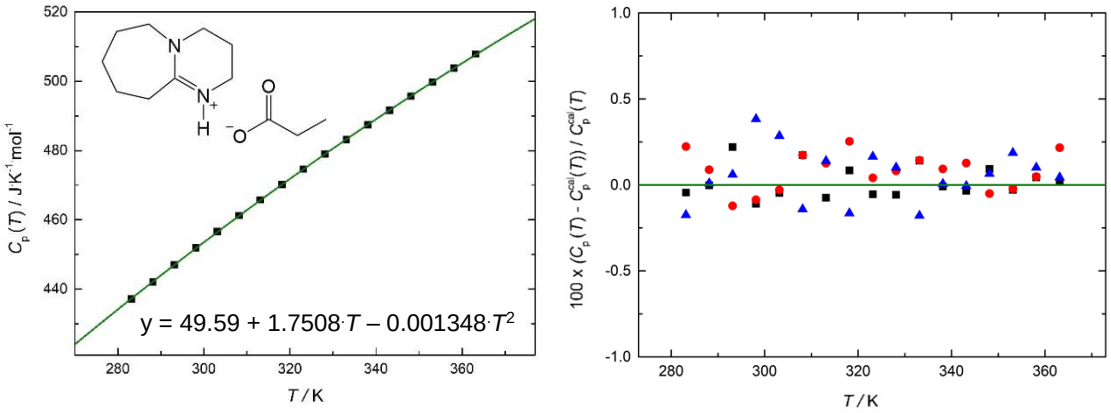

Figure 5.48. Experimental results obtained for [DBUH][EtCOO] using μDSC. ━ (green line) values for C_p at different temperatures using the polynomial equation presented above. **Figure 5.49.** Deviation between the polynomial fitting of C_p (T) and the individual values obtained experimentally (three independent series of experiments) for [DBUH][EtCOO].

Table 5.29. Experimental results obtained by μDSC for [DBUH][nPrCOO]. The presented values of C_p (T) and ΔT are the average value of all three independent series of experiments made for this compound.

T/ K	C_p (T) / J·K^{-1}·mol^{-1}	ΔT
283.15	474.3	4.9883
288.15	478.8	4.9952
293.15	483.2	4.9998
298.15	**487.5**	**5.0007**
303.15	491.7	5.0009
308.15	495.9	5.0006
313.15	500.0	5.0009
318.15	504.0	5.0006
323.15	507.9	5.0009
328.15	511.8	5.0007
333.15	515.6	5.0010
338.15	519.4	5.0012
343.15	523.1	5.0008
348.15	526.7	5.0007
353.15	530.3	5.0006
358.15	533.9	5.0003
363.15	537.4	5.0009

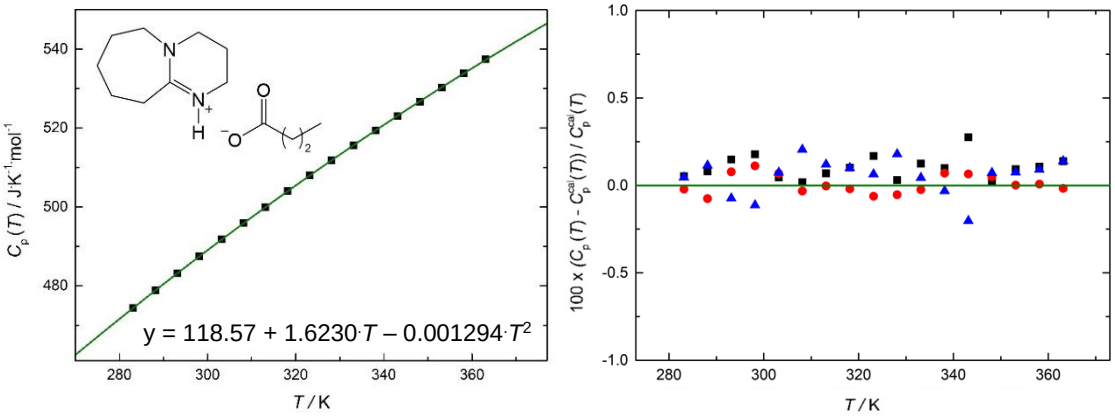

Figure 5.50. Experimental results obtained for [DBUH][nPrCOO] using μDSC. ━ (green line) values for C_p at different temperatures using the polynomial equation presented above. **Figure 5.51.** Deviation between the polynomial fitting of C_p (T) and the individual values obtained experimentally (three independent series of experiments) for [DBUH][nPrCOO].

Table 5.30. Experimental results obtained by μDSC for [DBUH][nPentCOO]. The presented values of C_p (T) and ΔT are the average value of all three independent series of experiments made for this compound.

T/ K	C_p (T) / J·K^{-1}·mol^{-1}	ΔT
283.15	540.7	4.9955
288.15	545.2	4.9983
293.15	549.6	5.0014
298.15	**554.0**	**5.0017**
303.15	558.2	5.0011
308.15	562.3	5.0009
313.15	566.3	5.0009
318.15	570.3	5.0011
323.15	574.2	5.0008
328.15	577.9	5.0011
333.15	581.6	5.0009
338.15	585.3	5.0010
343.15	588.9	4.9972
348.15	592.4	5.0012
353.15	595.8	5.0009
358.15	599.2	5.0001
363.15	602.5	5.0044

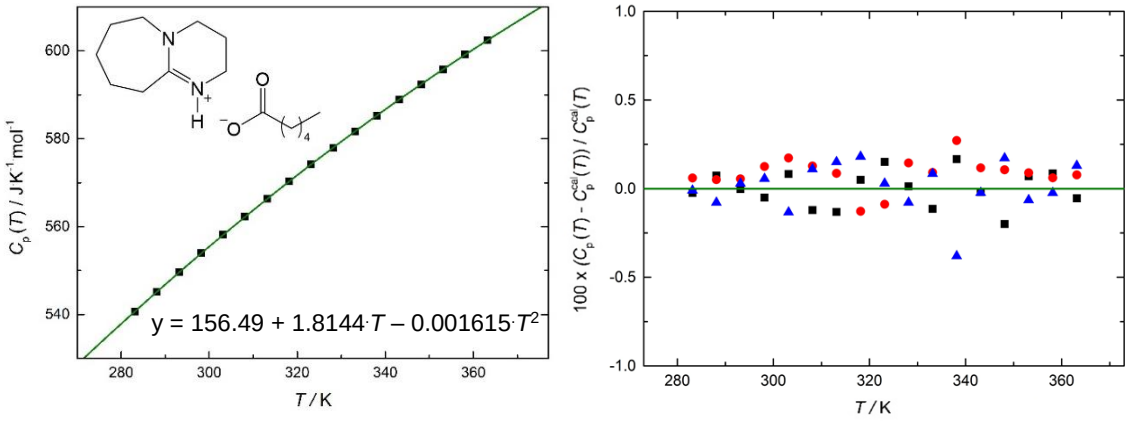

Figure 5.52. Experimental results obtained for [DBUH][nPentCOO] using μDSC. — (green line) values for C_p at different temperatures using the polynomial equation presented above. **Figure 5.53.** Deviation between the polynomial fitting of C_p (T) and the individual values obtained experimentally (three independent series of experiments) for [DBUH][nPentCOO].

Table 5.31. Experimental results obtained by μDSC for [DBUH][nHeptCOO]. The presented values of C_p (T) and ΔT are the average value of all three independent series of experiments made for this compound.

T/ K	C_p (T) / J·K^{-1}·mol^{-1}	ΔT
283.15	607.5	4.9870
288.15	611.3	4.9946
293.15	615.1	4.9998
298.15	**618.8**	**5.0014**
303.15	622.3	5.0010
308.15	625.7	5.0012
313.15	629.0	5.0008
318.15	632.4	5.0009
323.15	635.5	5.0008
328.15	638.5	5.0011
333.15	641.5	5.0008
338.15	644.5	5.0013
343.15	647.4	5.0011
348.15	650.2	5.0011
353.15	652.9	5.0020
358.15	655.6	5.0009
363.15	658.2	4.9906

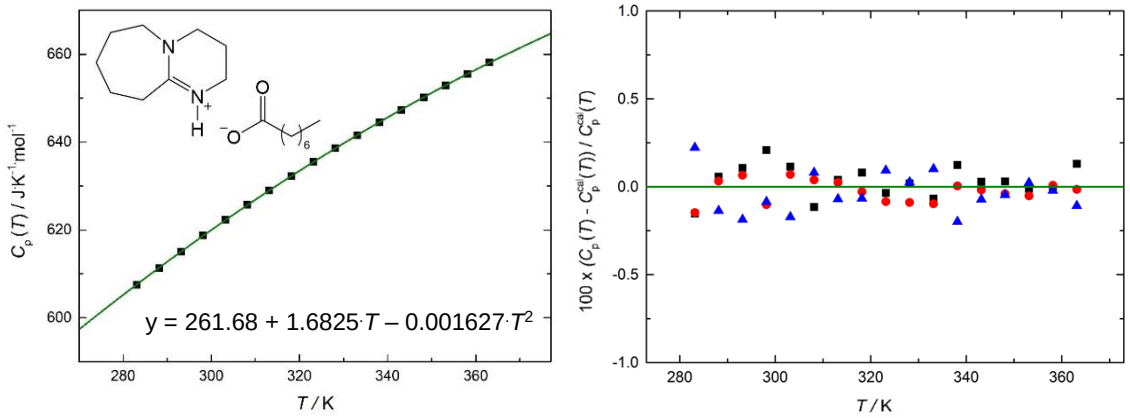

Figure 5.54. Experimental results obtained for [DBUH][nHeptCOO] using μDSC. — (green line) values for C_p at different temperatures using the polynomial equation presented above. **Figure 5.55.** Deviation between the polynomial fitting of C_p (T) and the individual values obtained experimentally (three independent series of experiments) for [DBUH][nHeptCOO].

Table 5.32. Experimental results obtained with the two methods for each compound, at T = 298.15 K.

Compound	M / g·mol^{-1}	Drop	μDSC	S_r / %
		C_p (298.15 K)	C_p (298.15 K)	
DBN	124.18	210.75 ± 0.21	210.9 ± 2.1	0.07
DBU	152.24	264.11 ± 0.23	264.0 ± 2.6	-0.04
[DBNH][EtCOO]	198.26	374.26 ± 0.25	372.7 ± 3.7	-0.42
[DBNH][nPrCOO]	212.29	406.39 ± 0.29	407.0 ± 4.1	0.15
[DBNH][nPentCOO]	240.34	474.91 ± 0.35	474.3 ± 4.7	-0.13
[DBNH][nHeptCOO]	268.40	545.17 ± 0.34	543.2 ± 5.4	-0.36
[DBUH][EtCOO]	226.32	452.27 ± 0.31	451.9 ± 4.5	-0.08
[DBUH][nPrCOO]	240.34	489.38 ± 0.34	487.5 ± 4.9	-0.38
[DBUH][nPentCOO]	268.40	553.49 ± 0.35	554.0 ± 5.5	0.09
[DBUH][nHeptCOO]	296.44	621.98 ± 0.55	618.8 ± 6.2	-0.51

S_r = 100·((C$_p$ μDSC - C$_p$ Drop) / C$_p$ μDSC. For all compounds, the presented value is the average value of all experiments. Heat capacity values at J·K^{-1}·mol^{-1}.

Table 5.32 presents the experimental results, at T = 298.15 K, obtained with the two methods, drop calorimetry and micro-differential scanning calorimetry. As can be seen with the values of ΔC_p between both methods, the results are in excellent agreement. The experimental heat capacities of the condensed phases obtained in this work are presented in figures 5.56 and 5.57. The heat capacity values for both PILs families are quite similar in slope, which was expected since both superbases are quite similar.

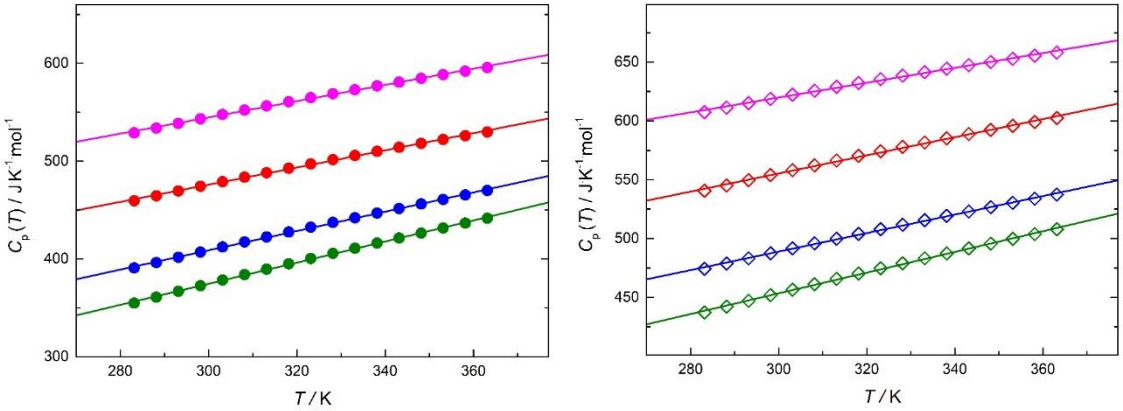

Figure 5.56. Experimental results obtained by μDSC for all DBN-based protic ionic liquids. ● – [DBNH][EtCOO]; ● – [DBNH][nPrCOO]; ● – [DBNH][nPentCOO]; ● – [DBNH][nHeptCOO]. **Figure 5.57.** Experimental results obtained by μDSC for all DBU-based protic ionic liquids. ◊ – [DBUH][EtCOO]; ◊ – [DBUH][nPrCOO]; ◊ – [DBUH][nPentCOO]; ◊ – [DBUH][nHeptCOO].

In the experimental temperature range the experimental results could be well described by a polynomial temperature-dependence (applied for each individual IL) as follows:

$$C_p(T)\ /\mathrm{J\cdot K^{-1}\cdot mol^{-1}} = a + b\cdot T + c\cdot T^2 \qquad \textbf{(5.14)}$$

The fitted coefficients, *a*, *b* and *c* of equation 5.14 are listed in table 5.33.

Table 5.33. Fitted polynomial parameters, *a*, *b* and *c* of equation 5.13 for the compounds studied.

Compound	T_{range} / K	a / J·K^{-1}·mol^{-1}	b / J·K^{-2}·mol^{-1}	c / J·K^{-3}·mol^{-1}	S_r / %
DBN	283-363	-144.09	1.6056	-0.001392	0.37
DBU	283-363	-95.73	1.6831	-0.001599	0.06
[DBNH][EtCOO]	283-363	-88.97	1.9491	-0.001345	1.51
[DBNH][nPrCOO]	283-363	-21.29	1.8215	-0.001292	0.21
[DBNH][nPentCOO]	283-363	51.10	1.8818	-0.001552	1.07
[DBNH][nHeptCOO]	283-363	126.20	1.8845	-0.001630	0.58
[DBUH][EtCOO]	283-363	49.59	1.7508	-0.001348	1.21
[DBUH][nPrCOO]	283-363	118.57	1.6230	-0.001294	0.13
[DBUH][nPentCOO]	283-363	156.49	1.8144	-0.001615	0.29
[DBUH][nHeptCOO]	283-363	261.68	1.6825	-0.001627	0.47

$S_r = 100 \times \left\{ \sum_{i=1}^{n} \frac{\left[\left(C_p - C_p^{calc} \right) / C_p^{calc} \right]_i^2}{n-m} \right\}^{\frac{1}{2}}$, where *n* is the number of fitted data points, and *m* is the number of independently adjustable parameters. Standard pressure ($p^0 = 10^5$ Pa). Standard uncertainties, *u*, are $u(T) = 0.02$ K, at the 0.95 confidence level ($k \approx 2$).

Due to the short temperature range (283-363 K) it was observed a linear dependence of the heat capacities with *T* and *n.* In this way, the equations 5.15 and 5.16 were derived for the [DBN][C_nOOH] and [DBUH][C_nOOH] PIL series, where, "*n"* is the total number of carbons in the carboxylic acid. Using a simple and linear functional in the form of: k + l*n* + m*T,* the molar heat capacity of the PILs studied can be described quite well (errors lower than 1%).

For DBN-based PILs:

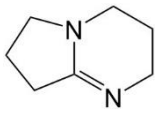

$$C_p(n,T)\ /\mathrm{J{\cdot}K^{-1}{\cdot}mol^{-1}} = -4.5504 + 32.84{\cdot}n + 0.9438{\cdot}T \qquad \textbf{(5.15)}$$

And for DBU-based PILs:

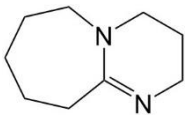

$$C_p(n,T)\ /\mathrm{J{\cdot}K^{-1}{\cdot}mol^{-1}} = 130.3355 + 32.19{\cdot}n + 0.7669{\cdot}T \qquad \textbf{(5.16)}$$

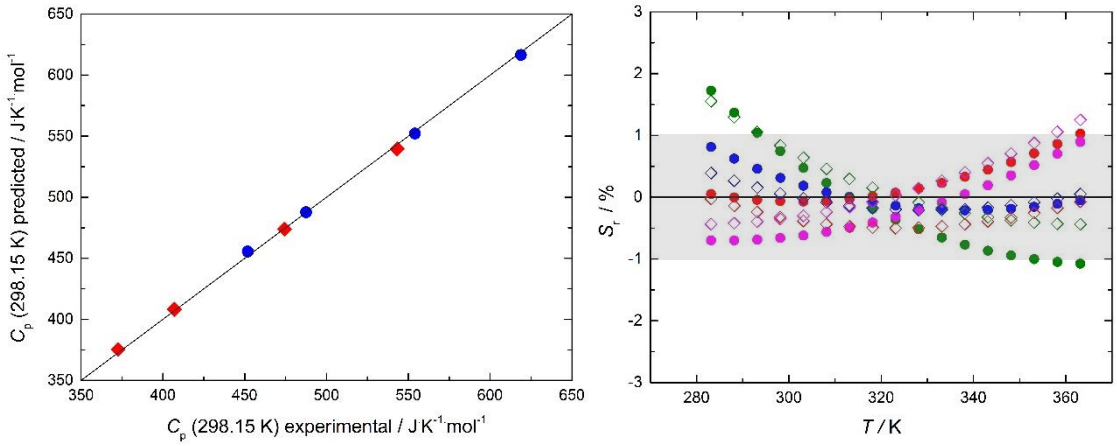

Figure 5.58. Predicted molar heat capacities at T = 298.15 K versus the experimental results obtained using the μDSC, for the 1:1 PIL mixtures of DBN-based protic ionic liquids (●) and DBU-based protic ionic liquids (♦). **Figure 5.59.** Deviation of the predicted results all protic ionic liquids. ● – [DBNH][EtCOO]; ● – [DBNH][nPrCOO]; ● – [DBNH][nPentCOO]; ● – [DBNH][nHeptCOO]. ◊ – [DBUH][EtCOO]; ◊ – [DBUH][nPrCOO]; ◊ – [DBUH][nPentCOO]; ◊ – [DBUH][nHeptCOO].

Figures 5.58 and 5.59 present the relation between the predicted heat capacities (using equations 5.15 and 5.16) and the obtained experimentally using the μDSC and the respective deviation in %. With these equations the heat capacity values of other PILs studied in this work were estimated: C_p (298.15 K) [DBNH][nButCOO]: 441.04 J·K^{-1}·mol^{-1}; C_p (298.15 K) [DBNH][nHexCOO]: 506.72 J·K^{-1}·mol^{-1}; C_p (298.15 K) [DBUH][nButCOO]: 519.94 J·K^{-1}·mol^{-1}; C_p (298.15 K) [DBUH][nHexCOO]: 584.32 J·K^{-1}·mol^{-1}.

5.4. References

[5.1] Haines, P. J. (Ed.), *Principles of Thermal Analysis and Calorimetry*, RSC Paperbacks, Royal Society of Chemistry, Cambridge **2002**.

[5.2] Stull, D. R.; Westrum, E. F. Jr.; Sinke, G. C., *The Chemical Thermodynamics of Organic Compounds*, John Wiley & Sons, Inc., New York **1969**.

[5.3] Martinho Simões, J. A.; Minas da Piedade, M. E., chapter 12, in: *Molecular Energetics: Condensed-Phase Thermochemical Techniques*, University Press, Oxford **2008**.

[5.4] Höhne, G.; Hemminger, W.; Flammersheim, H. J., *Differential Scanning Calorimetry: An Introduction for Practitioners*, Springer-Verlag, Berlin *1996*.

[5.5] Papon, P.; J. Leblond; P.E. Meijer, *Phase Transitions in Liquids and Solids: Solidi.cation and Melting*, in *The Physics of Phase Transitions* **2006**, Springer Berlin Heidelberg.

[5.6] Wellen, R. M. R.; Rabello, M. S., *J. Mat. Science*, **2005**. 40(23), 6099-6104.

[5.7] MacFarlane, D. R., et al., *Journal of Physics: Condensed Matter* **2001**, 13(36) 8257.

[5.8] Kalogeras, I. M.; Lobland, H. E. H., *Journal of Materials Education* **2012**, 34 69 - 94.

[5.9] Castner, J.E.W. and J.F. Wishart, *J. Chem. Phys*. **2010**, 132 (12), 120901-9.

[5.10] Yu, X., et al., *Chem. Phys.* **2007**, 332(1), 115-118.

[5.11] Lazzús, J.A., *Thermochim. Acta* **2012**, 528 (0), 38-44.

[5.12] Haida, O.; Suga, H.; Seki S., *J. Chem Thermod*. **1977**, 9 (12) 1133-1148.

[5.13] Dierking, I., *Chem. Phys. Chem*. **2003**, 4 (4), 401-402.

[5.14] Dean, P. M., Pringle, J. M.; MacFarlane, D. R., *Phys. Chem. Chem. Phys.* **2010**, 12 (32) 9144-9153.

[5.15] Rocha, M. A. A., *Thermodynamic Properties of Ionic Liquids*, *PhD Thesis* **2013**, Porto, Portugal.

[5.16] Wilhelm, E.; Letcher, T. M. Eds., *Heat Capacities: Liquids, Solutions and Vapours*, The Royal Society of Chemistry, Cambridge, UK, **2010**.

[5.17] Zábranský, M.; Růžička Jr., V.; Domalski, E. S. *J. Phys. Chem. Ref. Data* **2001**, 30, 1199–1689.

[5.18] Zábranský, M.; Kolská, Z.; Růžička Jr., V.; Domalski, E. S. *J. Phys. Chem. Ref. Data* **2010**, 39, 013103.

[5.19] Kasper, M. *Anal. Bioanal. Chem.* **2004**, 380, 366–367.

[5.20] González-Salgado, D.; Valencia, J. L.; Troncoso, J.; Carballo, E.; Peleteiro, J.; Romaní, L.; Bessières, D. *Rev. Sci. Instrum.* **2007**, 78, 055103.

[5.21] Hansen, L. D.; Hart, R. M. *Thermochim. Acta* **2004**, 417, 257–273.

[5.22] Suurkuusk, J.; Wadsö, I. *J. Chem. Thermodyn.* **1974**, 6, 667–679.

[5.23] Konicek, J.; Suurkuusk, J.; Wadsö, I. *J. Chem. Scr.* **1971**, 1, 217–220.

[5.24] Santos, L. M. N. B. F.; Schröder, B.; Fernandes, O. O. P.; Ribeiro da Silva, M. A. V. *Thermochim. Acta* **2004**, 415, 15–20.

[5.25] Bernardes, C. E. S.; Santos, L. M. N. B. F.; Piedade, M. E. M. *Meas. Sci. Technol.* **2006**, 17, 1405–1408.

[5.26] Bastos, M.; Volkova, N. N.; Wadso, I. *J. Chem. Soc., Faraday Trans.* **1993**, 189, 1351–1352.

[5.27] Ng, K.; Rosenberg, A.; Bastos, M.; Wadsö, I. *Thermochim. Acta* **1990**,169, 339–346.

[5.28] Wadsö, I. *Thermochim. Acta* **1995**, 267, 45–59.

[5.29] Pyris User Manual (http://mdi.as.nyu.edu/docs/CP/4738/DSC.Manual.pdf)

[5.30] Carvalho, A. P. S. M. C.; Amaral, L. M. P. F., *private communication* **2015**.

[5.31] Gatta, G. D.; Richardson, M. J.; Sarge, S. M.; Stølen, S., *Pure Appl. Chem.* **2006**, 78, 1455-1476.

[5.32] Sabbah, R.; Xu-Wu, A.; Chickos, J. S.; Planas Leitão, M. L.; Roux, M. V.; Torres, L. A., *Thermochim. Acta* **1999**, 331, 93-204.

[5.33] Santos, L. M. N. B. F.; Rocha, M. A. A.; Rodrigues, A. S. M. C.; Štejfa, V.; Fulem, M.; Bastos, M., *J. Chem. Thermodyn.* **2011**, 43 (12), 1818–1823.

[5.34] Bernardes, C. E. S.; Santos, L. M. N. B. F.; Piedade, M. E. M. da., *Meas. Sci. Technol.* **2006**, *17* (6), 1405–1408.

[5.35] Agilent VEE Pro; Agilent Technologies, Inc.: Santa Clara, CA.

[5.36] Sabbah R., C.; Xu-wu, A.; Chickos, J. S.; Leitão, M. L. P.; Roux, M. V; Torres, L. A., *Thermochim. Acta* **1999**, 331 (2), 93–204.

[5.37] Marsh, K. N.; Brennecke, J. F.; Chirico, R. D.; Frenkel, M.; Heintz, A.; Magee, J. W.; Peters, C. J.; Rebelo, L. P. N.; Seddon, K. R., *Pure Appl. Chem.* **2009**, 81 (5), 781–790.

[5.38] Fulem, M., et al*., J. Chem. Eng. Data* **2008**, 53 (9), 2175-2181.

[5.39] Serra, P., "*Thermal Behavior and Heat capacity of Ionic Liquids: Benziliimidazolium and alklimidazolium derivatives*", *MSc* thesis, **2013**, Porto.

[5.40] Serra, P. B. P.; Ribeiro, F. M. S.; Rocha, M. A. A.; Fulem, M.; Růžička, K.; Coutinho, J. A. P.; Santos, L. M. N. B. F., *J. Mol.Liq*. **2017**, 248, 678-687.

[5.41] Biros, J.; Sikora, A.; Zivny, A.; Pouchly, J., *Collect Czech. Chem. Commun*. **1982**, 47 (10), 2692-2701.

[5.42] Martin, J. F.; Andon, R. J. L., *J. Chem. Thermodynam*., **1982**, 14, 679-688.

[5.43] Konicek, J.; Wadso, I., *Acta Chem. Scand.*, **1971**, 25, 1541-1551.

[5.44] von Reis, M.A., *Ann. Physik*, **1881**, 13, 447-464.

[5.45] Labban, A. L.; Westrum, E. F.; *Can. J. Chem.*, **1991**, 69, 1796-1803.

[5.46] Schaake, R. C. F.; van Miltenburg, J. C.; De Kruif, C. G., *J. Chem. Thermodynam.,* **1982**, 14, 771-778.

CHAPTER 6

Speciation of Protic Ionic Liquids

6. Speciation of Protic Ionic Liquids

After the phase behavior study and the heat capacity measurements at T = 298.15K and several temperatures, the speciation topic in PILs is presented in this chapter. Considering the vapor pressures measurements at a specific temperature and how it varies with time for the same sample, this effect was studied in detail and for the first time, the equilibrium proportion of acid and base was determined and correlated with acid and base strength.

6.1. Fundamentals

As told in previously, protic ionic liquids (PILs) are ionic liquids (ILs) that can be prepared by mixing relatively strong Brönsted acids and bases in stoichiometric proportions. [6.1-6.3] However, while the typical aprotic ILs are virtually composed solely of ions, PILs may also contain significant quantities of neutral species due to an incomplete acid-base reaction. [6.1-6.3] For this reason, PILs are often categorized as “poor ionic liquids” and their properties can deviate significantly from those of aprotic ILs. [6.1-6.4] It was found that the extent of proton transfer in PILs correlates well with the ΔpK_a between acid and base, with larger differences yielding larger proportions of ions in the liquid phase. [6.3-6.4] However, this approach has the limitation of predicting the extent of the reaction based on the information of pK_a in different media, like in water or acetonitrile. [6.1-6.3] A correct evaluation of acid and base strength should be done in the PIL medium, where the proton transfer equilibrium is established. In PILs the existence of neutral molecular species reduces ionicity (fraction of ions in the liquid that can effectively conduct electricity) and consequently the ionic conductivity. [6.2, 6.5-6.7] The extent of the acid-base equilibrium in PILs adds complexity to the system regarding their properties and speciation, i.e. the molar fraction of all species (molecules, ions and ion pairs) in equilibrium at a given set of conditions.

As already seen in Chapter 2, due to their peculiar properties, PILs have found a vast display of applications, such as in: cellulose extraction, CO_2 absorption, organic and inorganic synthesis (as solvents, reactants and catalysts), lubrification, biochemistry, electrochemistry, among others. [6.1, 6.2, 6.8-6.10] Throughout this chapter, the PILs, composed of conjugate acid BH^+ and conjugate base A^-, are generally denoted as [BH][A] It was found that the acid/base equilibrium composition of PILs can deviate significantly from the 50:50 molar ratio. Some authors have already reported that the

drying of PILs can lead to nonstoichiometric mixtures enriched in the less volatile component. [6.2] Burrel et al. have reported the formation of PIL biphasic mixtures consisting of an acid-rich phase and another of unreacted neutral base. [6.11] For the PIL of acetic acid with *N*-methylpyrrolidine, another work has shown higher ionicity for the 3:1 acid/base molar ratio than for the 1:1 mixture. [6.12] Canongia Lopes and Rebelo have addressed the question of azeotropy in PILs, anticipating that the azeotropic composition of “weak” PILs (with high proportion of neutral species), will shift considerably from the stoichiometric 50:50. [6.4] However, to the best of my knowledge, a systematic experimental approach tackling azeotrope formation in PILs is still lacking.

The vapor pressures of the studied protic ionic liquids were measured as a function of time using a Knudsen effusion apparatus combined with a quartz crystal microbalance, KEQCM. Based on the results, the speciation phenomenon in protic ionic liquids was studied in detail and the results are presented and discussed in this chapter. The installation used is a combination of the Knudsen effusion technique and an in-vacuum quartz crystal microbalance for real-time mass loss detection, already described in detail in the literature. [6.13-6.14] In a typical KEQCM experiment, the measurement of the equilibrium vapor pressure at a given temperature, *T,* is achieved by the vapor effusion through the orifice of an effusion cell and condensation of a fraction of the vapor on the surface of the cooled quartz crystal microbalance, placed above the effusion cell, as depicted in figure 6.1. This apparatus comprises two mass loss detection techniques, gravimetric and quartz crystal microbalance: the weighed mass of the effusion cell before and after the respective experiment, and the change of the crystal's resonant frequency as the vapor condenses on its surface. The combination of these two mass loss detection techniques presents several advantages, e.g. short effusion times; small sample sizes; real-time monitoring of the effusion experiment.

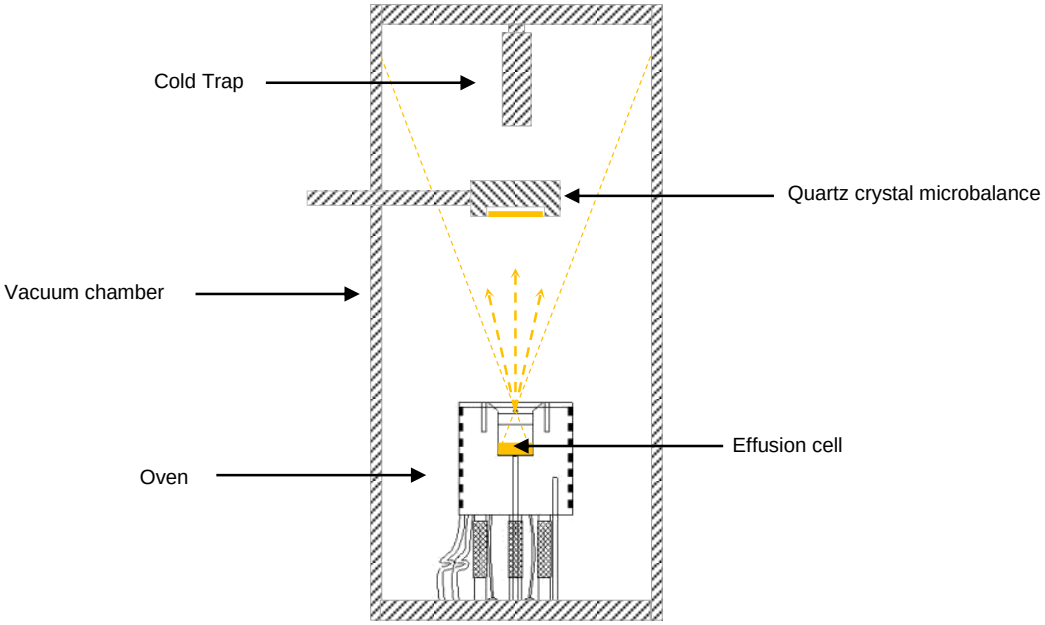

Figure 6.1. Schematic representation of the mass flow of vapor in a typical KEQCM experiment. [adapted from source [6.14])

6.1.1. Knudsen effusion method

Martin Knudsen published in 1909 the development of a vapor pressure measurement method based on the experimental observation of some effects of the *Kinetic Theory of Gases* on the analysis of the gas behavior at low pressures. [6.15, 6.19-6.21] This was the first study designed to test the consequences of this theory, where two cylindrical tubes and low pressures were used, in order to consider a molecular flow, in which the molecules of the gas can move freely, without mutual interference. Under these conditions, Knudsen concluded that the direction in which a molecule rebounds from a solid wall is independent of the direction in which it approaches the wall and is ruled by the Lambert's cosine law. [6.15, 6.19-6.21] Nowadays, Knudsen effusion is one of the most widely used methods for measuring vapor pressures. This method is based on the measurements of the effusion rate, ν_{eff}, of the vapor inside the effusion cell, in thermal equilibrium, through a small orifice of well-known area, A_o, into a vacuum. [6.15, 6.19-6.22]

According to the *Kinetic Theory of Gases*, and considering the collision frequency of the gaseous molecules with the wall, Z_{wall}, with an orifice of known area, A_o, the effusion rate of the vapor inside the effusion cell can be calculated using the equation 6.1:

$$v_{eff} = \frac{dN}{dt} = w_o \cdot Z_{wall} \cdot A_o = w_o \cdot \frac{p \cdot N_A}{\sqrt{(2 \cdot \pi \cdot R \cdot T \cdot M)}} \cdot A_o \qquad \textbf{(6.1)}$$

Where, (dN / dt) is the number of molecules, N, effusing from the cell in a time interval, dt, w_o represents the transmission probability factor, and p is the pressure inside the effusion cell. Considering that (N / N_A) = n and (m / M) = n, and solving for p, the equation 6.1 becomes the Knudsen equation:

$$p = \frac{\Delta m}{w_o \cdot A_o \cdot \Delta t} \cdot \sqrt{\frac{2 \cdot \pi \cdot R \cdot T}{M}} \qquad \textbf{(6.2)}$$

Since the effusing orifice has a finite thickness, l, there is the possibility of a small fraction of the effusing molecules to hit the orifice walls, after in which they can continue their way out of the cell or go back inside the cell. It is important to evaluate the fraction of gaseous molecules that effuse through the cell orifice, so, in this work the w_o value was calculated using the Dushman equation [6.15]:

$$w_o = \left\{ 1 + \left(\frac{3 \cdot l}{8 \cdot r} \right) \right\}^{-1} \qquad \textbf{(6.3)}$$

Where r is the orifice radius.

The characteristics of the effusion orifices used in the effusion cell of the KEQCM installation are listed in table 6.1.

Table 6.1. Areas and transmission probability factors of the effusion orifices.

Effusion cell	***l* / *r***	***r* / mm**	**A_o / mm^2**	**w_o**
KEQCM	0.0208	0.5996	1.1310	0.9897

Effusion Cell and Evaluation of the Orifice Area and Roughness

The most crucial part of a Knudsen effusion cell is the effusion orifice. In this apparatus the cell is made of a platinum disk, in order to minimize the effect of thermal expansion and to maximize the shape stability, as well as to avoid chemical reactivity. The platinum disk (diameter 21 mm and thickness 0.050 mm) is placed in the aluminum lid and compressed with a brass disk and ring, according to the scheme presented in figure 6.2. The platinum disk was acquired from Metal Goodfellow, where the circular orifice (diameter 1.2 mm) was made using a patented technology of the company, according to our specifications. The size and roughness of the platinum disk's orifice were evaluated using an optical microscope Leica, model M205 C, connected to a digital camera Leica, model DFC295, with a metric linear resolution of 0.002 mm, calibrated with an optical scale of (2.000 ± 0.002) mm. The effusion orifice diameter was found to be (1.199 ± 0.004) mm, and the orifice circular regularity was better than 0.3%, with a maximum observed wall roughness of 0.01 mm.

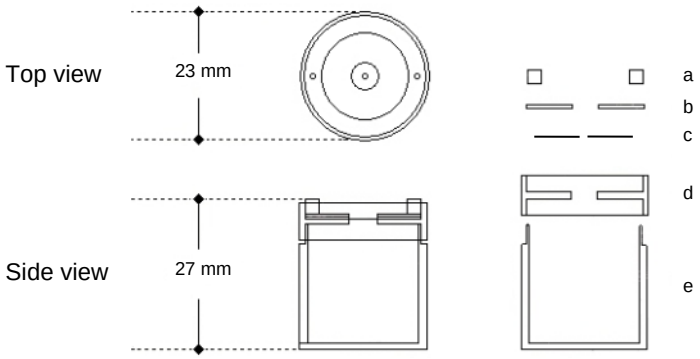

Figures 6.2 and 6.3. Side and top views of the effusion cell: a - brass ring; b - brass disk; c - platinum disk; d - aluminum lid; e - aluminum cell. (adapted from source [6.22])

6.2. Experimental methodologies

6.2.1. Knudsen effusion quartz crystal microbalance - KEQCM

Apparatus

The Knudsen effusion apparatus combined with a quartz crystal microbalance, KEQCM, was constructed and tested in our laboratory and was previously described in detail. [6.13-6.14]

Basically, KEQCM consist of four main parts:

Vacuum pumping system and vacuum chamber;
Temperature measurement and control;
Quartz crystal microbalance;
Data acquisition and control.

The KEQCM is schematically represented in figure 6.4.

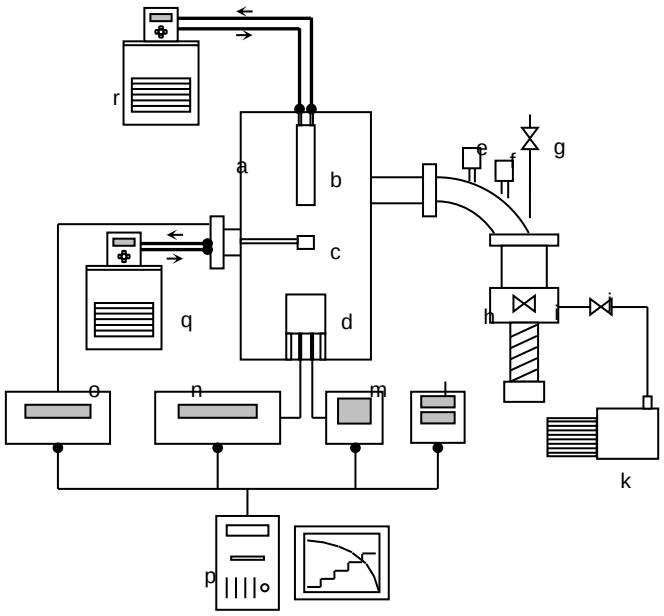

Figure 6.4. Schematic representation of the Knudsen effusion apparatus combined with a quartz crystal microbalance. a - vacuum chamber; b – cold trap; c - quartz crystal microbalance; d – aluminum block (oven); e - Varian high vacuum gauge model Cold cathode; f - Varian vacuum gauge model ConvetTorr; g - gas admittance valve; h - oil diffusion pump (Ilmvac model PDH100); i - butterfly valve; j – two-ways valve; k - rotary pump (Alcatel model Pascal 2010SD); l - CC2C SenTorr reader and vacuum controller; m - PID temperature controller (Omron model E5AR); n - Digital Multimeter (Keithley model 2010, 7½ digit resolution) ; o - high accurate crystal impedance meter (Agilent model E4915A); p - computer; q - quartz crystal microbalance refrigeration; r - trap refrigeration. (adapted from source [6.14]).

Vacuum pumping system and vacuum chamber

The vacuum pumping system (figure 6.5) consists of a rotary vane pump (Alcatel model Pascal 2010SD), which is used to pre-evacuate the system and to support an oil diffusion pump (Ilmvac model PDH100). The chamber pressure is monitored using two pressure sensors, a Varian vacuum gauge model ConvetTorr for pressures above (1×10^{-1}) Pa and a Varian high vacuum gauge model Cold cathode for the high vacuum stage. Connected to the vacuum pumping system is the vacuum chamber, which is basically a cylindrical chamber, containing a quartz crystal microbalance positioned above the aluminum block (oven), wherein the effusion cell is placed.

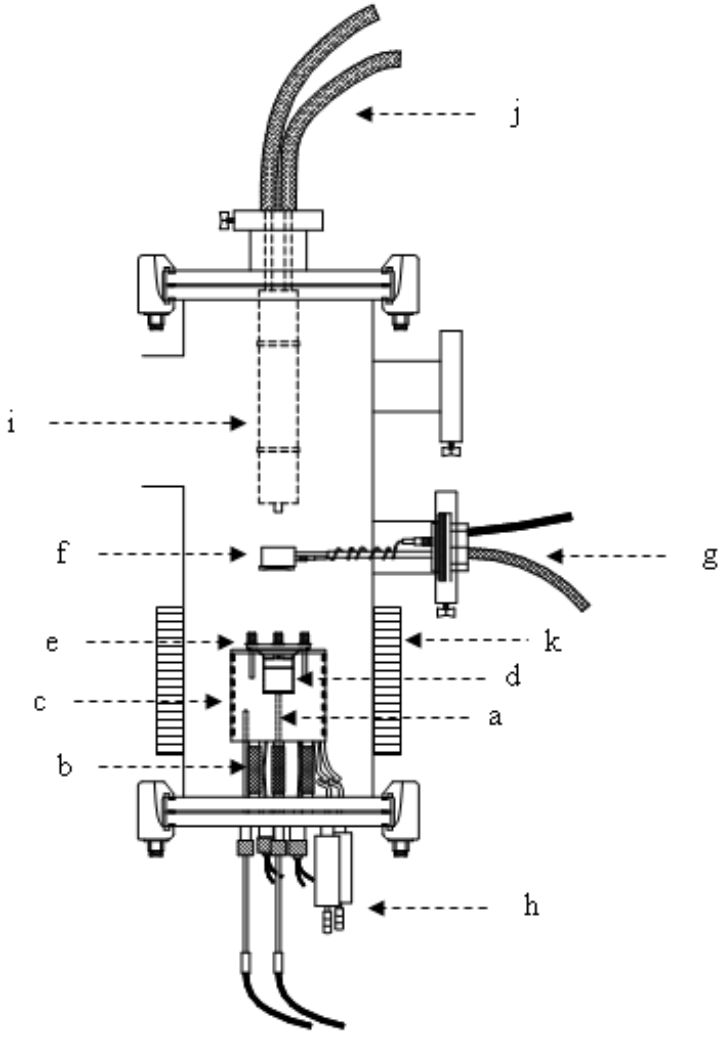

Figure 6.5. Schematic representation of the vacuum chamber: a) Pt100 for temperature measurement; b) Pt100 for temperature control; c) aluminium cylinder block and heaters; d) cell cavity and Knudsen cell; e) pressing disc; f) quartz crystal microbalance's head; g) quartz crystal's cooling liquid circulators; h) oven's cooling connector; i) vacuum chamber trap; j) vacuum chamber trap's cooling liquid circulators; k) forced-air coolers. [6.24]

Temperature measurement and control

The temperature of the aluminum block (oven) is measured using a platinum resistance thermometer, Pt100 class 1/10. The temperature sensor, which is used to measure the temperature during the experiment, is positioned at the center of the block, in close proximity to the base of the cavity containing the effusion cell. The temperature is controlled within a temperature fluctuation of ± (1×10^{-2}) K, measured with a resolution better than 1×10^{-3} K and with an overall uncertainty lower than ± (2×10^{-2}) K in the working temperature range.

Quartz crystal microbalance

The quartz crystal microbalance is based on a commercial Inficon - Maxtek liquid cool drawer single sensor head and feedthrough model CDS-A0F38. The quartz crystal is placed in a circular support, where the surface of the crystal is exposed to the condensation of the compound, as illustrated in figure 6.6. The refrigeration of the microbalance is achieved by means of a cooled circulator bath, Huber, model CC1-K6, in order to maintain the system at low temperatures, ($T \approx 266.0 \pm 0.5$) K. The quartz crystal resonance frequency is measured using a highly accurate crystal impedance meter, Agilent model E4915A, in a network analyzer resonator measuring mode.

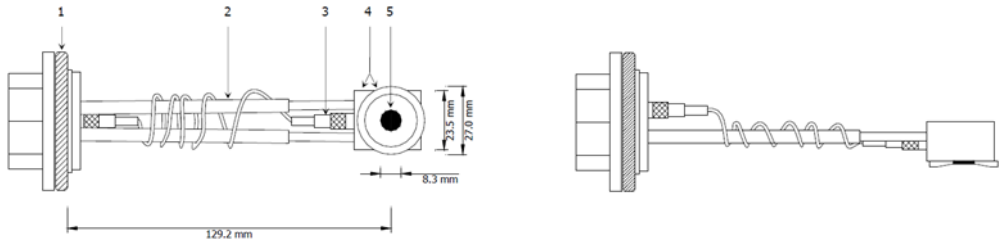

Figure 6.6. Technical drawing of the quartz crystal microbalance used in KEQCM. **A** − bottom view: 1 − o-ring; 2 − refrigeration; 3 − coaxial cable; 4 − quartz crystal support; 5 − quartz crystal. **B** − side view. (adapted from source [6.14]).

Data acquisition and control

The software of the instrument was developed [6.13] in LABVIEW 8.2, which is used for programming, control and data acquisition of the KEQCM. The program of the temperature profile in the PID temperature controller and the acquisition of the vacuum data from the Varian is done using an RS485 interface. The programming and data acquisition of the 7½ digit resolution digital multimeter (Keithley, model 2010) is performed via IEEE488 interface.

Experimental methodology

The purified PILs were studied by Knudsen effusion by placing ~200/300 mg of each PIL in the Knudsen effusion cell, which was kept in an oven at a fixed temperature (T = 306.2 ± 0.1 K), and under high vacuum ($p < 10^{-3}$ Pa), in runs of 1 to 6 hours.

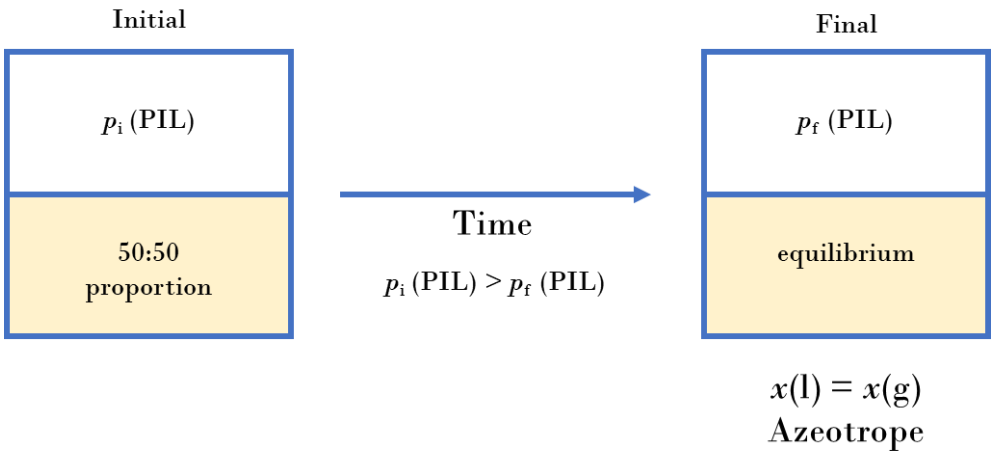

Figure 6.7. Schematic representation of the adopted experimental strategy.

Successive Knudsen experiments at these conditions were carried out, being verified that the apparent equilibrium vapor pressure (proportional to the mass flow of PIL effused from the cell) decreases with each run until it stabilizes at some point, the $p_{equilibrium}$, figure 6.7.After each individual run, a sample of the PIL in the Knudsen cell was collected for evaluation of the acid/base molar ratio by NMR, being verified that the PIL in the cell continuously becomes richer in acid, until the equilibrium composition is reached. This was made considering the integration of each NMR peak and their correspondent deviations.

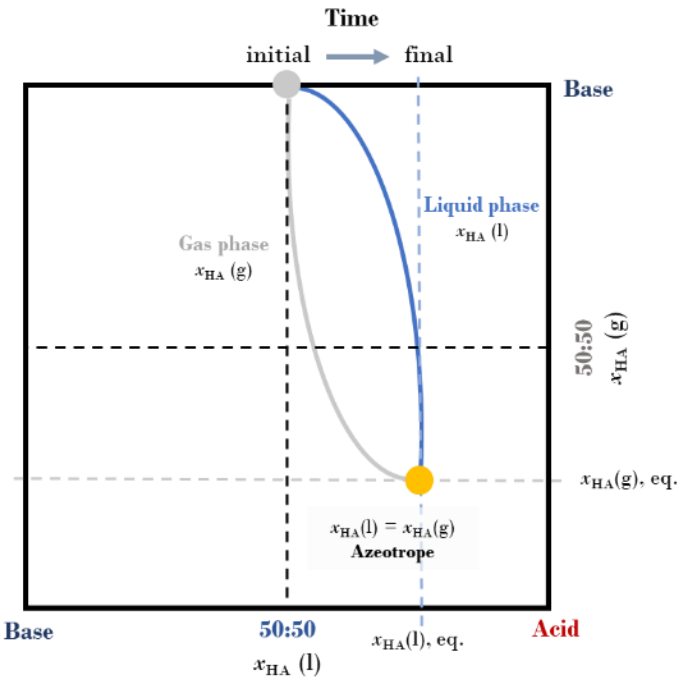

Figure 6.8. Schematic representation of the time evolution of the liquid and gas phase composition until formation of the azeotrope mixture [$x_{HA(l)} = x_{HA(g)}$].

Figure 6.8 shows a schematic representation of the time evolution of the liquid and gas phase composition until the formation of the azeotrope mixture and figure 6.9 depicts an example of the decrease in the measured vapor pressure during successive Knudsen runs for one PIL, in this case [DBNH][nPentCOO], alongside with the corresponding acid/base molar ratio at the end of each run, as evaluated by ^{1}H NMR.

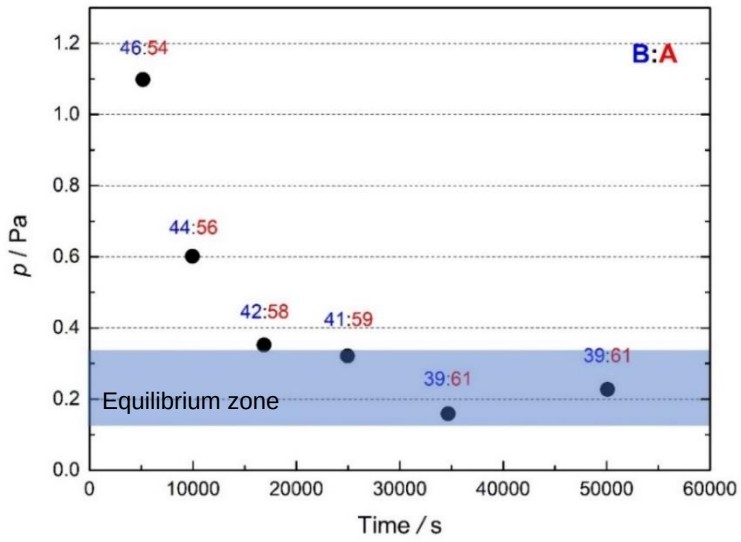

Figure 6.9. Example of a plot of pressure vs total effusion time, at *T* = (306.2 ± 0.1) K, showing the progressive decrease of the measured vapor pressure in successive Knudsen runs of [DBNH][nPentCOO], and the observed base:acid (**B**:**A**) proportion ratio (inside the Knudsen effusion cell) at the end of each run.

6.3. Results and discussion

The results obtained for the PILs studied are presented in tables 6.2 to 6.20. The experiment number, mass effused Δm, time of effusion t_{ef}, calculated vapor pressure p, fraction of base and acid in % x_B:x_A, and the molar effusion rates $\Delta n/t_{ef}$ are presented in detail for each experiment.

The ^{1}H NMR spectrum of the last Knudsen experiment for each PIL, the plot of p vs effusion time and a plot of the calculated molar effusion rates for each experiment are presented in figures 6.10 to 6.55.

Note that the vapor pressures presented in tables and figures are not the vapor pressures at the end of the experiment but an average vapor pressure of all the experiment at the studied temperature T. The figures serve as a guide to understand how the vapor pressures decrease as the PIL stabilizes and reaches equilibrium. x_B:x_A are the molar fractions, in %, of base (*B*) and acid (*A*) after each experiment. The term $\Delta n \cdot t_{ef}^{-1}$ is the molar effusion rate of base (*B*, left value) or acid (*A*, right value) in each experiment, where $\Delta n = x_i \cdot (m_i/\widehat{M}_M) - x_f \cdot (m_f/\widehat{M}_M)$, x_i and x_f are the molar fractions of acid or base at the beginning and end of each experiment, m_i and m_f are the initial and final masses of PIL sample in the Knudsen cell, $\widehat{M}_M$ the average molar mass calculated as $\widehat{M}_M = x_{\text{acid}} \cdot M_{\text{M,acid}} + x_{\text{base}} \cdot M_{\text{M,base}}$, and t_{ef} the effusion time in each experiment. The initial x_B:x_A, before the Knudsen experiments, was of nearly 50:50 for every PIL studied.

Table 6.2. Knudsen effusion results for [DBNH][EtCOO], at T = (306.2 ± 0.1) K.

Experiment	m_i / mg	m_f / mg	Δm / mg	t_{ef} / s	$\langle p \rangle$ / Pa	final x_B:x_A / %	$\Delta n \cdot t_{ef}^{-1}$ / μmol.s^{-1}
1	250.45	234.01	16.44	5765	0.74	48:52	0.019 : 0.007
2	219.26	208.17	11.09	5834	0.48	46:54	0.014 : 0.002
3	194.87	184.06	10.81	6128	0.45	45:55	0.012 : 0.004
4	166.65	159.42	7.23	5265	0.35	43:57	0.010 : 0.001
5	146.21	136.93	9.28	6777	0.35	43:57	0.007 : 0.006
6	129.80	122.51	7.29	5894	0.31	42:58	0.006 : 0.006
7	110.01	102.41	7.60	7174	0.27	42:58	0.005 : 0.006
8	85.54	76.96	8.58	7822	0.28	42:58	0.005 : 0.007

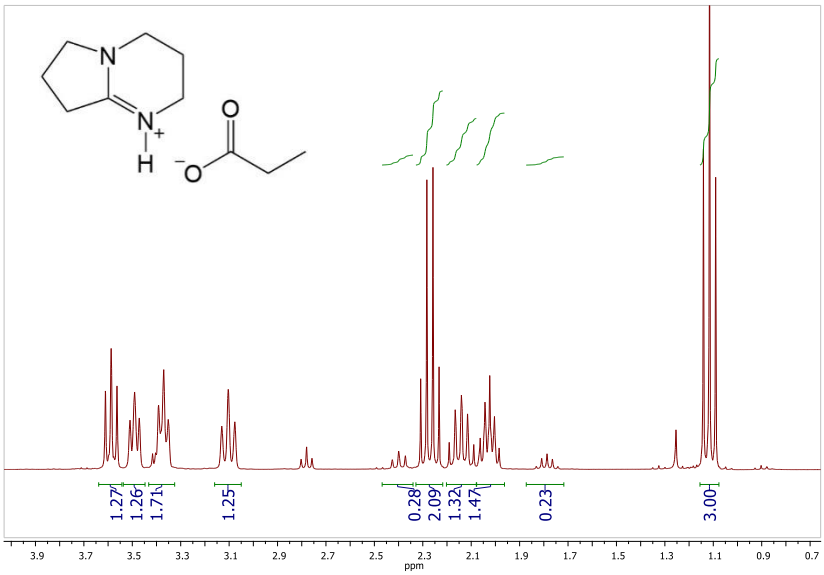

Figure 6.10. ^{1}H NMR spectrum of the last Knudsen experiment of [DBNH][EtCOO].

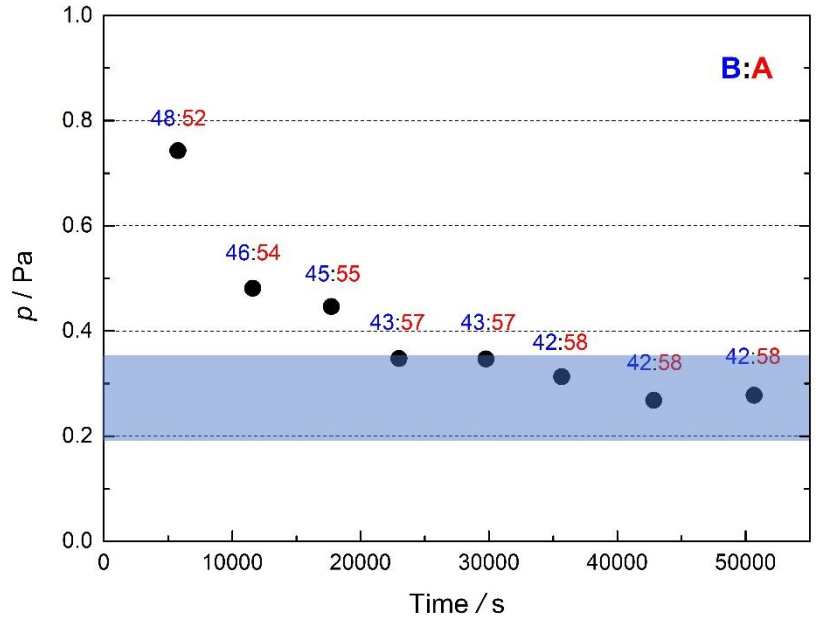

Figure 6.11. Plot of pressure vs total effusion time, at T = (306.2 ± 0.1) K, showing the progressive decrease of the measured vapor pressure in successive Knudsen runs of [DBNH][EtCOO], and the observed base:acid (**B**:**A**) proportion ratio (inside the Knudsen effusion cell) at the end of each run.

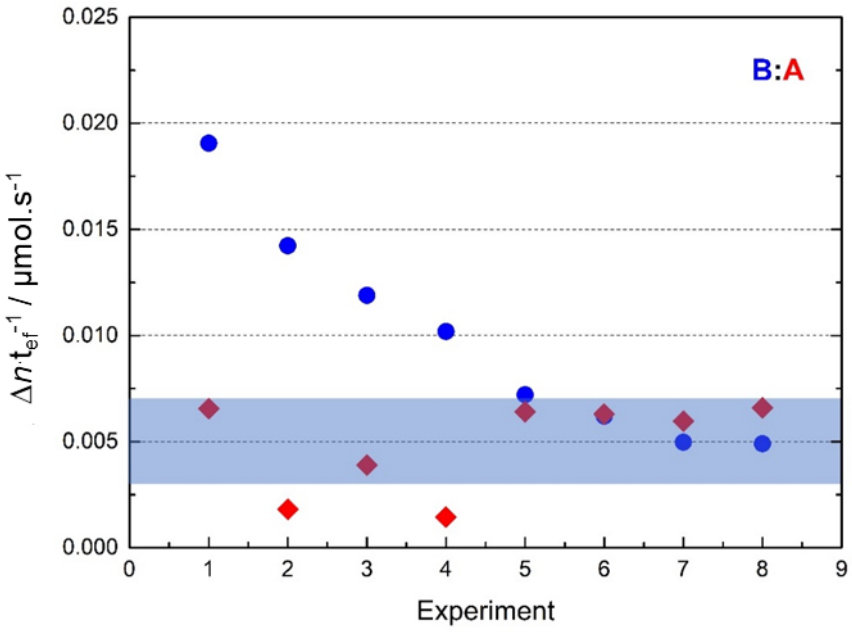

Figure 6.12. Calculated molar effusion rates, at T = (306.2 ± 0.1) K, of base (blue circles) and acid (red diamonds) in each Knudsen run of [DBNH][EtCOO].

Table 6.3. Knudsen effusion results for [DBNH][nPrCOO], at T = (306.2 ± 0.1) K.

Experiment	m_i / mg	m_f / mg	Δm / mg	t_{ef} / s	$\langle p \rangle$ / Pa	final x_B:x_A / %	$\Delta n \cdot t_{ef}^{-1}$ / μmol.s^{-1}
1	237.35	220.49	16.86	5157	0.52	45:55	0.019 : 0.010
2	211.77	201.26	10.51	4789	0.31	43:57	0.014 : 0.005
3	200.73	180.86	19.87	6931	0.33	43:57	0.012 : 0.015
4	174.81	165.35	9.46	8070	0.21	42:58	0.006 : 0.005
5	163.95	150.38	13.57	9716	0.25	42:58	0.006 : 0.007
6	145.88	137.39	8.49	15416	0.18	41:59	0.003 : 0.003
7	141.55	121.51	20.04	18413	0.34	42:58	0.004 : 0.006
8	115.96	107.21	8.75	22086	0.18	42:58	0.002 : 0.002

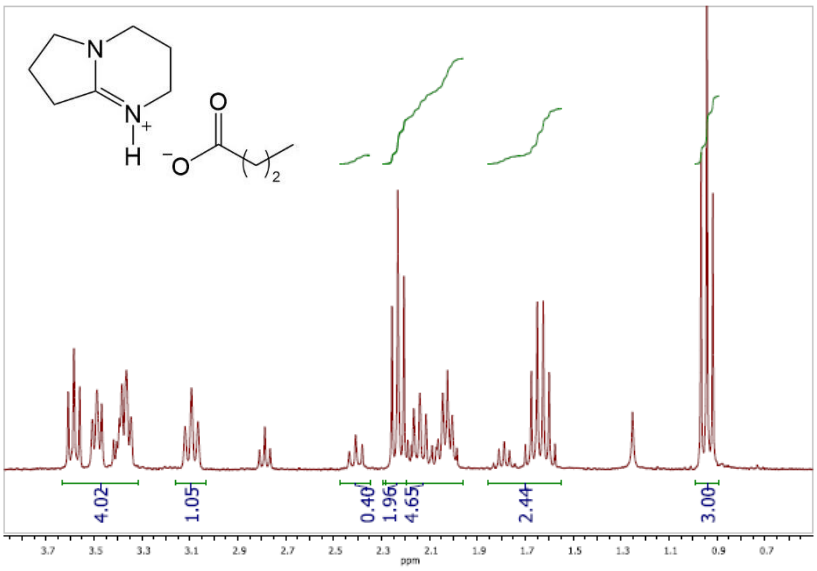

Figure 6.13. ^{1}H NMR spectrum of the last Knudsen experiment of [DBNH][nPrCOO].

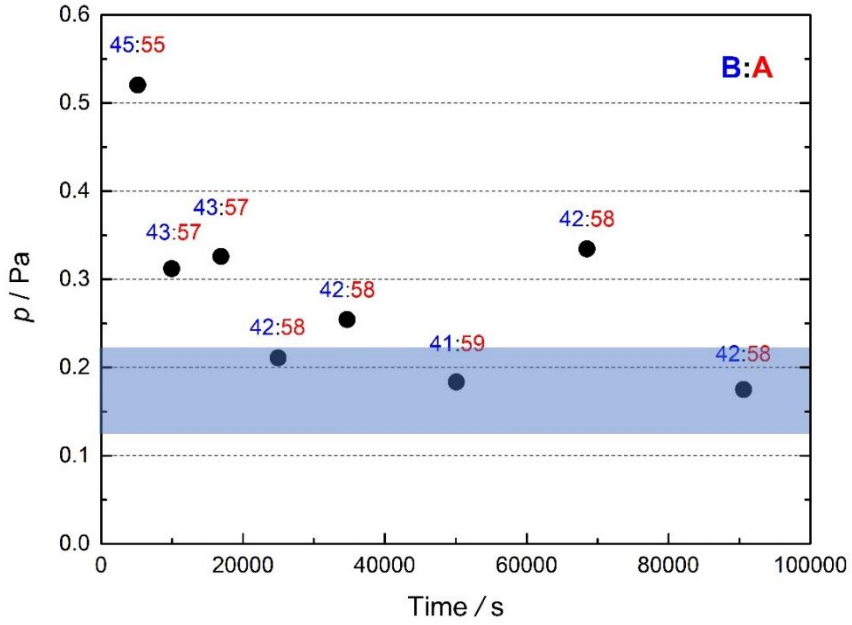

Figure 6.14. Plot of pressure vs total effusion time, at *T* = (306.2 ± 0.1) K, showing the progressive decrease of the measured vapor pressure in successive Knudsen runs of [DBNH][nPrCOO], and the observed base:acid (**B**:**A**) proportion ratio (inside the Knudsen effusion cell) at the end of each run.

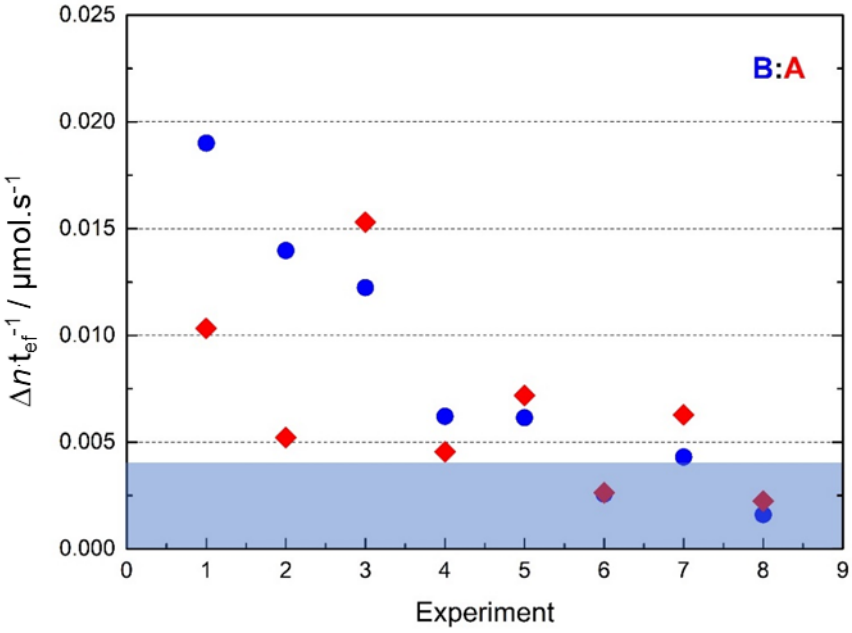

Figure 6.15. Calculated molar effusion rates, at *T* = (306.2 ± 0.1) K, of base (blue circles) and acid (red diamonds) in each Knudsen run of [DBNH][nPrCOO].

Table 6.4. Knudsen effusion results for [DBNH][nButCOO], at T = (306.2 ± 0.1) K.

Experiment	m_i / mg	m_f / mg	Δm / mg	t_{ef} / s	$\langle p \rangle$ / Pa	final x_B:x_A / %	$\Delta n \cdot t_{ef}^{-1}$ / μmol.s^{-1}
1	359.27	342.69	16.58	7475	0.53	46:54	0.025 : 0.000
2	335.74	322.43	13.31	10066	0.31	44:56	0.011 : 0.000
3	320.25	304.03	16.22	11750	0.33	43:57	0.007 : 0.005
4	295.30	284.39	10.91	14668	0.18	42:58	0.004 : 0.002
5	286.78	273.16	13.62	14873	0.22	42:58	0.003 : 0.005
6	270.55	254.57	15.98	18555	0.20	41:59	0.004 : 0.003

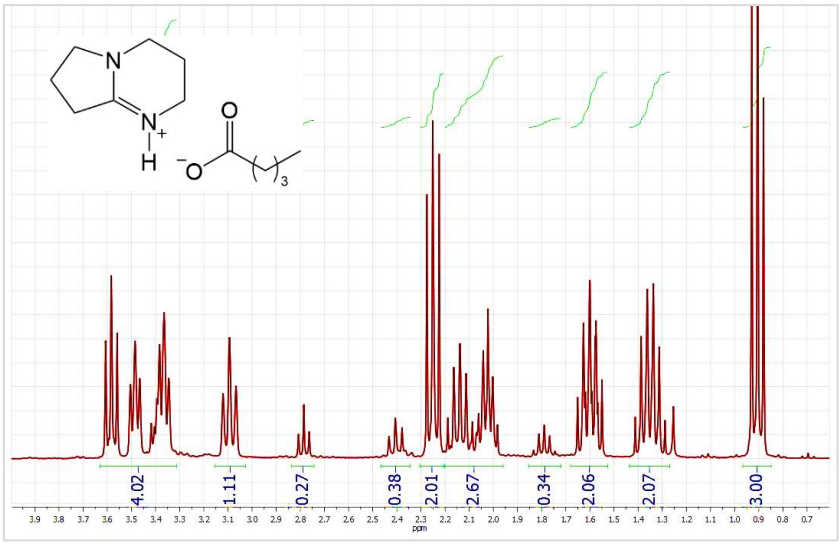

Figure 6.16. ^{1}H NMR spectrum of the last Knudsen experiment of [DBNH][nButCOO].

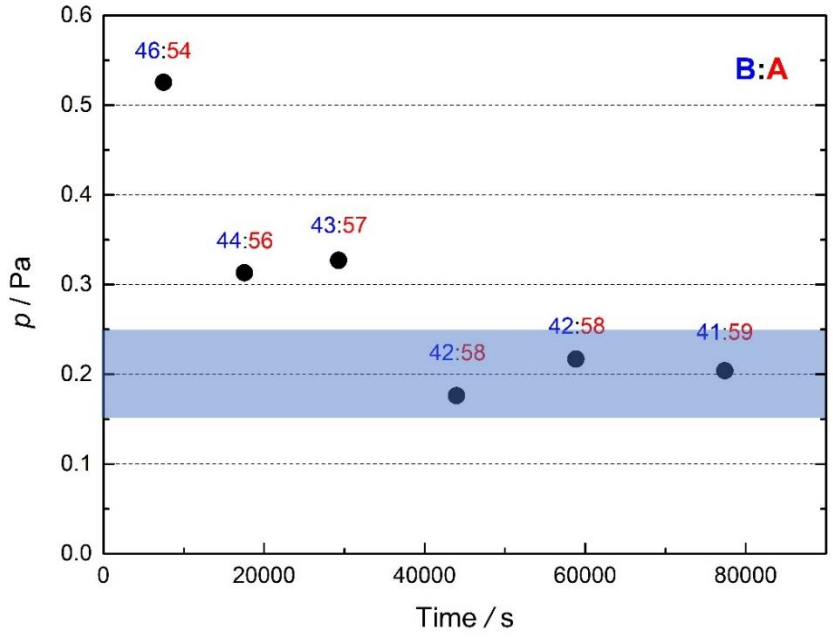

Figure 6.17. Plot of pressure vs total effusion time, at *T* = (306.2 ± 0.1) K, showing the progressive decrease of the measured vapor pressure in successive Knudsen runs of [DBNH][nButCOO], and the observed base:acid (**B**:**A**) proportion ratio (inside the Knudsen effusion cell) at the end of each run.

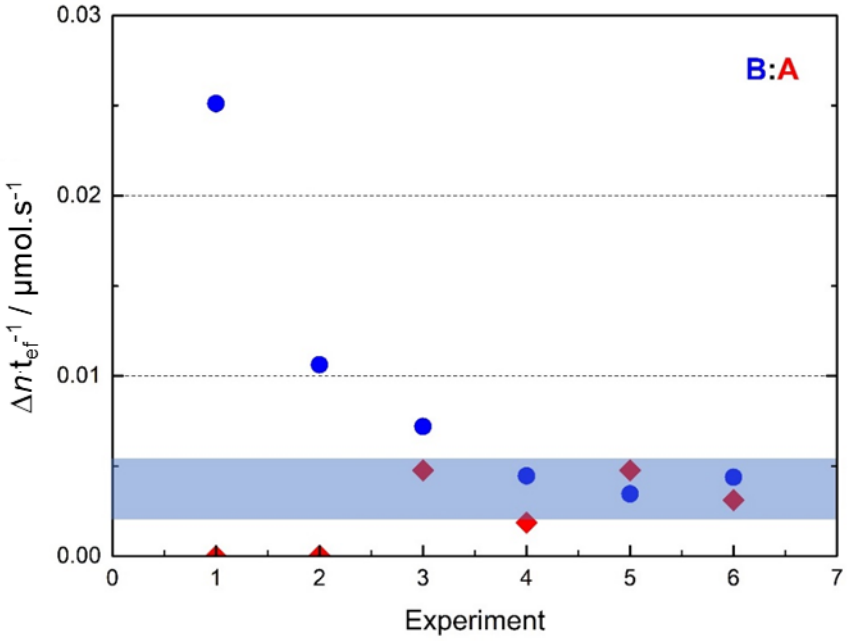

Figure 6.18. Calculated molar effusion rates, at *T* = (306.2 ± 0.1) K, of base (blue circles) and acid (red diamonds) in each Knudsen run of [DBNH][nButCOO].

Table 6.5. Knudsen effusion results for [DBNH][nPentCOO], at T = (306.2 ± 0.1) K.

Experiment	m_i / mg	m_f / mg	Δm / mg	t_{ef} / s	$<p>$ / Pa	final x_B:x_A / %	$\Delta n \cdot t_{ef}^{-1}$ / μmol.s^{-1}
1	309.70	285.06	24.64	5157	1.10	46:54	0.037 : 0.001
2	271.32	258.79	12.53	4789	0.60	44:56	0.019 : 0.002
3	250.35	239.72	10.63	6931	0.35	42:58	0.010 : 0.003
4	230.06	218.77	11.29	8070	0.32	41:59	0.008 : 0.004
5	206.08	196.25	9.83	9716	0.16	39:61	0.006 : 0.002
6	196.25	181.01	15.24	15416	0.23	39:61	0.003 : 0.005

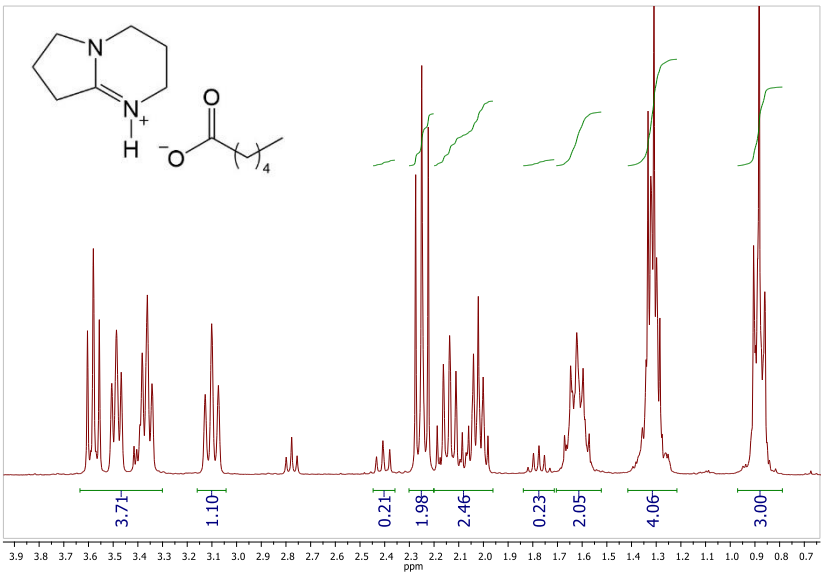

Figure 6.19. ^{1}H NMR spectrum of the last Knudsen experiment of [DBNH][nPentCOO].

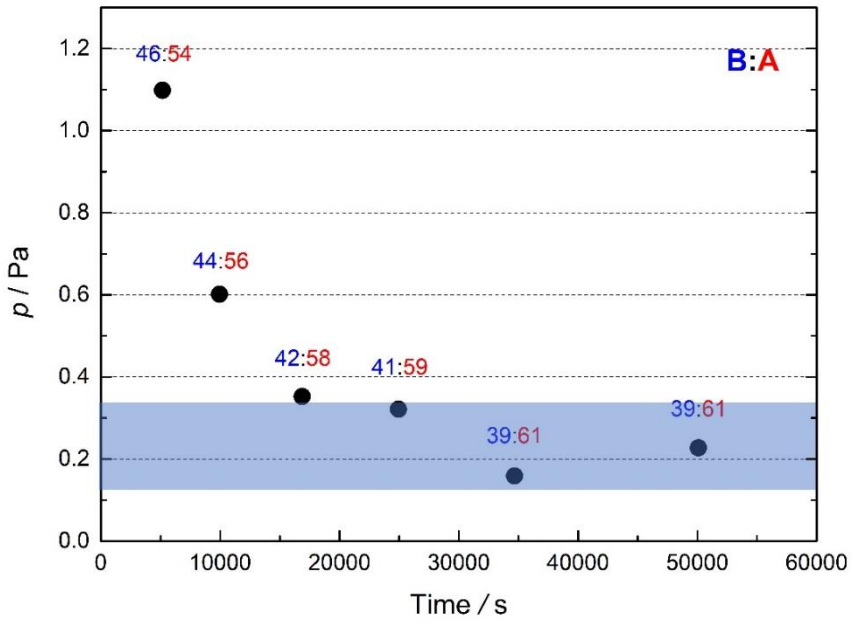

Figure 6.20. Plot of pressure vs total effusion time, at *T* = (306.2 ± 0.1) K, showing the progressive decrease of the measured vapor pressure in successive Knudsen runs of [DBNH][nPentCOO], and the observed base:acid (**B**:**A**) proportion ratio (inside the Knudsen effusion cell) at the end of each run.

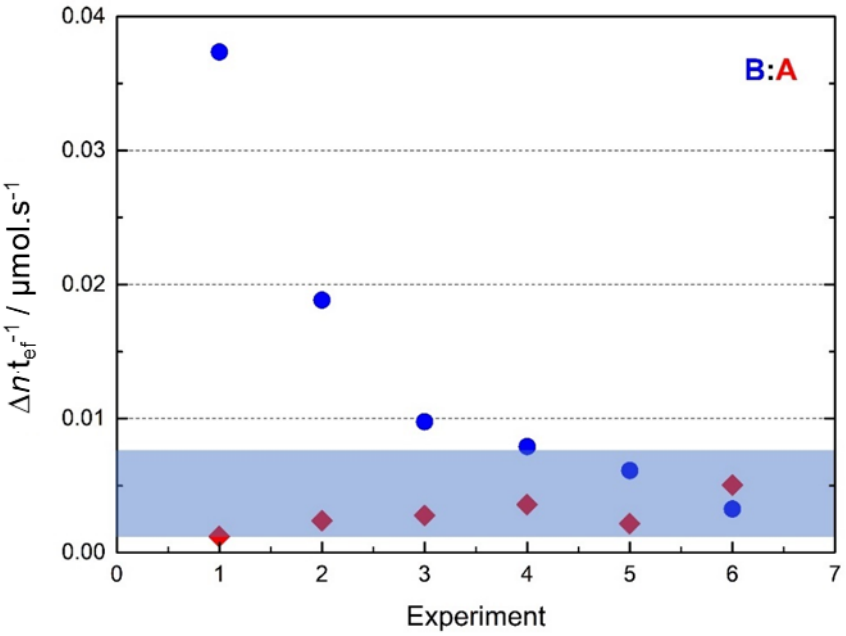

Figure 6.21. Calculated molar effusion rates, at *T* = (306.2 ± 0.1) K, of base (blue circles) and acid (red diamonds) in each Knudsen run of [DBNH][nPentCOO].

Table 6.6. Knudsen effusion results for [DBNH][nHexCOO], at T = (306.2 ± 0.1) K.

Experiment	m_i / mg	m_f / mg	Δm / mg	t_{ef} / s	$<p>$ / Pa	final x_B:x_A / %	$\Delta n \cdot t_{ef}^{-1}$ / μmol.s^{-1}
1	207.61	190.02	17.59	16592	0.24	42:58	0.012 : 0.000
2	194.11	176.26	17.85	19785	0.20	41:59	0.004 : 0.000
3	171.97	164.90	7.07	11272	0.14	40:60	0.004 : 0.001
4	159.04	153.06	5.98	14628	0.09	40:60	0.001 : 0.002
5	152.24	143.92	8.32	29256	0.06	39:61	0.001 : 0.001
6	139.41	132.26	7.15	23810	0.07	38:62	0.001 : 0.001
7	131.98	124.58	7.40	30047	0.06	37:63	0.001 : 0.001

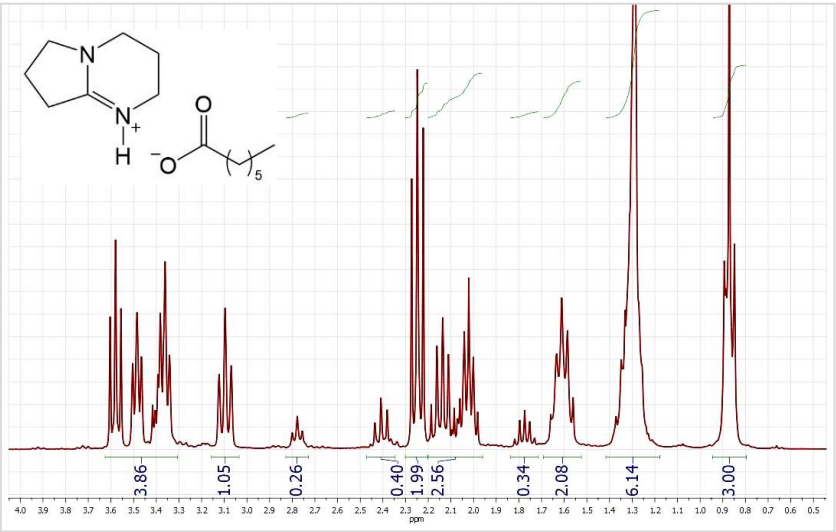

Figure 6.22. ^{1}H NMR spectrum of the last Knudsen experiment of [DBNH][nHexCOO].

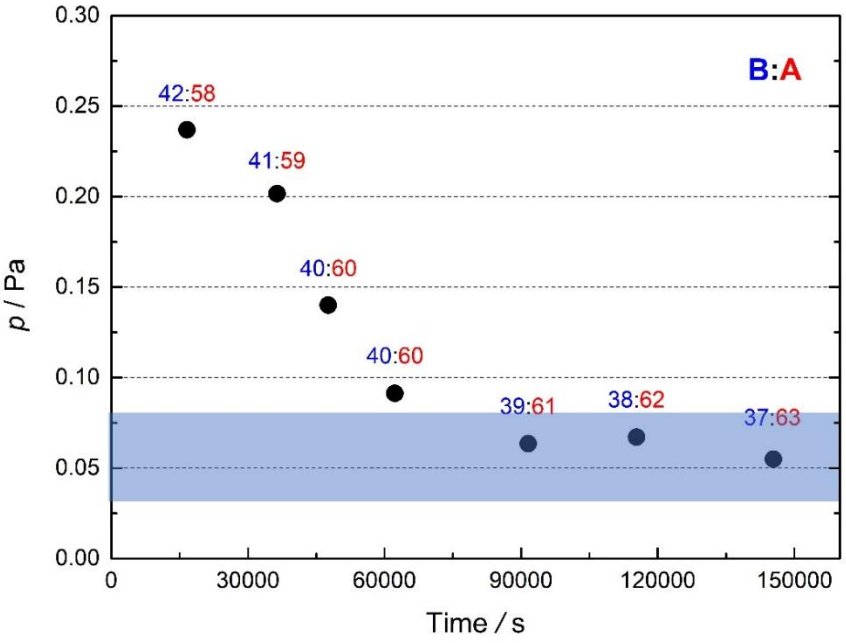

Figure 6.23. Plot of pressure vs total effusion time, at *T* = (306.2 ± 0.1) K, showing the progressive decrease of the measured vapor pressure in successive Knudsen runs of [DBNH][nHexCOO], and the observed base:acid (**B**:**A**) proportion ratio (inside the Knudsen effusion cell) at the end of each run.

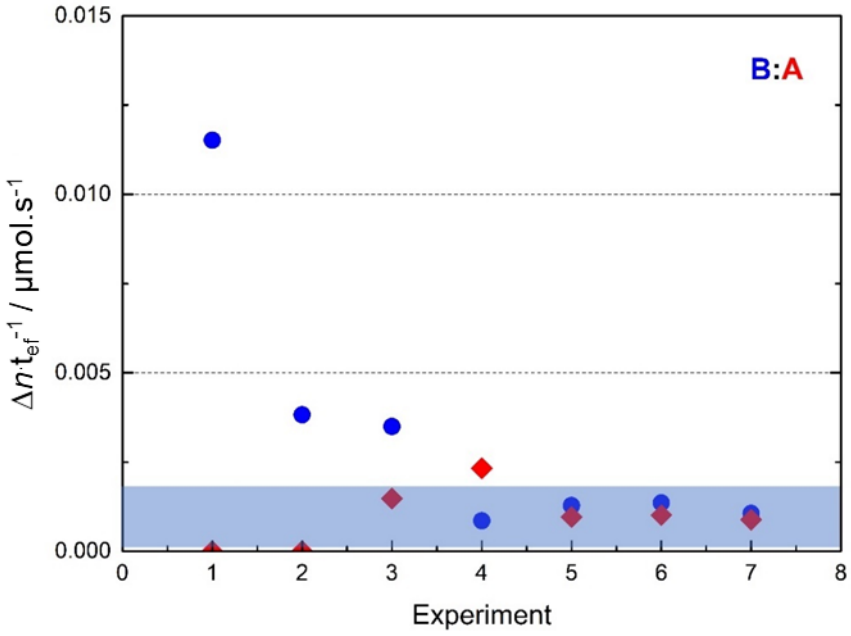

Figure 6.24. Calculated molar effusion rates, at *T* = (306.2 ± 0.1) K, of base (blue circles) and acid (red diamonds) in each Knudsen run of [DBNH][nHexCOO].

Table 6.7. Knudsen effusion results for [DBNH][nHeptCOO], at T = (306.2 ± 0.1) K.

Experiment	m_i / mg	m_f / mg	Δm / mg	t_{ef} / s	$\langle p \rangle$ / Pa	final x_B:x_A / %	$\Delta n \cdot t_{ef}^{-1}$ / μmol.s^{-1}
1	227.92	202.62	25.30	10434	0.53	48:52	0.014 : 0.005
2	197.10	188.18	8.92	8787	0.22	41:59	0.015 : 0.006
3	185.08	176.57	8.51	9146	0.20	40:60	0.005 : 0.002
4	170.27	166.06	4.21	9335	0.10	38:62	0.004 : 0.000
5	160.28	157.45	2.83	8681	0.07	37:63	0.001 : 0.001
6	153.12	147.89	5.23	13852	0.08	37:63	0.001 : 0.001
7	142.11	139.73	2.38	11370	0.05	36:64	0.001 : 0.000

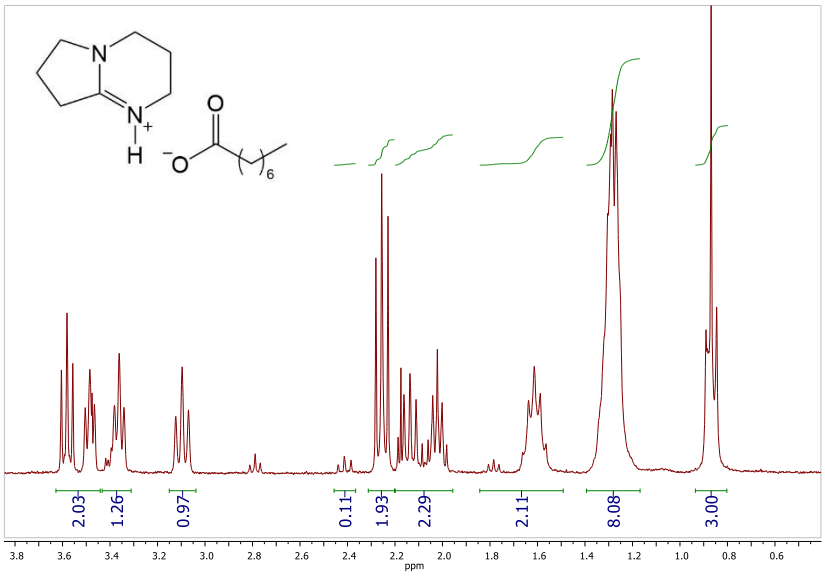

Figure 6.25. ^{1}H NMR spectrum of the last Knudsen experiment of [DBNH][nHeptCOO].

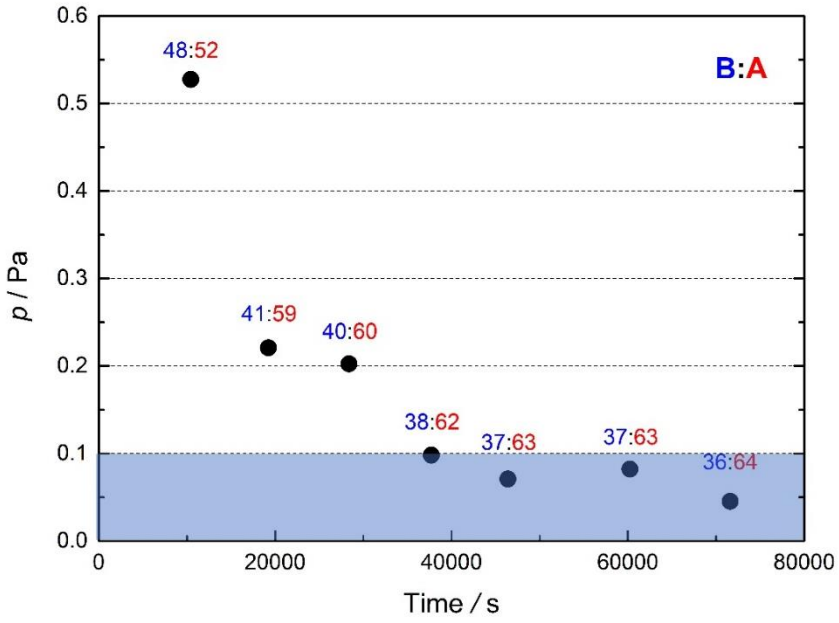

Figure 6.26. Plot of pressure vs total effusion time, at *T* = (306.2 ± 0.1) K, showing the progressive decrease of the measured vapor pressure in successive Knudsen runs of [DBNH][nHeptCOO], and the observed base:acid (**B**:**A**) proportion ratio (inside the Knudsen effusion cell) at the end of each run.

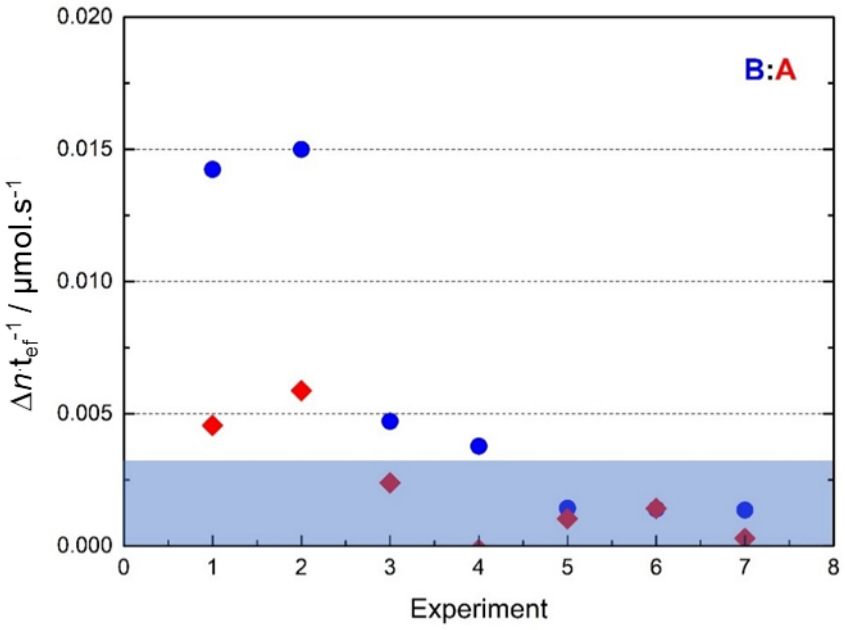

Figure 6.27. Calculated molar effusion rates, at *T* = (306.2 ± 0.1) K, of base (blue circles) and acid (red diamonds) in each Knudsen run of [DBNH][nHeptCOO].

Table 6.8. Knudsen effusion results for [DBNH][FPrCOO], at T = (306.2 ± 0.1) K.

Experiment	m_i / mg	m_f / mg	Δm / mg	t_{ef} / s	$<p>$ / Pa	final x_B:x_A / %	$\Delta n \cdot t_{ef}^{-1}$ / μmol.s^{-1}
1	767.45	764.25	3.20	5111	0.12	51:49	0.004 : 0.005
2	740.56	736.56	4.00	15169	0.05	51:49	0.004 : 0.001
3	731.71	721.60	10.11	17987	0.11	50:50	0.005 : 0.000
4	716.93	707.56	9.37	16152	0.11	50:50	0.001 : 0.002
5	690.78	686.36	4.42	11140	0.08	50:50	0.001 : 0.001
6	676.80	672.99	3.81	12303	0.06	50:50	0.001 : 0.001
7	669.85	665.36	4.49	10076	0.09	50:50	0.001 : 0.001
8	656.38	652.44	3.94	10224	0.08	50:50	0.001 : 0.001

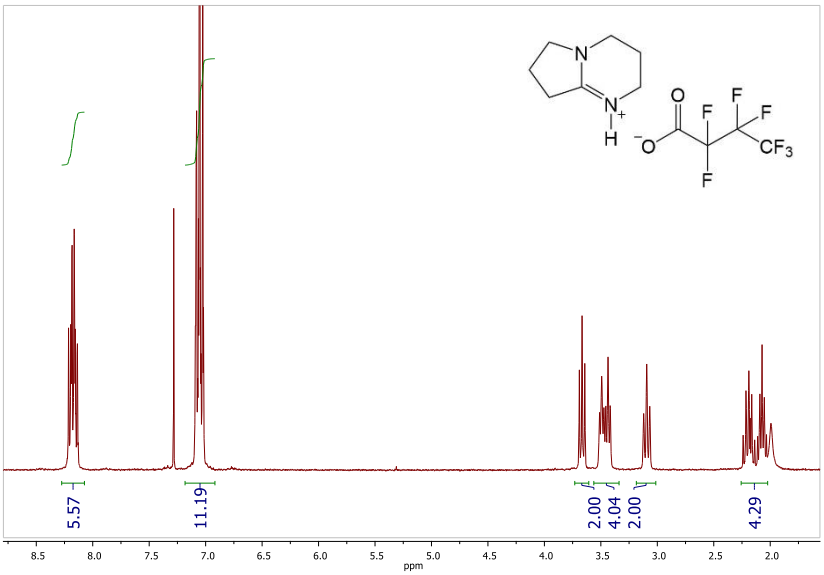

Figure 6.28. ^{1}H NMR spectra of the last Knudsen experiment of [DBNH][FPrCOO]. The peaks at [7; 8] ppm correspond to the aromatic protons of 2,4-difluoronitrobenzene, which was used as a reference for the quantification of the acid:base molar fraction.

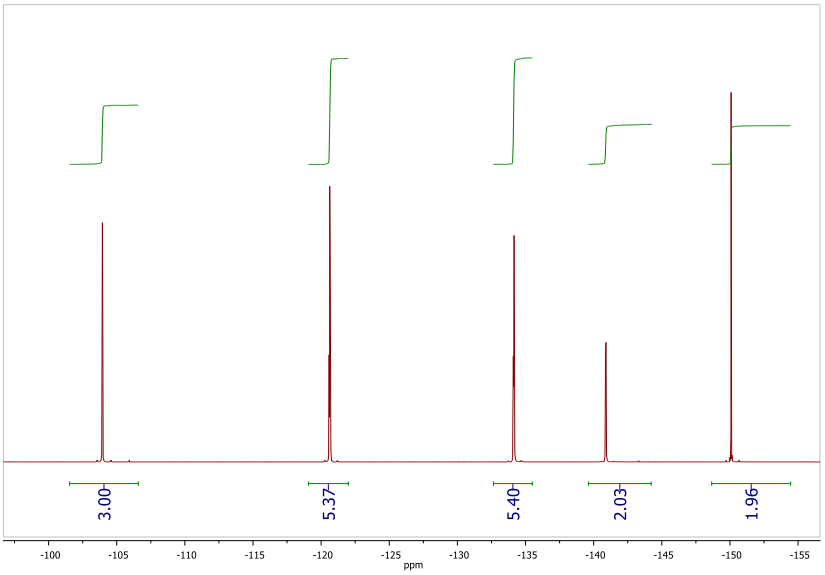

Figure 6.29. ^{19}F NMR spectra of the last Knudsen experiment of [DBNH][FPrCOO]. The peaks at [-120; -135] ppm correspond to the aromatic protons of 2,4-difluoronitrobenzene, which was used as a reference for the quantification of the acid:base molar fraction.

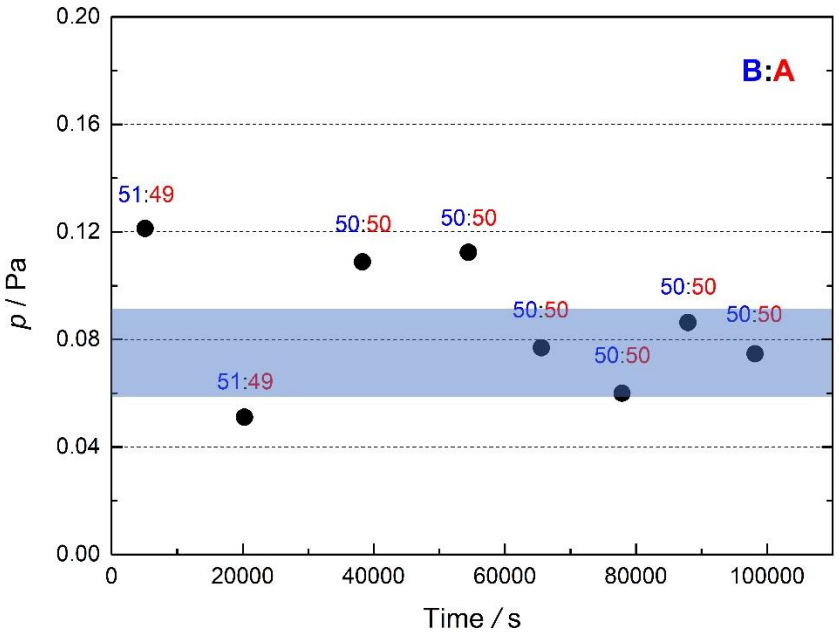

Figure 6.30. Plot of pressure vs total effusion time, at T = (306.2 ± 0.1) K, showing the progressive decrease of the measured vapor pressure in successive Knudsen runs of [DBNH][FPrCOO], and the observed base:acid (**B**:**A**) proportion ratio (inside the Knudsen effusion cell) at the end of each run.

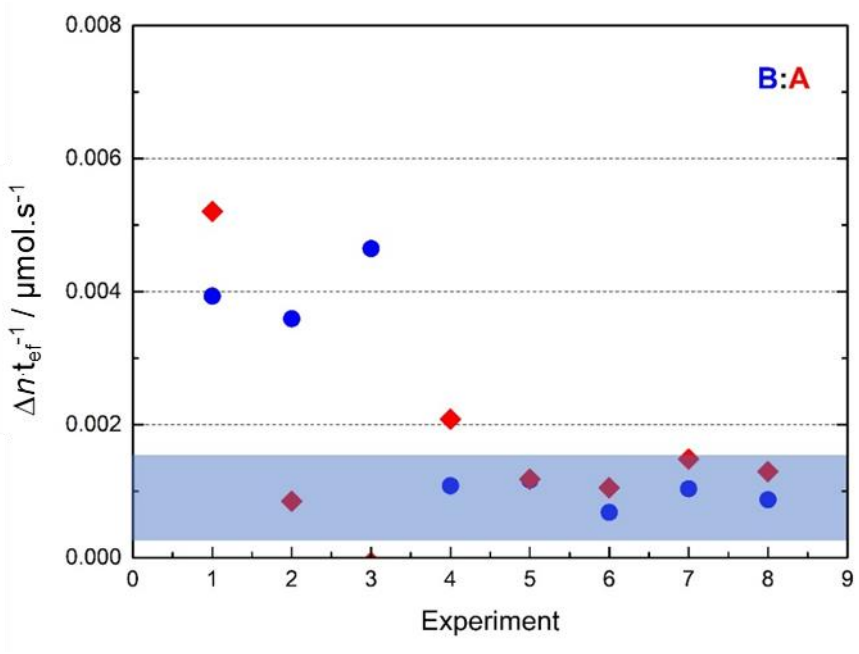

Figure 6.31. Calculated molar effusion rates, at *T* = (306.2 ± 0.1) K, of base (blue circles) and acid (red diamonds) in each Knudsen run of [DBNH][FPrCOO].

Table 6.9. Knudsen effusion results for [DBUH][EtCOO], at T = (306.2 ± 0.1) K.

Experiment	m_i / mg	m_f / mg	Δm / mg	t_{ef} / s	$\langle p \rangle$ / Pa	final x_B:x_A / %	$\Delta n \cdot t_{ef}^{-1}$ / μmol.s^{-1}
1	262.10	245.21	16.89	8349	0.48	48:52	0.010 : 0.006
2	237.24	227.59	9.65	9372	0.24	47:53	0.005 : 0.003
3	225.81	213.08	12.73	11260	0.27	47:53	0.005 : 0.005
4	188.87	176.91	11.96	10533	0.27	47:53	0.005 : 0.005
5	166.71	156.85	9.86	10096	0.23	46:54	0.005 : 0.004
6	144.94	134.05	10.89	9228	0.28	46:54	0.005 : 0.006
7	122.47	111.05	11.42	10404	0.26	46:54	0.005 : 0.005
8	109.08	101.60	7.48	9038	0.20	46:54	0.003 : 0.004
9	99.78	81.99	17.79	18439	0.23	46:54	0.004 : 0.005
10	80.96	66.68	14.28	21617	0.16	46:54	0.003 : 0.003
11	63.52	51.26	12.26	19884	0.15	46:54	0.003 : 0.003
12	51.15	42.38	8.77	14489	0.14	46:54	0.003 : 0.003

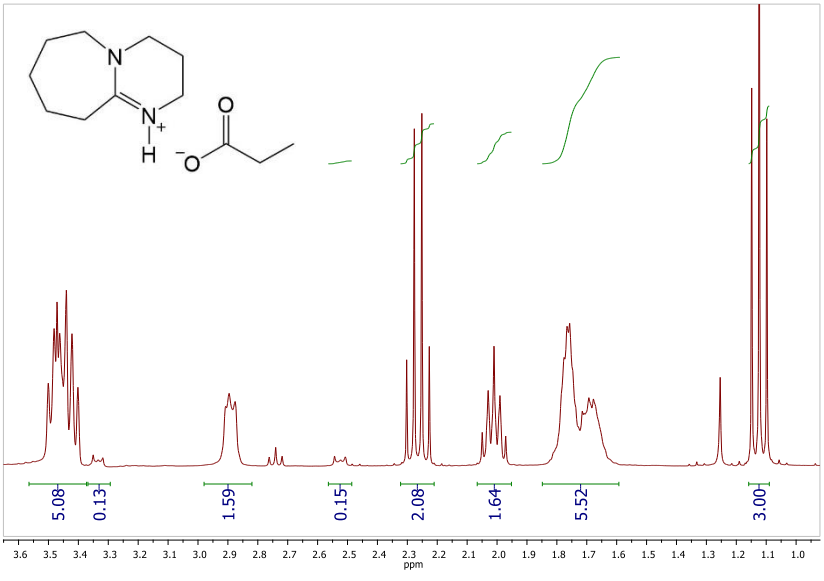

Figure 6.32. ^{1}H NMR spectra of the last Knudsen experiment of [DBUH][EtCOO].

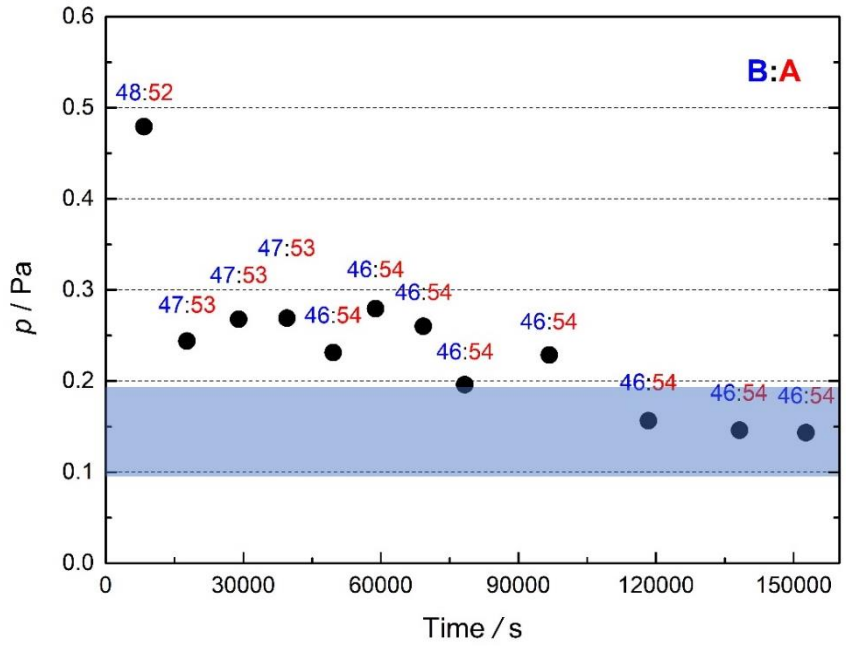

Figure 6.33. Plot of pressure vs total effusion time, at T = (306.2 ± 0.1) K, showing the progressive decrease of the measured vapor pressure in successive Knudsen runs of [DBUH][EtCOO], and the observed base:acid (**B**:**A**) proportion ratio (inside the Knudsen effusion cell) at the end of each run.

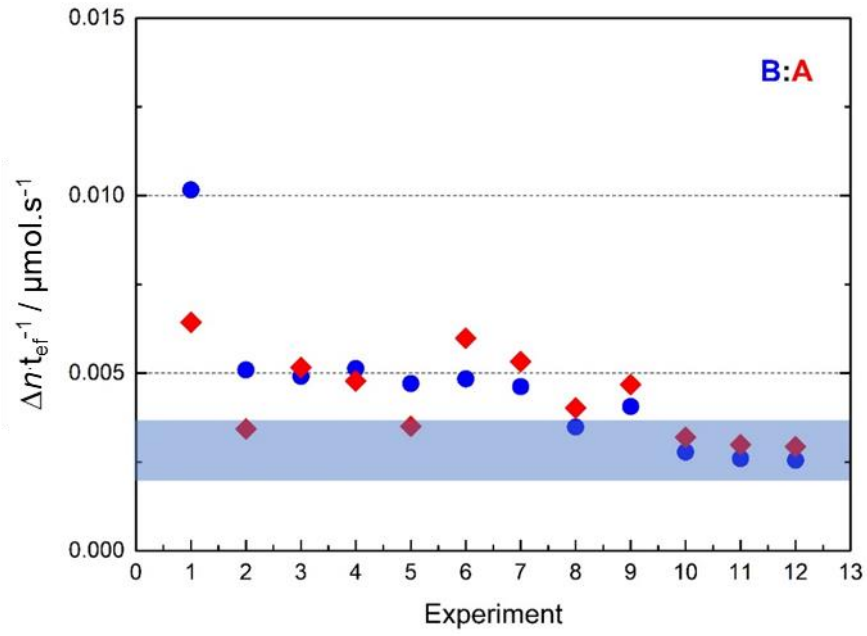

Figure 6.34. Calculated molar effusion rates, at T = (306.2 ± 0.1) K, of base (blue circles) and acid (red diamonds) in each Knudsen run of [DBUH][EtCOO].

Table 6.10. Knudsen effusion results for [DBUH][nPrCOO], at T = (306.2 ± 0.1) K.

Experiment	m_i / mg	m_f / mg	Δm / mg	t_{ef} / s	$\langle p \rangle$ / Pa	final x_B:x_A / %	$\Delta n \cdot t_{ef}^{-1}$ / μmol.s^{-1}
1	219.32	211.71	7.61	10792	0.16	47:53	0.004 : 0.001
2	202.76	195.70	7.06	11894	0.14	47:53	0.003 : 0.002
3	192.10	180.52	11.58	18577	0.14	45:55	0.003 : 0.001
4	170.27	164.98	5.29	11873	0.10	45:55	0.002 : 0.001
5	161.73	151.05	10.68	21138	0.12	45:55	0.002 : 0.003
6	147.41	143.66	3.75	7688	0.11	44:56	0.003 : 0.001
7	134.99	126.49	8.50	20190	0.10	44:56	0.002 : 0.002

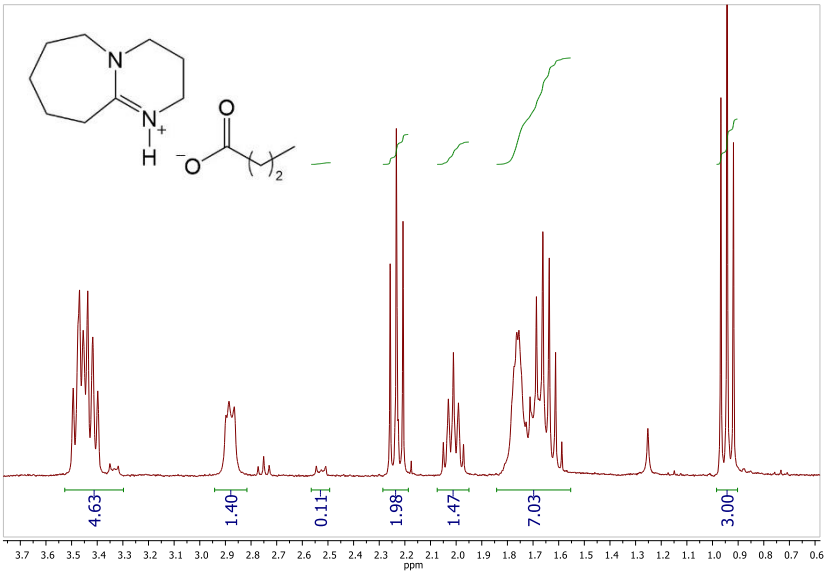

Figure 6.35. ^{1}H NMR spectra of the last Knudsen experiment of [DBUH][nPrCOO].

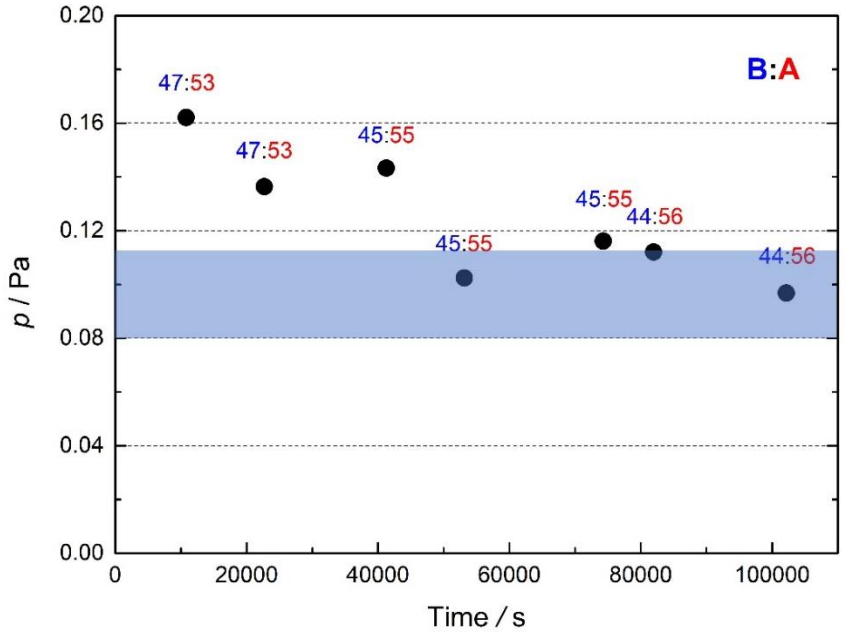

Figure 6.36. Plot of pressure vs total effusion time, at T = (306.2 ± 0.1) K, showing the progressive decrease of the measured vapor pressure in successive Knudsen runs of [DBUH][nPrCOO], and the observed base:acid (**B**:**A**) proportion ratio (inside the Knudsen effusion cell) at the end of each run.

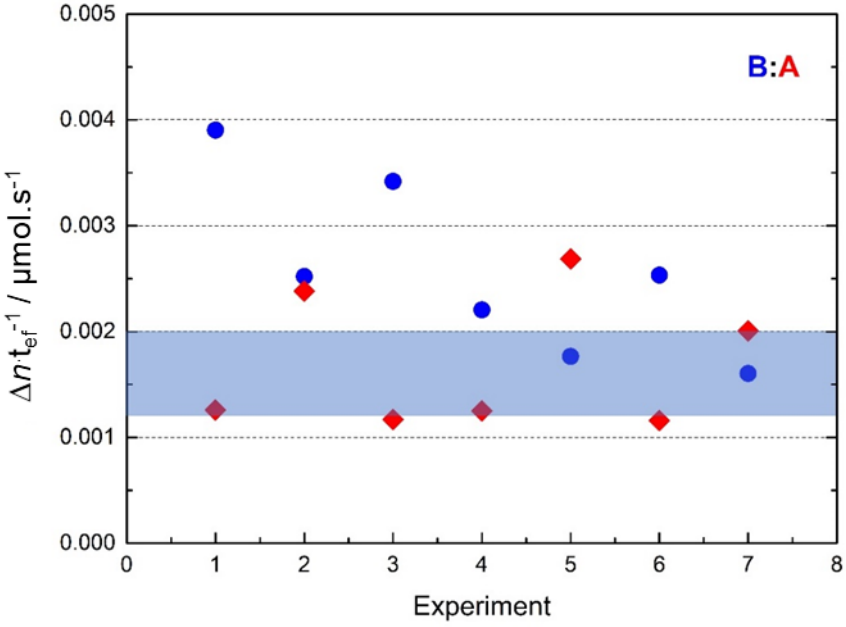

Figure 6.37. Calculated molar effusion rates, at T = (306.2 ± 0.1) K, of base (blue circles) and acid (red diamonds) in each Knudsen run of [DBUH][nPrCOO].

Table 6.11. Knudsen effusion results for [DBUH][nButCOO], at T = (306.2 ± 0.1) K.

Experiment	m_i / mg	m_f / mg	Δm / mg	t_{ef} / s	$\langle p \rangle$ / Pa	final x_B:x_A / %	$\Delta n \cdot t_{ef}^{-1}$ / μmol.s^{-1}
1	231.46	220.69	10.77	13497	0.18	48:52	0.005 : 0.000
2	218.12	209.96	8.16	11894	0.15	47:53	0.004 : 0.001
3	202.47	195.91	6.56	12908	0.11	46:54	0.003 : 0.001
4	190.89	184.47	6.42	12609	0.11	45:55	0.003 : 0.001
5	177.95	172.76	5.19	12942	0.09	45:55	0.001 : 0.002
6	166.80	158.91	7.89	19713	0.09	44:56	0.002 : 0.001

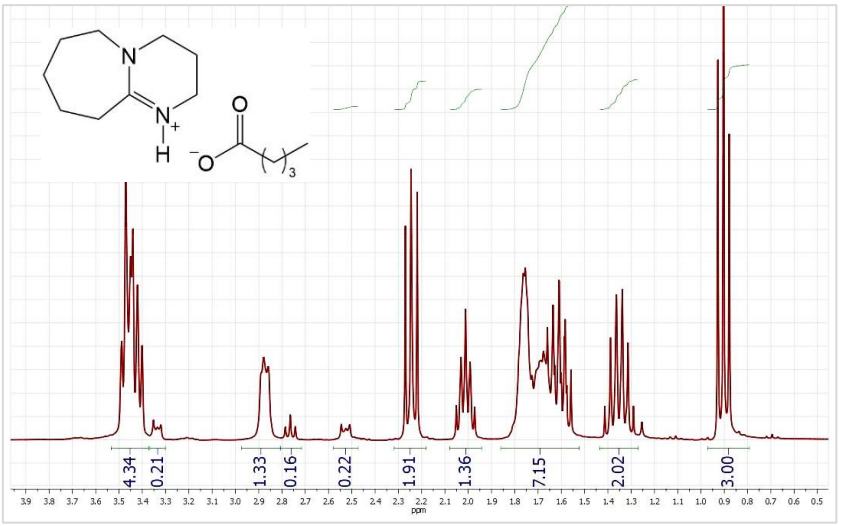

Figure 6.38. ^{1}H NMR spectrum of the last Knudsen experiment of [DBUH][nButCOO].

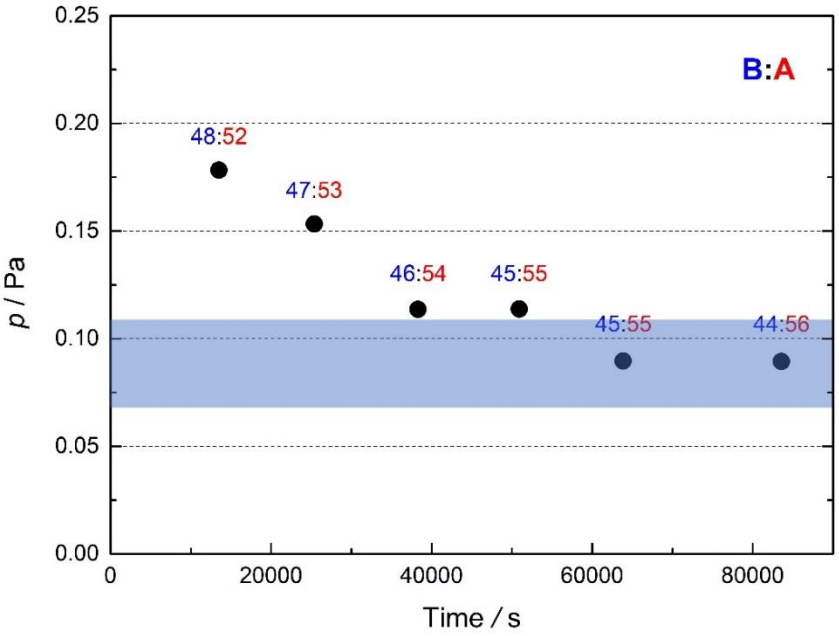

Figure 6.39. Plot of pressure vs total effusion time, at T = (306.2 ± 0.1) K, showing the progressive decrease of the measured vapor pressure in successive Knudsen runs of [DBUH][nButCOO], and the observed base:acid (**B**:**A**) proportion ratio (inside the Knudsen effusion cell) at the end of each run.

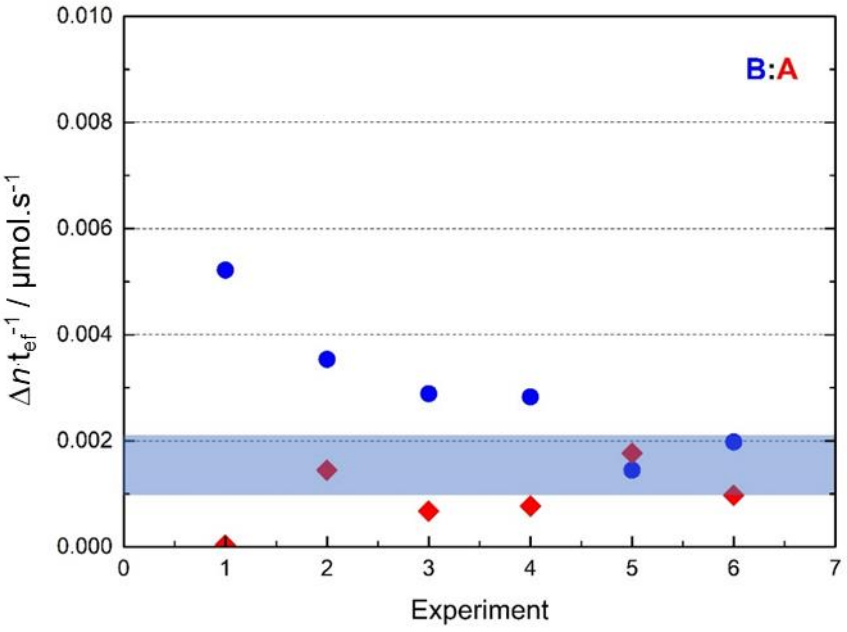

Figure 6.40. Calculated molar effusion rates, at T = (306.2 ± 0.1) K, of base (blue circles) and acid (red diamonds) in each Knudsen run of [DBUH][nButCOO].

Table 6.12. Knudsen effusion results for [DBUH][nPentCOO], at T = (306.2 ± 0.1) K.

Experiment	m_i / mg	m_f / mg	Δm / mg	t_{ef} / s	$\langle p \rangle$ / Pa	final x_B:x_A / %	$\Delta n \cdot t_{ef}^{-1}$ / μmol.s^{-1}
1	212.10	206.00	6.10	6067	0.22	48:52	0.004 : 0.003
2	199.78	192.34	7.44	13119	0.13	46:54	0.004 : 0.000
3	190.90	178.15	12.75	14916	0.19	44:56	0.004 : 0.002
4	172.04	167.36	4.68	10401	0.10	43:57	0.003 : 0.000
5	165.64	156.14	9.50	25906	0.08	43:57	0.001 : 0.001
6	154.12	146.24	7.88	24173	0.07	42:58	0.001 : 0.001

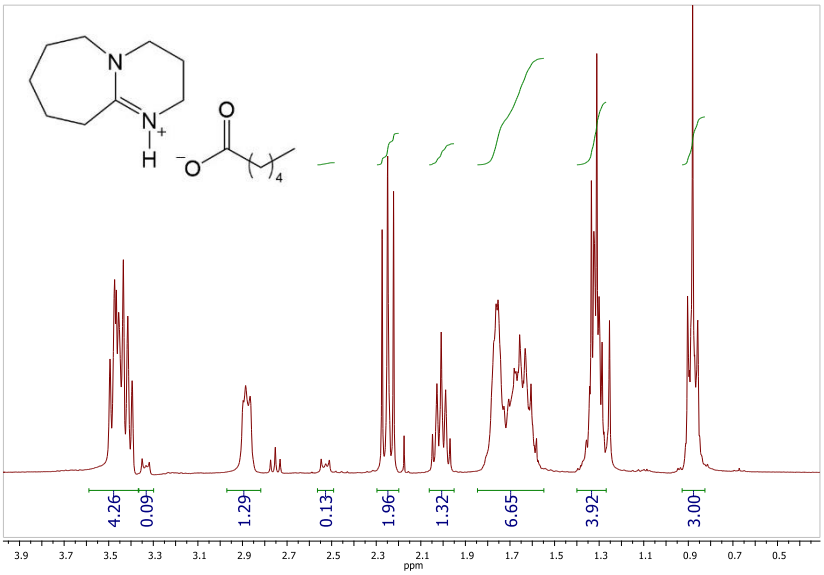

Figure 6.41. ^{1}H NMR spectra of the last Knudsen experiment of [DBUH][nPentCOO].

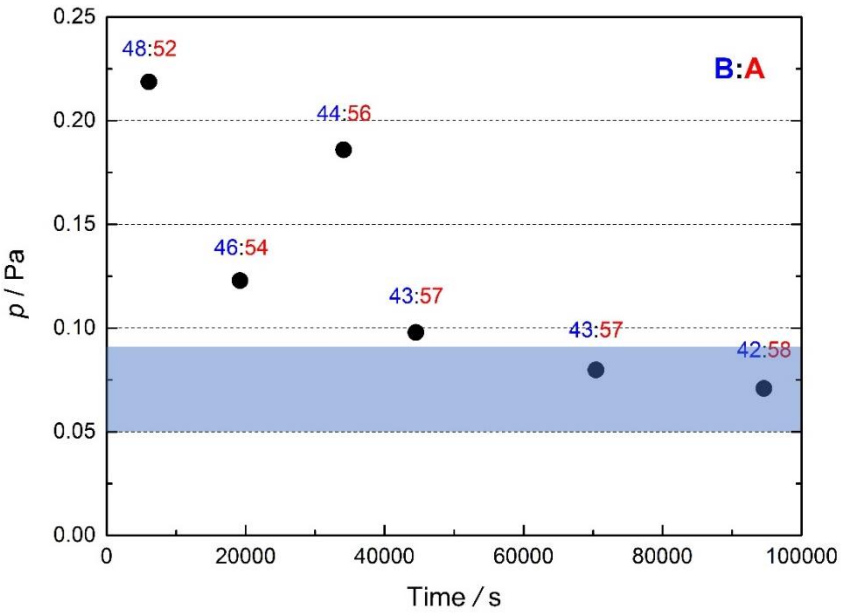

Figure 6.42. Plot of pressure vs total effusion time, at T = (306.2 ± 0.1) K, showing the progressive decrease of the measured vapor pressure in successive Knudsen runs of [DBUH][nPentCOO], and the observed base:acid (**B**:**A**) proportion ratio (inside the Knudsen effusion cell) at the end of each run.

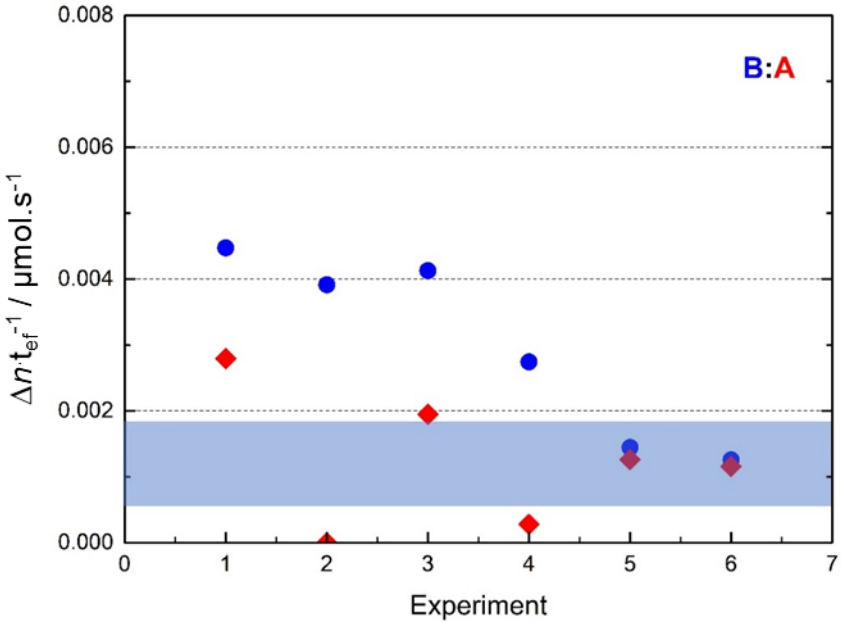

Figure 6.43. Calculated molar effusion rates, at T = (306.2 ± 0.1) K, of base (blue circles) and acid (red diamonds) in each Knudsen run of [DBUH][nPentCOO].

Table 6.13. Knudsen effusion results for [DBUH][nHexCOO], at T = (306.2 ± 0.1) K.

Experiment	m_i / mg	m_f / mg	Δm / mg	t_{ef} / s	$\langle p \rangle$ / Pa	final x_B:x_A / %	$\Delta n \cdot t_{ef}^{-1}$ / μmol.s^{-1}
1	293.32	281.98	11.34	12509	0.19	47:53	0.008 : 0.000
2	272.41	265.60	6.81	12611	0.12	46:54	0.003 : 0.000
3	262.42	254.91	7.51	11831	0.14	45:55	0.003 : 0.001
4	246.56	240.69	5.87	13894	0.09	44:56	0.003 : 0.000
5	237.85	228.38	9.47	22422	0.09	43:57	0.002 : 0.001
6	222.82	214.67	8.15	23305	0.07	43:57	0.001 : 0.001

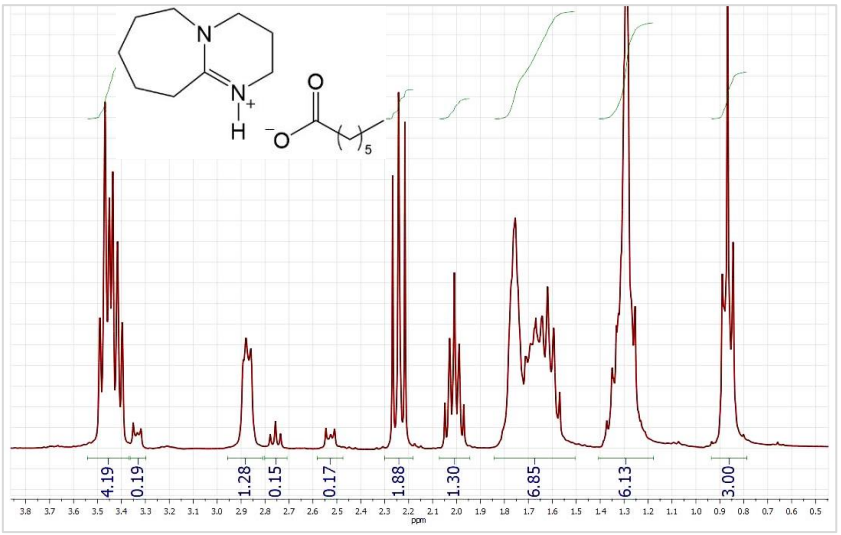

Figure 6.44. ^{1}H NMR spectrum of the last Knudsen experiment of [DBUH][nHexCOO].

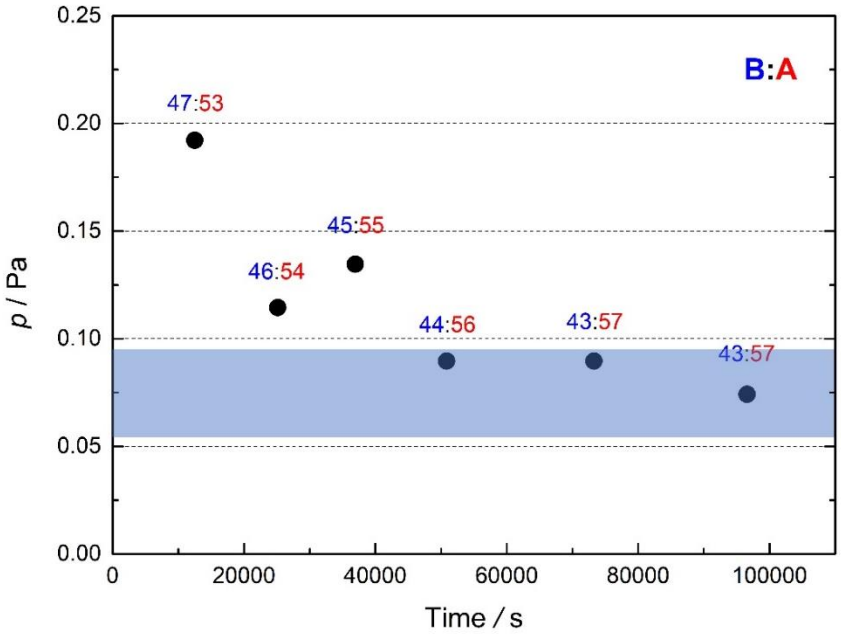

Figure 6.45. Plot of pressure vs total effusion time, at T = (306.2 ± 0.1) K, showing the progressive decrease of the measured vapor pressure in successive Knudsen runs of [DBUH][nHexCOO], and the observed base:acid (**B**:**A**) proportion ratio (inside the Knudsen effusion cell) at the end of each run.

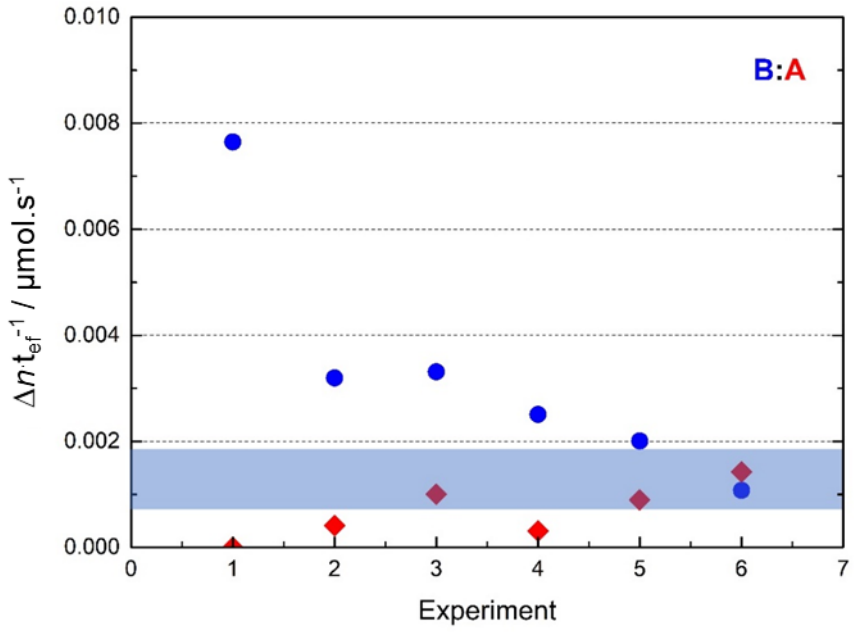

Figure 6.46. Calculated molar effusion rates, at T = (306.2 ± 0.1) K, of base (blue circles) and acid (red diamonds) in each Knudsen run of [DBUH][nHexCOO].

Table 6.14. Knudsen effusion results for [DBUH][nHeptCOO], at T = (306.2 ± 0.1) K.

Experiment	m_i / mg	m_f / mg	Δm / mg	t_{ef} / s	$\langle p \rangle$ / Pa	final x_B:x_A / %	$\Delta n \cdot t_{ef}^{-1}$ / μmol.s^{-1}
1	280.01	270.02	9.99	12008	0.17	45:55	0.004 : 0.001
2	270.02	262.03	7.99	17650	0.09	44:56	0.003 : 0.000
3	261.89	244.01	17.88	23806	0.16	42:58	0.003 : 0.002
4	225.24	213.27	11.97	32175	0.08	40:60	0.002 : 0.001
5	203.04	194.71	8.33	26242	0.07	39:61	0.001 : 0.001
6	191.56	181.48	10.08	27203	0.08	39:61	0.001 : 0.002
7	170.87	160.39	10.48	29206	0.07	39:61	0.001 : 0.001

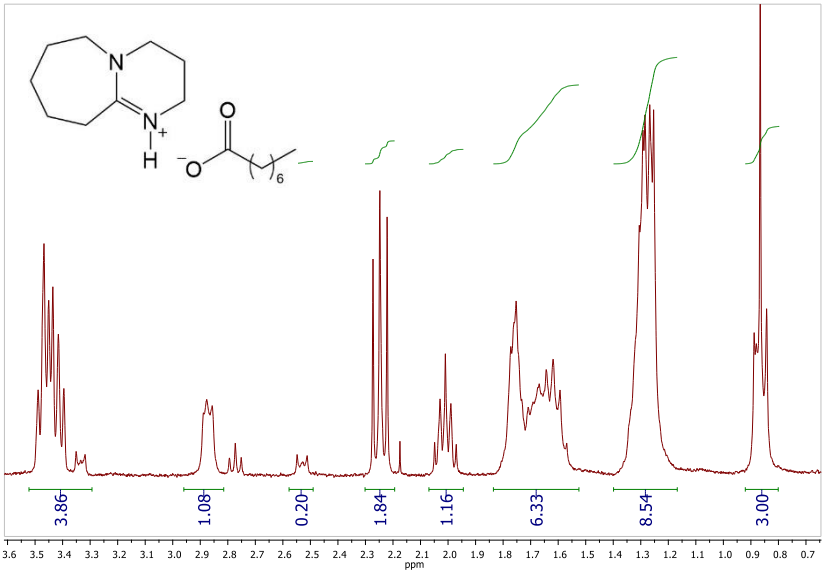

Figure 6.47. ^{1}H NMR spectra of the last Knudsen experiment of [DBUH][nHeptCOO].

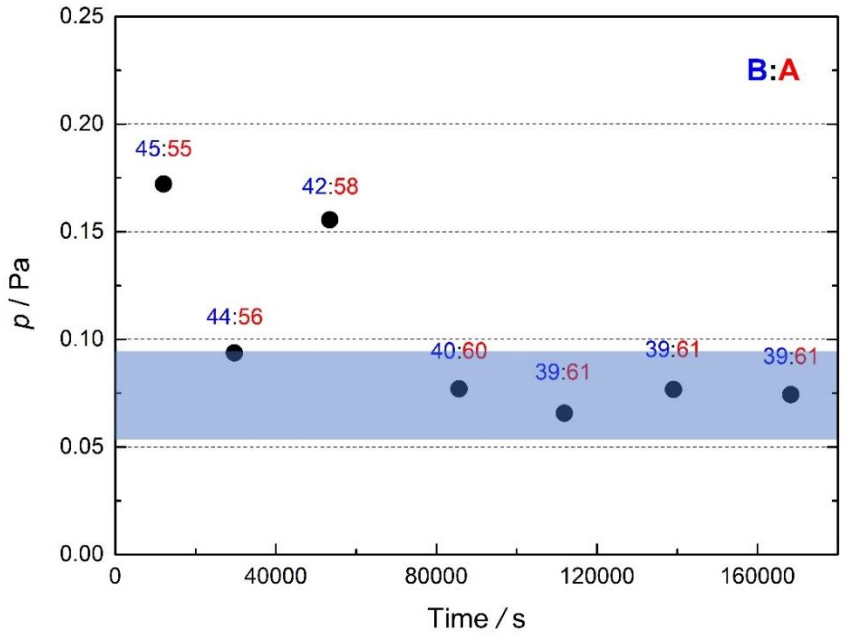

Figure 6.48. Plot of pressure vs total effusion time, at T = (306.2 ± 0.1) K, showing the progressive decrease of the measured vapor pressure in successive Knudsen runs of [DBUH][nHeptCOO], and the observed base:acid (**B**:**A**) proportion ratio (inside the Knudsen effusion cell) at the end of each run.

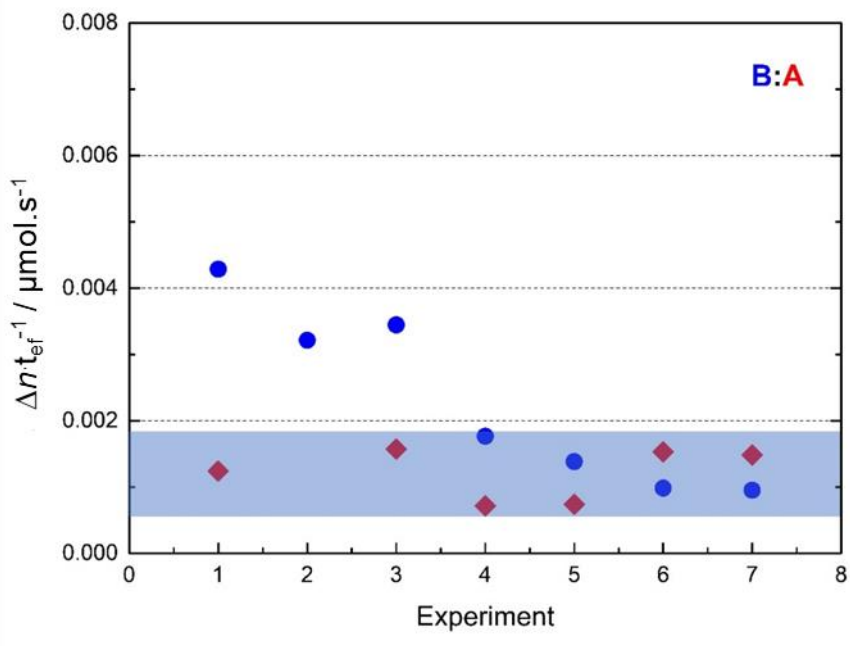

Figure 6.49. Calculated molar effusion rates, at T = (306.2 ± 0.1) K, of base (blue circles) and acid (red diamonds) in each Knudsen run of [DBUH][nHeptCOO].

Table 6.15. Knudsen effusion results for [DMTHPH][EtCOO], at T = (306.2 ± 0.1) K.

Experiment	m_i / mg	m_f / mg	Δm / mg	t_{ef} / s	$\langle p \rangle$ / Pa	final x_B:x_A / %	$\Delta n \cdot t_{ef}^{-1}$ / μmol.s^{-1}
1	259.27	247.00	12.27	7549	0.41	42:58	0.014 : 0.000
2	241.89	227.58	14.31	11189	0.32	41:59	0.008 : 0.005
3	224.86	207.23	17.63	12069	0.37	41:59	0.007 : 0.010
4	202.12	183.91	18.21	15752	0.29	40:60	0.006 : 0.006
5	177.52	162.01	15.51	8470	0.46	39:61	0.010 : 0.010
6	153.75	133.57	20.18	13800	0.37	40:60	0.006 : 0.011
7	133.25	114.34	18.91	12097	0.39	39:61	0.009 : 0.011
8	110.69	95.65	15.04	12105	0.31	40:60	0.005 : 0.010

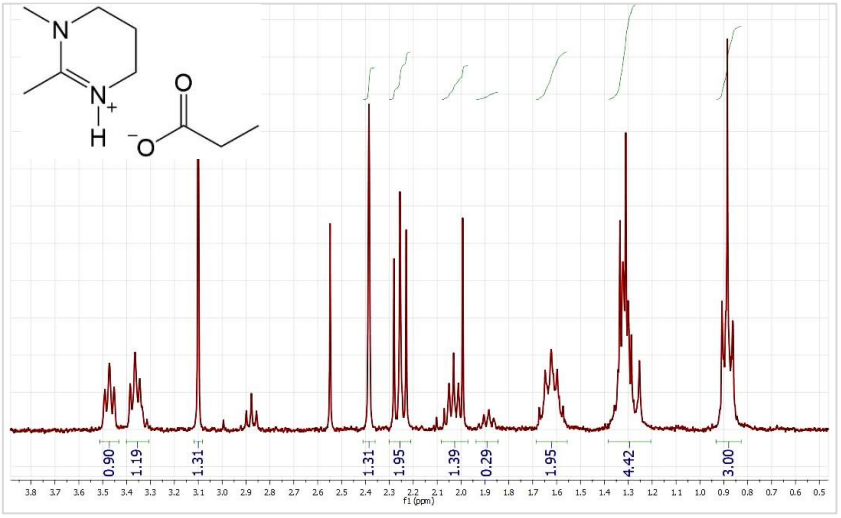

Figure 6.50. ^{1}H NMR spectrum of the last Knudsen experiment of [DMTHPH][EtCOO].

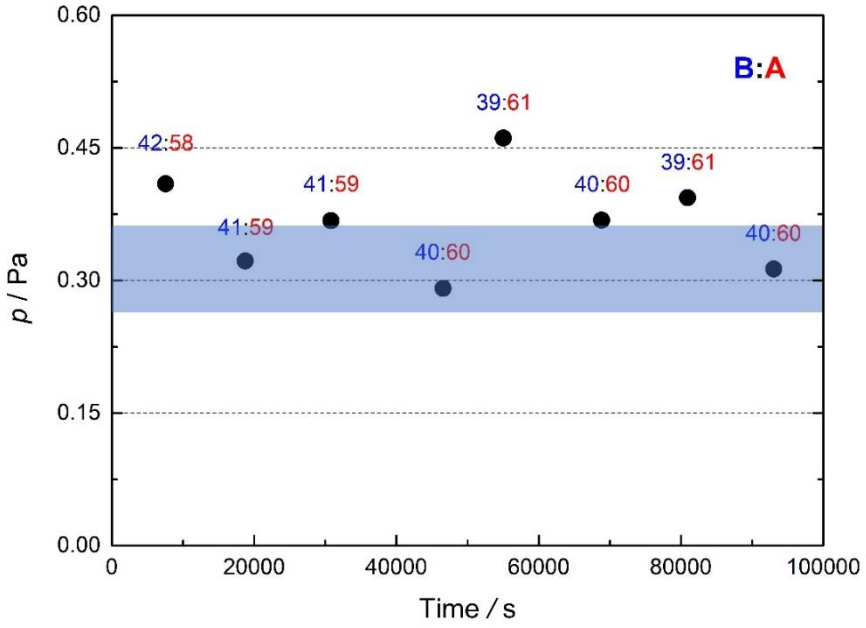

Figure 6.51. Plot of pressure vs total effusion time, at T = (306.2 ± 0.1) K, showing the progressive decrease of the measured vapor pressure in successive Knudsen runs of [DMTHPH][EtCOO], and the observed base:acid (**B**:**A**) proportion ratio (inside the Knudsen effusion cell) at the end of each run.

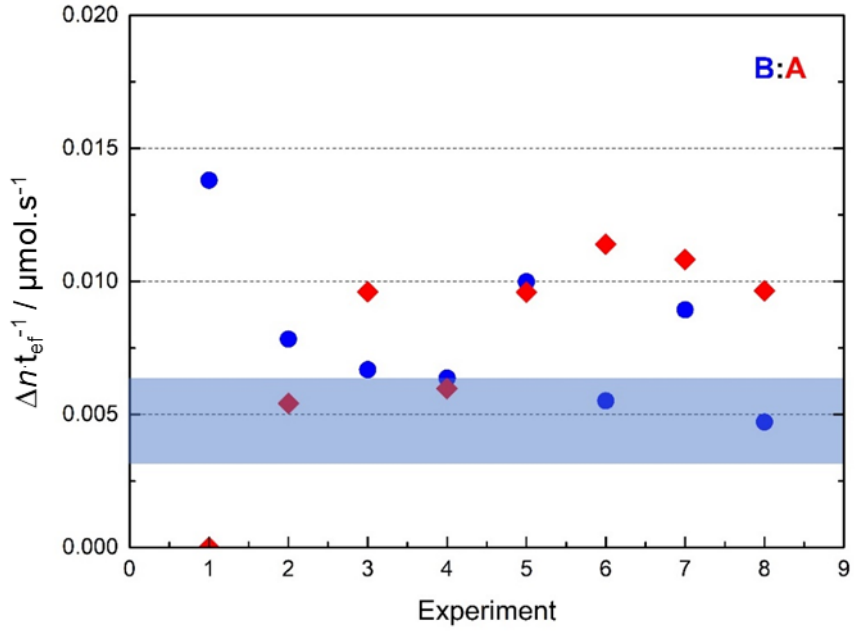

Figure 6.52. Calculated molar effusion rates, at T = (306.2 ± 0.1) K, of base (blue circles) and acid (red diamonds) in each Knudsen run of [DMTHPH][EtCOO].

Table 6.16. Knudsen effusion results for [DMTHPH][nPentCOO], at T = (306.2 ± 0.1) K.

Experiment	m_i / mg	m_f / mg	Δm / mg	t_{ef} / s	$\langle p \rangle$ / Pa	final x_B:x_A / %	$\Delta n \cdot t_{ef}^{-1}$ / μmol.s^{-1}
1	293.72	280.94	12.78	3423	0.88	44:56	0.042 : 0.008
2	265.11	248.04	17.07	7786	0.52	42:58	0.014 : 0.005
3	210.81	200.42	10.39	10587	0.23	40:60	0.007 : 0.001
4	179.72	164.37	15.35	17491	0.21	39:61	0.004 : 0.004
5	128.57	116.33	12.24	22747	0.13	37:63	0.003 : 0.002
6	97.49	86.69	10.80	17401	0.15	36:64	0.002 : 0.003
7	71.69	60.19	11.50	15356	0.18	34:66	0.003 : 0.004

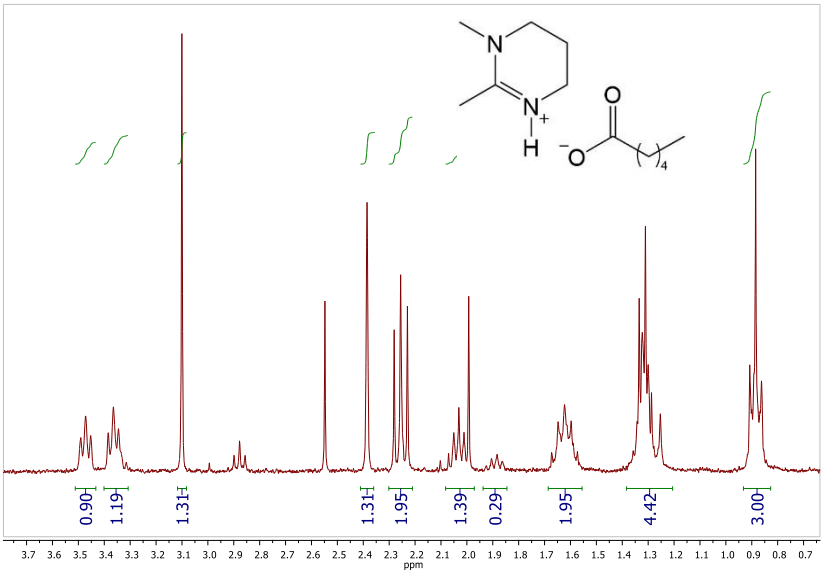

Figure 6.53. ^{1}H NMR spectra of the last Knudsen experiment of [DMTHPH][nPentCOO].

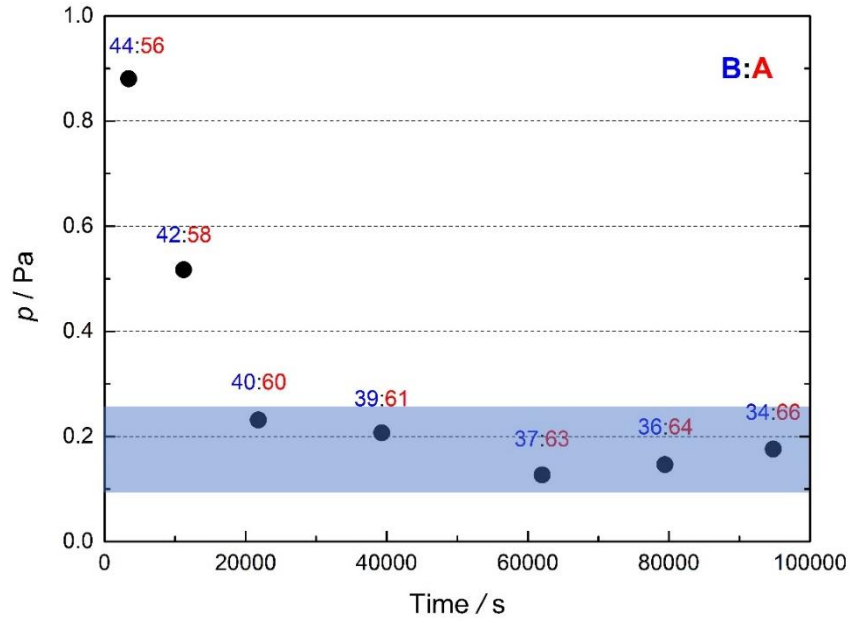

Figure 6.54. Plot of pressure vs total effusion time, at *T* = (306.2 ± 0.1) K, showing the progressive decrease of the measured vapor pressure in successive Knudsen runs of [DMTHPH][nPentCOO], and the observed base:acid (**B**:**A**) proportion ratio (inside the Knudsen effusion cell) at the end of each run.

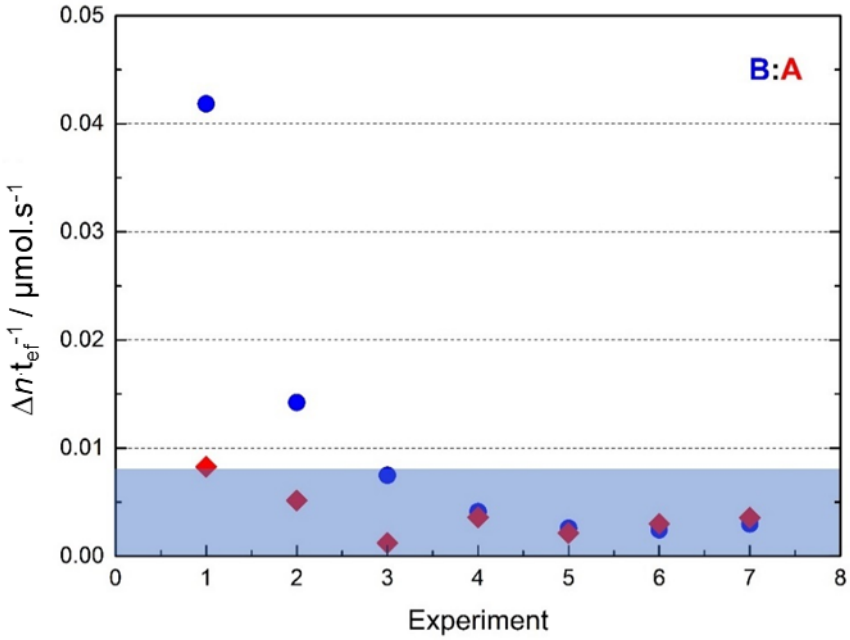

Figure 6.55. Calculated molar effusion rates, at *T* = (306.2 ± 0.1) K, of base (blue circles) and acid (red diamonds) in each Knudsen run of [DMTHPH][nPentCOO].

Table 6.17 sums the obtained results for all the PILs studied, namely, the equilibrium vapor pressures, molar fractions and activity coefficients.

Table 6.17. Equilibrium vapor pressures, molar fractions and activity coefficients concerning the PILs studied; p_{eq}, p^*_{acid} and p^*_{base} are, respectively, the equilibrium vapor pressures of the PILs at the azeotropic composition, pure acid and pure base; x_{acid} and x_{base} are the molar fractions of each constituent of the PIL in the azeotrope; and γ_{acid} and γ_{base} are the calculated activity coefficients.

PIL	p_{eq} / Pa	p^*_{base} / Pa	p^*_{acid} / Pa	x_{base}	x_{acid}	γ_{base}	γ_{acid}
[DBNH][EtCOO]	0.27	21.7	902	0.42	0.58	0.0125	0.0003
[DBNH][nPrCOO]	0.18	21.7	270	0.42	0.58	0.0083	0.0007
[DBNH][nButCOO]	0.18	21.7	55.9	0.41	0.59	0.0081	0.0032
[DBNH][nPentCOO]	0.16	21.7	14.3	0.39	0.61	0.0073	0.0111
[DBNH][nHexCOO]	0.09	21.7	4.4	0.37	0.63	0.0042	0.0206
[DBNH][nHeptCOO]	0.08	21.7	1.6	0.36	0.64	0.0039	0.0527
[DBNH][FPrCOO]	0.08	21.7	1471	0.50	0.50	0.0034	0.0001
[DBUH][EtCOO]	0.14	4.7	902	0.46	0.54	0.0305	0.0002
[DBUH][nPrCOO]	0.10	4.7	270	0.44	0.56	0.0206	0.0004
[DBUH][nButCOO)	0.09	4.7	55.9	0.44	0.56	0.0190	0.0016
[DBUH][nPentCOO]	0.07	4.7	14.3	0.42	0.58	0.0151	0.0050
[DBUH][nHexCOO]	0.07	4.7	4.4	0.42	0.58	0.0158	0.0169
[DBUH][nHeptCOO]	0.07	4.7	1.6	0.39	0.61	0.0140	0.0411
[DMTHPH][EtCOO]	0.29	-*	902	0.40	0.60	-	-
[DMTHPH][nPentCOO]	0.13	-*	14.3	0.35	0.65	-	-

References of vapor pressures for carboxylic acids and superbases used in this study. [6.25-6.27]
*- No value in literature.

The activity coefficients, γ, of each component, at T = (306.2 ± 0.1) K and at the azeotropic composition of the PILs studied, were calculated using equation 6.4:

$$\gamma_i = \frac{p(\text{PIL}) \cdot x_i(g)}{p_i^* \cdot x_i(l)} = \frac{p(\text{PIL})}{p_i^*} \qquad \textbf{(6.4)}$$

where p(PIL) is the equilibrium vapor pressure of the PIL at the azeotropic composition, p_i^* is the vapor pressure of each pure component, acid and base, at T = (306.2 ± 0.1) K, and x_i(g) and x_i(l) are their molar fraction in gas and liquid phase, respectively; x_i(g) = x_i(l) at the azeotrope. The equilibrium vapor pressures of the acids and bases, at T = (306.2 ± 0.1) K, were taken from the literature. [6.25-6.27] The variation of γ_{acid} and γ_{base} with the chain length of the acid is shown in figure 6.56.

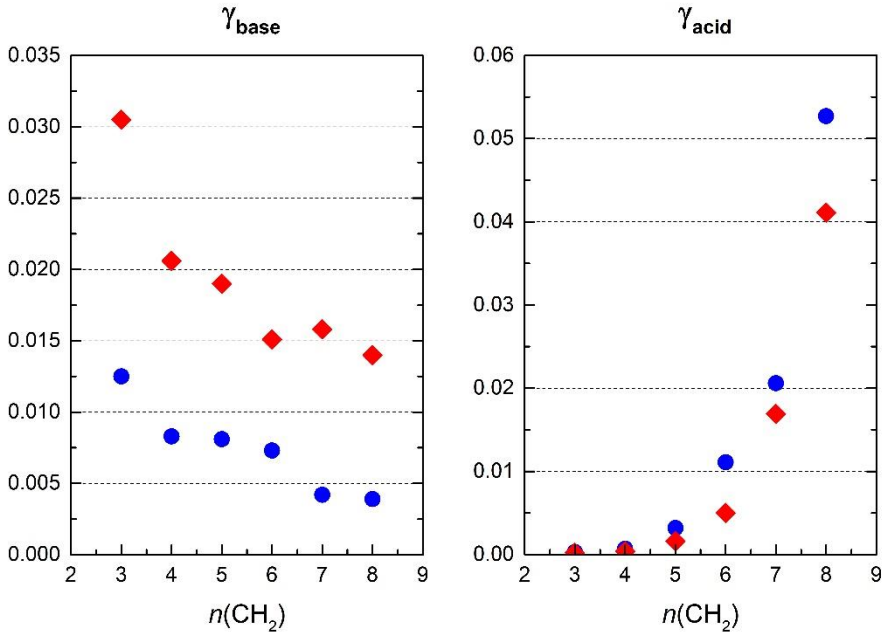

Figure 6.56. Activity coefficients of the base and acid, γbase and γacid, at T = (306.2 ± 0.1) K, as a function of the chain length of the acid for the DBN (blue circles) and DBU (red diamonds) PILs studied.

All PILs show pronounced negative deviations from Raoult's Law, with a significant decrease of vapor pressure, corroborating that the mixture is significantly stabilized relative to the pure separated acids and bases. The trends in γ depend on the

trends in the vapor pressures of the PILs and of the pure components. Since *p*(PILs) varies very little on changing the acid or the base when compared to p^*_{acid} and p^*_{base} the derived *γ* follow mostly the change in volatility of the pure components. Nonetheless, these results are further evidence that the PILs have strong ionic character.

Concerning the pK_a of the carboxylic acids it is well established that fluorination increases significantly the acidity of heptafluorobutyric acid, while the increase in chain length has a negligible effect on pK_a. [6.28] Literature reports have shown that the trends in pK_a of carboxylic acids are similar in other solvents, [6.28-6.29] and hence there are no reasons to suspect that the relative acid strength of the acids studied will change significantly in the PIL medium. However, the relative base strength of DMTHP, DBN and DBU is harder to evaluate. According to the literature DBU is the strongest base in acetonitrile and gas phase, [6.30] and that should be followed in the PIL medium as well. Although DBN is also considered an organic superbase, it is not clear if DMTHP is the weaker base. Hence, it was evaluated the relative basicity of the three bases studied by recording the ^{1}H NMR spectra of the DBN:DBU:nPrOOH (1:1:1) and DMTHP:DBN:FPrCOOH (1:1:1) mixtures in $CDCl_3$, and by calculating the gas phase proton affinities using computational chemistry methods. The results indicate the following order of base strength: DBU > DBN ≈ DMTHP. In terms of relative volatility, the trends in the pure liquid acids and bases follow classical rules and are well documented in the literature. [6.25-6.27, 6.31-6.35] In the acids the volatility decreases with increasing chain length and the perfluoroacids are more volatile than the corresponding non-fluorinated analogues. [6.25] In the bases studied the decrease in volatility follows the increase in molecular size: DMTHP > DBN > DBU. [6.31, 6.34-6.35]

The information about relative acid and base strength and volatility helps rationalizing the results of table 6.21 and figure 6.56. In the perfluorinated PIL the stronger acidity of FPrCOOH ensures that the acid-base reaction is virtually complete and the 50:50 ratio results from most species being ions. This PIL has the highest ionicity and a negligible proportion of neutral species. In the other PILs, the acidity of the carboxylic group is not strong enough to convert all species into ions and consequently a significant fraction of neutral acid and base remain in the liquid mixture. Neutral species establish weaker interactions than the ions and are more prone to vaporize. The azeotropic composition will thus depend on the extent of the acid-base equilibrium and on the relative stability of the neutral species in the liquid mixture. The increase in the azeotrope molar fraction of the acid as its alkyl chain increases follows the decrease of the acid's volatility. It is also expected that the acid-base equilibrium will be less shifted to the ions side as the PIL medium becomes increasingly less polar. Hence, both reasons contribute for an azeotrope farther from 50:50. The trend on changing the base

is due to differences in base strength and volatility. The azeotropic composition for the DBU PILs is closer to 50:50 because DBU is the strongest and least volatile of the bases. Although DBN and DMTHP are similarly basic, DMTHP is more volatile and thus its azeotropic proportion is lower. The effect of the volatility of the pure components in their activity in the PIL mixtures is nicely evidenced in the experimental results: the lower γ_{base} of DBN in the azeotrope (table 6.21 and figure 6.56) is explained by its higher volatility in comparison to DBU. Furthermore, the lower γ_{acid} in the DBU PILs translate the greater stabilization of the mixture due to the stronger ionic character of these PILs. [6.31]

Figure 6.57 depicts the fraction of base at equilibrium, x_{base}, as a function of the size of the acid (region A: shorter acids and region B: longer acids). For shorter acids (namely propionic, butyric and pentanoic) the fraction of base at equilibrium is quite similar in both PIL families. For longer acids the fraction of base decreases quite linearly. These results also suggest some sort of change in the structure of the PIL azeotrope after a certain size of the acid. The plot gives an indication that the proportion will decrease asymptotically to x_{base} = 0.33 in agreement with a complex 1:2 (base:acid) formation (figure 6.58) for longer acids.

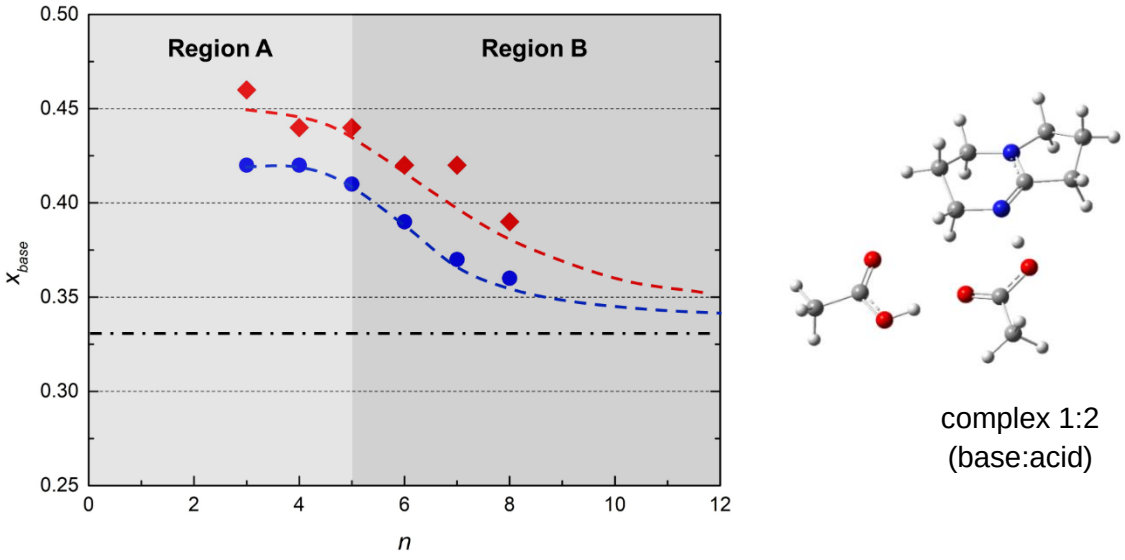

Figure 6.57. Fraction of base at the equilibrium, x_{base}, at T = (306.2 ± 0.1) K, as a function of the chain length of the acid for the DBN (blue circles) and DBU (red diamonds) PILs studied and a schematic representation of the hydrogen bond between the PIL ion pair and the excess acid. The geometry of the gaseous trimer complex was optimized using M06-2X/6-311++G(d,p).

6.4. References

[6.1] Greaves, T. L.; Drummond, C. J. *Chem. Rev.* **2008**, *108*, 206-237.

[6.2] Greaves, T. L.; Drummond, C. J. *Chem. Rev.* **2015**, *115*, 11379-11448.

[6.3] Yoshizawa, M.; Xu, W.; Angell, C. A. *J. Am. Chem. Soc.* **2003**, *125*, 15411-15419.

[6.4] Lopes, J. N. C.; Rebelo, L. P. N. *Phys. Chem. Chem. Phys.* **2010**, *12*, 1948-1952.

[6.5] MacFarlane, D. R.; Forsyth, M.; Izgorodina, E. I.; Abbott, A. P.; Annat, G.; Fraser, K. *Phys. Chem. Chem. Phys.* **2009**, *11*, 4962−4967.

[6.6] Yaghini, N.; Nordstierna, L.; Martinelli, A. *Phys. Chem. Chem. Phys.* **2014**, *16*, 9266−9275.

[6.7] Ueno, K.; Tokuda, H.; Watanabe, M. *Phys. Chem. Chem. Phys.* **2010**, *12*, 1649−1658.

[6.8] Walker, A. J. *Chim. Oggi* **2007**, *25*, 17−19.

[6.9] Olivier-Bourbigou, H.; Magna, L.; Morvan, D. *Appl. Catal. A* **2010**, *373*, 1−56.

[6.10] Pourcelly, G. *Pet. Chem.* **2011**, *51*, 480−491.

[6.11] Burrell, G. L.; Burgar, I. M.; Separovic, F.; Dunlop, N. F. *Phys. Chem. Chem. Phys.* **2010**, *12*, 1571−1577.

[6.12] Johansson, K. M.; Izgorodina, E. I.; Forsyth, M.; MacFarlane, D. R.; Seddon, K. R. *Phys. Chem. Chem. Phys.* **2008**, *10*, 2972−2978

[6.13] Santos, L. M. N. B. F.; Lima, L. M. S. S.; Lima, C. F. R. A. C.; Magalhães, F. D.; Torres, M. C.; Schröder, B.; Ribeiro da Silva, M. A. V. *J. Chem. Thermodyn.* 43 (**2011**) 834–843.

[6.14] Lima, L. M. S. S., Ph.D. Thesis, University of Porto, **2009**.

[6.15] Clarke, E. C. W.; Glew, D. N. *Trans. Faraday Soc.* 62 (**1966**) 539–547.

[6.16] Dushman, S., *Scientific Foundations of Vacuum Technique*, John Wiley & Sons, New York, **1949**.

[6.17] Oonk, H. A. J.; Van der Linde, P. R.; Huinink, J.; Blok, J. G. *J. Chem. Thermodyn.* 30 (**1998**) 897–907.

[6.18] Vanderlinde, P.; Blok, J.; Oonk, H. *J. Chem. Thermodyn.* 30 (**1998**) 909–917.

[6.19] Mohr, P. J.; Taylor, B. N.; Newell, D. B. *Rev. Mod. Phys.* 84 (**2012**) 1527–1605.

[6.20] Knudsen, M. *Annalen der Physik* 333 (**1909**) 75–130.

[6.21] Knudsen, M. *Annalen der Physik* 333 (**1909**) 999–1016.

[6.22] Knudsen, M. *Annalen der Physik* 334 (**1909**) 179–193.

[6.23] Ribeiro da Silva, M. A. V.; Monte, M. J. S.; Santos, L. M. N. B. F. *J. Chem. Thermodyn.* 38 (**2006**) 778–787.

[6.24] Sauerbrey, G. *Z. Phys.* 155 (1959) 206–222.

[6.25] “Physical Constants of Organic Compounds”, in *CRC Handbook of Chemistry and Physics, Internet Version 2007, (87th Edition)*, David R. Lide, ed., Taylor and Francis, Boca Raton, FL.

[6.26] Clifford, S. L.; Ramjugernath, D.; Raal, J. D. *J. Chem. Eng. Data* **2004**, *49*, 1189–1192.

[6.27] Verevkin, S. P. *J. Chem. Eng. Data* **2000**, *45*, 953–960.

[6.28] “Dissociation Constants of Organic Acids and Bases”, in *CRC Handbook of Chemistry and Physics, Internet Version 2007, (87th Edition)*, David R. Lide, ed., Taylor and Francis, Boca Raton, FL.

[6.29] Grunwald, E.; Berkowitz, B. J. *J. Am. Chem. Soc.* **1951**, *73*, 4939–4944.

[6.30] Ishikawa, T., *Superbases for Organic Synthesis: Guanidines, Amidines, Phosphazenes and Related Organocatalysts*, John Wiley & Sons, 2009.

[6.31] Ribeiro, F. M. S.; Lima, C. F. R. A. C.; Vaz, I. C. M.; Rodrigues, A. S. M. C.; Sapei, E.; Melo, A.; Silva, A. M. S.; Santos, L. M. N. B. F. *Phys. Chem. Chem. Phys.* **2017**, *19*, 16693–16701.

[6.32] https://www.nist.gov/ in 07-June-2017.

[6.33] Steele, W. V.; Chirico, R. D.; Knipmeyer, S. E.; Nguyen. A. *J. Chem. Eng. Data* **2002**, *47*, 715–724.

[6.34] Lipkind, D.; Rath, N.; Chickos, J. S.; Pozdeev, V. A.; Verevkin, S. P. *J. Phys. Chem. B* **2011**, *115*, 8785–8796.

[6.35] Boys, S. F.; Bernardi, F. *Mol. Phys.* **1970**, *19*, 553−566.

CHAPTER 7

Cohesive Energies of Protic Ionic Liquids

7. Cohesive Energies of Protic Ionic Liquids

In this chapter, Calvet microcalorimetry was used to measure the enthalpies of vaporization, Δ*H*vap, of the superbases, 1:1 PILs and PILs with different compositions. These enthalpies were used to evaluate the effect of small molecular changes in the acid and/or base (e.g. increase of chain length) on the cohesive enthalpy of the liquid phase. This knowledge can also give insights about the ionicity and speciation of the PILs in the liquid and gas phases, already presented in the last chapter.

7.1. Experimental methodology

7.1.1. Calvet microcalorimetry

Fundamentals

Tian Calvet [7.1] used the heat conduction principle for constructing calorimeters. He [7.2-7.3] developed a calorimeter based on twin Tian systems, symmetrically placed inside an isothermic block, providing an effective compensation for uneven heat effects. These systems are well described in literature. [7.4-7.5]

The Calvet microcalorimeters are mainly suited for the study of slow reactions and the measurement of processes that deal with very small amounts of energy, hence the designation ‘microcalorimeter’. These systems can be divided into two groups: high-temperature calorimeters, which are used to study/determine slower thermal processes, phase transitions and heat capacities, and low-temperature calorimeters, commonly used in the study of biological processes. These microcalorimeters have some disadvantages, such as longer response times and very slow heating and cooling rates, when compared to a Differential scanning calorimeter for example. The Calvet microcalorimeter, as schematically shown in figure 7.1, is basically composed of two identical calorimetric cells, placed in symmetrically arranged cavities in a large metal block (1). The process under study occurs in the sample cell (2), while the other cell (3) operates as the reference. The heat transfer between the two cells and the isothermal block is monitored by high thermal conductivity thermopiles containing many identical thermocouples, connected in series, regularly arranged around the calorimetric cells. The thermopiles (4) act as the measuring sensor of the difference in temperature between the outer surface of the calorimetric cell and the inner surface of the isothermal block and, simultaneously, as a thermal bridge between the cells and the isothermal block. The two calorimetric cells thermopiles are connected in opposition (5) so that the

measured output signal results in a potential difference generated by the two thermopiles. The heat flow is directly proportional to the temperature gradient between these two calorimetric cells and compensated by Peltier effect (for exothermic processes) or Joule heating (for endothermic processes), to keep the temperature as constant as possible in the system.

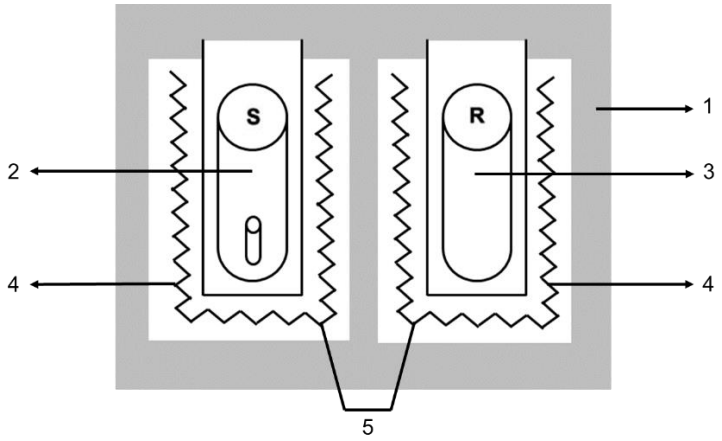

Figure 7.1. General schematic representation of a heat flux Calvet microcalorimeter (S. sample cavity; R. reference cavity;1. isothermal block; 2. sample cell; 3. reference cell; 4. thermopiles; 5. differential connection between thermopiles).

The experimental procedure used in these calorimeters is quite similar to the one used in the Drop calorimeter (Chapter 5), “the drop technique”. It was developed by Skinner et al. [7.6] for the determination of enthalpies of sublimation. A known mass of sample is putted in a small glass capillary, at room temperature, and dropped into the sample cell of the calorimeter. To compensate the thermal disturbance produced by dropping the glass capillary into the sample cell, an empty capillary, with similar mass to the one (empty) used in the sample, is simultaneously dropped into the reference cell. With this technique the determination of the heat associated solely with the process taking place inside the sample cell is assured. In the past few years, this technique has been adapted to the study of liquid compounds by Ribeiro da Silva and co-workers [7.7], here in our group, to obtain molar enthalpies of vaporization. Note that the processes do not occur under equilibrium conditions, which can compromise the accuracy of the obtained results. Some works [7.6] showed that the results obtained by Calvet microcalorimetry can vary up to 5 % from the results derived from vapor pressures. For the Calvet microcalorimeter used in this work [7.8], it was concluded previously, that the uncertainty of the method is lower than 2 %, however, it is always conditioned by the compound’s purity and thermal stability, the appropriate choice of the reference

compounds used in calibration, and the uncertainty introduced by the enthalpic corrective term, $\Delta_{298.15\,K}^{T}H_m^0(g)$.

Typical thermogram and results

The thermal processes studies occurring inside the calorimeter are performed by measuring the heat flow over time, which defines the thermogram, a typical one, illustrated in figure 7.2.

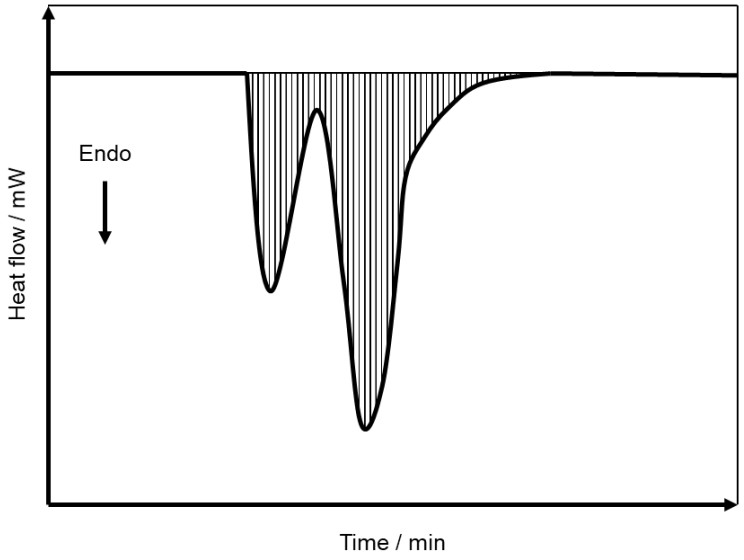

Figure 7.2. Schematic representation of a typical Calvet microcalorimetry thermogram.

When the thermal equilibrium between the cells and the calorimetric block is reached, at a predefined temperature *T*, the initial baseline is defined. When the capillary tubes are dropped at room temperature (ca. 298 K) into the respective calorimetric cells, the first endothermic peak, the smaller one, is observed due to the heating of the sample from 298 K to the temperature of the calorimeter. Note that if *T* is larger than the temperature of fusion of the compound, the first endothermic peak will include not only this heating, but also the enthalpy of fusion at that temperature *T*. When both capillaries reach thermal stability inside the calorimeter, the system is evacuated, and the sample is rapidly removed from the calorimetric cell originating a second endothermic curve in the thermogram, which is generally attributed to the sublimation or vaporization of the sample.

Then, the enthalpic variation of the total process can be determined from the integration of the total area (both peaks) under the baseline of the thermogram. This thermogram includes the following enthalpic contributions:

- Thermal disturbances produced by dropping the glass capillaries into the calorimetric cells;
- Heating of the glass capillaries and sample, in the condensed state, from 298 K to the temperature of the calorimeter;
- Phase transition(s) of the sample.

The standard molar enthalpy of sublimation or vaporization determination, at T = 298.15 K, is obtained from the experimental result of $\Delta^{g,T}_{cr/l,298.15\,K}H^0_m$, according to the thermodynamic cycle shown in figure 7.3.

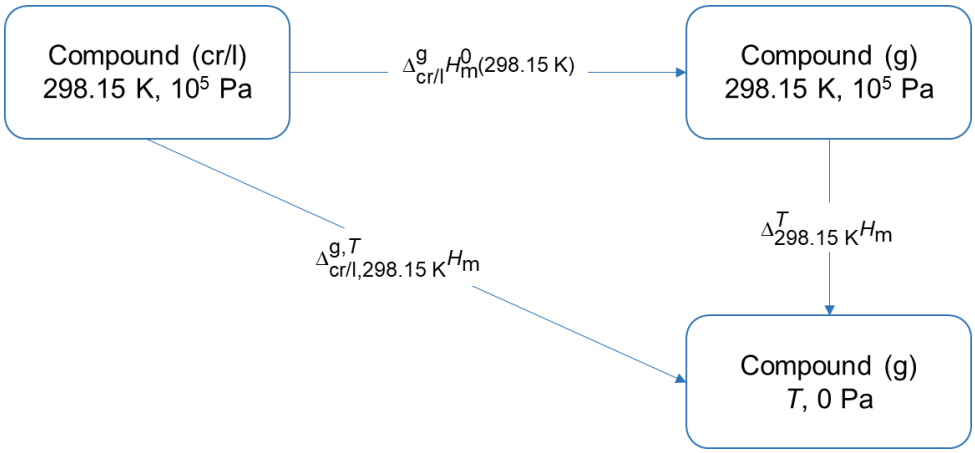

Figure 7.3. Illustrative thermodynamic cycle showing the representative processes of a Calvet microcalorimetry sublimation or vaporization experiment.

The standard molar enthalpy of sublimation or vaporization, at the reference temperature T = 298.15 K, can then be determined from the following expression:

$$\Delta^{g}_{cr/l}H^0_m(298.15\ K) = \Delta^{g,T}_{cr/l,298.15\,K}H_m - \Delta^{T}_{298.15\,K}H_m(g) \qquad \textbf{(7.3)}$$

where the term $\Delta^{T}_{298.15\,K}H_m(g)$ corresponds to the thermal correction of enthalpy, in the gaseous state, and can be estimated by computational methods, more details in chapter 4, or by group additivity methods [7.9]

Calibration

Temperature calibration

The temperature's calibration of the calorimeter's isothermal block was performed in previous works [7.8] and was achieved by establishing a relation (given by expression 7.4) between the actual temperature of the calorimetric cells as measured by a PT100 temperature sensor calibrated against a SPRT temperature probe (25 Ω; Tinsley, 5187A), and that indicated by the Setaram G11 temperature controller.

$$\theta_{real}/^{o}C = 1.0054\ \theta_{G11}/^{o}C - 3.822 \qquad \textbf{(7.4)}$$

Blank calibration

The mass of the capillaries (sample and reference) is not the same in each experiment, so the heat capacities of the capillary tubes do not cancel each other completely, and their contributions are not insignificant for the value of the total enthalpy change. So, to take this difference into account and, also for, the different sensibilities of the two measuring cells, this additional enthalpic contribution was determined through blank experiments. For the calorimetric system used, blank experiments were performed in another work [7.8], using capillaries with masses ranging between 20 and 30 mg (similar to those used in the present work) and the same procedure, where empty capillary tubes of similar masses are simultaneously dropped into both calorimetric cells. Expression 7.5 was used for the determination of the enthalpic blank correction, ΔH_{corr} (blank), as a function of the temperature difference between the calorimetric cell and 298.15 K, and the masses of the reference, m_{ref}, and empty sample capillary tubes, m_{exp}. Where the values of the fitter coefficients are: a = –20.3902, b = –0.88204, c = 0.816818, d = 1.814894). [7.8]

$$\Delta H_{corr}(\text{blank})/\text{mJ} = a+[b(m_{exp}/\text{mg})+ c(m_{ref}/\text{mg})+ d]\cdot[(T/\text{K})-298.15] \qquad \textbf{(7.5)}$$

Calorimeter calibration

Both calorimetric cells are not covered by thermocouples and through this small and uncovered area, some thermal leakage can occur by convection and/or radiation processes. To take this into account and other heat transfer processes, calibration

experiments were performed, under the same conditions carried out in the experiments with the compounds under study, to determine a proportionality factor, K_{cal}, between the heat involved in the reaction and the area of the thermogram obtained experimentally, according to equation 7.6.

$$K_{cal}(T) = \frac{\Delta^{g,T}_{cr/l,298.15\,K} H^0_m}{\Delta^{g,T}_{cr/l,298.15\,K} H^0_m(cal)} \qquad \textbf{(7.6)}$$

Note that the standard substance selected as calibrant should have volatility comparable to that of the compound under study, within the experimental temperature range. The calibrations in this work were performed using recommended primary standard substances, [7.16] ferrocene and undecane, whose molar enthalpies of sublimation are rigorously established. The calibration constant (average), at a given temperature T, (K_{cal}), was determined as the mean of at least eight concordant values.

Apparatus

The calorimeter used is based on a commercial high-temperature Calvet microcalorimeter Setaram HT1000D, in isothermal mode, which can be operated from room temperature to 1300 K, using the drop calorimetric technique referred above. Both the apparatus and technique have been previously and well described in the literature [7.8] and the complete system, schematized in figure 7.4, includes, in addition to the Calvet microcalorimeter (A), a pumping system (B) and a glass vacuum line (C), which will be briefly described next.

Calvet microcalorimeter

The microcalorimeter Setaram HT1000D consists of an internal isothermal metal block of high heat capacity (1) externally lined with ceramic material (2), containing two identical cavities in which the calorimetric cells (3) are introduced. The base of each cavity is surrounded by a thermopile (4) composed of 496 radially arranged thermocouples (Pt-Pt/Rh) connected in series. The temperature of the metal block is regulated by a Setaram G11 control system, which also has the function of amplifying and registering the electronic signal from the thermocouples. The temperature is programmed through the Setaram 3.20 software, installed in an interfaced computer that is also used for the data acquisition, graphical representation of the thermogram in real time, and for the related calculations.

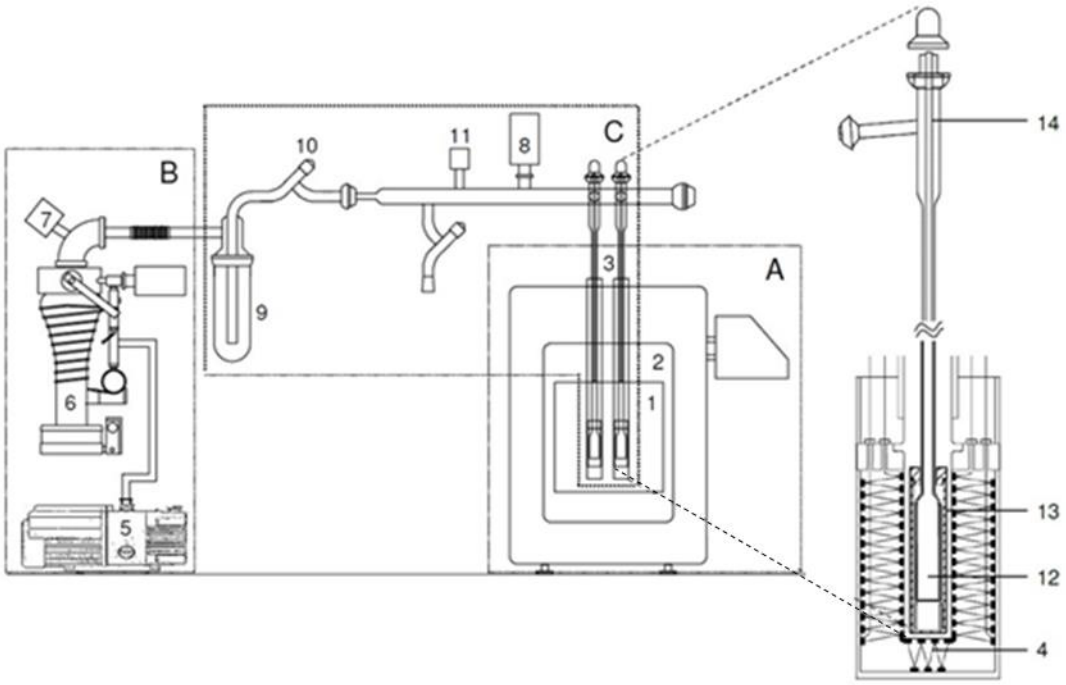

Figure 7.4. Schematic representation of the complete Calvet microcalorimeter: A. Calvet microcalorimeter Setaram HT1000D (1. isothermal metal block; 2. ceramic lining; 3. calorimetric cells; 4. thermopile); B. Vacuum pumping system (5. rotary pump; 6. oil diffusion pump; 7. Pirani gauge; 8. Penning gauge); C. Vacuum line (9. Liquid nitrogen glass trap; 10. isolation Teflon valve; 11. air inlet Teflon valve; 12. pyrex vessel; 13. kanthal cylinder; 14. Inner pyrex tube). Image adapted from ref. [7.8]

Vacuum pumping system

The vacuum pumping system consists of an Edwards RV5 rotary pump (5), which is used both for pre-evacuating the system and also for backing up the Edwards Diffstak 63 oil diffusion pump (6). An Edwards APG-M Pirani gauge (7) is used to measure the pressure of the system during the pre-evacuation process and an Edwards AIM-S Penning gauge (8) is used to measure the pressure throughout the sublimation process.

Vacuum line and calorimetric cells

The twin cells are connected to the vacuum pumping system through a glass line that includes a liquid nitrogen trap (9) to condense the sublimated samples and prevent contamination of the pumping system. Between the trap and the calorimetric cells there are two valves, one allowing the isolation of the pumping system (10) and the other used to admit air in the system (11) for restoring the atmospheric pressure and allowing the cleaning of the trap. All glass connections in the system are made of greaseless

spherical joints from Young. The calorimetric cells (3) consist of long inlet tubes made of Pyrex® glass that extend to the inside of the thermal block ending in cylindrical small vessels (12). The vessels are tightly fitted into cylinders made of kanthal® (iron-chromium-aluminium alloy used for high-temperature applications) (13), which promote good thermal contact between the calorimetric vessel and the isothermal block. The calorimetric cells are equipped with inner tubes (14), through which the capillaries are dropped. They can be removed and cleaned without disturbing the calorimetric cells, allowing consecutive experiments.

Experimental

The standard molar enthalpies of vaporization, $\Delta_l^g H_m^0$ at T = 298.15 K, for several 1:1 PILs, superbases, and PILs with non-stoichiometric compositions were measured in a high temperature Calvet microcalorimeter, SETARAM model HT1000D, using a similar technique of the drop method described by Skinner *et al.*.[7.6] The measurement procedure and the description of the apparatus have been described in detail by Santos *et al.*.[7.8] Samples of about 2-6 mg each are placed into thin capillary tubes, sealed at one end, and dropped, simultaneously with the corresponding blank tube, at T = 298.15 K, into the hot reaction zone of the calorimeter, which is kept at a fixed temperature T. The heating of the sample from room temperature to the calorimeter hot zone temperature, T, is recorded, and after thermostability is reached, the sample is vaporized into the vacuum.

7.2. Results and discussion

7.2.1. Equimolar PILs and superbases

Tables 7.1 presents the experimental results for the calibration of the calorimeter of each pure compound and tables 7.2 to 7.25 show the experimental data obtained for the PILs studied.

Table 7.1. Experimental results obtained by Calvet microcalorimetry for the calibration experiments of each pure compound. *T* (at K) being the temperature at which the Calvet measurements were performed.

Compound	*T* / K	Calibrant	n	*k*
DBN	340.0	Undecane	7	0.997 ± 0.018
DBU	340.0	Undecane	7	0.997 ± 0.018
DMTHP	339.8	Undecane	5	0.996 ± 0.017
[DBNH][MeCOO]	375.8	Ferrocene	7	1.000 ± 0.020
[DBNH][EtCOO]	375.9	Ferrocene	7	1.000 ± 0.020
[DBNH][nPrCOO]	375.7	Ferrocene	7	1.000 ± 0.020
[DBNH][nButCOO]	396.6	Ferrocene	7	1.009 ± 0.018
[DBNH][nPentCOO]	396.3	Ferrocene	7	1.009 ± 0.018
[DBNH][nHexCOO]	396.4	Ferrocene	7	1.009 ± 0.018
[DBNH][nHeptCOO]	396.3	Ferrocene	7	1.009 ± 0.018
[DBUH][MeCOO]	375.8	Ferrocene	7	1.000 ± 0.020
[DBUH][EtCOO]	375.9	Ferrocene	7	1.000 ± 0.020
[DBUH][nPrCOO]	375.9	Ferrocene	7	1.000 ± 0.020
[DBUH][nButCOO]	396.4	Ferrocene	7	1.009 ± 0.018
[DBUH][nPentCOO]	396.4	Ferrocene	7	1.009 ± 0.018
[DBUH][nHexCOO]	396.4	Ferrocene	7	1.009 ± 0.018
[DBUH][nHeptCOO]	396.6	Ferrocene	7	1.009 ± 0.018
[DMTHP][EtCOO]	396.4	Ferrocene	7	1.009 ± 0.018
[DMTHP][nPrCOO]	396.4	Ferrocene	7	1.009 ± 0.018
[DMTHP][nButCOO]	396.4	Ferrocene	7	1.009 ± 0.018
[DMTHP][nPentCOO]	396.4	Ferrocene	7	1.009 ± 0.018
[DMTHP][nHexCOO]	396.3	Ferrocene	7	1.009 ± 0.018
[DMTHP][nHeptCOO]	396.3	Ferrocene	7	1.009 ± 0.018

The correction H_m^0 (g, *T*) - H_m^0 (g, 298.15 K) / kJ·mol^{-1} was calculated for all the compounds. The full geometry optimizations, with no symmetry restrictions, were performed at the B3LYP/6-311++G(d,p) levels of theory and the enthalpy values were calculated at 298.15 K and at *T* (temperature at which the Calvet measurements were performed).

Table 7.2. Experimental results obtained by Calvet microcalorimetry for the vaporization of DBN (*T*=340.0 K). *T* (at K) being the temperature at which the Calvet measurements were performed.

	$m_{compound}$ / mg	$\Delta_l^g H_m^0$ / kJ·mol^{-1}	$\langle\Delta_l^g H_m^0\rangle$ / kJ·mol^{-1}	H_m^0 (g, *T*) - H_m^0 (g, 298.15 K) / kJ·mol^{-1}
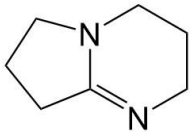	4.00	68.67	70.3 ± 1.1	6.3 ± 1.0
	3.10	71.42		
	3.88	72.52		
	4.27	70.35		
	4.05	69.77		
	2.39	68.95		
	2.74	70.18		
	$\Delta_l^g H_m^0$ (298.15 K) / kJ·mol^{-1} = (63.9 ± 1.5)			

Table 7.3. Experimental results obtained by Calvet microcalorimetry for the vaporization of DBU (*T*=340.0 K). *T* (at K) being the temperature at which the Calvet measurements were performed.

	$m_{compound}$ / mg	$\Delta_l^g H_m^0$ / kJ·mol^{-1}	$\langle\Delta_l^g H_m^0\rangle$ / kJ·mol^{-1}	H_m^0 (g, *T*) - H_m^0 (g, 298.15 K) / kJ·mol^{-1}
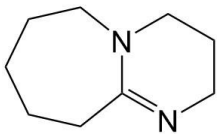	3.84	76.71	77.9 ± 1.1	8.1 ± 1.0
	4.00	78.51		
	2.18	76.84		
	3.58	77.21		
	5.23	79.41		
	4.45	79.57		
	3.46	76.71		
	$\Delta_l^g H_m^0$ (298.15 K) / kJ·mol^{-1} = (69.7 ± 1.5)			

Table 7.4. Experimental results obtained by Calvet microcalorimetry for the vaporization of DMTHP (*T*=339.8 K). *T* (at K) being the temperature at which the Calvet measurements were performed.

	$m_{compound}$ / mg	$\Delta_l^g H_m^0$ / kJ·mol^{-1}	$\langle\Delta_l^g H_m^0\rangle$ / kJ·mol^{-1}	H_m^0 (g, *T*) - H_m^0 (g, 298.15 K) / kJ·mol^{-1}
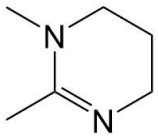	3.83	69.72	69.9 ± 1.1	6.4 ± 1.0
	3.57	70.82		
	4.22	67.99		
	1.18	71.19		
	2.24	71.17		
	4.01	69.54		
	3.64	68.97		
	$\Delta_l^g H_m^0$ (298.15 K) / kJ·mol^{-1} = (63.5 ± 1.5)			

Table 7.5. Experimental results obtained by Calvet microcalorimetry for the vaporization of [DBNH][MeCOO] (*T*=375.8 K). *T* (at K) being the temperature at which the Calvet measurements were performed.

	$m_{compound}$ / mg	$\Delta_l^g H_m^0$ / kJ·mol^{-1}	$\langle\Delta_l^g H_m^0\rangle$ / kJ·mol^{-1}	H_m^0 (g, *T*) - H_m^0 (g, 298.15 K) / kJ·mol^{-1}
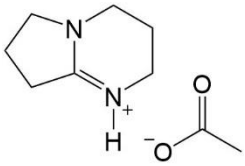	2.59	173.82	171.2 ± 1.2	18.3 ± 1.0
	4.32	170.58		
	4.63	169.60		
	3.22	172.82		
	6.01	168.26		
	3.69	172.68		
	4.62	171.91		
	3.68	170.14		
	$\Delta_l^g H_m^0$ (298.15 K) / kJ·mol^{-1} = (152.9 ± 1.6)			

Table 7.6. Experimental results obtained by Calvet microcalorimetry for the vaporization of [DBNH][EtCOO] (*T*=375.9 K). *T* (at K) being the temperature at which the Calvet measurements were performed.

	$m_{compound}$ / mg	$\Delta_l^g H_m^0$ / kJ·mol^{-1}	$\langle\Delta_l^g H_m^0\rangle$ / kJ·mol^{-1}	H_m^0 (g, *T*) - H_m^0 (g, 298.15 K) / kJ·mol^{-1}
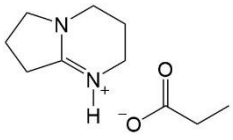	6.25	180.87	179.5 ± 1.1	20.2 ± 1.0
	6.29	181.55		
	7.08	179.47		
	6.42	181.20		
	4.57	176.18		
	5.15	178.08		
	6.37	178.02		
	5.70	180.41		
	5.22	178.14		
	5.88	179.44		
	5.68	180.80		
	$\Delta_l^g H_m^0$(298.15 K) / kJ·mol^{-1} = (159.3 ± 1.6)			

Table 7.7. Experimental results obtained by Calvet microcalorimetry for the vaporization of [DBNH][nPrCOO] (*T*=375.7 K). *T* (at K) being the temperature at which the Calvet measurements were performed.

	$m_{compound}$ / mg	$\Delta_l^g H_m^0$ / kJ·mol^{-1}	$\langle\Delta_l^g H_m^0\rangle$ / kJ·mol^{-1}	H_m^0 (g, *T*) - H_m^0 (g, 298.15 K) / kJ·mol^{-1}
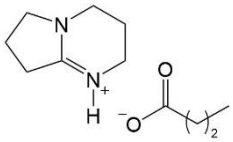	3.92	185.04	186.3 ± 1.1	22.0 ± 1.0
	4.08	185.26		
	3.82	186.76		
	3.54	187.07		
	3.36	185.70		
	4.18	186.86		
	3.30	187.62		
	$\Delta_l^g H_m^0$ (298.15 K) / kJ·mol^{-1} = (164.4 ± 1.5)			

Table 7.8. Experimental results obtained by Calvet microcalorimetry for the vaporization of [DBNH][nButCOO] (*T*=396.6 K). *T* (at K) being the temperature at which the Calvet measurements were performed.

	$m_{compound}$ / mg	$\Delta_l^g H_m^0$ / kJ·mol^{-1}	$\langle\Delta_l^g H_m^0\rangle$ / kJ·mol^{-1}	H_m^0 (g, *T*) - H_m^0 (g, 298.15 K) / kJ·mol^{-1}
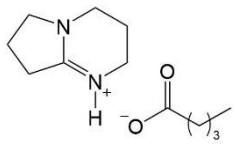	2.96	195.22	198.1 ± 1.4	31.1 ± 1.0
	2.58	199.21		
	2.69	195.27		
	3.13	199.11		
	2.85	199.80		
	2.69	199.82		
	$\Delta_l^g H_m^0$ (298.15 K) / kJ·mol^{-1} = (167.0 ± 1.6)			

Table 7.9. Experimental results obtained by Calvet microcalorimetry for the vaporization of [DBNH][nPentCOO] (*T*=396.3 K). *T* (at K) being the temperature at which the Calvet measurements were performed.

	$m_{compound}$ / mg	$\Delta_l^g H_m^0$ / kJ·mol^{-1}	$\langle\Delta_l^g H_m^0\rangle$ / kJ·mol^{-1}	H_m^0 (g, *T*) - H_m^0 (g, 298.15 K) / kJ·mol^{-1}
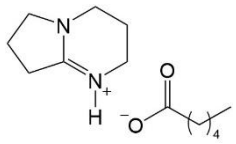	4.04	198.00	201.3 ± 1.2	33.4 ± 1.0
	5.93	197.16		
	5.48	203.91		
	4.29	199.13		
	6.37	202.15		
	7.12	200.94		
	3.24	203.77		
	4.69	203.61		
	5.94	202.23		
	5.23	201.30		
	4.89	199.73		
	4.23	203.14		
	$\Delta_l^g H_m^0$ (298.15 K) / kJ·mol^{-1} = (167.9 ± 1.5)			

Table 7.10. Experimental results obtained by Calvet microcalorimetry for the vaporization of [DBNH][nHexCOO] (*T*=396.4 K). *T* (at K) being the temperature at which the Calvet measurements were performed.

	$m_{compound}$ / mg	$\Delta_l^g H_m^0$ / kJ·mol^{-1}	$\langle\Delta_l^g H_m^0\rangle$ / kJ·mol^{-1}	H_m^0 (g, *T*) - H_m^0 (g, 298.15 K) / kJ·mol^{-1}
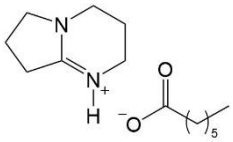	4.44	207.1	207.7 ± 1.1	35.8 ± 1.0
	5.30	208.6		
	4.91	206.3		
	3.45	208.3		
	3.64	206.5		
	2.28	209.4		
	3.03	207.9		
	$\Delta_l^g H_m^0$ (298.15 K) / kJ·mol^{-1} = (171.9 ± 1.5)			

Table 7.11. Experimental results obtained by Calvet microcalorimetry for the vaporization of [DBNH][nHeptCOO] (*T*=375.9 K for first 2 experiments and *T*=396.3 K for the rest). *T* (at K) being the temperature at which the Calvet measurements were performed.

	$m_{compound}$ / mg	$\Delta_l^g H_m^0$ / kJ·mol^{-1}	$\langle\Delta_l^g H_m^0\rangle$ / kJ·mol^{-1}	H_m^0 (g, *T*) - H_m^0 (g, 298.15 K) / kJ·mol^{-1}
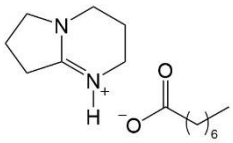	4.46	208.7	211.6 ± 1.5	35.1 ± 1.0 (29.4 ± 1.0 for 375.9 K) * (38.1 ± 1.0 for 396.3 K) *
	2.24	206.2		
	6.17	209.8		
	5.43	210.6		
	5.04	211.0		
	4.34	219.2		
	4.39	216.5		
	4.87	218.4		
	$\Delta_l^g H_m^0$ (298.15 K) / kJ·mol^{-1} = (176.5 ± 1.6)			

* -values for the correction at different temperatures, according to the experiment temperatures.

Table 7.12. Experimental results obtained by Calvet microcalorimetry for the vaporization of [DBUH][MeCOO] (*T*=375.8 K). *T* (at K) being the temperature at which the Calvet measurements were performed.

	$m_{compound}$ / mg	$\Delta_l^g H_m^0$ / kJ·mol^{-1}	$\langle\Delta_l^g H_m^0\rangle$ / kJ·mol^{-1}	$H_m^0(g, T) - H_m^0(g, 298.15\ K)$ / kJ·mol^{-1}
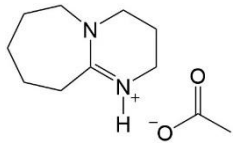	3.42	197.50		
	4.24	200.11		
	3.68	202.38		
	2.28	203.50	200.4 ± 1.4	21.8 ± 1.0
	3.41	198.47		
	2.77	203.23		
	4.90	197.44		
	$\Delta_l^g H_m^0$ (298.15 K) / kJ·mol^{-1} = (178.5 ± 1.7)			

Table 7.13. Experimental results obtained by Calvet microcalorimetry for the vaporization of [DBUH][EtCOO] (*T*=375.9 K). *T* (at K) being the temperature at which the Calvet measurements were performed.

	$m_{compound}$ / mg	$\Delta_l^g H_m^0$ / kJ·mol^{-1}	$\langle\Delta_l^g H_m^0\rangle$ / kJ·mol^{-1}	$H_m^0(g, T) - H_m^0(g, 298.15\ K)$ / kJ·mol^{-1}
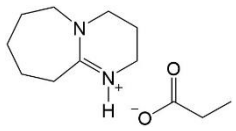	3.48	210.84		
	3.65	210.00		
	3.69	210.91		
	4.78	205.26		
	5.50	204.53		
	4.26	209.60		
	3.64	205.28	208.6 ± 1.2	23.7 ± 1.0
	3.76	208.37		
	4.08	213.06		
	7.76	209.17		
	4.26	208.41		
	5.04	211.07		
	3.02	207.09		
	3.87	206.89		
	$\Delta_l^g H_m^0$ (298.15 K) / kJ·mol^{-1} = (184.9 ± 1.6)			

Table 7.14. Experimental results obtained by Calvet microcalorimetry for the vaporization of [DBUH][nPrCOO] (*T*=375.9 K). *T* (at K) being the temperature at which the Calvet measurements were performed.

	$m_{compound}$ / mg	$\Delta_l^g H_m^0$ / kJ·mol^{-1}	$\langle\Delta_l^g H_m^0\rangle$ / kJ·mol^{-1}	H_m^0 (g, *T*) - H_m^0 (g, 298.15 K) / kJ·mol^{-1}
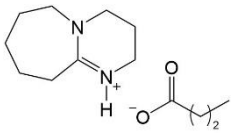	3.22	207.70	209.3 ± 1.8	25.6 ± 1.0
	5.45	201.09		
	3.41	213.19		
	3.95	209.54		
	3.77	207.15		
	3.75	212.97		
	3.39	201.78		
	2.51	210.38		
	2.63	214.57		
	3.37	214.42		
	$\Delta_l^g H_m^0$ (298.15 K) / kJ·mol^{-1} = (183.7 ± 1.8)			

Table 7.15. Experimental results obtained by Calvet microcalorimetry for the vaporization of [DBUH][nButCOO] (*T*=396.4 K). *T* (at K) being the temperature at which the Calvet measurements were performed.

	$m_{compound}$ / mg	$\Delta_l^g H_m^0$ / kJ·mol^{-1}	$\langle\Delta_l^g H_m^0\rangle$ / kJ·mol^{-1}	H_m^0 (g, *T*) - H_m^0 (g, 298.15 K) / kJ·mol^{-1}
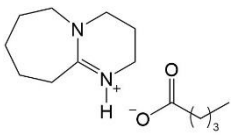	3.72	224.28	221.7 ± 1.5	35.6 ± 1.0
	3.16	219.93		
	5.07	218.45		
	3.97	224.44		
	3.98	224.05		
	4.79	218.95		
	$\Delta_l^g H_m^0$ (298.15 K) / kJ·mol^{-1} = (186.1 ± 1.6)			

Table 7.16. Experimental results obtained by Calvet microcalorimetry for the vaporization of [DBUH][nPentCOO] (*T*=396.4 K). *T* (at K) being the temperature at which the Calvet measurements were performed.

	$m_{compound}$ / mg	$\Delta_l^g H_m^0$ / kJ·mol^{-1}	$\langle\Delta_l^g H_m^0\rangle$ / kJ·mol^{-1}	H_m^0 (g, *T*) - H_m^0 (g, 298.15 K) / kJ·mol^{-1}
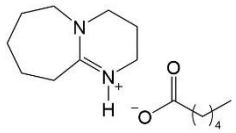	6.72	222.52	224.3 ± 1.2	38.0 ± 1.0
	5.55	223.03		
	2.26	225.71		
	5.12	223.47		
	3.36	225.68		
	5.16	225.46		
	$\Delta_l^g H_m^0$ (298.15 K) / kJ·mol^{-1} = (186.4 ± 1.5)			

Table 7.17. Experimental results obtained by Calvet microcalorimetry for the vaporization of [DBUH][nHexCOO] (*T*=396.4 K). *T* (at K) being the temperature at which the Calvet measurements were performed.

	$m_{compound}$ / mg	$\Delta_l^g H_m^0$ / kJ·mol^{-1}	$\langle\Delta_l^g H_m^0\rangle$ / kJ·mol^{-1}	H_m^0 (g, *T*) - H_m^0 (g, 298.15 K) / kJ·mol^{-1}
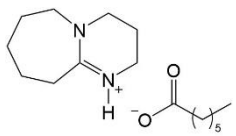	3.56	232.68	232.4 ± 1.1	40.4 ± 1.0
	4.77	231.26		
	3.83	233.48		
	3.36	231.00		
	2.3	232.33		
	4.37	233.73		
	2.39	232.13		
	$\Delta_l^g H_m^0$ (298.15 K) / kJ·mol^{-1} = (192.0 ± 1.6)			

Table 7.18. Experimental results obtained by Calvet microcalorimetry for the vaporization of [DBUH][nHeptCOO] (*T*=396.3 K). *T* (at K) being the temperature at which the Calvet measurements were performed.

	$m_{compound}$ / mg	$\Delta_l^g H_m^0$ / kJ·mol^{-1}	$\langle\Delta_l^g H_m^0\rangle$ / kJ·mol^{-1}	H_m^0 (g, *T*) - H_m^0 (g, 298.15 K) / kJ·mol^{-1}
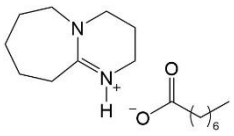	6.06	239.97		
	3.78	240.87		
	2.99	243.33		
	4.32	247.08	242.1 ± 1.4	42.7 ± 1.0
	4.40	241.91		
	5.89	240.14		
	4.21	241.48		
	$\Delta_l^g H_m^0$ (298.15 K) / kJ·mol^{-1} = (199.4 ± 1.6)			

Table 7.19. Experimental results obtained by Calvet microcalorimetry for the vaporization of [DMTHPH][EtCOO] (*T*=396.4 K). *T* (at K) being the temperature at which the Calvet measurements were performed.

	$m_{compound}$ / mg	$\Delta_l^g H_m^0$ / kJ·mol^{-1}	$\langle\Delta_l^g H_m^0\rangle$ / kJ·mol^{-1}	H_m^0 (g, *T*) - H_m^0 (g, 298.15 K) / kJ·mol^{-1}
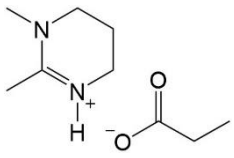	3.41	184.40		
	4.74	183.77		
	4.42	184.97		
	3.60	185.02	184.8 ± 1.1	26.1 ± 1.0
	3.94	185.31		
	4.22	186.36		
	4.67	183.70		
	$\Delta_l^g H_m^0$ (298.15 K) / kJ·mol^{-1} = (158.7 ± 1.5)			

Table 7.20. Experimental results obtained by Calvet microcalorimetry for the vaporization of [DMTHPH][nPrCOO] (*T*=396.4 K). *T* (at K) being the temperature at which the Calvet measurements were performed.

	$m_{compound}$ / mg	$\Delta_l^g H_m^0$ / kJ·mol^{-1}	$\langle\Delta_l^g H_m^0\rangle$ / kJ·mol^{-1}	H_m^0 (g, *T*) - H_m^0 (g, 298.15 K) / kJ·mol^{-1}
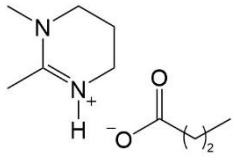	3.48	185.63		
	3.59	184.67		
	4.71	184.18		
	5.11	186.48	185.1 ± 1.1	28.5 ± 1.0
	4.41	184.13		
	3.39	186.25		
	3.95	184.39		
	$\Delta_l^g H_m^0$ (298.15 K) / kJ·mol^{-1} = (156.6 ± 1.5)			

Table 7.21. Experimental results obtained by Calvet microcalorimetry for the vaporization of [DMTHPH][nButCOO] (*T*=396.4 K). *T* (at K) being the temperature at which the Calvet measurements were performed.

	$m_{compound}$ / mg	$\Delta_l^g H_m^0$ / kJ·mol^{-1}	$\langle\Delta_l^g H_m^0\rangle$ / kJ·mol^{-1}	H_m^0 (g, *T*) - H_m^0 (g, 298.15 K) / kJ·mol^{-1}
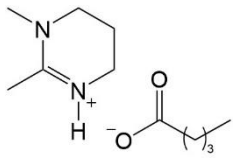	3.19	193.28		
	3.55	191.94		
	4.31	192.49		
	5.04	192.23	194.2 ± 1.3	30.9 ± 1.0
	6.29	196.72		
	3.51	195.74		
	4.11	196.66		
	$\Delta_l^g H_m^0$ (298.15 K) / kJ·mol^{-1} = (163.3 ± 1.6)			

Table 7.22. Experimental results obtained by Calvet microcalorimetry for the vaporization of [DMTHPH][nPentCOO] (*T*=396.4 K). *T* (at K) being the temperature at which the Calvet measurements were performed.

	$m_{compound}$ / mg	$\Delta_l^g H_m^0$ / kJ·mol^{-1}	$\langle\Delta_l^g H_m^0\rangle$ / kJ·mol^{-1}	H_m^0 (g, *T*) - H_m^0 (g, 298.15 K) / kJ·mol^{-1}
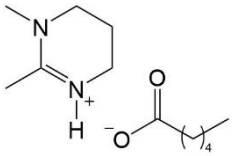	3.50	202.03		
	3.66	201.38		
	3.59	200.67		
	4.80	198.29	200.5 ± 1.1	33.3 ± 1.0
	3.24	199.52		
	3.79	200.56		
	4.96	200.83		
	$\Delta_l^g H_m^0$ (298.15 K) / kJ·mol^{-1} = (167.2 ± 1.5)			

Table 7.23. Experimental results obtained by Calvet microcalorimetry for the vaporization of [DMTHPH][nHexCOO] (*T*=396.3 K). *T* (at K) being the temperature at which the Calvet measurements were performed.

	$m_{compound}$ / mg	$\Delta_l^g H_m^0$ / kJ·mol^{-1}	$\langle\Delta_l^g H_m^0\rangle$ / kJ·mol^{-1}	H_m^0 (g, *T*) - H_m^0 (g, 298.15 K) / kJ·mol^{-1}
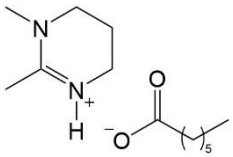	3.40	206.91		
	3.59	206.61		
	3.37	208.95		
	4.19	205.47	206.6 ± 1.1	35.6 ± 1.0
	3.43	206.24		
	3.63	205.57		
	4.15	207.06		
	$\Delta_l^g H_m^0$ (298.15 K) / kJ·mol^{-1} = (171.1 ± 1.5)			

Table 7.24. Experimental results obtained by Calvet microcalorimetry for the vaporization of [DMTHPH][nHeptCOO] (*T*=396.3 K). *T* (at K) being the temperature at which the Calvet measurements were performed.

	$m_{compound}$ / mg	$\Delta_l^g H_m^0$ / kJ·mol^{-1}	$\langle\Delta_l^g H_m^0\rangle$ / kJ·mol^{-1}	H_m^0 (g, *T*) - H_m^0 (g, 298.15 K) / kJ·mol^{-1}
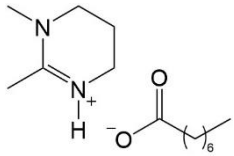	3.88	211.28		
	4.00	216.43		
	3.27	212.76		
	3.85	215.21	214.2 ± 1.2	38.0 ± 1.0
	3.72	215.43		
	4.13	215.41		
	3.38	212.61		
$\Delta_l^g H_m^0$ (298.15 K) / kJ·mol^{-1} = (176.1 ± 1.6)				

Table 7.25. Standard molar enthalpies of vaporization for the pure compounds studied, as determined by Calvet microcalorimetry.

Compound	Proportion	Molar Mass* / g·mol^{-1}	$\Delta_l^g H_m^0$ (298.15 K) / kJ·mol^{-1}
DBN	1:0	124.18	63.9 ± 1.5
DBU	1:0	152.24	69.7 ± 1.5
DMTHP	1:0	112.17	63.5 ± 1.5
[DBNH][MeCOO]	1:1	184.23	152.9 ± 1.6
[DBNH][EtCOO]	1:1	198.26	159.3 ± 1.6
[DBNH][nPrCOO]	1:1	212.29	164.4 ± 1.5
[DBNH][nButCOO]	1:1	226.32	167.0 ± 1.6
[DBNH][nPentCOO]	1:1	240.35	167.9 ± 1.5
[DBNH][nHexCOO]	1:1	254.37	171.9 ± 1.5
[DBNH][nHeptCOO]	1:1	268.40	176.5 ± 1.6
[DBUH][MeCOO]	1:1	212.29	178.5 ± 1.7
[DBUH][EtCOO]	1:1	226.32	184.9 ± 1.6
[DBUH][nPrCOO]	1:1	240.35	183.7 ± 1.8
[DBUH][nButCOO]	1:1	254.37	186.1 ± 1.6
[DBUH][nPentCOO]	1:1	268.40	186.4 ± 1.5
[DBUH][nHexCOO]	1:1	282.43	192.0 ± 1.6
[DBUH][nHeptCOO]	1:1	296.45	199.4 ± 1.6
[DMTHPH][EtCOO]	1:1	186.25	158.7 ± 1.5
[DMTHPH][nPrCOO]	1:1	200.28	156.6 ± 1.5
[DMTHPH][nButCOO]	1:1	214.31	163.3 ± 1.6
[DMTHPH][nPentCOO]	1:1	228.33	167.2 ± 1.5
[DMTHPH][nHexCOO]	1:1	242.35	171.1 ± 1.5
[DMTHPH][nHeptCOO]	1:1	256.38	176.1 ± 1.6

The enthalpies of vaporization, $\Delta_l^g H_m^0$, of the PILs, as measured by Calvet microcalorimetry, were used to evaluate the effect of small molecular changes in the acid and/or base (e.g. increase of chain length) on the cohesive energy of the liquid phase. This knowledge can also give insights about the ionicity and speciation of the PILs in the liquid and gas phases. The experimental results of the standard (p^0 = 10^5 Pa) molar enthalpies of vaporization, at T = 298.15 K, $\Delta_l^g H_m^0$, are presented in table 7.25 and are plotted in figure 7.5 as a function of the number of carbons, n, in the carboxylic acid of the PIL.

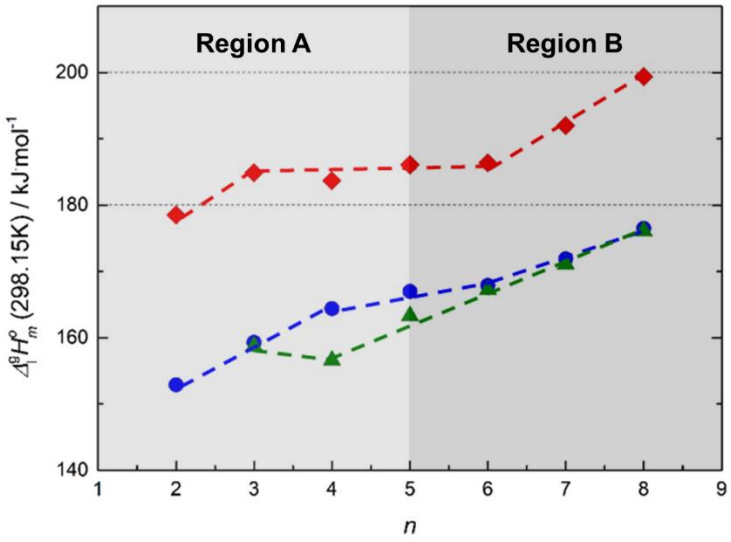

Figure 7.5. Standard molar enthalpies of vaporization, $\Delta_l^g H_m^0$ at T = 298.15 K, ΔH_{vap} (as measured by Calvet microcalorimetry), of each protic ionic liquid as a function of the alkyl chain of the acid. DBN-based protic ionic liquids – blue circles, DBU-based protic ionic liquids – red diamonds and DMTHP-based protic ionic liquids – green triangles.

The most direct observation that can be drawn from these results is the magnitude of $\Delta_l^g H_m^0$ for the PILs: [150; 200] kJ·mol^{-1}. These values are in the same order of magnitude of $\Delta_l^g H_m^0$ for aprotic ILs. For example, the standard (p^0 = 10^5 Pa) $\Delta_l^g H_m^0$, at T = 298.15 K, for the 1-alkyl-3-methylimidazolium bis(trifluoromethylsulfonyl)imide series, [$C_nC_1$im][Ntf_2] (n=2-12) range from 133 for [C_2C_1im][Ntf_2] to 171 kJ·mol^{-1} for [$C_{12}C_1$im][Ntf_2]. [7.10-7.11] For imidazolium ILs with other anions (e.g. [PF_6], [BF_4] and bis(perfluoroethylsulfonyl)imide, [beti]) the literature indicates experimental values of $\Delta_l^g H_m^0$ in similar range, 135 to 170 kJ·mol^{-1}. [7.11] The same is observed for [Ntf_2] ILs with alkylpyridinium cations, for which $\Delta_l^g H_m^0$, at T = 298.15 K, is in the order of 140 kJ·mol^{-1}. [7.12] Using the Calvet Methodology, the measurement of the enthalpy of vaporization of a

substance can only be done if its vapour pressure at the working temperature is higher than 10 Pa. The Calvet experiments for the PILs studied were performed at T = 376 K, a temperature at which most aprotic ILs have negligible vapour pressures (much lower than 10 Pa). [7.10-7.14] Given that the PILs measured in this work have values of $\Delta_l^g H_m^0$ comparable to those of typical aprotic ILs, the higher volatility of PILs must result from a substantially higher $\Delta_l^g S_m^0$. This strongly suggests that PILs, contrary to aprotic ILs, [7.10-7.11, 7.15] don't vaporize as ion pairs. This preliminary analysis suggests that the PILs studied are liquids composed of a significant fraction of ion pairs, which upon vaporization dissociate into neutral species to large extent. The magnitude of $\Delta_l^g H_m^0$ for the PILs is much higher than the sum of $\Delta_l^g H_m^0$ of their isolated constituents (acid + base), as can be seen in tables 7.25 and 7.27. These observations evidence that electrostatic interactions between charged species in the PILs contribute significantly for the cohesive enthalpy. This confirms that the PILs studied have significant ionic character in the liquid phase – proton transfer between acid and base occurs in considerable extent and many species are ions.

These results also show, that the identity of the base affects $\Delta_l^g H_m^0$ more significantly than altering the acid: incrementing $-CH_2-$ groups in the base leads to a larger increase in $\Delta_l^g H_m^0$. This is nicely evidenced by comparing the isomers [DBNH][nPrCOO] and [DBUH][MeCOO], for which the difference in $\Delta_l^g H_m^0$ is of 13.1 ± 1.6 kJ·mol^{-1}. The dependence of $\Delta_l^g H_m^0$ with the chain length of the acid is similar for both DBN and DBU bases for most PILs: there is an increase of around 6 kJ·mol^{-1} per $-CH_2-$ group. This increment is comparable, but slightly higher than those observed for the $[C_nC_1im][Ntf_2]$ aprotic ILs family, [7.10] and for *n*-alkanes, [7.16-7.17] 1-alkanols [7.18] and 1-aminoalkanes series. [7.18] This indicates that the major effect of increasing the chain length of the acid is to strengthen the van der Waals interactions between the nonpolar regions of the PILs (alkyl tails of the acid and cyclic alkyl groups of the base). However, the $-CH_2-$ increment in the base (DBN and DBU differ by two cyclic $-CH_2-$) leads to an average increase in ΔH_{vap}, from the DBN to DBU based PILs, of 25.4 kJ·mol^{-1}. This is much higher than the difference in $\Delta_l^g H_m^0$ between the DBN and DBU pure bases, which is of 5.8 kJ·mol^{-1} (see table 7.25). The difference between the DBN and DBU PILs corresponds to an average increase of 12.7 kJ·mol^{-1} per $-CH_2-$ group, which is also substantially higher than the same modification in the acids, and thus cannot be explained solely by stronger van der Waals interactions in the

bigger base. A test experiment was also performed to support these findings: a mixture of DBN/DBU/nPrCOOH (1:1:1) (prepared by adding pure DBU to [DBNH][nPrCOO]) was distilled under vacuum ($p \approx 10$ Pa) at $T \approx 358$ K. The NMR analysis revealed that the distillate was mostly pure DBN and the remaining liquid [DBUH][nPrCOO]. This result evidences the higher affinity of DBU, relative to DBN, to form PILs with carboxylic acids of short chain length.

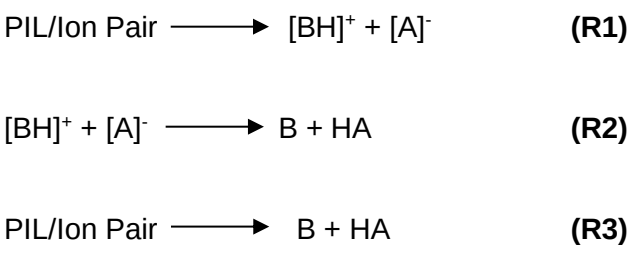

Figure 7.6. Reactions and species that may exist in the gas phase of PILs and their participation in acid-base and ion pair equilibria.

It's of fundamental importance to start by properly defining thermodynamically the initial and final states of the vaporization process. For that, it's necessary to know the extent of all equilibria occurring inside the Calvet apparatus in the experimental measurements, considering the conditions of temperature and pressure. In a Calvet type apparatus the experimental vaporization measurements are performed at relatively low pressures (under 10 Pa). Concerning the composition of the liquid phase, (i.e. the extent of ionization) we can only say that it is dominated by ionized species, but not to which extent exactly. However, we can have more information about the equilibria in the gas phase. As referred before, while the ion pair is enthalpically favoured in the gas phase, the entropic contribution can be significant enough, depending on the conditions of (T, p), to overcome the ΔH term in ΔG and hence increase the population of the isolated neutral species, which are favoured for higher T and lower p. The vaporization process of the PILs in the Calvet apparatus occurs at $T \approx 376$ K and vacuum ($p < 10$ Pa) conditions. To quantify the effect of these conditions on equilibrium, the M06-2X enthalpies, ΔH_r, entropies, ΔS_r, and Gibbs energies, ΔG_r, of reaction, at $T = 376$ K and $p = 10$ Pa, were calculated for the R3 reaction, figure 7.6 (PIL/Ion Pair → B + HA). The value of 10 Pa was considered as the maximum pressure that can be achieved inside the Calvet apparatus during vaporization of the sample. The pressure correction from $p^0 = 10^5$ Pa to $p = 10$ Pa

is negligible for ΔH_r but is quite substantial for ΔS_r and can be calculated, assuming ideal gas behaviour, using equation 7.7:

$$\Delta\Delta S_r(10^5 \rightarrow 10\ \text{Pa}) = R \cdot \ln(10/10^5) = -76.6\ \text{J}\cdot\text{K}^{-1}\cdot\text{mol}^{-1} \qquad \textbf{(7.7)}$$

where R is the gas constant. Thus, $\Delta S_r(10\ \text{Pa}) = \Delta\Delta S_r(10^5\ \text{Pa}) + 76.6$, confirming that the entropy contribution favors significantly the separated species at the experimental conditions. The term ΔG_r at the actual experimental conditions can then be calculated using equation 7.8:

$$\Delta G_r(376\ \text{K}, 10\ \text{Pa}) = \Delta H_r(376\ \text{K}) - 376 \cdot \Delta S_r(376\ \text{K}, 10\ \text{Pa}) \qquad \textbf{(7.8)}$$

The results are shown in table 7.26, alongside with the values for T = 298.15 K and $p = p^0 = 10^5$ Pa, for comparison. Although, at 298.15 K and 10^5 Pa the ion pair is probably the preferred species, the results indicate that dissociation of the ion pair into the neutral isolated species, [BH][A] → B + HA, in the gas phase becomes thermodynamically spontaneous at T > 300 K and p < 10 Pa, for all PILs studied. The magnitude of the calculated ΔG_r(376 K, 10 Pa) for all PILs is enough to assure that computational errors are not changing the sign of ΔG_r.

The vaporization process that is being measured in the Calvet experiment can thus be translated by the following equation:

$$[\text{BH}][\text{A}](\text{liq}) \rightarrow \text{B}(\text{g}) + \text{HA}(\text{g}) \qquad \textbf{(7.9)}$$

Hence, the experimentally derived $\Delta_l^g H_m^0$ values shown in table 7.25 for the PILs are the enthalpies of the processes described by equation 7.9, which can be divided into two simpler steps:

a) the vaporization of the PIL as an ion pair, [BH][A](liq) → [BH][A](g), followed by gas phase dissociation, [BH][A](g) → B(g) + HA(g);

or

b) dissociation in the liquid phase, [BH][A](liq) → B(liq) + HA(liq), followed by vaporization of the neutral species, B(l) → B(g) and HA(liq) → HA(g).

Table 7.26. Enthalpies, entropies and Gibbs energies of reaction for R3 (figure 7.6), calculated at the M06-2X/6-311++G(d,p) level of theory, for two specified set of (*T*, *p*) conditions; values of Δ*H* and Δ*G* in kJ·mol^{-1} and of Δ*S* in J·K^{-1}·mol^{-1}.

PIL	*T* = 298.15 K, *p* = 10^5 Pa			*T* = 396 K, *p* = 10 Pa [a]		
	Δ*H*	Δ*S*	Δ*G*	Δ*H*	Δ*S*	Δ*G*
[DBNH][MeCOO]	62	141	20	61	215	-20
[DBNH][EtCOO]	61	155	15	60	229	-26
[DBNH][nPrCOO]	57	138	16	56	211	-24
[DBNH][nButCOO]	61	146	18	60	219	-23
[DBNH][nPentCOO]	64	168	14	63	214	-18
[DBNH][nHexCOO]	61	144	18	60	218	-22
[DBNH][nHeptCOO]	61	157	14	61	226	-24
[DBUH][MeCOO]	53	130	15	51	201	-24
[DBUH][EtCOO]	51	158	4	50	231	-37
[DBUH][nPrCOO]	47	152	2	45	224	-39
[DBUH][nButCOO)	52	149	8	51	224	-33
[DBUH][nPentCOO]	56	183	1	55	229	-32
[DBUH][nHexCOO]	51	171	1	50	245	-42
[DBUH][nHeptCOO]	47	173	-5	46	252	-48

[a] These values reproduce the real experimental (*T*, *p*) conditions verified during the measurements of ΔH_{vap} in the Calvet microcalorimeter.

This vaporization mechanism was already reported for other cases, [7.19-7.20] and conforms to the generally accepted interpretation of distillation of PILs. [7.21-7.22] For example, Vitorino et al. have reported a mass spectrometry study showing that in 1,1,3,3-tetramethylguanidinium chloride there are no charged species, separated or as ion pairs, in the vapour over the condensed phase. [7.19]

The thermodynamic cycle presented in figure 7.7 shows all the relevant equilibrium processes involved in the vaporization of the PILs studied. Based on this cycle the enthalpies of PIL formation in the liquid phase, B(liq) + HA(liq) → [BH][A](liq), $\Delta H_{reaction}$, and the cohesive enthalpies of the PILs, [BH][A](liq) → [BH][A](g), were derived and are shown in table 7.27.

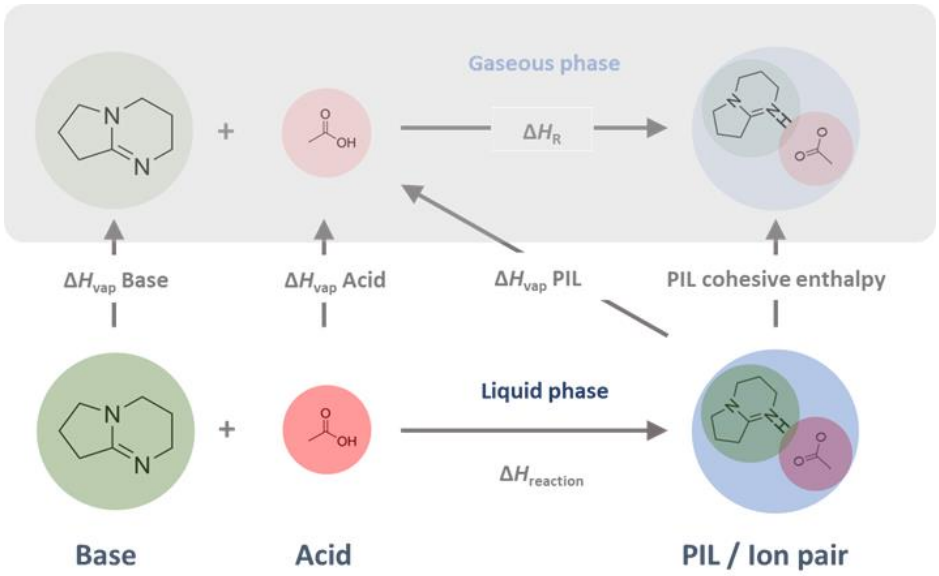

Figure 7.7. Hypothetical thermodynamic cycle for interpreting the vaporization process of the PILs studied; the PIL [DBNH][MeCOO] is presented as an example.

These were calculated by considering the experimental enthalpies of vaporization of the separated acids and bases and the computationally calculated enthalpies for R3, ΔH_{R3}, presented in Annex B, table B.8. $\Delta H_{reaction}$ corresponds to the enthalpy change associated to the mixing of the pure base and acid to form the PIL, as it happens in the course of their solvent-free synthesis. While the derivation of $\Delta H_{reaction}$ is based solely on experimental values, that of the PIL cohesive enthalpy has the contribution of the theoretical ΔH_{R3} value and should be regarded with more care, considering the limitations of the computational methods used for the calculations.

Table 7.27. Derived $\Delta H_{reaction}$ and cohesive enthalpies (see figure 7.6), at T = 298.15 K and $p = p^0 = 10^5$ Pa, for the PILs studied; values in kJ·mol^{-1}.

Compound	Proportion	$\Delta H^0_{reaction}$ (298.15 K)	Cohesive enthalpy
[DBNH][MeCOO]	1:1	-38.7 ± 1.8	93.0 ± 1.6
[DBNH][EtCOO]	1:1	-40.5 ± 1.8	99.8 ± 1.6
[DBNH][nPrCOO]	1:1	-39.8 ± 1.8	106.2 ± 1.5
[DBNH][nButCOO]	1:1	-37.2 ± 1.8	107.6 ± 1.5
[DBNH][nPentCOO]	1:1	-32.7 ± 1.7	108.1 ± 1.3
[DBNH][nHexCOO]	1:1	-32.3 ± 1.7	113.2 ± 1.2
[DBNH][nHeptCOO]	1:1	-32.8 ± 1.8	117.6 ± 1.6
[DBUH][MeCOO]	1:1	-58.5 ± 1.9	127.7 ± 1.7
[DBUH][EtCOO]	1:1	-60.3 ± 1.9	135.3 ± 1.6
[DBUH][nPrCOO]	1:1	-53.3 ± 1.9	134.2 ± 1.8
[DBUH][nButCOO]	1:1	-50.5 ± 1.8	136.0 ± 1.6
[DBUH][nPentCOO]	1:1	-45.4 ± 1.7	132.7 ± 1.3
[DBUH][nHexCOO]	1:1	-46.6 ± 1.7	141.8 ± 1.2
[DBUH][nHeptCOO]	1:1	-49.9 ± 1.8	150.9 ± 1.5
[DMTHPH][EtCOO]	1:1	-40.3 ± 1.8	104.4 ± 1.5
[DMTHPH][nPrCOO]	1:1	-32.4 ± 1.8	102.3 ± 1.5
[DMTHPH][nButCOO]	1:1	-33.9 ± 1.8	106.6 ± 1.6
[DMTHPH][nPentCOO]	1:1	-32.4 ± 1.8	112.2 ± 1.5
[DMTHPH][nHexCOO]	1:1	-31.9 ± 1.8	113.8 ± 1.5
[DMTHPH][nHeptCOO]	1:1	-31.4 ± 1.8	118.8 ± 1.6

Figure 7.8 presents the cohesive enthalpies obtained for each PIL as a function of the alkyl chain of the acid.

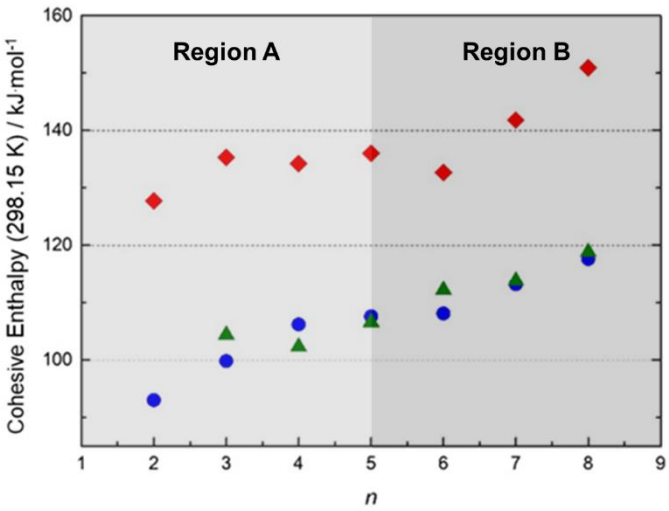

Figure 7.8. Cohesive enthalpies of each protic ionic liquid (1:1) as a function of the alkyl chain of the acid in each protic ionic liquid. DBN-based protic ionic liquids – blue circles, DBU-based protic ionic liquids – red diamonds and DMTHP-based protic ionic liquids – green triangles.

The values of ΔH_{vap} (in kJ·mol^{-1}) for DBN (61.9 ± 0.2), DBU (70.7 ± 0.2) and [DBNH][MeCOO] (154.9 ± 4.2) were determined in previous works, [7.23-7.24] and are in good agreement with those reported herein. In the work of Ostonen *et al*., [7.23] the authors distinguish between the two possible vaporization processes for [DBNH][MeCOO]: a) [DBNH][MeCOO](liq) → DBN(g) + MeCOOH(g), ΔH = 154.9 ± 4.2 kJ·mol^{-1} (corresponds to ΔH_{vap} in figure 7.7); b) [DBNH][MeCOO](liq) → [DBNH][MeCOO](g), ΔH = 98.5 ± 3.3 kJ·mol^{-1} (corresponds to cohesive enthalpy in figure 7.7). In the same work, the authors have also calculated the value of $\Delta_{diss}H$ = 58.1 ± 3.5 kJ·mol^{-1}, using the G4 method, for the reaction: [DBNH][MeCOO](g) → DBN(g) + MeCOOH(g), which corresponds to $-\Delta H_R$ in figure 7.7, or ΔH_{R3} in figure 7.6 and table B.8. of Annex B. These values show good agreement with our results, and help validating the interpretation of the vaporization process of the PILs, as schematized in figure 7.7.

The trends in the results presented in table 7.27 go in line with that already verified for the ΔH_{vap} in table 7.25, i.e. changing the base has more effect than changing the acid, and the DBU PILs have enthalpies greater in magnitude. While the acid has little effect on $\Delta H_{reaction}$, changing from DBN to DBU increases it by about 20 kJ·mol^{-1}. The cohesive enthalpy increases slightly by 7-8 kJ·mol^{-1} on incrementing the alkyl chain of the acid by one $-CH_2-$, which is mostly a result of the stronger van der Waals interactions between bigger non-polar domains. On the other hand, the replacement of DBN by DBU increases significantly the cohesive enthalpy of the PIL by about 35 kJ·mol^{-1}. The more exothermic $\Delta H_{reaction}$ and greater cohesive enthalpy of the DBU PILs can be explained by the stronger basicity of DBU, when compared to DBN. $\Delta H_{reaction}$ is virtually independent of the acid because their pK_a is similar, and thus increasing the acid only enhances van der Waals interactions, an effect that is similar in the pure liquid acids and PILs and thus cancels out.

It is important to note that, while ΔH_{vap} measured in the Calvet apparatus corresponds to the process given by equation 7.9; at T = 298.15 K and $p^0 = 10^5$ Pa, the ion pair is probably the dominant species in the gas phase. Hence, at these conditions the vaporization process is better described as: [BH][A](liq) → [BH][A](g), and the enthalpy associated to this vaporization pathway corresponds to the cohesive enthalpy as defined in figure 7.7 and table 7.27. However, ion pair dissociation in the gas phase must be considered in most practical applications involving vaporization of PILs, like distillation or vapour pressure measurements, since low pressures and high temperatures are usually required in these processes. The major contribution for the observed differences in ΔHreaction (figure

7.9) could be the significant difference in the enthalpy proton exchange (R3) and the expected contribution of the higher extent of the acid-base equilibrium in the liquid phase as expressed by equation (7.10):

$$B + HA \leftrightarrow [BH][A] \qquad \textbf{(7.10)}$$

In the DBU PIL derivatives, this equilibrium occurs in higher extent and those liquids have higher ionic character. It can also be concluded that the DBN PILs have a significant proportion of neutral species in the liquid phase at equilibrium. Hence, for the DBU PILs the derived $\Delta H_{reaction}$ is more exothermic mostly because the proton transfer reaction occurs in more extent.

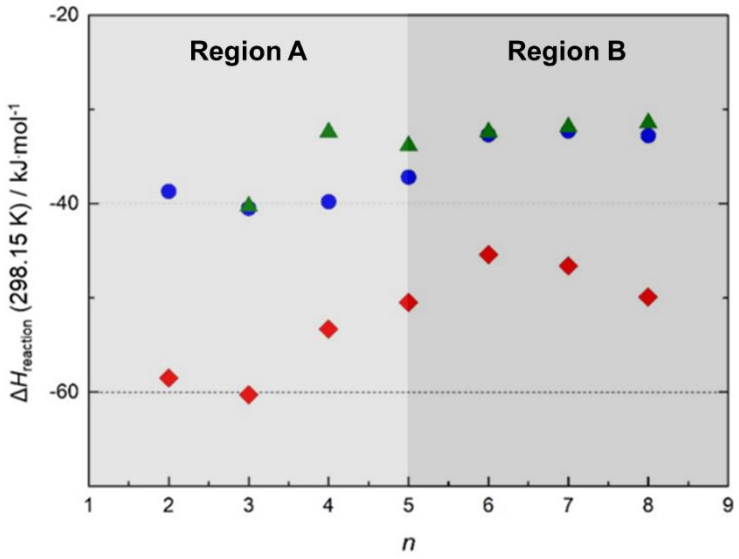

Figure 7.9. Derived $\Delta H_{reaction}$ of each protic ionic liquid as a function of the alkyl chain of the acid in each protic ionic liquid. DBN-based protic ionic liquids – blue circles, DBU-based protic ionic liquids – red diamonds and DMTHP-based protic ionic liquids – green triangles.

As can been seen in figure 7.9 the $\Delta H_{reaction}$ of DBN and DMTHP based PILs are quite similar. These values are in accordance with the strength of the superbases. Stronger bases lead to more negative $\Delta H_{reaction}$. It was also observed a trend shift between short (region A) and long acids (region B) for all the superbase families. This trend shift is between n = 4 to 6, for DBN and DBU-based PILs and n = 3 for the smaller superbase DMTHP.

7.2.2. Non-stoichiometric proportion PILs

Table 7.28 presents the experimental results for the calibration of the calorimeter for each non-stoichiometric studied PIL and tables 7.29 to 7.45 show the experimental data obtained for the PILs studied.

Table 7.28. Experimental results obtained by Calvet microcalorimetry for the calibration experiments of each compound with different proportions of base and acid (B:A). *T* (at K) being the temperature at which the Calvet measurements were performed.

Compound	*T* / K	Calibrant	n	*k*
[DBNH][nPrCOO] (3:1)	396.4	Ferrocene	5	1.007 ± 0.018
[DBNH][nPrCOO] (2:1)	396.3	Ferrocene	5	1.007 ± 0.018
[DBNH][nPrCOO] (eq)	396.3	Ferrocene	5	1.007 ± 0.018
[DBNH][nPrCOO] (1:3)	396.4	Ferrocene	5	1.007 ± 0.018
[DBNH][nHeptCOO] (3:1)	396.4	Ferrocene	5	1.007 ± 0.018
[DBNH][nHeptCOO] (2:1)	396.4	Ferrocene	5	1.007 ± 0.018
[DBNH][nHeptCOO] (eq)	396.3	Ferrocene	5	1.007 ± 0.018
[DBNH][nHeptCOO] (1:3)	396.3	Ferrocene	5	1.007 ± 0.018
[DBUH][nPrCOO] (3:1)	396.3	Ferrocene	5	1.007 ± 0.018
[DBUH][nPrCOO] (2:1)	396.3	Ferrocene	5	1.007 ± 0.018
[DBUH][nPrCOO] (eq)	375.9	Ferrocene	7	1.000 ± 0.020
[DBUH][nPrCOO] (1:3)	396.4	Ferrocene	5	1.007 ± 0.018
[DBUH][nHeptCOO] (3:1)	386.4	Ferrocene	5	1.007 ± 0.018
[DBUH][nHeptCOO] (2:1)	386.4	Ferrocene	5	1.007 ± 0.018
[DBUH][nHeptCOO] (eq)	396.3	Ferrocene	5	1.007 ± 0.018
[DBUH][nHeptCOO] (1:3)	386.4	Ferrocene	5	1.007 ± 0.018

Table 7.29. Experimental results obtained by Calvet microcalorimetry for the vaporization of [DBNH][nPrCOO] (3:1) (*T*=396.4 K). *T* (at K) being the temperature at which the Calvet measurements were performed.

	$m_{compound}$ / mg	$\Delta_l^g H_m^0$ / kJ·mol^{-1}	$\langle\Delta_l^g H_m^0\rangle$ / kJ·mol^{-1}	H_m^0 (g, *T*) - H_m^0 (g, 298.15 K) / kJ·mol^{-1}
3:1 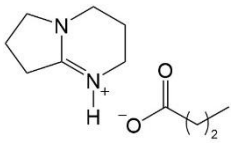	3.39	161.59		
	4.72	161.81		
	6.39	160.54		
	3.44	161.28	161.9 ± 1.1	30.5 ± 1.0
	5.84	161.83		
	2.87	162.91		
	2.78	163.35		
	$\Delta_l^g H_m^0$ (298.15 K) / kJ·mol^{-1} = (131.4 ± 1.5)			

Table 7.30. Experimental results obtained by Calvet microcalorimetry for the vaporization of [DBNH][nPrCOO] (2:1) (*T*=396.3 K). *T* (at K) being the temperature at which the Calvet measurements were performed.

	$m_{compound}$ / mg	$\Delta_l^g H_m^0$ / kJ·mol^{-1}	$\langle\Delta_l^g H_m^0\rangle$ / kJ·mol^{-1}	H_m^0 (g, *T*) - H_m^0 (g, 298.15 K) / kJ·mol^{-1}
2:1 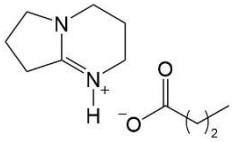	5.41	164.50		
	4.54	165.12	165.0 ± 1.0	29.9 ± 1.0
	4.43	165.35		
	$\Delta_l^g H_m^0$ (298.15 K) / kJ·mol^{-1} = (135.1 ± 1.5)			

Table 7.31. Experimental results obtained by Calvet microcalorimetry for the vaporization of [DBNH][nPrCOO] (eq) (*T*=396.3 K). *T* (at K) being the temperature at which the Calvet measurements were performed.

	$m_{compound}$ / mg	$\Delta_l^g H_m^0$ / kJ·mol^{-1}	$\langle\Delta_l^g H_m^0\rangle$ / kJ·mol^{-1}	H_m^0 (g, *T*) - H_m^0 (g, 298.15 K) / kJ·mol^{-1}
equilibrium 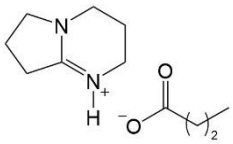	4.75	194.92		
	4.92	192.20		
	2.30	193.66		
	3.40	195.51	193.6 ± 1.1	28.0 ± 1.0
	4.50	191.54		
	3.34	193.46		
	4.10	193.15		
	$\Delta_l^g H_m^0$ (298.15 K) / kJ·mol^{-1} = (165.5 ± 1.5)			

Table 7.32. Experimental results obtained by Calvet microcalorimetry for the vaporization of [DBNH][nPrCOO] (1:3) (*T*=396.4 K). *T* (at K) being the temperature at which the Calvet measurements were performed.

	$m_{compound}$ / mg	$\Delta_l^g H_m^0$ / kJ·mol^{-1}	$\langle\Delta_l^g H_m^0\rangle$ / kJ·mol^{-1}	H_m^0 (g, *T*) - H_m^0 (g, 298.15 K) / kJ·mol^{-1}
1:3 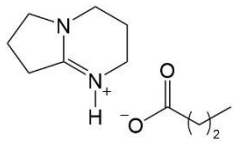	4.31	180.35		
	4.86	181.19		
	4.90	181.34		
	6.90	179.89	180.2 ± 1.1	26.7 ± 1.0
	4.46	179.34		
	5.71	181.00		
	5.24	178.48		
	$\Delta_l^g H_m^0$ (298.15 K) / kJ·mol^{-1} = (153.6 ± 1.5)			

Table 7.33. Experimental results obtained by Calvet microcalorimetry for the vaporization of [DBNH][nHeptCOO] (3:1) (*T*=396.4 K). *T* (at K) being the temperature at which the Calvet measurements were performed.

	$m_{compound}$ / mg	$\Delta_l^g H_m^0$ / kJ·mol^{-1}	$\langle\Delta_l^g H_m^0\rangle$ / kJ·mol^{-1}	H_m^0 (g, *T*) - H_m^0 (g, 298.15 K) / kJ·mol^{-1}
3:1 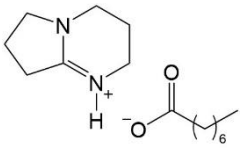	3.89	175.10		
	3.62	175.78	175.8 ± 1.1	35.3 ± 1.0
	4.34	176.64		
	$\Delta_l^g H_m^0$ (298.15 K) / kJ·mol^{-1} = (140.5 ± 1.5)			

Table 7.34. Experimental results obtained by Calvet microcalorimetry for the vaporization of [DBNH][nHeptCOO] (2:1) (*T*=396.4 K). *T* (at K) being the temperature at which the Calvet measurements were performed.

	$m_{compound}$ / mg	$\Delta_l^g H_m^0$ / kJ·mol^{-1}	$\langle\Delta_l^g H_m^0\rangle$ / kJ·mol^{-1}	H_m^0 (g, *T*) - H_m^0 (g, 298.15 K) / kJ·mol^{-1}
2:1 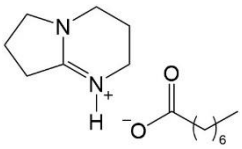	5.84	184.40		
	3.52	186.78	185.4 ± 1.2	36.2 ± 1.0
	4.68	185.08		
	$\Delta_l^g H_m^0$ (298.15 K) / kJ·mol^{-1} = (149.2 ± 1.5)			

Table 7.35. Experimental results obtained by Calvet microcalorimetry for the vaporization of [DBNH][nHeptCOO] (eq) (*T*=396.3 K). *T* (at K) being the temperature at which the Calvet measurements were performed.

	$m_{compound}$ / mg	$\Delta_l^g H_m^0$ / kJ·mol^{-1}	$\langle\Delta_l^g H_m^0\rangle$ / kJ·mol^{-1}	H_m^0 (g, *T*) - H_m^0 (g, 298.15 K) / kJ·mol^{-1}
equilibrium 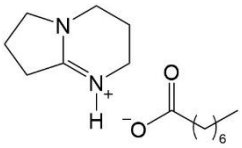	5.16	227.01	225.7 ± 1.0	39.7 ± 1.0
	4.50	225.35		
	4.92	225.58		
	4.61	225.12		
	4.20	225.77		
	4.31	225.23		
	$\Delta_l^g H_m^0$ (298.15 K) / kJ·mol^{-1} = (186.0 ± 1.5)			

Table 7.36. Experimental results obtained by Calvet microcalorimetry for the vaporization of [DBNH][nHeptCOO] (1:3) (*T*=396.3 K). *T* (at K) being the temperature at which the Calvet measurements were performed.

	$m_{compound}$ / mg	$\Delta_l^g H_m^0$ / kJ·mol^{-1}	$\langle\Delta_l^g H_m^0\rangle$ / kJ·mol^{-1}	H_m^0 (g, *T*) - H_m^0 (g, 298.15 K) / kJ·mol^{-1}
1:3 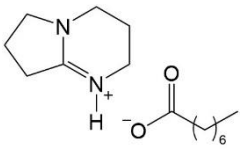	4.48	224.64	225.4 ± 1.0	41.0 ± 1.0
	5.00	225.59		
	3.84	226.92		
	5.05	225.54		
	2.87	224.91		
	4.68	224.71		
	4.92	225.62		
	$\Delta_l^g H_m^0$ (298.15 K) / kJ·mol^{-1} = (184.4 ± 1.5)			

Table 7.37. Experimental results obtained by Calvet microcalorimetry for the vaporization of [DBUH][nPrCOO] (3:1) (*T*=396.3 K). *T* (at K) being the temperature at which the Calvet measurements were performed.

	$m_{compound}$ / mg	$\Delta_l^g H_m^0$ / kJ·mol^{-1}	$\langle\Delta_l^g H_m^0\rangle$ / kJ·mol^{-1}	H_m^0 (g, *T*) - H_m^0 (g, 298.15 K) / kJ·mol^{-1}
3:1 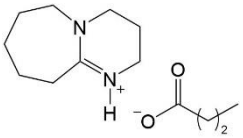	6.30	179.89		
	4.85	184.31		
	7.01	181.97		
	4.34	183.84	182.7 ± 1.1	37.4 ± 1.0
	4.57	183.59		
	4.92	182.78		
	4.97	182.31		
	$\Delta_l^g H_m^0$ (298.15 K) / kJ·mol^{-1} = (145.3 ± 1.5)			

Table 7.38. Experimental results obtained by Calvet microcalorimetry for the vaporization of [DBUH][nPrCOO] (2:1) (*T*=396.3 K). *T* (at K) being the temperature at which the Calvet measurements were performed.

	$m_{compound}$ / mg	$\Delta_l^g H_m^0$ / kJ·mol^{-1}	$\langle\Delta_l^g H_m^0\rangle$ / kJ·mol^{-1}	H_m^0 (g, *T*) - H_m^0 (g, 298.15 K) / kJ·mol^{-1}
2:1 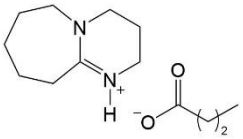	5.38	183.84		
	5.55	183.20	183.5 ± 1.0	36.4 ± 1.0
	5.09	183.49		
	$\Delta_l^g H_m^0$ (298.15 K) / kJ·mol^{-1} = (147.1 ± 1.5)			

Table 7.39. Experimental results obtained by Calvet microcalorimetry for the vaporization of [DBUH][nPrCOO] (eq) (*T*=396.3 K). *T* (at K) being the temperature at which the Calvet measurements were performed.

	$m_{compound}$ / mg	$\Delta_l^g H_m^0$ / kJ·mol^{-1}	$\langle\Delta_l^g H_m^0\rangle$ / kJ·mol^{-1}	H_m^0 (g, *T*) - H_m^0 (g, 298.15 K) / kJ·mol^{-1}
equilibrium 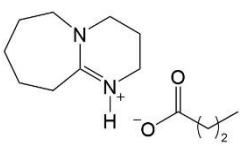	4.31	213.75		
	5.61	216.56		
	3.66	216.25	216.1 ± 1.1	32.2 ± 1.0
	3.59	217.19		
	2.68	214.96		
	6.29	217.48		
	$\Delta_l^g H_m^0$ (298.15 K) / kJ·mol^{-1} = (183.9 ± 1.5)			

Table 7.40. Experimental results obtained by Calvet microcalorimetry for the vaporization of [DBUH][nPrCOO] (1:3) (*T*=396.4 K). *T* (at K) being the temperature at which the Calvet measurements were performed.

	$m_{compound}$ / mg	$\Delta_l^g H_m^0$ / kJ·mol^{-1}	$\langle\Delta_l^g H_m^0\rangle$ / kJ·mol^{-1}	H_m^0 (g, *T*) - H_m^0 (g, 298.15 K) / kJ·mol^{-1}
1:3 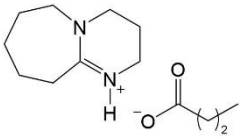	5.21	185.71		
	5.05	188.40		
	4.97	189.94		
	3.63	188.22	188.2 ± 1.1	29.0 ± 1.0
	5.48	187.49		
	4.76	189.22		
	3.98	188.33		
	$\Delta_l^g H_m^0$ (298.15 K) / kJ·mol^{-1} = (159.2 ± 1.5)			

Table 7.41. Experimental results obtained by Calvet microcalorimetry for the vaporization of [DBUH][nHeptCOO] (3:1) (*T*=386.4 K). *T* (at K) being the temperature at which the Calvet measurements were performed.

	$m_{compound}$ / mg	$\Delta_l^g H_m^0$ / kJ·mol^{-1}	$\langle\Delta_l^g H_m^0\rangle$ / kJ·mol^{-1}	H_m^0 (g, *T*) - H_m^0 (g, 298.15 K) / kJ·mol^{-1}
3:1 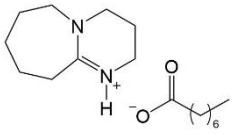	3.61	190.90		
	5.20	188.65	189.9 ± 1.2	36.3 ± 1.0
	3.43	190.23		
	$\Delta_l^g H_m^0$ (298.15 K) / kJ·mol^{-1} = (153.6 ± 1.5)			

Table 7.42. Experimental results obtained by Calvet microcalorimetry for the vaporization of [DBUH][nHeptCOO] (2:1) (*T*=386.4 K). *T* (at K) being the temperature at which the Calvet measurements were performed.

	$m_{compound}$ / mg	$\Delta_l^g H_m^0$ / kJ·mol^{-1}	$\langle\Delta_l^g H_m^0\rangle$ / kJ·mol^{-1}	H_m^0 (g, *T*) - H_m^0 (g, 298.15 K) / kJ·mol^{-1}
2:1 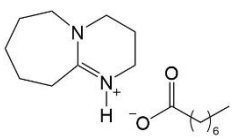	4.32	205.67		
	4.89	200.50	203.0 ± 1.7	37.5 ± 1.0
	4.96	202.96		
	$\Delta_l^g H_m^0$ (298.15 K) / kJ·mol^{-1} = (165.6 ± 1.8)			

Table 7.43. Experimental results obtained by Calvet microcalorimetry for the vaporization of [DBUH][nHeptCOO] (eq) (*T*=396.3 K). *T* (at K) being the temperature at which the Calvet measurements were performed.

equilibrium 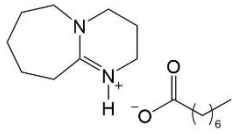	$m_{compound}$ / mg	$\Delta_l^g H_m^0$ / kJ·mol^{-1}	$\langle\Delta_l^g H_m^0\rangle$ / kJ·mol^{-1}	$H_m^0(g,T) - H_m^0(g,298.15\ K)$ / kJ·mol^{-1}
	5.19	246.85		
	4.20	244.63	245.6 ± 1.2	42.8 ± 1.0
	5.80	245.26		
$\Delta_l^g H_m^0$ (298.15 K) / kJ·mol^{-1} = (202.8 ± 1.5)				

Table 7.44. Experimental results obtained by Calvet microcalorimetry for the vaporization of [DBUH][nHeptCOO] (1:3) (*T*=386.4 K). *T* (at K) being the temperature at which the Calvet measurements were performed.

1:3 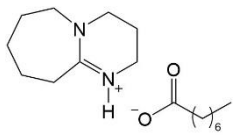	$m_{compound}$ / mg	$\Delta_l^g H_m^0$ / kJ·mol^{-1}	$\langle\Delta_l^g H_m^0\rangle$ / kJ·mol^{-1}	$H_m^0(g,T) - H_m^0(g,298.15\ K)$ / kJ·mol^{-1}
	3.14	224.8		
	4.84	226.4	225.7 ± 1.1	38.3 ± 1.0
	3.69	225.7		
$\Delta_l^g H_m^0$ (298.15 K) / kJ·mol^{-1} = (187.4 ± 1.5)				

Table 7.45. Standard molar enthalpies of vaporization for the studied compounds with different proportions of acid and base (B:A), as determined by Calvet microcalorimetry.

Compound	Proportion	Molar Mass* / g·mol^{-1}	$\Delta_l^g H_m^0$ (298.15 K) / kJ·mol^{-1}
[DBNH][nPrCOO]	1:1	212.29	164.4 ± 1.5
	3:1	115.88	131.4 ± 1.5
	2:1	111.66	135.1 ± 1.5
	eq (1:1.4)	103.62	165.5 ± 1.5
	1:3	97.49	153.6 ± 1.5
[DBNH][nHeptCOO]	1:1	268.40	176.5 ± 1.6
	3:1	129.59	140.5 ± 1.6
	2:1	130.99	149.2 ± 1.5
	eq (1:1.8)	137.20	186.0 ± 1.5
	1:3	139.00	184.4 ± 1.5
[DBUH][nPrCOO]	1:1	240.35	183.7 ± 1.8
	3:1	137.49	145.3 ± 1.5
	2:1	130.76	147.1 ± 1.5
	eq (1:1.3)	116.97	183.9 ± 1.5
	1:3	104.78	159.2 ± 1.5
[DBUH][nHeptCOO]	1:1	296.45	199.4 ± 1.6
	3:1	150.23	153.6 ± 1.5
	2:1	149.51	165.6 ± 1.8
	eq (1:1.6)	147.34	202.8 ± 1.5
	1:3	146.22	187.4 ± 1.5

***** Molar masses of the PILs (proportions) calculated as the proportion of the molar masses of the acid and base.

In this work, two approaches were studied and developed to understand how the ΔH_{vap} changed with different proportions of acid or base in their composition. One considering that the PIL is a mixture of pure base with pure acid (approach 1) and the other as a mixture of the 1:1 PIL with excess base or acid (approach 2). ΔH_{vap} of excess was calculated for both approaches as:

$$\Delta H_{vap}\,(\text{excess}) = \Delta H_{vap}\,(\text{ideal}) - \Delta H_{vap}\,(\text{observed}) \qquad \textbf{(7.11)}$$

For approach 1:

$$\Delta H_{vap}\,(\text{ideal 1}) = x_{acid} \cdot \Delta H_{vap}\,(\text{acid}) + x_{base} \cdot \Delta H_{vap}\,(\text{base}) \qquad \textbf{(7.12)}$$

$$\Delta H_{vap}\,(\text{observed 1}) = \Delta H_{vap}\,(\text{PIL}) / 2 \qquad \textbf{(7.13)}$$

For approach 2:

Excess of base:

$$\Delta H_{vap}\ (\text{ideal 2}) = x_{base} \cdot \Delta H_{vap}\ (\text{base}) + x_{PIL} \cdot \Delta H_{vap}\ (\text{PIL}) \quad \textbf{(7.14)}$$

Excess of acid:

$$\Delta H_{vap}\ (\text{ideal 3}) = x_{acid} \cdot \Delta H_{vap}\ (\text{acid}) + x_{PIL} \cdot \Delta H_{vap}\ (\text{PIL}) \quad \textbf{(7.15)}$$

$$\Delta H_{vap}\ (\text{observed 2}) = \Delta H_{vap}\ (\text{observed 1}) \cdot MM_{mixture} / \langle MM \rangle \quad \textbf{(7.16)}$$

$$MM_{mixture} = x_{PIL} \cdot MM_{PIL} + x_{base} \cdot MM_{base} + x_{acid} \cdot MM_{acid} \quad \textbf{(7.17)}$$

$$\langle MM \rangle = x_{base} \cdot MM_{base} + x_{acid} \cdot MM_{acid} \quad \textbf{(7.18)}$$

The first approach, table 7.46 and figure 7.10, shows how the ΔH_{vap} would change if the PIL was only constituted by acid and base. As can be seen, at the equilibrium proportion, the ΔH_{vap} excess would be greater when compared to other proportions. DBU-based PILs present higher excess of ΔH_{vap} and PILs with shorter acids seem to have also higher ΔH_{vap} of excess.

Table 7.46. Standard molar enthalpies of vaporization of excess, at T = 298.15 K, ΔH_{vap} (excess), of protic ionic liquid in function of the fraction of the acid, x_{acid} in each protic ionic liquid and using Approach 1 (Acid + Base). Values of ΔH in kJ·mol^{-1}.

Acid fraction x_{acid}	ΔH_{vap} **(excess)**			
	[DBNH][nPrCOO]	**[DBNH][nHeptCOO]**	**[DBUH][nPrCOO]**	**[DBUH][nHeptCOO]**
0.23	-2.5	-	-5.0	-
0.25	-	-	-	-4.6
0.27	-	-2.0	-	-
0.33	-4.7	-	-6.8	-
0.34	-	-5.3	-	-9.6
0.49	-	-16.5	-	-
0.52	-	-	-26.8	-
0.54	-20.0	-	-	-24.5
0.55	-	-	-27.2	-
0.57	-20.7	-	-	-
0.61	-	-	-	-25.5
0.65	-	-18.7	-	-
0.74	-15.2	-16.5	-16.6	-
0.75	-	-	-	-16.4

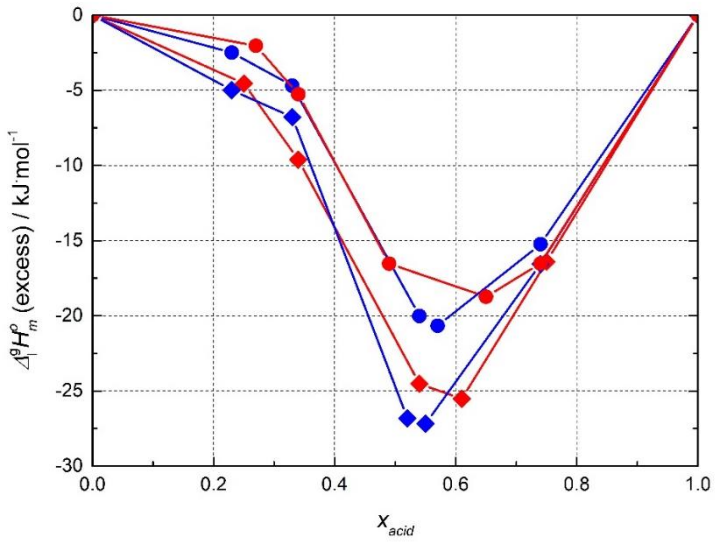

Figure 7.10. Standard molar enthalpies of vaporization, at T = 298.15 K, ΔH_{vap} (excess), of protic ionic liquid in function of the fraction of the acid, x_{acid} in each protic ionic liquid and using Approach 1 (Acid + Base). DBN-based protic ionic liquids – circles, DBU-based protic ionic liquids – diamonds. Butyric acid – **blue** color and Octanoic acid – **red** color.

The excess enthalpy of mixing by considering the mixture of pure base with pure acid (approach 1) is plotted in figure 7.10 as a function of the molar fraction of the acid, x_{acid}. In this figure the PILs [DBNH][nPrCOO], [DBNH][nHeptCOO], [DBUH][nPrCOO] and [DBUH][nHeptCOO] were considered to evaluate both the effect of the acid and base. As it can be seen, the mixing is exothermic for all compositions, although significant in the acid-rich region. The maxima exothermically speaking, are found for $x_{acid} \approx 0.5$, but, not exactly the stoichiometric composition. The maxima occur at the azeotropic composition found for each PIL. This corroborate that these non-stoichiometric compositions are thermodynamically preferred and suggests that the main driving force for the PILs to acquire non-stoichiometric ratio is the gain in cohesive energy on adding excess acid to the mixture.

Approach 2 (table 7.47 and figure 7.11) shows the variation in ΔH_{vap} if the PIL it's a mixture of PIL and excess of one component (base or acid). The four different studied PILs like more acid in their composition and dislike more base. And bigger acids and proportions nearby equilibrium seem to increase the ΔH_{vap} of excess.

Table 7.47. Standard molar enthalpies of vaporization of excess, at T = 298.15 K, ΔH_{vap} (excess), of protic ionic liquid in function of the fraction of the acid, x_{acid} and in function of the fraction of the base, x_{base} in each protic ionic liquid and using Approach 2 (PIL + base and PIL + acid). Values of ΔH in kJ·mol^{-1}.

	fraction *x*	ΔH_{vap} (excess)			
		[DBNH][nPrCOO]	[DBNH][nHeptCOO]	[DBUH][nPrCOO]	[DBUH][nHeptCOO]
Base	0.70	8.8	-	9.4	-
	0.67	-	-	-	8.2
	0.63	-	9.3	-	-
	0.51	12.2	-	15.8	-
	0.48	-	8.9	-	7.4
Acid	0.18	-	-	-5.8	-
	0.25	-5.9	-	-	-
	0.36	-	-	-	-14.6
	0.46	-	-11.2	-	-
	0.65	-6.5	-10.8	-3.7	-
	0.67	-	-	-	-7.7

Figure 7.11 shows the excess enthalpy of mixing for the mixture of the 1:1 PIL with excess base (left) or acid (right) (approach 2). The results indicate clearly that the mixture is enthalpically stabilized upon addition of excess acid but destabilized by adding excess base. As in approach 1 the maximum occurs at the azeotropic composition of the PILs.

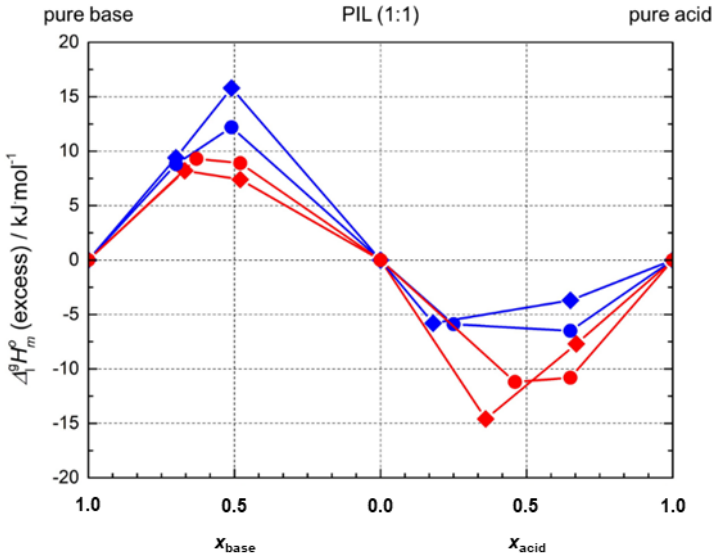

Figure 7.11. Standard molar enthalpies of vaporization, at T = 298.15 K, ΔH_{vap} (excess), of protic ionic liquid in function of the fraction of the acid, x_{acid} and in function of the fraction of the base, x_{base} in each protic ionic liquid and using Approach 2 (PIL + base and PIL + acid). DBN-based protic ionic liquids – circles, DBU-based protic ionic liquids – diamonds. Butyric acid – **blue** color and Octanoic acid – **red** color.

Destabilization by adding excess base is easily understood by analyzing the figures B.1 and B.2, presented in Annex B. High proportion of base decreases the molar fraction of PIL in equilibrium, thus reducing the cohesive energy of the less ionic liquid. Although the effect of increasing the acid in the PIL molar fraction is identical, the excess acid can compensate for this by establishing H-bonds with the ion pair. Hence, the azeotropic composition reflects the compromise between these two effects: the decrease of PIL concentration as that of the acid increases and the function of ion pair ---- neutral acid H-bonds.

7.3. References

[7.1] Tian, A.; *Bull. Soc. Chim. Fr. Ser*. **1923**, 4 (33), 427.

[7.2] Calvet, E., *C. R. Acad. Sci. Paris* **1948**, 226, 1702.

[7.3] Calvet, E.; Prat, H., *Recent Progress in Microcalorimetry*, Pergamon Press, New York **1963**.

[7.4] Calvet, E., chapter 12, in: *Experimental Thermochemistry*, vol. 1, F.D. Rossini (Ed.), Interscience, New York **1956**.

[7.5] Calvet, E. chapter 17, in: *Experimental Thermochemistry*, vol. 2, H.A. Skinner (Ed.), Interscience, New York **1962**.

[7.6] Adedeji, F. A.; Brown, D. L. S.; Connor, J. A.; Leung, M. L.; Paz-Andrade, M. I.; Skinner, H. A., *J. Organomet. Chem*. **1975**, 97, 221-228.

[7.7] Ribeiro da Silva, M. A. V.; Matos, M. A. R.; Amaral, L. M. P. F., *J. Chem. Thermodyn*. **1995**, 27, 565-574.

[7.8] Santos, L. M. N. B. F.; Schröder, B.; Fernandes, O. O. P.; Ribeiro da Silva, M. A. V., *Thermochim. Acta* **2004**, 415, 15-20.

[7.9] Stull, D. R.; Westrum, E. F. Jr.; Sinke, G. C., *The Chemical Thermodynamics of Organic Compounds*, John Wiley & Sons, Inc., New York **1969**.

[7.10] Rocha, M. A. A.; Lima, C. F. R. A. C.; Gomes, L. R.; Schröder, B.; Coutinho, J. A. P.; Marrucho, I. M.; Esperança, J. M. S. S.; Rebelo, L. P. N.; Shimizu, K.; Lopes, J. N. C.; Santos, L. M. N. B. F., *J. Phys. Chem. B* **2011**, 115, 10919-10926.

[7.11] Esperança, J. M. S. S.; Lopes, J. N. C.; Tariq, M.; Santos, L. M. N. B. F.; Magee J. W.; Rebelo, L. P. N. *J. Chem. Eng. Data* **2010**, 55, 3-12.

[7.12] Rocha, M. A. A.; Santos, L. M. N. B. F., *Chem. Phys. Let*. **2013**, 585, 59-62.

[7.13] Rocha, M. A. A.; Coutinho, J. A. P.; Santos, L. M. N. B. F., *J. Chem. Phys*. **2014**, 141, 134502.

[7.14] Rocha, M. A. A.; Coutinho, J. A. P.; Santos, L. M. N. B. F., *J. Phys. Chem. B* **2012**, 116, 10922-10927.

[7.15] Santos, L. M. N. B. F.; Lopes, J. N. C.; Coutinho, J. A. P.; Esperança, J. M. S. S.; Gomes, L. R.; Marrucho, I. M.; Rebelo, L. P. N., *J. Am. Chem. Soc.* **2007**, 129, 284-285.

[7.16] Růžička, K.; Majer, V., *J. Phys. Chem. Ref. Data* **1994**, 23, 1-39.

[7.17] Chickos J. S.; Hanshaw, W., *J. Chem. Eng. Data* **2004**, 49, 77-85.

[7.18] Matulis, D. *Biophys. Chem*. **2001**, 93, 67-82.

[7.19] Vitorino, J.; Leal, J. P.; Minas da Piedade, M. E.; Lopes, J. N. C.; Esperança, J. M. S. S.; Rebelo, L. P. N., *J. Phys. Chem. B* **2010**, 114, 8905–8909.

[7.20] Vitorino, J.; Bernardes, C. E. S.; Minas da Piedade, M. E., *Phys. Chem. Chem. Phys.* **2012**, 14, 4440–4446.

[7.21] Yoshizawa, M.; Xu, W.; Angell, C.A., *J. Am. Chem. Soc.* **2003**, 125, 15411-15419.

[7.22] Earle, M. J.; Esperança, J. M. S. S.; Gilea, M. A.; Canongia Lopes, J. N.; Rebelo, L. P. N.; Magee, J. W.; Seddon K. R.; Widegren, J. A., *Nature* **2006**, 439, 831-834.

[7.23] Ostonen, A.; Bervas, J.; Uusi-Kyyny, P.; Alopaeus, V.; Zaitsau, D. H.; Emel'yanenko, V. N.; Schick, C.; King, A. W. T.; Helminen, J.; Kilpeläinen, I.; Khachatrian, A. A.; Varfolomeev M. A.; Verevkin, S.P., *Ind. Eng. Chem. Res.* **2016**, 55, 10445–10454.

[7.24] Lipkind, D.; Rath, N.; Chickos, J. S.; Pozdeev, V. A.; Verevkin, S. P., *J. Phys. Chem. B* **2011**, 115, 8785–8796.

CHAPTER 8

Concluding Remarks and Perspectives

8. Concluding Remarks and Perspectives

8.1. Final remarks

Throughout this project some key physicochemical properties of PILs were measured in order to contribute to the comprehensive study of the stability of PILs. The main achievements and conclusions of this work are summarized according the studied properties and experimental strategies.

Gas phase quantum chemical

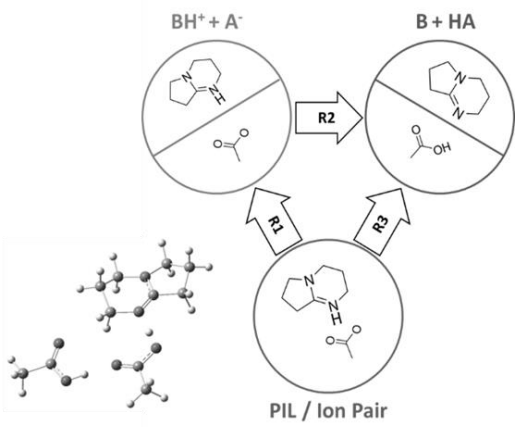

The experimental and theoretical studies of the studied superbases proton affinity indicate the following order of basicity: TBD > DBU > DBN ≥ DMTHP >TMG. It was found that the ion pair is enthalpically preferred in all PILs and that in the gas phase, the PILs exist mostly as a distribution of ion pair and isolated neutral species, this distribution being dependent on the equilibrium temperature and pressure. The accessible surface areas of several PILs were studied and the distances between the acids and superbases were calculated. A nice correlation between the basicity strength of the superbases and the accessible surface area was found.

Phase behavior and heat capacities

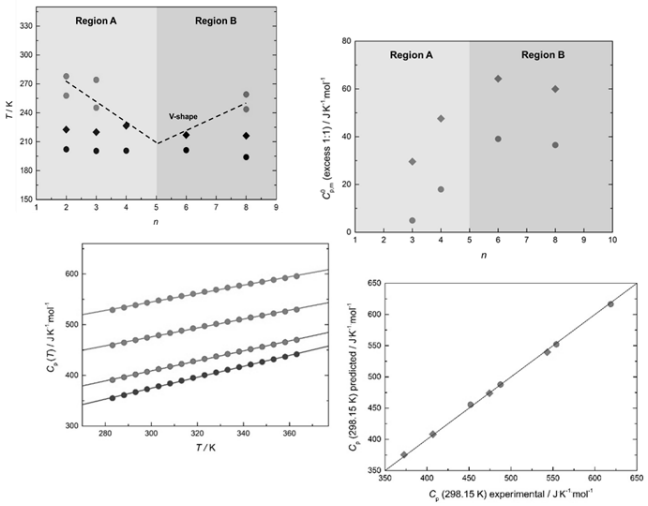

Crystal forms of PILs composed with acids of intermediate chain length, seems to not be accessible. The observed “V-Shape” profile is quite similar than the observed in previous studies dealing with aprotic ILs. This intermediate region arises a consequence of the weakening of the electrostatic interactions and decrease of the symmetry of the anions or cations. The increase of the melting temperature after that, appears a consequence of the impact of the increase of the alkyl chain dispersive interaction. The higher (about 20 K) T_g of DBU PILs compared to the DBN analogues, can be explained by their higher ionicity. The T_g/T_m ratio was found to be around 0.75 for these two PILs families (DBN and DBU-based), quite similar to those of AILs.

High accurate (1% uncertainty) molar heat capacity of the PILs (derived from the combination of the DBU and DBN with carboxylic acid series) were measured in the temperature range (283 to 363 K). A good linear dependence of the molar heat capacity at (298.15 K) with the number of methylene groups “-CH_2-“ was found, with a “-CH_2-“ Cp contribution very similar than in alkanes. A trend shift at n = 5 and two different regions (A for short acids and B for long acids) was found following the similar profile observed in the the molar heat capacities of the carboxylic acids. A linear multivariable (T, n) dependence of the molar heat capacities (applied to each base DBN and DBU) with the temperature T and alkyl chain length n, was found to fit quite well (better than 1%) the experimental results. At T = 298.15 K, the excess molar heat capacities are positive being around 30 $J \cdot K^{-1} \cdot mol^{-1}$ higher for the DBU-based protic ionic liquids when compared to the DBN-based protic ionic liquids. These positive values are in agreement with a higher iconicity character of the studied PILs.

Speciation study of PILs

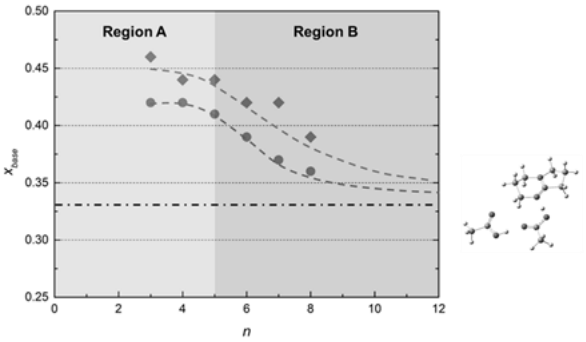

All PILs show pronounced negative deviations from Raoult's Law, with a significant decrease of vapor pressure, indicating that the mixture is significantly stabilized. The azeotropic composition was found to be depend on the extent of the acid-base equilibrium and also on the alkyl chain length of the carboxylic acid. The increase in the azeotrope molar fraction of the acid as its alkyl chain increases follows the decrease of the acid's volatility and seems to converge to the 2 (acid) to 1(base) molar ratio. The azeotropic composition for the DBU PILs is closer to 50:50 because DBU is the strongest and least volatile of the bases. Although DBN and DMTHP are similarly basic, DMTHP is more volatile and thus its azeotropic proportion is lower.

Cohesive energy of PILs

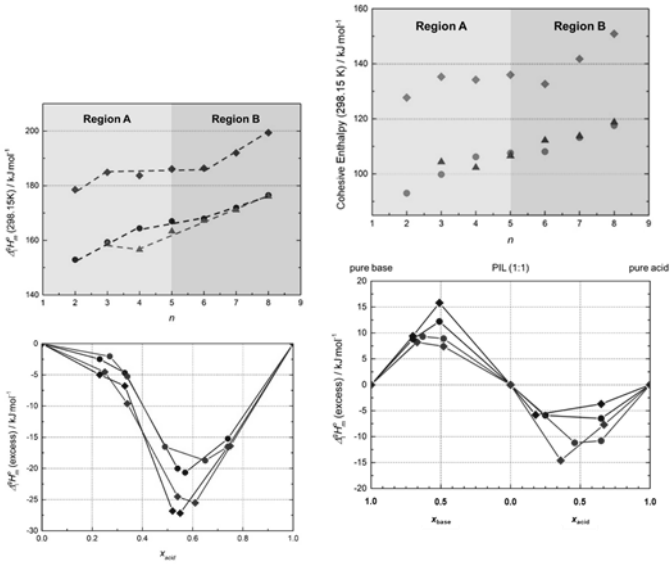

The strong effect of changing the base was also evident in the ΔH_{vap} of the studied PILs, as measured by Calvet microcalorimetry. The results indicate that the physicochemical properties of the PILs are more dependent on the strength of the acid-base interaction than on the alkyl chain length of the carboxylic acid. From the magnitude of ΔH_{vap} it can be concluded that in the studied PILs, the proton transfer between acid and base occurs at a large extent and a significant fraction of species exist as ions. Increasing the alkyl chain of the acid generally increases ΔH_{vap} of the PILs due to stronger van der Waals interactions. The change of the superbase (from DBN to DBU) increases ΔH_{vap} significantly. This is due to the higher proton exchange enthalpy of DBU, in minor scale due to the increase of the proportion of ions in liquid PILs and also due to the shape/size/structuration of the liquid. A trend-shift along the acid's alkyl chain length was observed for the vaporization. This change in trend occurs at n = 4-6 and may be related with nanostructuration pattern in the liquid phase of PILs which is similar than the observed in some other AILs series. The results suggest that the liquid-phase azeotropic composition of the PILs is dominated by an H-bonded interaction and the complex formed between the ion-pair and a neutral acid molecule.

8.2. Future work and perspectives

For future work and perspectives considering the topic studied in this work, one can say that several studies and properties are still a “world to discover”.

Measurements of the viscosities and densities of PILs are quite essential to understand better their behaviour as a function of the temperature. Mixtures of PILs with different proportions, solubility and or solvation of gases and other solvents (H_2O, alcohols etc.) in PILs, thermophysical properties of new PILs with new superbases and other acids, simulation of PILs and their clusters etc., the effect of the acid in the PIL and their properties (trend shift in heat capacities), are some topics that should be considered to think, work and investigate in the future.

As a major perspective and motivation for the future will be the robust study of the biomass processing and the participation in the optimization of a successful industrial application.

Annexes

Annex A	*NMR and FTIR data*
Annex B	*Quantum chemical calculations data*
Annex C	*Phase behavior data*

Annex A

Annex A

A.1.

^{1}H, ^{13}C and ^{19}F NMR data

NMR description of the PILs synthesized:

[DBNH][MeCOO]:

^{1}H NMR (300 MHz, $CDCl_3$), δ / ppm, 10.76 (s, 1H), 3.66 (t, J = 7.2 Hz, 2H), 3.50-3.40 (m, 4H), 3.04 (t, J = 8.1 Hz, 2H), 2.17 (dt, $J_1 \approx J_2$ = 7.6 Hz, 2H), 2.05 (dt, $J_1 \approx J_2$ = 6.0 Hz, 2H), 1.94 (s, 3H); ^{13}C NMR (75 MHz, $CDCl_3$), δ / ppm, 177.2, 163.8, 52.6, 42.2, 37.7, 29.4, 24.5, 18.6, 18.5.

[DBNH][EtCOO]:

^{1}H NMR (300 MHz, $CDCl_3$), δ / ppm, 12.99 (s, 1H), 3.66 (t, J = 7.2 Hz, 2H), 3.52-3.41 (m, 4H), 3.07 (t, J = 8.1 Hz, 2H), 2.25-2.12 (m, 4H), 2.05 (dt, $J_1 \approx J_2$ = 6.0 Hz, 2H), 1.10 (t, J = 7.5 Hz, 3H); ^{13}C NMR (75 MHz, $CDCl_3$), δ / ppm, 180.3, 163.7, 52.6, 42.1, 37.5, 30.6, 29.4, 18.6, 18.5, 10.7.

[DBNH][nPrCOO]:

^{1}H NMR (300 MHz, $CDCl_3$), δ / ppm, 11.79 (s, 1H), 3.65 (t, J = 7.2 Hz, 2H), 3.51-3.40 (m, 4H), 3.07 (t, J = 8.1 Hz, 2H), 2.22-2.10 (m, 4H), 2.04 (dt, $J_1 \approx J_2$ = 6.0 Hz, 2H), 1.63 (sextet, J = 7.5 Hz, 2H), 0.94 (t, J = 7.5 Hz, 3H); ^{13}C NMR (75 MHz, $CDCl_3$), δ / ppm, 179.7, 163.8, 52.6, 42.2, 40.0, 37.6, 29.4, 19.7, 18.6, 18.5, 14.1.

[DBNH][nButCOO]:

^{1}H NMR (300 MHz, $CDCl_3$), δ / ppm, 3.57 (t, J = 7.2 Hz, 2H), 3.49 (t, J = 5.7 Hz, 2H), 3.36 (m, 2H), 3.11 (t, J = 8.1 Hz, 2H), 2.24 (t, J = 7.2 Hz, 2H), 2.13 (dt, $J_1 \approx J_2$ = 7.8 Hz, 2H), 2.02 (dt, $J_1 \approx J_2$ = 5.7 Hz, 2H), 1.74-1.55 (m, 2H), 1.43-1.25 (m, 3H), 0.91 (t, J = 7.2 Hz, 3H); ^{13}C NMR (75 MHz, $CDCl_3$), δ / ppm, 180.6, 164.3, 52.9, 42.5, 38.0, 37.7, 29.7, 28.7, 22.8, 19.0, 18.9, 14.0.

[DBNH][nPentCOO]:

^{1}H NMR (300 MHz, $CDCl_3$), δ / ppm, 3.60 (t, J = 7.2 Hz, 2H), 3.47 (t, J = 6.0 Hz, 2H), 3.39 (t, J = 6.0 Hz, 2H), 3.06 (t, J = 8.1 Hz, 2H), 2.25-2.07 (m, 4H), 2.02 (dt, $J_1 \approx J_2$ = 6.0 Hz, 2H), 1.71-1.56 (m, 2H), 1.40-1.25 (m, 4H), 0.88 (t, J = 6.9 Hz, 3H); ^{13}C NMR (75 MHz, $CDCl_3$), δ / ppm, 180.4, 163.8, 52.6, 42.3, 38.3, 38.1, 31.9, 29.6, 26.3, 22.4, 18.8, 13.9.

[DBNH][nHexCOO]:

^{1}H NMR (300 MHz, $CDCl_3$), δ / ppm, 3.58 (t, J = 6.9 Hz, 2H), 3.49 (t, J = 5.7 Hz, 2H), 3.36 (m, 2H), 3.10 (t, J = 7.8 Hz, 2H), 2.27-2.07 (m, 4H), 2.02 (dt, $J_1 \approx J_2$ = 5.7 Hz, 2H), 1.77-1.54 (m, 2H), 1.40-1.18 (m, 6H), 0.87 (t, J = 6.6 Hz, 3H); ^{13}C NMR (75 MHz, $CDCl_3$), δ / ppm, 180.6, 164.4, 52.9, 42.5, 38.0, 37.9, 31.8, 29.7, 29.5, 26.5, 22.6, 19.0, 18.9, 14.1.

[DBNH][nHeptCOO]:

^{1}H NMR (300 MHz, $CDCl_3$), δ / ppm, 3.59 (t, J = 7.2 Hz, 2H), 3.48 (t, J = 5.7 Hz, 2H), 3.38 (t, J = 6.0 Hz, 2H), 3.08 (t, J = 8.1 Hz, 2H), 2.25-2.07 (m, 4H), 2.02 (dt, $J_1 \approx J_2$ = 6.0 Hz, 2H), 1.70-1.54 (m, 2H), 1.41-1.18 (m, 8H), 0.86 (t, J = 6.9 Hz, 3H); ^{13}C NMR (75 MHz, $CDCl_3$), δ / ppm, 180.6, 164.0, 52.7, 42.4, 38.5. 38.0, 31.7, 29.7, 29.6, 29.2, 26.7, 22.5, 18.9, 18.8, 14.0.

[DBUH][MeCOO]:

^{1}H NMR (300 MHz, $CDCl_3$), δ / ppm, 3.55-3.40 (m, 6H), 2.94-2.81 (m, 3H), 2.03 (dt, $J_1 \approx J_2$ = 6.0 Hz, 2H), 1.97 (s, 3H), 1.83-1.62 (m, 6H); ^{13}C NMR (75 MHz, CDCl3), δ / ppm, 177.6, 165.8, 54.0, 48.4, 37.8, 31.7, 29.0, 26.9, 24.5, 24.0, 19.5.

[DBUH][EtCOO]:

^{1}H NMR (300 MHz, $CDCl_3$), δ / ppm, 3.56-3.41 (m, 6H), 2.95-2.82 (m, 3H), 2.23 (q, J = 7.5 Hz, 2H), 2.02 (dt, $J_1 \approx J_2$ = 6.0 Hz, 2H), 1.85-1.62 (m, 6H), 1.11 (t, J = 7.5 Hz, 3H); ^{13}C NMR (75 MHz, $CDCl_3$), δ / ppm, 180.7, 165.7, 53.9, 48.4, 37.8, 31.7, 30.8, 28.9, 26.8, 24.0, 19.5, 10.8.

[DBUH][nPrCOO]:

^{1}H NMR (300 MHz, $CDCl_3$), δ / ppm, 3.57-3.41 (m, 6H), 2.96-2.84 (m, 3H), 2.18 (t, J = 7.5 Hz, 2H), 2.03 (dt, $J_1 \approx J_2$ = 6.0 Hz, 2H), 1.83-1.56 (m, 8H), 0.93 (t, J = 7.5 Hz, 3H); ^{13}C NMR (75 MHz, $CDCl_3$), δ / ppm, 179.8, 165.5, 53.8, 48.3, 40.4, 37.7, 31.5, 28.8, 26.7, 23.9, 19.8, 19.4, 14.1.

[DBUH][nButCOO]:

^{1}H NMR (300 MHz, $CDCl_3$), δ / ppm, 3.54-3.38 (m, 6H), 2.96-2.84 (m, 3H), 2.23 (t, J = 7.2 Hz, 2H), 2.00 (dt, $J_1 \approx J_2$ = 5.7 Hz, 2H), 1.85-1.55 (m, 8H), 1.43-1.27 (dt, $J_1 \approx J_2$ = 7.5 Hz, 2H), 0.90 (t, J = 7.5 Hz, 3H); ^{13}C NMR (75 MHz, $CDCl_3$), δ / ppm,180.8, 165.9, 54.1, 48.6, 38.0, 32.0, 29.2, 28.9, 27.1, 26.5, 24.2, 22.9, 19.8, 14.1.

[DBUH][nPentCOO]:

^{1}H NMR (300 MHz, $CDCl_3$), δ / ppm, 3.54-3.41 (m, 6H), 2.95-2.84 (m, 3H), 2.21 (t, J = 7.5 Hz, 2H), 2.02 (dt, $J_1 \approx J_2$ = 6.0 Hz, 2H), 1.84-1.56 (m, 8H), 1.40-1.23 (m, 4H), 0.88 (t, J = 6.9 Hz, 3H); ^{13}C NMR (75 MHz, $CDCl_3$), δ / ppm, 180.5, 165.7, 53.9, 48.5, 38.5, 37.9, 32.0, 31.7, 29.0, 27.0, 26.5, 24.1, 22.5, 19.6, 14.0.

[DBUH][nHexCOO]:

^{1}H NMR (300 MHz, $CDCl_3$), δ / ppm, 3.54-3.37 (m, 6H), 2.96-2.84 (m, 3H), 2.22 (t, J = 7.5 Hz, 2H), 2.01 (dt, $J_1 \approx J_2$ = 5.7 Hz, 2H), 1.84-1.55 (m, 8H), 1.40-1.23 (m, 6H), 0.87 (t, J = 6.3 Hz, 3H); ^{13}C NMR (75 MHz, $CDCl_3$), δ / ppm,180.8, 165.9, 54.1, 48.6, 38.4, 38.0, 32.0, 31.9, 29.6, 29.2, 27.1, 26.8, 24.2, 22.7, 19.8, 14.1.

[DBUH][nHeptCOO]:

^{1}H NMR (300 MHz, $CDCl_3$), δ / ppm, 3.53-3.37 (m, 6H), 2.96-2.84 (m, 3H), 2.22 (t, J = 7.5 Hz, 2H), 2.00 (dt, $J_1 \approx J_2$ = 6.0 Hz, 2H), 1.84-1.56 (m, 8H), 1.41-1.18 (m, 8H), 0.86 (t, J = 6.9 Hz, 3H).

[DMTHPH][EtCOO]:

^{1}H NMR (300 MHz, $CDCl_3$), δ / ppm, 3.47 (t, *J* = 6.0 Hz, 2H), 3.41-3.29 (m, 2H), 3.11 (s, 2H), 2.54 (s, 2H), 2.39 (s, 3H), 2.30-2.15 (m, 2H), 2.14-1.95 (m, 2H), 1.11 (t, *J* = 7.5 Hz, 3H).

[DMTHPH][nPentCOO]:

^{1}H NMR (300 MHz, $CDCl_3$), δ / ppm, 3.48 (t, *J* = 5.7 Hz, 2H), 3.37 (t, *J* = 5.7 Hz, 2H), 3.10 (s, 3H), 2.41 (s, 3H), 2.22 (t, *J* = 7.5 Hz, 2H), 2.02 (dt, $J_1 \approx J_2$ = 6.0 Hz, 2H), 1.71-1.56 (m, 3H), 1.41-1.24 (m, 4H), 0.88 (t, *J* = 6.9 Hz, 3H); ^{13}C NMR (75 MHz, $CDCl_3$), δ / ppm, 180.8, 160.6, 48.1, 38.7, 38.3_3, 38.2_6, 32.1, 26.5, 22.6, 19.3, 18.1, 14.1.

[DBNH][IPrCOO]:

^{1}H NMR (300 MHz, $CDCl_3$), δ / ppm, 11.69 (s, 1H), 3.66 (t, *J* = 7.2 Hz, 2H), 3.52-3.40 (m, 4H), 3.07 (t, *J* = 7.8 Hz, 2H), 2.46-2.29 (m, 1H), 2.24-2.10 (m, 2H), 2.10-1.99 (m, 2H), 1.20-1.08 (m, 6H); ^{13}C NMR (75 MHz, $CDCl_3$), δ / ppm, 180.2, 162.8, 52.2, 42.1, 38.5, 36.0, 29.6, 20.2, 19.1, 18.9, 17.7.

[DBNH][FPrCOO]:

^{1}H NMR (300 MHz, $CDCl_3$), δ / ppm, 3.66 (t, *J* = 7.2 Hz, 2H), 3.49 (t, *J* = 5.7 Hz, 2H), 3.43 (t, *J* = 5.7 Hz, 2H), 3.10 (t, *J* = 8.1 Hz, 2H), 2.26-1.96 (m, 5H); ^{19}F NMR (282 MHz, $CDCl_3$), δ / ppm, −103.94 (t, *J* = 8.7 Hz, 3F), −140.84 (q, *J* = 8.7 Hz, 2F), −150.06 (s, 2F).

[DBUH][IPrCOO]:

^{1}H NMR (300 MHz, $CDCl_3$), δ / ppm, 3.58-3.40 (m, 6H), 2.96-2.82 (m, 2H), 2.47-2.31 (m, 1H), 2.10-1.95 (m, 2H), 1.85-1.60 (m, 6H), 1.20-1.06 (m, 6H); ^{13}C NMR (75 MHz, $CDCl_3$), δ / ppm, 183.5, 165.5, 53.8, 48.3, 37.7, 36.7, 31.6, 28.8, 28.2, 26.7, 23.9, 20.4, 19.5.

A.2.

ATR-FTIR data

FTIR data for the PILs studied:

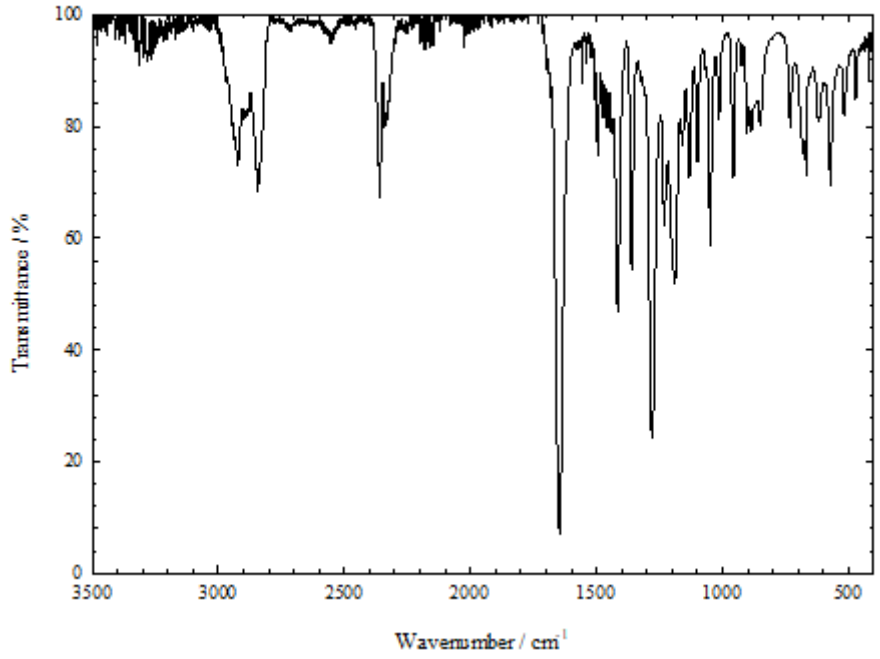

Figure A.1. FTIR spectrum of DBN, at *T* = 298 K.

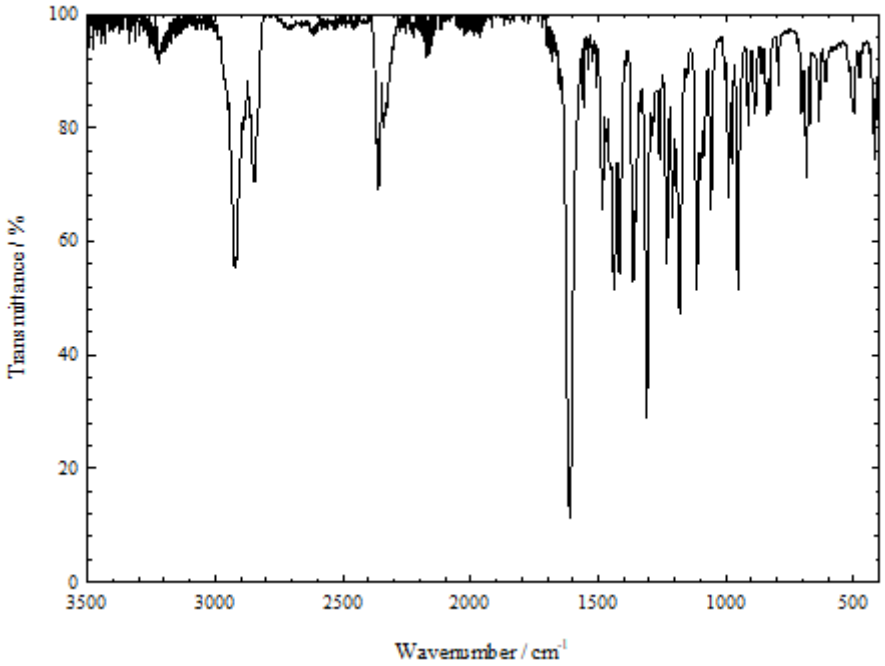

Figure A.2. FTIR spectrum of DBU, at *T* = 298 K.

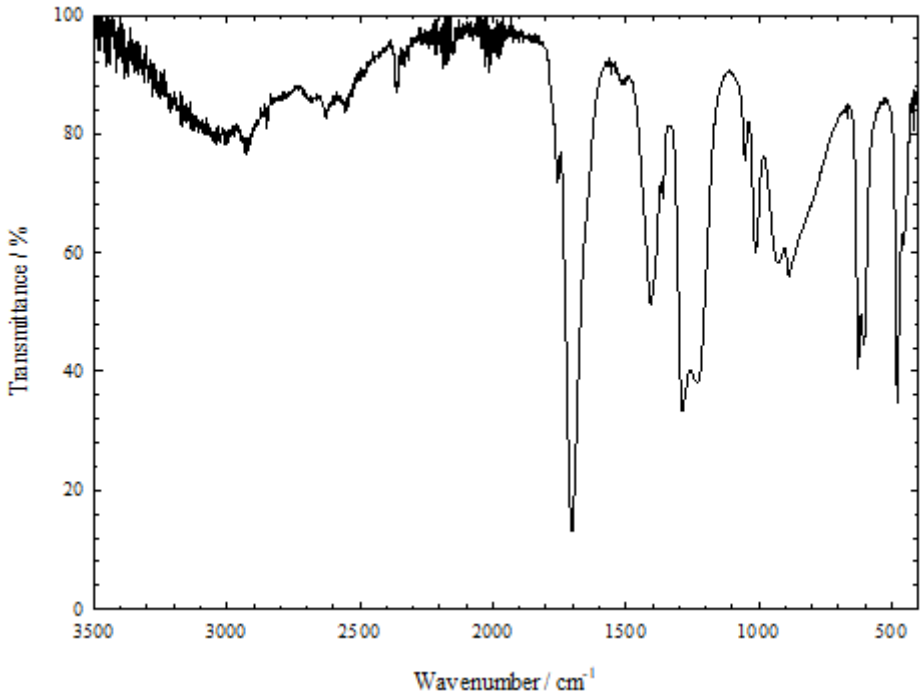

Figure A.3. FTIR spectrum of MeCOOH, at *T* = 298 K.

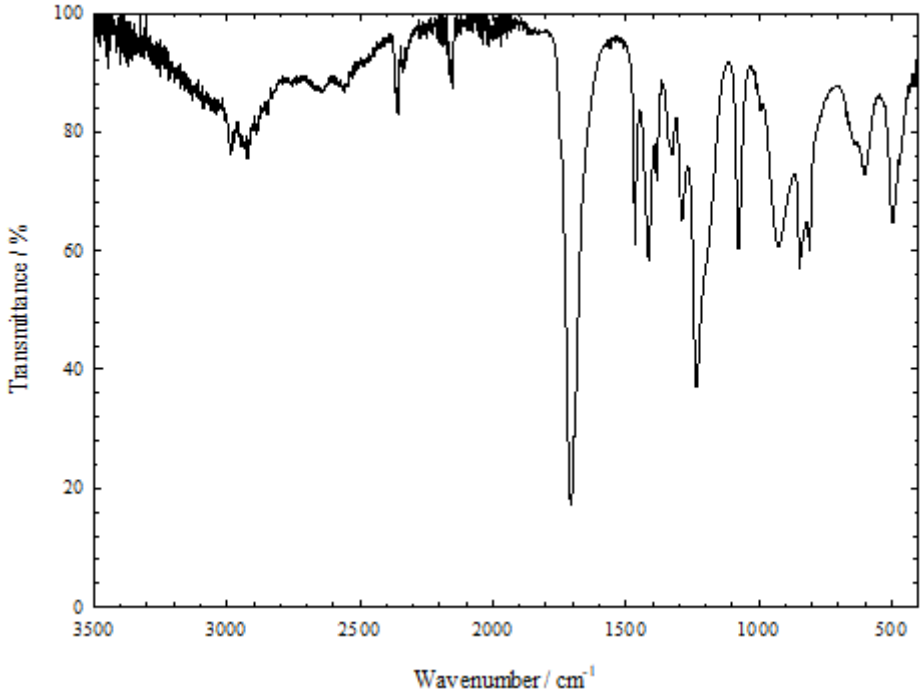

Figure A.4. FTIR spectrum of EtCOOH, at *T* = 298 K.

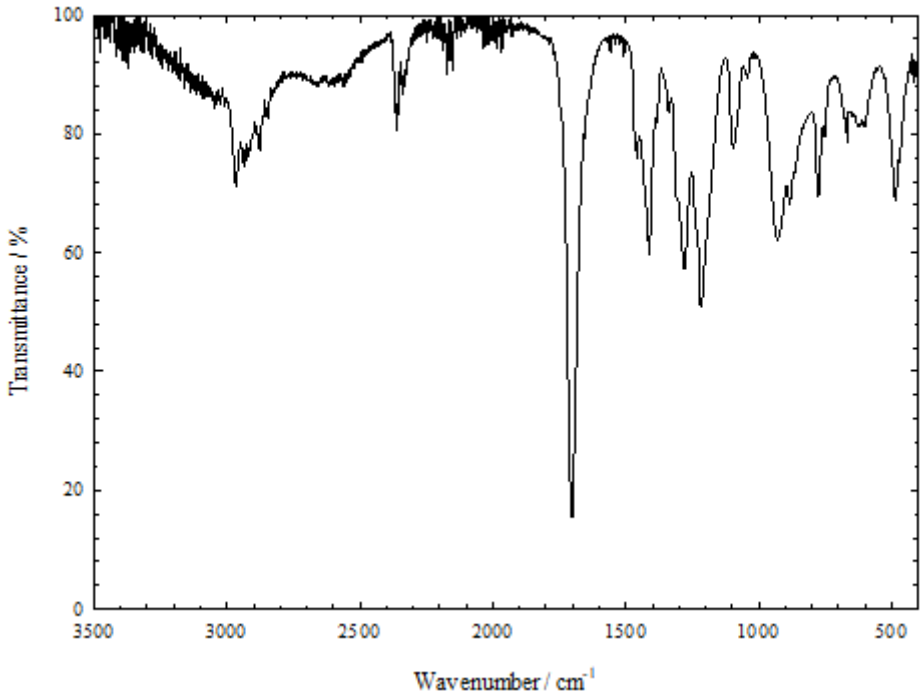

Figure A.5. FTIR spectrum of nPrCOOH, at *T* = 298 K.

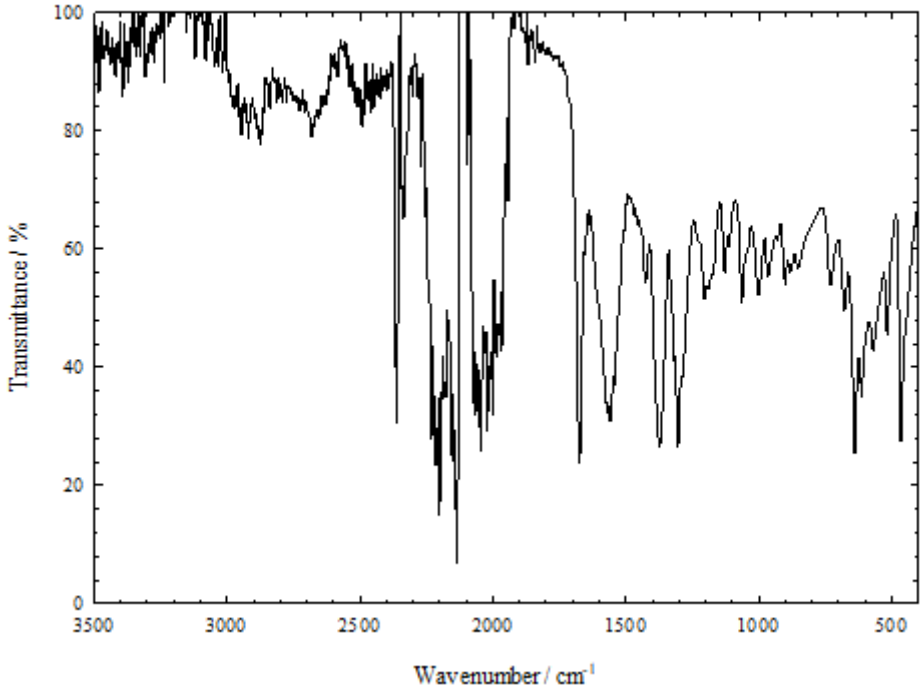

Figure A.6. FTIR spectrum of [DBNH][MeCOO], at *T* = 298 K.

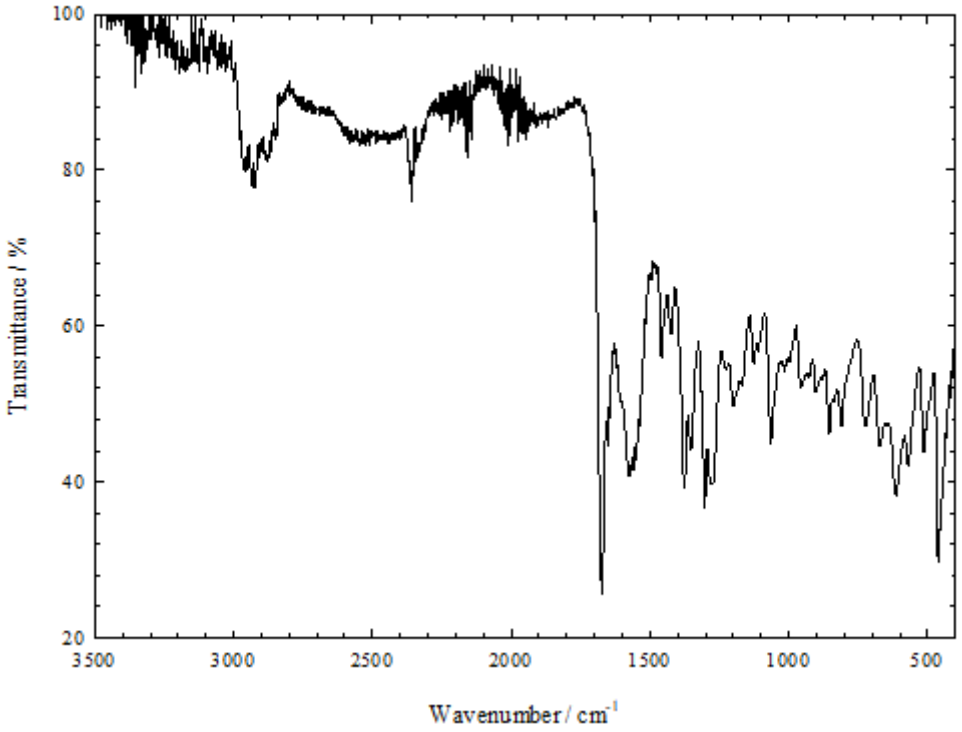

Figure A.7. FTIR spectrum of [DBNH][EtCOO], at *T* = 298 K.

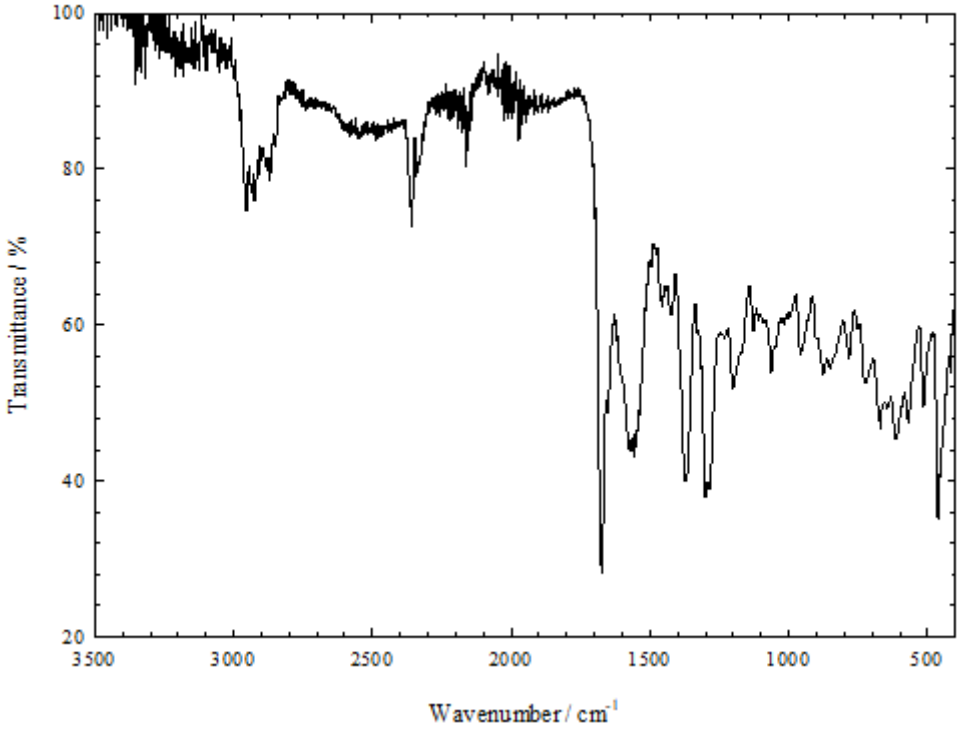

Figure A.8. FTIR spectrum of [DBNH][nPrCOO], at *T* = 298 K.

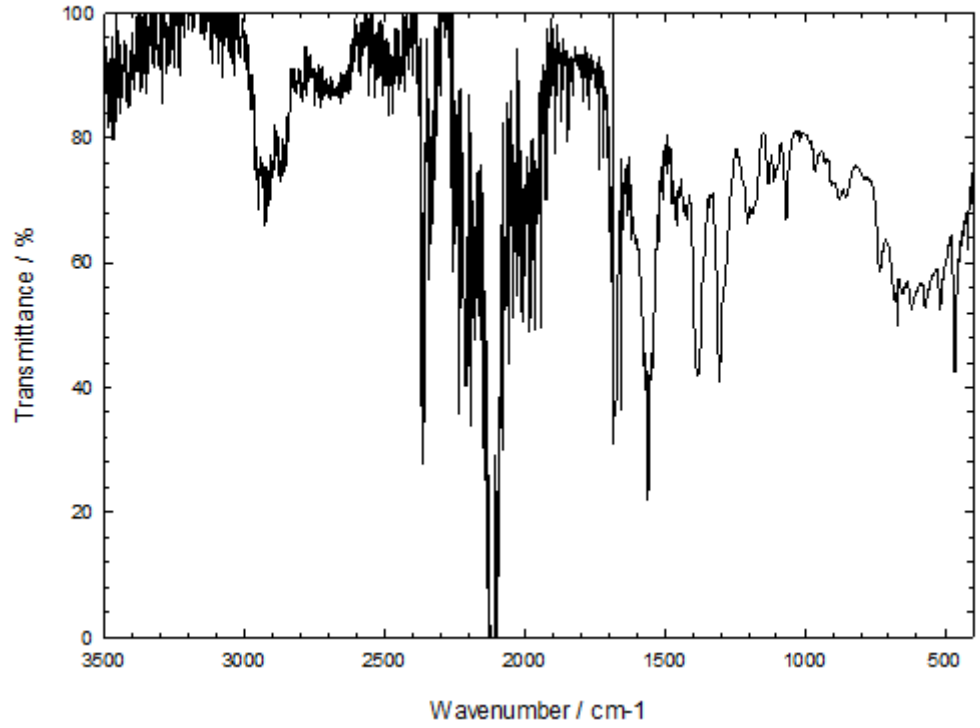

Figure A.9. FTIR spectrum of [DBNH][nPentCOO], at *T* = 298 K.

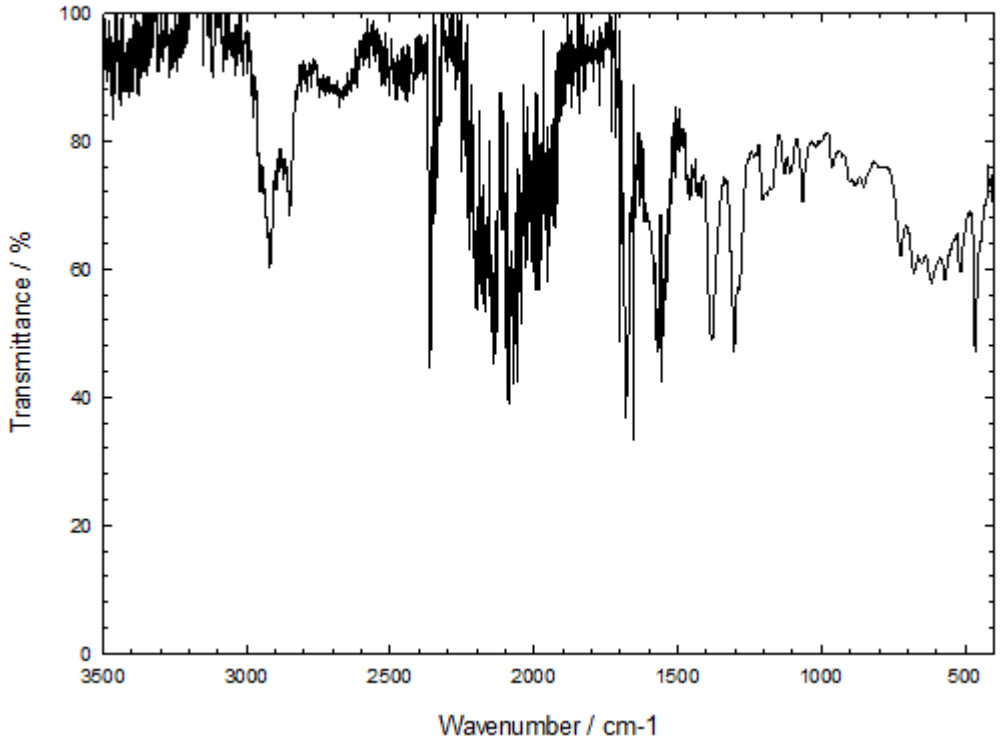

Figure A.10. FTIR spectrum of [DBNH][nHeptCOO], at *T* = 298 K.

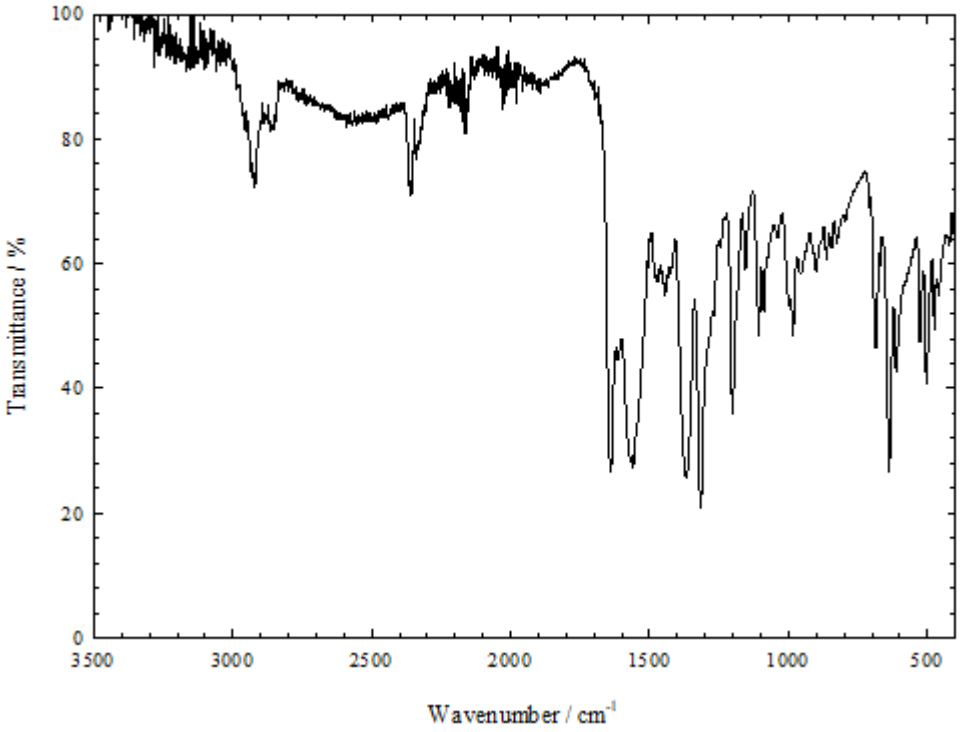

Figure A.11. FTIR spectrum of [DBUH][MeCOO], at *T* = 298 K.

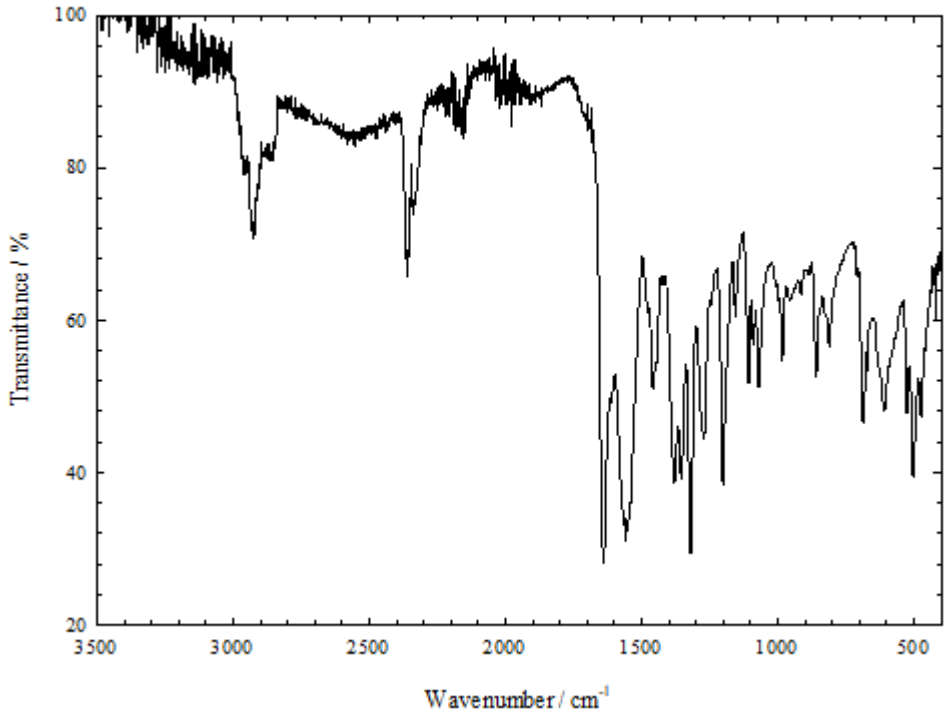

Figure A.12. FTIR spectrum of [DBUH][EtCOO], at *T* = 298 K.

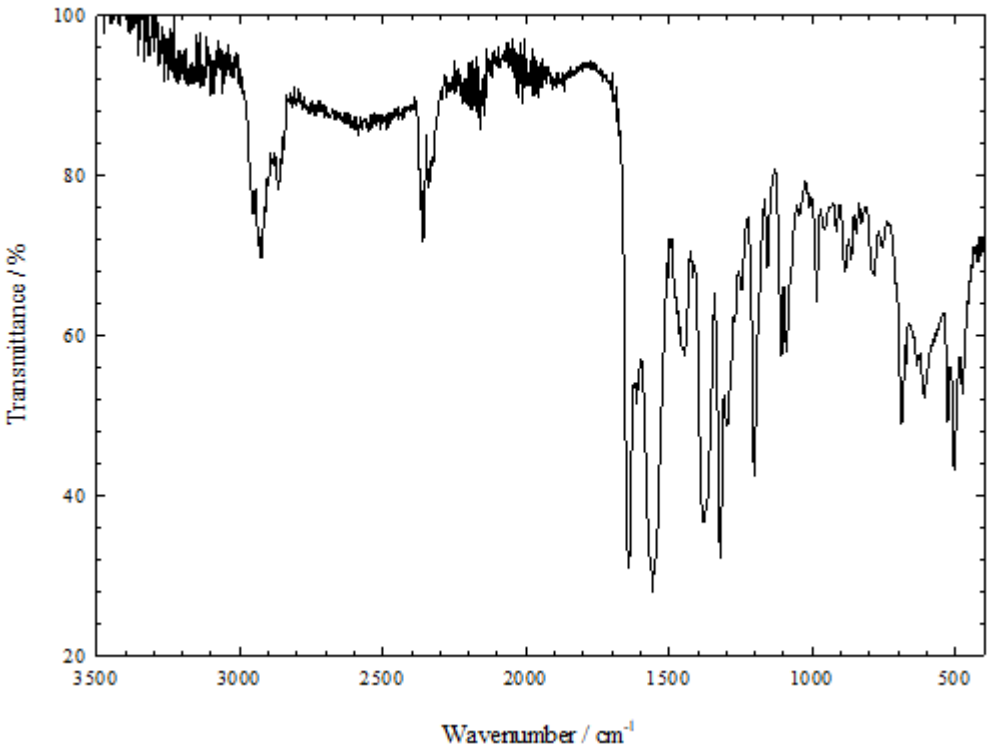

Figure A.13. FTIR spectrum of [DBUH][nPrCOO], at *T* = 298 K.

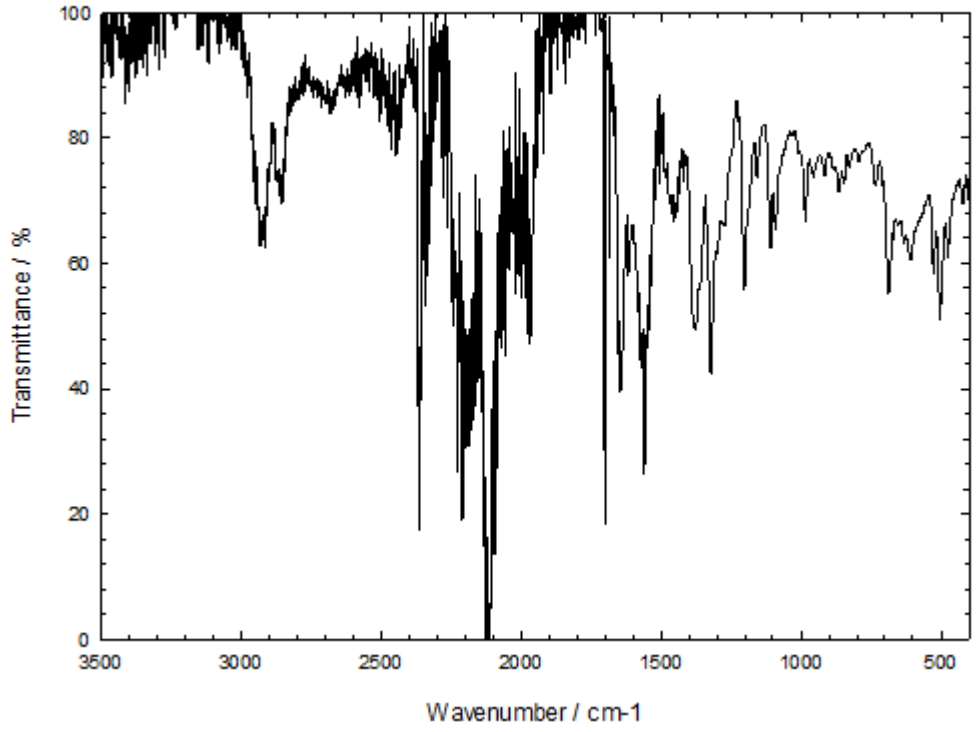

Figure A.14. FTIR spectrum of [DBUH][nPentCOO], at *T* = 298 K.

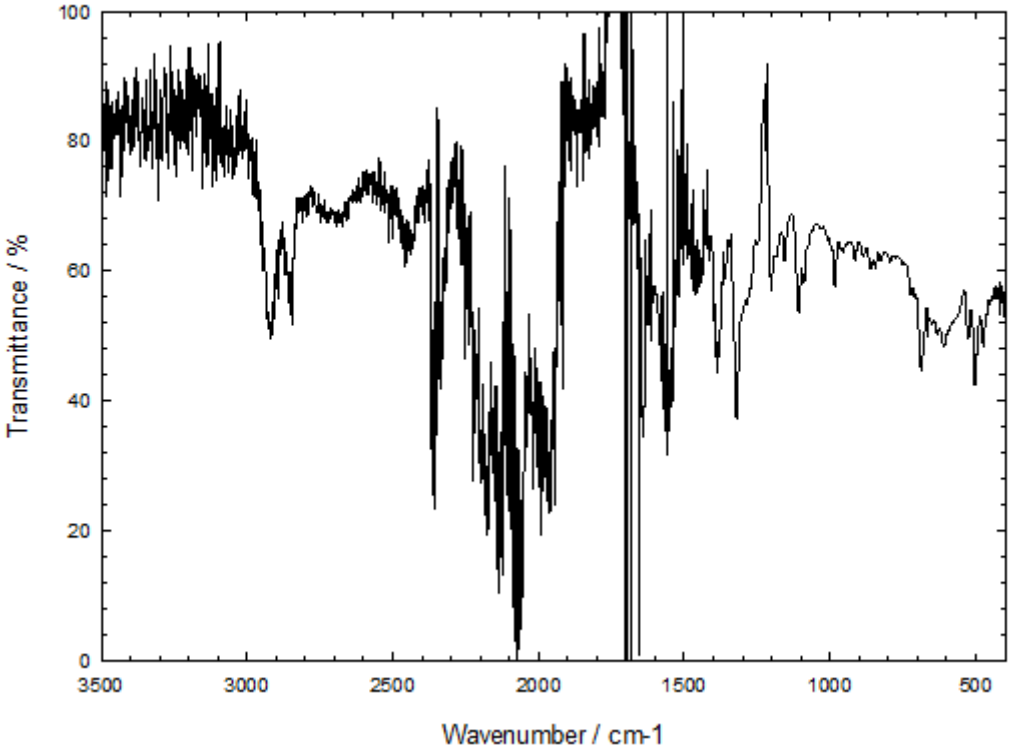

Figure A.15. FTIR spectrum of [DBUH][nHeptCOO], at *T* = 298 K.

Annex B

Annex B

Quantum chemical calculations data

Table B.1. (Part 1 of 2) Electronic energies, E_{el}, at T = 0K, and enthalpies, at T = 298.15K ($H_{298.15}$), for the optimized geometries of the compounds considered in this work, at the B3LYP/6-311++G(d,p), M06-2X/6-311++G(d,p) and the MP2/cc-pVDZ, levels of theory. Scaling factors applied.

Compound	E_{el} / Hartree·particle^{-1}			$H_{298.15}$ / Hartree·particle^{-1}		
	B3LYP	M06-2X	MP2	B3LYP	M06-2X	MP2
DBN	-383.57380	-383.39972	-382.27592	-383.37827	-383.20231	-382.07809
DBNH	-383.98440	-383.80645	-382.68517	-383.77385	-383.59418	-382.47232
DBU	-462.21207	-462.00293	-460.63336	-461.95627	-461.74479	-460.37463
DBUH	-462.62591	-462.41189	-461.04374	-462.35522	-462.13874	-460.77012
TBD	-438.94412	-438.75117	-437.47703	-438.72967	-438.53444	-437.25979
TBDH	-439.36208	-439.16542	-437.89432	-439.13272	-438.93416	-437.66241
TMG	-362.69998	-362.52783	-361.46779	-362.50170	-362.32727	-361.26707
TMGH	-363.05521	-362.87819	-361.82529	-362.84377	-362.66553	-361.61242
DMTHP	-345.45419	-345.28982	-344.27145	-345.26653	-345.10032	-344.08139
DMTHPH	-345.86424	-345.69669	-344.68125	-345.66152	-345.49225	-344.47616
Acetic acid	-229.16483	-229.06486	-228.47198	-229.09778	-228.99683	-228.40406
Acetate	-228.60249	-228.50079	-227.88222	-228.55029	-228.44792	-227.82835
Propionic acid	-268.48961	-268.36908	-267.65379	-268.39281	-268.27105	-267.55562
Propanoate	-267.92770	-267.80575	-267.06732	-267.84589	-267.72178	-266.98420
Butyric acid	-307.81385	-307.67232	-306.83446	-307.68734	-307.54568	-306.70626
Butanoate	-307.25257	-307.10974	-306.24919	-307.14117	-306.99746	-306.13617
Pentanoic acid	-347.13826	-346.97585	-346.01529	-346.98207	-346.81765	-345.85703
Pentanoate	-346.57726	-346.41366	-345.43056	-346.43621	-346.26980	-345.28753
Hexanoic acid	-386.46265	-386.27930	-385.19610	-386.27676	-386.09154	-385.00777
Hexanoate	-385.90185	-385.71732	-384.61167	-385.73112	-385.54488	-384.43860
Heptanoic acid	-425.78700	-425.58277	-424.37687	-425.57141	-425.36450	-424.15848
Heptanoate	-425.22631	-425.02094	-423.79214	-425.02590	-424.81706	-423.58898
Octanoic acid	-465.11136	-464.88620	-463.55763	-464.86608	-464.63817	-463.30918
Octanoate	-464.55074	-464.32445	-462.97344	-464.32065	-464.09086	-462.74028
Pentafluoropropanoic acid	-764.82335	-764.57668	-762.83337	-764.76258	-764.51409	-762.77123
Pentafluoropropanoate	-764.38404	-764.13851	-762.41810	-764.30809	-764.06153	-762.34073
Heptafluorobutyric acid	-1002.67900	-1002.4748	-1000.08273	-1002.6034	-1002.3992	-1000.0052

Table B.1. (Part 2 of 2) Electronic energies, E_{el}, at T = 0K, and enthalpies, at T = 298.15K ($H_{298.15}$), for the optimized geometries of the compounds considered in this work, at the B3LYP/6-311++G(d,p), M06-2X/6-311++G(d,p) and the MP2/cc-pVDZ, levels of theory. Scaling factors applied.

Compound	E_{el} / Hartree·particle^{-1}			$H_{298.15}$ / Hartree·particle^{-1}		
	B3LYP	M06-2X	MP2	B3LYP	M06-2X	MP2
Heptafluorobutanoate	-1002.2397	-1002.0366	-999.66746	-1002.1489	-1001.9466	-999.5747
[DBNH][MeCOO]	-612.76062	-612.48972	-610.77499	-612.49615	-612.22269	-610.50695
[DBNH][EtCOO]	-652.08512	-651.79375	-649.95697	-651.79087	-651.49648	-649.65873
[DBNH][nPrCOO]	-691.40923	-691.09691	-689.13768	-691.08534	-690.76968	-688.80943
[DBNH][nButCOO]	-730.73297	-730.40033	-728.31846	-730.37937	-730.04324	-727.96010
[DBNH][nPentCOO]	-770.05734	-769.70392	-767.49928	-769.67404	-769.31813	-767.11086
[DBNH][nHexCOO]	-809.38169	-809.00719	-806.68005	-808.96870	-808.59015	-806.26156
[DBNH][nHeptCOO]	-848.70564	-848.31036	-845.86081	-848.26305	-847.86401	-845.41227
[DBUH][MeCOO]	-691.39471	-691.08971	-689.12892	-691.07034	-690.76190	-688.80021
[DBUH][EtCOO]	-730.71898	-730.39309	-728.31090	-730.36448	-730.03545	-727.95191
[DBUH][nPrCOO]	-770.04351	-769.69663	-767.49195	-769.66023	-769.30836	-767.10289
[DBUH][nButCOO]	-809.36780	-809.00021	-806.67286	-808.95362	-808.58232	-806.25372
[DBUH][nPentCOO]	-848.69315	-848.30465	-845.85473	-848.24983	-847.85856	-845.40577
[DBUH][nHexCOO]	-888.01674	-887.60703	-885.03468	-887.54336	-887.12874	-884.55539
[DBUH][nHeptCOO]	-927.33951	-926.90925	-924.21347	-926.84143	-926.40078	-923.70401
[DBNH][FEtCOO]	-1148.43311	-1148.0178	-1145.14027	-1148.1748	-1147.7538	-1144.8769
[DBNH][FPrCOO]	-1386.28965	-1385.8032	-1382.39196	-1386.0164	-1385.6339	-1382.1138
[DBUH][FEtCOO]	-1227.07201	-1226.6208	-1223.50086	-1226.7530	-1226.2869	-1223.1775
[DBUH][FPrCOO]	-1464.92778	-1464.4075	-1460.75235	-1464.5940	-1464.1682	-1460.4141
[TBDH][EtCOO]	-707.46668	-707.14545	-705.15617	-707.15401	-706.82763	-704.83852
[TBDH][nPentCOO]	-825.43956	-825.05543	-822.69877	-825.03791	-824.64877	-822.29092
[TMGH][EtCOO]	-631.19551	-630.91027	-629.13906	-630.89776	-630.60923	-628.83764
[TMGH][nPentCOO]	-749.16894	-748.82080	-746.68182	-748.78199	-748.42976	-746.29018
[DMTHPH][EtCOO]	-613.96305	-613.68227	-611.95133	-613.67639	-613.39283	-611.66077
[DMTHPH][nPrCOO]	-653.28759	-652.98580	-651.13237	-652.97117	-652.66690	-650.81174
[DMTHPH][nButCOO]	-692.61213	-692.28933	-690.31341	-692.26595	-691.94097	-689.96271
[DMTHPH][nPentCOO]	-731.93638	-731.59265	-729.49408	-731.56062	-731.21341	-729.11331
[DMTHPH][nHexCOO]	-771.26081	-770.89599	-768.67509	-770.85511	-770.48871	-768.26425
[DMTHPH][nHeptCOO]	-810.58507	-810.19962	-807.85562	-810.14987	-809.76298	-807.41472

Table B.2. (Part 1 of 2) Heat capacities, at the gaseous phase and at constant pressure, C_p, at T = 298.15K, for the optimized geometries of the compounds considered in this work, at the B3LYP/6-311++G(d,p), M06-2X/6-311++G(d,p) and the MP2/cc-pVDZ, levels of theory.

Compound	C_p / J·K·mol^{-1}		
	B3LYP	M06-2X	MP2
DBN	140.417	136.985	141.836
DBNH	145.008	141.346	146.687
DBU	179.921	174.969	181.482
DBUH	185.232	179.940	187.143
TBD	157.582	153.376	158.076
TBDH	165.537	161.827	167.095
TMG	162.265	157.671	162.851
TMGH	160.828	147.482	153.410
DMTHP	142.570	139.484	143.776
DMTHPH	147.371	143.731	149.084
Acetic acid	69.822	68.178	69.987
Acetate	56.091	55.006	55.054
Propionic acid	90.786	88.858	90.846
Propanoate	77.176	83.458	77.445
Butyric acid	111.659	101.643	112.047
Butanoate	98.079	96.580	98.775
Pentanoic acid	132.743	129.618	133.230
Pentanoate	119.201	124.394	120.033
Hexanoic acid	153.684	150.838	154.413
Hexanoate	140.191	137.306	141.257
Heptanoic acid	174.678	170.531	175.603
Heptanoate	161.198	165.357	162.180
Octanoic acid	195.668	191.424	196.792
Octanoate	182.223	186.321	183.676
Pentafluoropropanoic acid	142.363	138.154	141.284
Pentafluoropropanoate	128.753	132.754	127.883
Heptafluorobutyric acid	186.778	182.569	185.053
Heptafluorobutanoate	173.236	177.345	171.856
[DBNH][MeCOO]	220.264	214.897	221.865
[DBNH][EtCOO]	241.180	234.615	242.655
[DBNH][nPrCOO]	262.266	255.268	263.858
[DBNH][nButCOO]	283.313	276.511	285.346
[DBNH][nPentCOO]	304.255	289.466	306.527
[DBNH][nHexCOO]	325.253	317.653	327.717
[DBNH][nHeptCOO]	346.211	334.693	348.909
[DBUH][MeCOO]	260.593	253.152	262.257
[DBUH][EtCOO]	280.357	272.763	281.905
[DBUH][nPrCOO]	293.004	292.251	303.068

Table B.2. (Part 2 of 2) Heat capacities, at the gaseous phase and at constant pressure, C_p, at T = 298.15K, for the optimized geometries of the compounds considered in this work, at the B3LYP/6-311++G(d,p), M06-2X/6-311++G(d,p) and the MP2/cc-pVDZ, levels of theory.

Compound	C_p / J·K·mol^{-1}		
	B3LYP	**M06-2X**	**MP2**
[DBUH][nButCOO]	322.243	313.252	324.226
[DBUH][nPentCOO]	344.033	327.229	346.148
[DBUH][nHexCOO]	363.987	353.621	366.525
[DBUH][nHeptCOO]	385.427	374.864	388.295
[DBNH][FEtCOO]	292.200	285.712	294.483
[DBNH][FPrCOO]	336.353	328.749	336.101
[DBUH][FEtCOO]	332.027	323.863	332.021
[DBUH][FPrCOO]	376.281	365.624	375.670
[TBDH][EtCOO]	254.125	249.811	256.558
[TBDH][nPentCOO]	317.162	303.995	320.184
[TMGH][EtCOO]	264.034	256.377	263.879
[TMGH][nPentCOO]	326.633	317.692	327.413
[DMTHPH][EtCOO]	242.878	238.863	244.014
[DMTHPH][nPrCOO]	263.610	258.458	265.201
[DMTHPH][nButCOO]	284.642	277.286	286.388
[DMTHPH][nPentCOO]	305.835	298.395	307.537
[DMTHPH][nHexCOO]	326.806	318.562	328.762
[DMTHPH][nHeptCOO]	347.654	337.838	349.915

Table B.3. (Part 1 of 2) Standard molar entropy, S_m^o, at *T* = 298.15K, and thermal enthalpy, $\Delta\Delta H$ also at *T* = 298.15K, for the optimized geometries of the compounds considered in this work, at the B3LYP/6-311++G(d,p), M06-2X/6-311++G(d,p) and the MP2/cc-pVDZ, levels of theory.

Compound	S_m^o / J·K·mol^{-1}			$\Delta\Delta H$ / kJ·mol^{-1}		
	B3LYP	M06-2X	MP2	B3LYP	M06-2X	MP2
DBN	365.558	363.383	364.266	23.519	23.124	23.504
DBNH	366.301	363.698	366.224	23.889	23.435	24.004
DBU	412.771	411.181	414.264	29.283	28.650	29.370
DBUH	411.524	405.651	411.365	29.744	28.906	29.889
TBD	387.346	384.792	387.499	26.168	25.678	26.114
TBDH	394.464	393.199	396.862	27.498	27.167	27.796
TMG	404.269	397.443	402.454	29.516	28.550	29.360
TMGH	411.365	376.531	387.142	29.236	25.780	27.040
DMTHP	372.412	375.039	373.231	24.941	24.845	25.042
DMTHPH	377.283	369.955	378.561	25.602	24.804	25.839
Acetic acid	291.943	283.666	287.719	14.780	14.230	14.621
Acetate	268.675	267.964	292.260	12.024	11.901	14.392
Propionic acid	319.136	314.589	317.922	17.914	17.475	17.810
Propanoate	296.955	316.749	295.408	15.236	17.136	15.102
Butyric acid	352.993	330.462	350.602	21.431	19.081	21.366
Butanoate	327.591	328.290	326.709	18.614	18.573	18.598
Pentanoic acid	383.545	375.153	383.439	25.015	24.329	25.004
Pentanoate	359.261	376.170	358.503	22.239	23.911	22.226
Hexanoic acid	415.977	416.466	416.501	28.642	28.355	28.668
Hexanoate	391.114	389.707	390.720	25.863	25.540	25.881
Heptanoic acid	447.273	436.519	448.850	32.268	31.393	32.352
Heptanoate	422.898	437.899	427.265	29.502	30.984	29.807
Octanoic acid	479.612	472.951	481.605	35.934	35.237	36.047
Octanoate	455.042	479.491	455.621	33.177	34.915	33.252
Pentafluoropropanoic acid	405.794	400.347	405.308	26.794	26.121	26.671
Pentafluoropropanoate	381.732	393.668	386.280	24.032	24.985	24.369
Heptafluorobutyric acid	467.351	461.258	466.258	34.473	33.952	34.246
Heptafluorobutanoate	443.289	454.579	447.230	31.711	32.816	31.944
[DBNH][MeCOO]	518.942	506.015	506.972	39.804	38.577	39.417
[DBNH][EtCOO]	545.530	523.275	536.282	43.113	41.447	42.743

Table B.3. (Part 2 of 2) Standard molar entropy, S_m^o, at *T* = 298.15K, and thermal enthalpy, $\Delta\Delta H$ also at *T* = 298.15K, for the optimized geometries of the compounds considered in this work, at the B3LYP/6-311++G(d,p), M06-2X/6-311++G(d,p) and the MP2/cc-pVDZ, levels of theory.

Compound	S_m^o / J·K·mol^{-1}			$\Delta\Delta H$ / kJ·mol^{-1}		
	B3LYP	M06-2X	MP2	B3LYP	M06-2X	MP2
[DBNH][nPrCOO]	580.357	555.707	569.185	46.843	45.060	46.420
[DBNH][nButCOO]	610.539	593.078	600.528	50.492	48.933	50.001
[DBNH][nPentCOO]	640.087	611.865	633.139	54.093	51.018	53.703
[DBNH][nHexCOO]	672.428	655.941	665.902	57.799	56.131	57.408
[DBNH][nHeptCOO]	703.155	679.591	698.721	61.435	58.897	61.122
[DBUH][MeCOO]	567.924	549.522	556.646	45.915	44.241	45.560
[DBUH][EtCOO]	590.698	569.853	578.663	48.863	47.087	48.438
[DBUH][nPrCOO]	596.135	587.370	610.546	50.184	50.085	52.102
[DBUH][nButCOO]	649.770	637.049	643.259	56.029	54.124	55.768
[DBUH][nPentCOO]	683.696	644.954	675.435	59.945	55.957	59.603
[DBUH][nHexCOO]	714.885	677.050	708.268	63.330	60.668	63.102
[DBUH][nHeptCOO]	740.595	711.531	758.008	66.661	64.682	67.334
[DBNH][FEtCOO]	635.879	579.244	596.089	52.112	49.436	50.946
[DBNH][FPrCOO]	688.968	655.302	664.494	59.656	57.605	58.627
[DBUH][FEtCOO]	667.028	636.724	649.782	57.760	55.563	56.688
[DBUH][FPrCOO]	732.867	687.855	698.856	65.509	62.652	64.274
[TBDH][EtCOO]	553.960	540.114	546.915	44.893	43.502	44.388
[TBDH][nPentCOO]	648.923	608.563	645.655	55.889	52.310	55.443
[TMGH][EtCOO]	585.737	566.409	575.434	48.906	47.190	48.308
[TMGH][nPentCOO]	680.210	661.140	673.064	59.753	57.865	59.341
[DMTHPH][EtCOO]	564.827	549.672	547.923	44.792	43.255	44.205
[DMTHPH][nPrCOO]	590.238	579.654	580.034	48.205	44.212	47.874
[DMTHPH][nButCOO]	628.155	598.775	612.145	52.054	49.850	51.543
[DMTHPH][nPentCOO]	660.613	636.183	645.278	55.796	53.998	55.230
[DMTHPH][nHexCOO]	692.377	664.627	676.367	59.392	57.243	58.881
[DMTHPH][nHeptCOO]	729.053	691.714	710.815	63.092	61.040	62.639

Table B.4. The distance between an acid (-OH) and base in each PIL, *d*, at the B3LYP/6-311++G(d,p), M06-2X/6-311++G(d,p) and the MP2/cc-pVDZ, levels of theory.

Compound	*d* / Å		
	B3LYP	**M06-2X**	**MP2**
[DBNH][MeCOO]	1.6504	1.6159	1.6587
[DBNH][EtCOO]	1.6545	1.6170	1.6562
[DBNH][nPrCOO]	1.6550	1.6121	1.6554
[DBNH][nButCOO]	1.6556	1.6609	1.6906
[DBNH][nPentCOO]	1.6560	1.6052	1.6905
[DBNH][nHexCOO]	1.6564	1.6741	1.6906
[DBNH][nHeptCOO]	1.6566	1.6743	1.6907
[DBUH][MeCOO]	1.6329	1.5763	1.6204
[DBUH][EtCOO]	1.6283	1.5706	1.6202
[DBUH][nPrCOO]	1.6325	1.5835	1.6207
[DBUH][nButCOO]	1.6708	1.5690	1.6206
[DBUH][nPentCOO]	1.6329	1.5800	1.6266
[DBUH][nHexCOO]	1.6516	1.5826	1.6384
[DBUH][nHeptCOO]	1.6519	1.5931	1.6384
[DBNH][FEtCOO]	1.0929	1.0185	1.0468
[DBNH][FPrCOO]	1.0895	1.0242	1.0801
[DBUH][FEtCOO]	1.0787	1.0365	1.0865
[DBUH][FPrCOO]	1.0777	1.0459	1.1045
[TBDH][EtCOO]	1.5901	1.9136	1.5552
[TBDH][nPentCOO]	1.5674	1.8171	1.5674
[TMGH][EtCOO]	1.9142	1.7820	1.7465
[TMGH][nPentCOO]	1.9116	1.7833	1.7476
[DMTHPH][EtCOO]	1.6429	1.5889	1.6357
[DMTHPH][nPrCOO]	1.6444	1.5967	1.6361
[DMTHPH][nButCOO]	1.6456	1.5924	1.6362
[DMTHPH][nPentCOO]	1.6435	1.5859	1.6362
[DMTHPH][nHexCOO]	1.6433	1.5860	1.6362
[DMTHPH][nHeptCOO]	1.6744	1.5870	1.6363

Table B.5. The distance between an acid (=O) and base in each PIL, *d*, at the B3LYP/6-311++G(d,p), M06-2X/6-311++G(d,p) and the MP2/cc-pVDZ, levels of theory.

Compound	*d* / Å		
	B3LYP	M06-2X	MP2
[DBNH][MeCOO]	3.5248	3.1652	3.1457
[DBNH][EtCOO]	3.5346	3.1792	3.1401
[DBNH][nPrCOO]	3.5343	3.1754	3.1400
[DBNH][nButCOO]	3.4668	3.0529	3.0788
[DBNH][nPentCOO]	3.4657	3.3131	3.0794
[DBNH][nHexCOO]	3.4580	3.0449	3.0795
[DBNH][nHeptCOO]	3.4604	3.0454	3.0795
[DBUH][MeCOO]	3.4447	3.2872	3.1793
[DBUH][EtCOO]	3.4020	3.1263	3.1351
[DBUH][nPrCOO]	3.3971	3.1329	3.1350
[DBUH][nButCOO]	3.6430	3.1325	3.1349
[DBUH][nPentCOO]	3.4002	3.1284	3.1337
[DBUH][nHexCOO]	3.6036	3.1322	3.0646
[DBUH][nHeptCOO]	3.6042	3.2770	3.0646
[DBNH][FEtCOO]	3.3493	3.0091	2.9514
[DBNH][FPrCOO]	3.4628	2.9287	2.8843
[DBUH][FEtCOO]	3.2702	2.9293	2.9326
[DBUH][FPrCOO]	3.6038	2.9222	2.9531
[TBDH][EtCOO]	2.7321	2.7079	2.5589
[TBDH][nPentCOO]	2.7302	2.6789	2.5640
[TMGH][EtCOO]	3.6374	3.3191	3.2780
[TMGH][nPentCOO]	3.6338	3.3211	3.2774
[DMTHPH][EtCOO]	3.3967	3.1433	3.1292
[DMTHPH][nPrCOO]	3.3979	3.1260	3.1293
[DMTHPH][nButCOO]	3.3983	3.1374	3.1292
[DMTHPH][nPentCOO]	3.3997	3.1404	3.1293
[DMTHPH][nHexCOO]	3.4218	3.1628	3.1292
[DMTHPH][nHeptCOO]	3.6415	3.1650	3.1293

Table B.6. (Part 1 of 2) Accessible surface area, *ASA,* and polar area, *PA,* for the optimized geometries of the compounds considered in this work, at the B3LYP/6-311++G(d,p), M06-2X/6-311++G(d,p) and the MP2/cc-pVDZ, levels of theory.

Compound	*ASA* / Å^2			*PA* / Å^2		
	B3LYP	**M06-2X**	**MP2**	**B3LYP**	**M06-2X**	**MP2**
DBN	161.4	161.2	161.6	14.7	14.9	14.9
DBNH	164.3	164.3	164.9	18.2	17.5	17.6
DBU	195.0	191.0	194.1	13.6	13.8	14.5
DBUH	198.9	198.7	201.7	17.2	16.8	17.1
TBD	173.1	173.0	171.9	28.9	29.3	29.5
TBDH	175.5	174.6	177.0	31.4	31.3	31.6
TMG	168.7	166.8	168.0	27.5	28.0	27.9
TMGH	175.3	172.3	175.1	31.7	31.3	31.3
DMTHP	157.6	153.7	156.7	14.7	14.2	14.7
DMTHPH	158.4	159.8	160.3	16.4	16.3	16.2
Acetic acid	83.7	83.8	83.9	40.7	40.7	40.4
Acetate	79.7	79.8	81.0	36.2	36.2	36.2
Propionic acid	104.3	103.6	104.1	38.9	38.4	38.6
Propanoate	103.0	102.2	102.6	35.8	35.3	35.3
Butyric acid	125.8	125.0	125.5	40.1	39.5	39.5
Butanoate	121.4	121.2	123.0	35.5	35.3	35.7
Pentanoic acid	151.1	149.2	148.6	40.0	39.8	39.8
Pentanoate	147.0	145.6	146.1	35.8	35.5	35.7
Hexanoic acid	171.3	170.7	172.0	40.1	39.9	40.4
Hexanoate	168.2	166.9	168.3	35.5	34.9	35.7
Heptanoic acid	196.2	194.7	194.9	40.0	39.8	39.4
Heptanoate	192.3	190.3	192.0	35.8	35.7	35.7
Octanoic acid	216.4	215.0	216.6	39.8	39.8	40.0
Octanoate	212.4	211.2	212.7	35.5	35.7	35.7
Pentafluoropropanoic acid	134.0	132.8	132.6	39.2	39.0	38.9
Pentafluoropropanoate	130.6	129.4	130.0	35.1	34.9	35.0
Heptafluorobutyric acid	166.3	161.8	162.9	39.4	39.9	39.8
Heptafluorobutanoate	162.1	157.7	159.6	35.2	35.7	35.8
[DBNH][MeCOO]	235.1	232.0	234.2	45.2	44.0	45.2
[DBNH][EtCOO]	254.4	250.2	255.0	44.3	42.4	44.2

Table B.6. (Part 2 of 2) Accessible surface area, *ASA,* and polar area, *PA,* for the optimized geometries of the compounds considered in this work, at the B3LYP/6-311++G(d,p), M06-2X/6-311++G(d,p) and the MP2/cc-pVDZ, levels of theory.

Compound	*ASA* / Å²			*PA* / Å²		
	B3LYP	M06-2X	MP2	B3LYP	M06-2X	MP2
[DBNH][nPrCOO]	275.7	270.4	276.7	44.0	41.6	44.3
[DBNH][nButCOO]	299.3	294.0	299.8	44.5	44.6	44.6
[DBNH][nPentCOO]	322.6	311.7	318.4	44.1	43.7	44.8
[DBNH][nHexCOO]	348.3	336.2	342.6	44.0	44.0	45.2
[DBNH][nHeptCOO]	372.6	363.9	370.6	43.6	43.5	43.8
[DBUH][MeCOO]	271.7	264.5	269.7	45.3	42.7	43.9
[DBUH][EtCOO]	290.5	287.1	293.6	43.1	42.0	44.1
[DBUH][nPrCOO]	313.8	306.4	312.8	42.8	42.3	43.6
[DBUH][nButCOO]	333.4	331.6	334.2	44.0	42.7	44.4
[DBUH][nPentCOO]	355.9	349.1	355.5	43.7	41.7	43.0
[DBUH][nHexCOO]	376.6	370.3	375.7	41.9	42.1	43.6
[DBUH][nHeptCOO]	396.1	393.8	395.6	43.0	42.3	44.3
[DBNH][FEtCOO]	282.5	270.4	273.5	42.3	40.7	40.4
[DBNH][FPrCOO]	311.3	305.8	307.4	42.4	41.9	40.8
[DBUH][FEtCOO]	316.0	305.1	310.7	40.9	38.3	38.7
[DBUH][FPrCOO]	344.4	337.2	343.2	40.4	39.3	40.1
[TBDH][EtCOO]	259.1	255.6	254.4	50.2	50.2	50.2
[TBDH][nPentCOO]	325.5	322.3	320.6	50.7	51.7	50.8
[TMGH][EtCOO]	261.9	256.0	259.6	59.9	57.5	57.4
[TMGH][nPentCOO]	324.1	325.6	327.6	58.6	58.1	58.4
[DMTHPH][EtCOO]	251.3	248.1	249.6	44.8	43.5	44.2
[DMTHPH][nPrCOO]	273.5	267.8	270.6	44.8	43.1	44.3
[DMTHPH][nButCOO]	294.2	292.9	293.2	44.7	43.4	44.3
[DMTHPH][nPentCOO]	316.4	311.3	313.2	44.8	43.1	44.4
[DMTHPH][nHexCOO]	340.1	339.2	333.6	44.7	43.8	44.4
[DMTHPH][nHeptCOO]	364.6	359.6	362.0	43.6	43.6	44.5

Table B.7. (Part 1 of 2) Molecular volume, *V*, of the optimized geometries of the compounds considered in this work, calculated at the B3LYP/6-311++G(d,p), M06-2X/6-311++G(d,p) and MP2/cc-pVDZ levels of theory.

Compound	*V* / Å^3		
	B3LYP	**M06-2X**	**MP2**
DBN	126.2	126.1	125.1
DBNH	127.9	126.8	126.9
DBU	157.1	156.4	157.9
DBUH	157.7	159.9	161.9
TBD	136.3	135.9	135.9
TBDH	137.6	138.1	139.3
TMG	125.7	124.0	124.4
TMGH	130.3	129.1	131.3
DMTHP	121.4	117.7	119.8
DMTHPH	120.6	121.9	121.9
Acetic acid	55.8	55.7	56.0
Acetate	53.3	53.3	54.1
Propionic acid	72.1	71.7	72.1
Propanoate	71.0	70.8	71.3
Butyric acid	89.1	88.6	89.1
Butanoate	86.4	86.5	87.5
Pentanoic acid	107.1	105.7	105.6
Pentanoate	104.4	103.9	104.1
Hexanoic acid	122.7	122.4	123.5
Hexanoate	121.0	120.0	121.4
Heptanoic acid	141.2	139.6	139.3
Heptanoate	138.0	137.6	138.3
Octanoic acid	156.7	155.7	157.7
Octanoate	155.0	154.2	155.0
Pentafluoropropanoic acid	96.5	96.3	96.2
Pentafluoropropanoate	94.8	94.5	94.4
Heptafluorobutyric acid	123.7	122.5	121.9
Heptafluorobutanoate	121.8	121.2	121.0
[DBNH][MeCOO]	182.3	179.6	181.6
[DBNH][EtCOO]	197.6	194.6	198.1

Table B.7. (Part 2 of 2) Molecular volume, *V*, of the optimized geometries of the compounds considered in this work, calculated at the B3LYP/6-311++G(d,p), M06-2X/6-311++G(d,p) and MP2/cc-pVDZ levels of theory.

Compound	*V* / Å^3		
	B3LYP	**M06-2X**	**MP2**
[DBNH][nPrCOO]	214.3	211.2	214.4
[DBNH][nButCOO]	230.5	227.3	232.8
[DBNH][nPentCOO]	247.3	244.0	246.0
[DBNH][nHexCOO]	267.5	262.0	264.3
[DBNH][nHeptCOO]	286.6	282.9	285.5
[DBUH][MeCOO]	211.6	209.1	214.0
[DBUH][EtCOO]	229.6	230.6	235.2
[DBUH][nPrCOO]	247.0	246.6	248.6
[DBUH][nButCOO]	262.6	262.8	264.7
[DBUH][nPentCOO]	281.6	276.0	279.6
[DBUH][nHexCOO]	295.1	292.0	297.9
[DBUH][nHeptCOO]	317.2	315.3	313.2
[DBNH][FEtCOO]	220.1	219.5	220.6
[DBNH][FPrCOO]	245.0	247.3	246.0
[DBUH][FEtCOO]	253.9	248.0	252.4
[DBUH][FPrCOO]	275.0	277.8	281.9
[TBDH][EtCOO]	205.0	205.7	205.6
[TBDH][nPentCOO]	254.1	254.6	258.3
[TMGH][EtCOO]	195.8	193.4	197.1
[TMGH][nPentCOO]	244.4	245.5	246.8
[DMTHPH][EtCOO]	189.4	189.0	190.4
[DMTHPH][nPrCOO]	208.8	206.1	206.7
[DMTHPH][nButCOO]	225.9	224.7	225.1
[DMTHPH][nPentCOO]	238.0	236.8	238.1
[DMTHPH][nHexCOO]	260.2	259.0	260.0
[DMTHPH][nHeptCOO]	275.8	275.3	276.5

Table B.8. Enthalpies of reaction, ΔH_r, at T = 298.15 K, for the R1, R2 and R3 reactions presented in figure 4.9, at the B3LYP/6-311++G(d,p), M06-2X/6-311++G(d,p) and the MP2/cc-pVDZ, levels of theory.

Compound	R1 / kJ·mol^{-1}			R2 / kJ·mol^{-1}			R3 / kJ·mol^{-1}		
	B3LYP	M06-2X	MP2	B3LYP	M06-2X	MP2	B3LYP	M06-2X	MP2
[DBNH][MeCOO]	452	474	542	-399	-412	-476	53	62	65
[DBNH][EtCOO]	449	474	531	-397	-413	-465	52	61	66
[DBNH][nPrCOO]	447	467	528	-395	-410	-462	52	57	66
[DBNH][nButCOO]	445	471	526	-395	-410	-460	50	61	66
[DBNH][nPentCOO]	444	470	525	-394	-406	-459	50	64	66
[DBNH][nHexCOO]	444	470	526	-394	-408	-460	50	61	66
[DBNH][nHeptCOO]	443	470	524	-393	-408	-459	49	62	66
[DBUH][MeCOO]	433	460	530	-390	-407	-473	43	53	57
[DBUH][EtCOO]	429	459	519	-388	-408	-462	40	51	57
[DBUH][nPrCOO]	430	452	516	-387	-405	-458	44	47	58
[DBUH][nButCOO]	426	456	515	-386	-404	-457	40	52	58
[DBUH][nPentCOO]	429	459	517	-385	-401	-456	44	58	61
[DBUH][nHexCOO]	426	454	515	-385	-403	-457	41	51	58
[DBUH][nHeptCOO]	435	449	508	-385	-403	-455	50	47	53
[DBNH][FEtCOO]	244	258	168	-155	-159	-159	89	98	72
[DBNH][FButCOO]	246	244	175	-155	-159	-159	91	85	80
[DBUH][FEtCOO]	235	227	175	-146	-154	-154	90	74	83
[DBUH][FButCOO]	236	218	182	-146	-154	-154	90	64	90
[TBDH][EtCOO]	461	451	504	-378	-393	-443	83	58	61
[TBDH][nPentCOO]	457	446	499	-374	-386	-437	83	60	61
[TMGH][EtCOO]	546	583	633	-538	-554	-594	9	29	39
[TMGH][nPentCOO]	544	576	628	-534	-547	-588	9	29	40
[DMTHPH][EtCOO]	444	469	526	-399	-413	-464	45	56	62
[DMTHPH][nPrCOO]	442	465	524	-397	-410	-460	45	55	63
[DMTHPH][nButCOO]	442	470	523	-396	-409	-459	46	60	64
[DMTHPH][nPentCOO]	441	463	521	-396	-406	-458	45	57	63
[DMTHPH][nHexCOO]	440	471	523	-395	-408	-459	45	63	64
[DMTHPH][nHeptCOO]	440	472	521	-395	-408	-457	45	64	63

In chapter 4 it was shown that a molecule of neutral acid can establish strong H-bonds with the PIL ion pair. Therefore, the excess neutral acid establishes strong interactions with the ion pair.

Using equation B.1 and observing the effect of different K_{eq} and total concentration of neutral species in the PIL media, the PIL equilibrium was also studied.

$$B + HA \leftrightarrow [BH][A] \qquad \textbf{(B.1)}$$

Tables B.9 and B.10 and figures a and b present the fractions of base, acid and PIL at equilibrium when different conditions (K_{eq} and total concentration) are met.

Table B.9. Fractions of base, acid and PIL at equilibrium at total concentration n = 1 and changing values of K_{eq} as a function of the x_{acid}.

K_{eq}	x(B)	x(HA)	x(PIL)	x_{acid}
	0.00	1.00	0.00	1.0
	0.01	0.89	0.10	0.9
	0.02	0.75	0.23	0.8
	0.04	0.59	0.37	0.7
	0.10	0.40	0.51	0.6
20	0.21	0.21	0.57	0.5
	0.40	0.10	0.51	0.4
	0.59	0.04	0.37	0.3
	0.75	0.02	0.23	0.2
	0.89	0.01	0.10	0.1
	1.00	0.00	0.00	0.0
	0.00	1.00	0.00	1.0
	0.00	0.89	0.11	0.9
	0.00	0.75	0.24	0.8
	0.01	0.58	0.41	0.7
	0.03	0.35	0.62	0.6
100	0.12	0.12	0.77	0.5
	0.35	0.03	0.62	0.4
	0.58	0.01	0.41	0.3
	0.75	0.00	0.24	0.2
	0.89	0.00	0.11	0.1
	1.00	0.00	0.00	0.0

Table B.10. Fractions of base, acid and PIL at equilibrium at same K_{eq} = 20 and changing values of total concentration *n*. as a function of x_{acid}.

n	*x*(B)	*x*(HA)	*x*(PIL)	x_{acid}
1	0.00	1.00	0.00	1.0
	0.01	0.89	0.10	0.9
	0.02	0.75	0.23	0.8
	0.04	0.59	0.37	0.7
	0.10	0.40	0.51	0.6
	0.21	0.21	0.57	0.5
	0.40	0.10	0.51	0.4
	0.59	0.04	0.37	0.3
	0.75	0.02	0.23	0.2
	0.89	0.01	0.10	0.1
	1.00	0.00	0.00	0.0
20	0.00	1.00	0.00	20
	0.00	0.89	0.11	18
	0.00	0.75	0.25	16
	0.00	0.57	0.42	14
	0.01	0.34	0.65	12
	0.06	0.06	0.87	10
	0.34	0.01	0.65	8
	0.57	0.00	0.42	6
	0.75	0.00	0.25	4
	0.89	0.00	0.11	2
	1.00	0.00	0.00	0

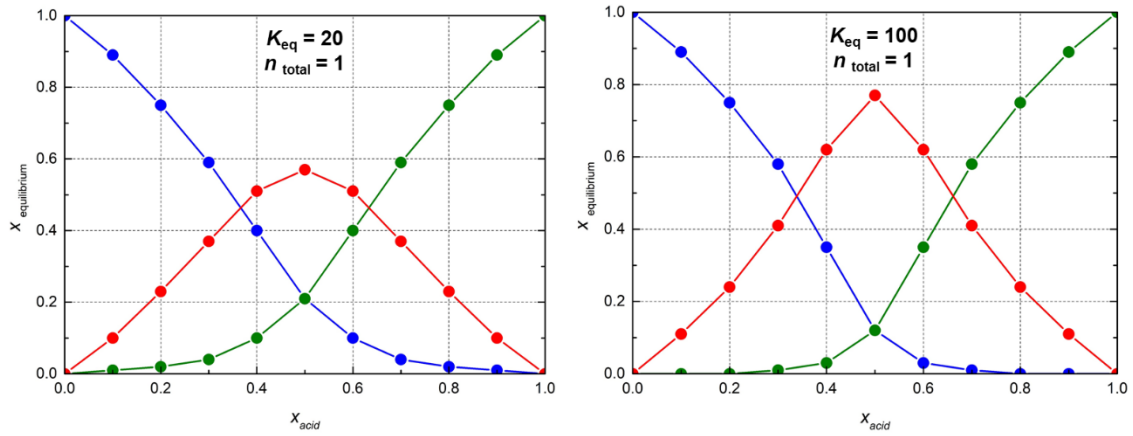

Figure B.1. Fractions of base, acid and PIL at equilibrium at total concentration *n* = 1 and changing values of K_{eq} as a function of the x_{acid}. Base fraction – blue circles, PIL fraction – red circles and Acid fraction – green circles.

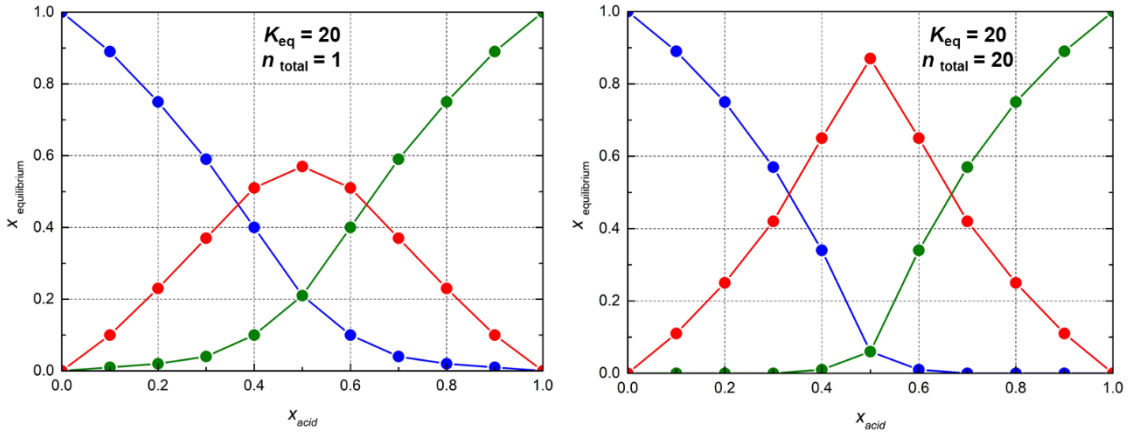

Figure B.2. Fractions of base, acid and PIL at equilibrium at same K_{eq} = 20 and changing values of total concentration n. as a function of x_{acid}. Base fraction – blue circles, PIL fraction – red circles and Acid fraction – green circles.

Annex C

Annex C

Phase behavior data

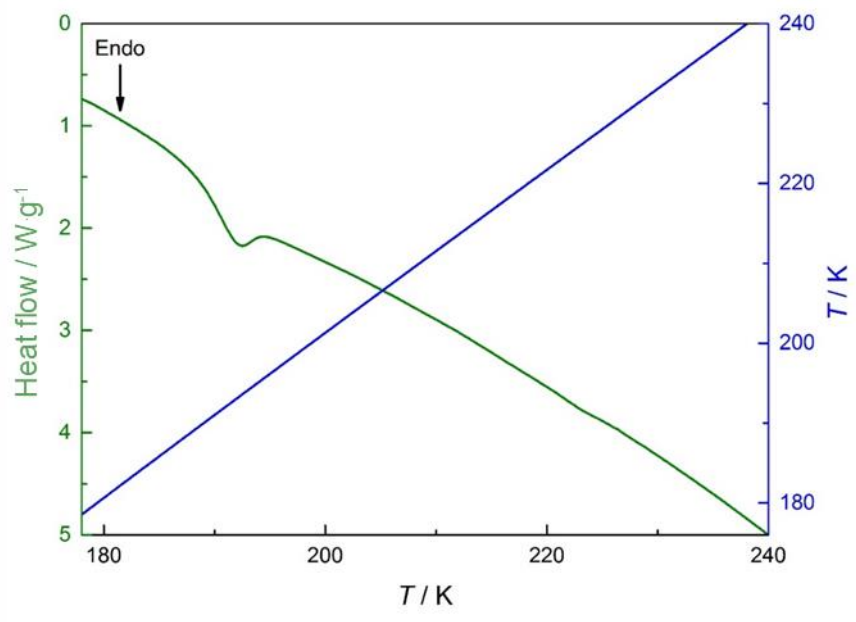

Figure C.1. Thermogram obtained for superbase DBN.

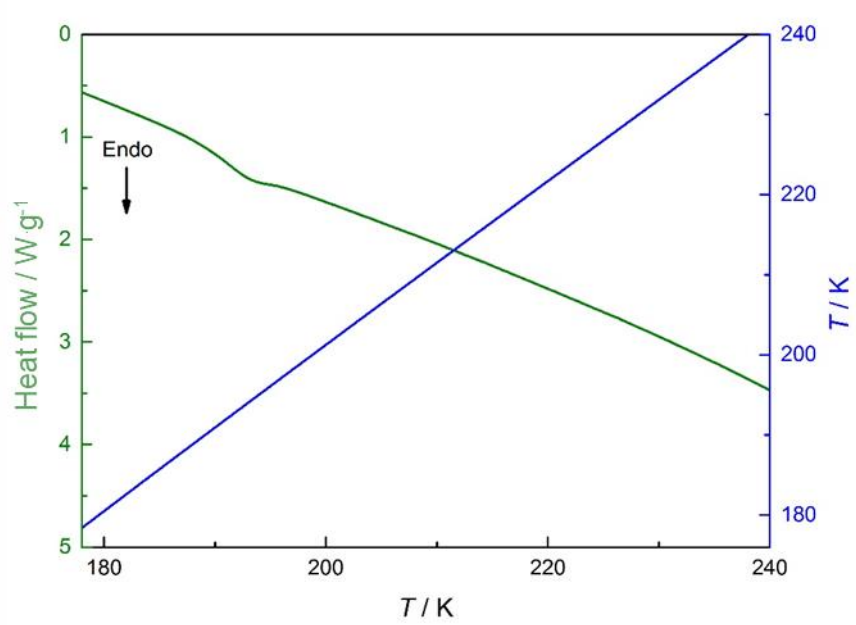

Figure C.2. Thermogram obtained for superbase DBU.

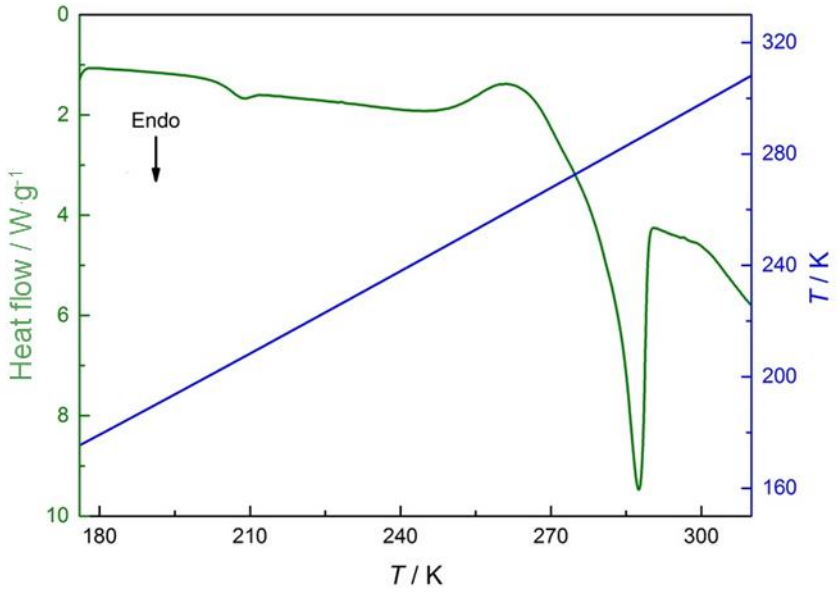

Figure C.3. Thermogram obtained for the protic ionic liquid [DBNH][MeCOO]. For this protic ionic liquid, a T_{cc} = 257.8 K was found.

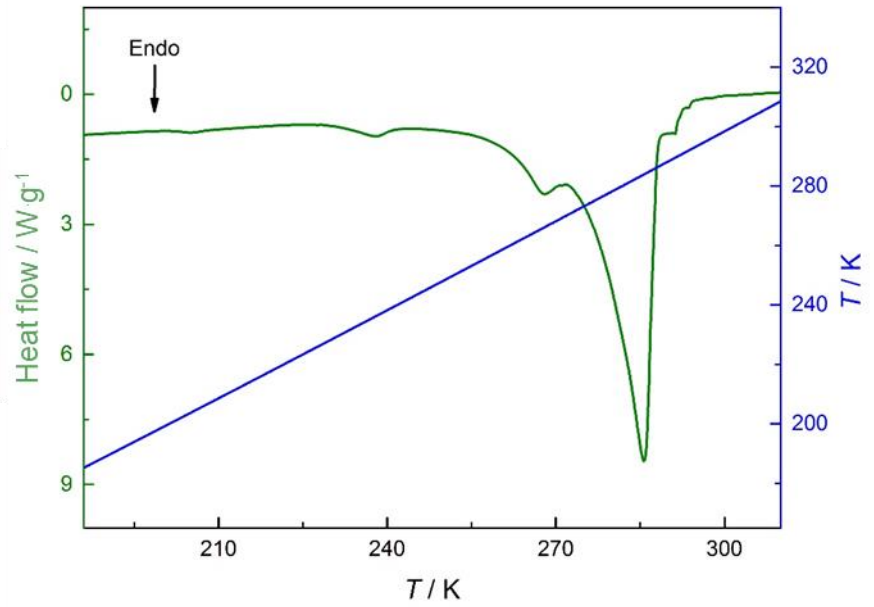

Figure C.4. Thermogram obtained for the protic ionic liquid [DBNH][EtCOO].

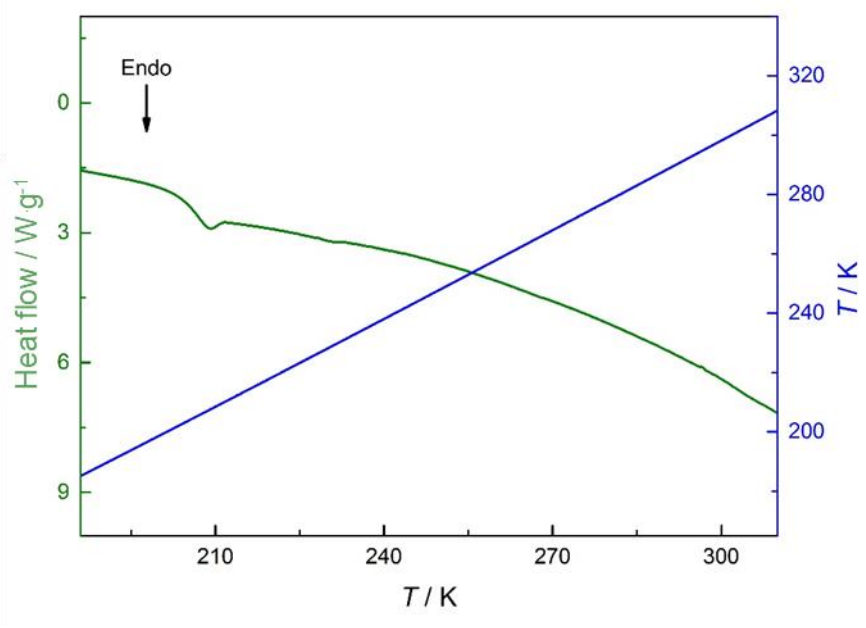

Figure C.5. Thermogram obtained for the protic ionic liquid [DBNH][nPrCOO].

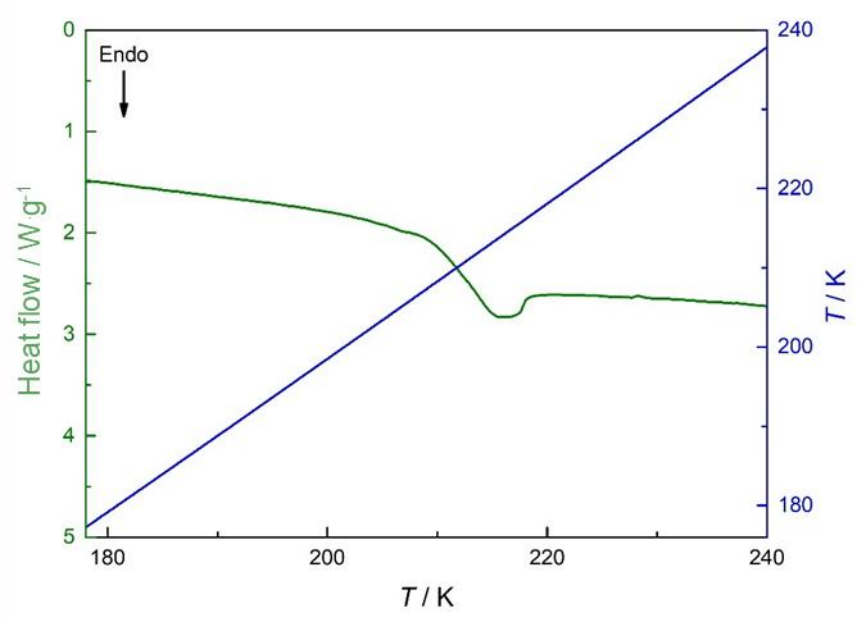

Figure C.6. Thermogram obtained for the protic ionic liquid [DBNH][iPrCOO].

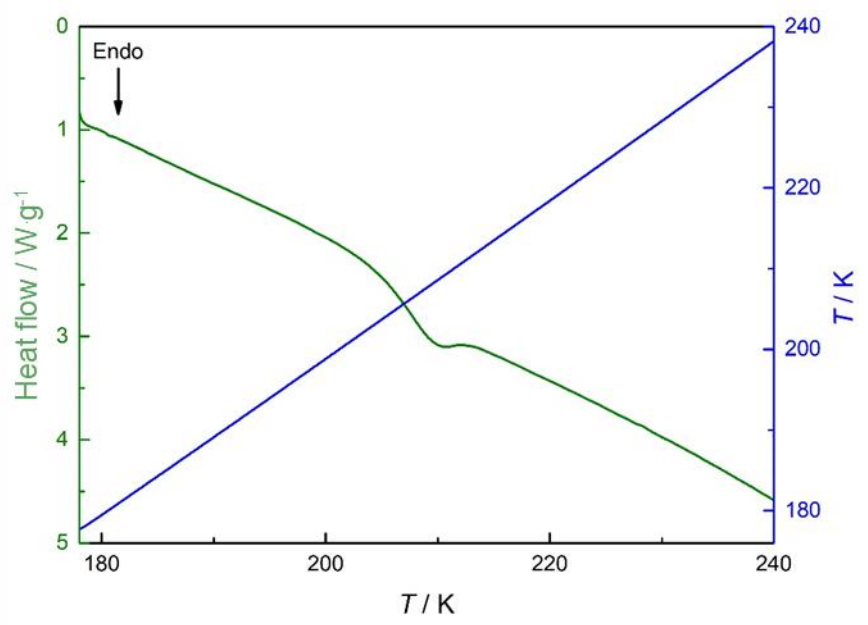

Figure C.7. Thermogram obtained for the protic ionic liquid [DBNH][nPentCOO].

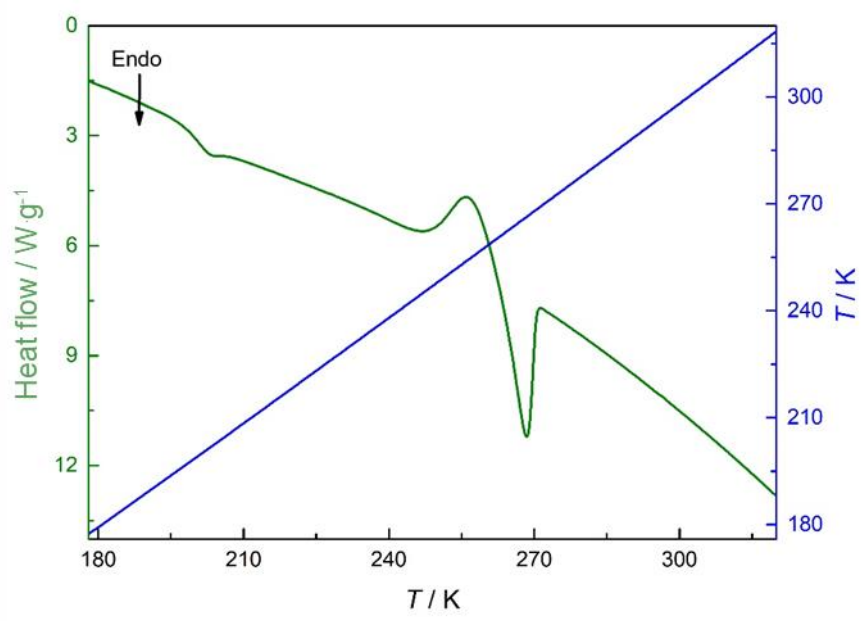

Figure C.8. Thermogram obtained for the protic ionic liquid [DBNH][nHeptCOO]. For this protic ionic liquid, a T_{cc} = 243.7 K was found.

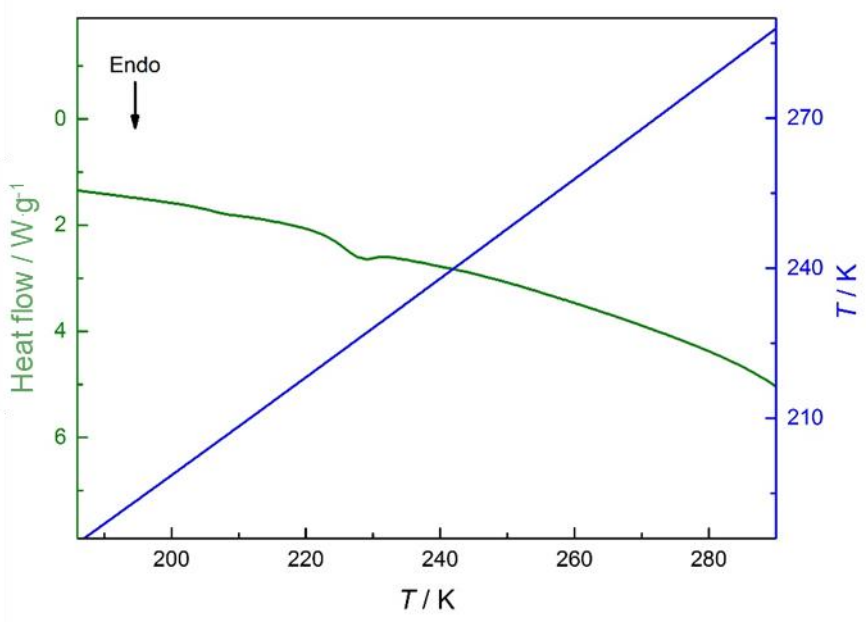

Figure C.9. Thermogram obtained for the protic ionic liquid [DBUH][MeCOO].

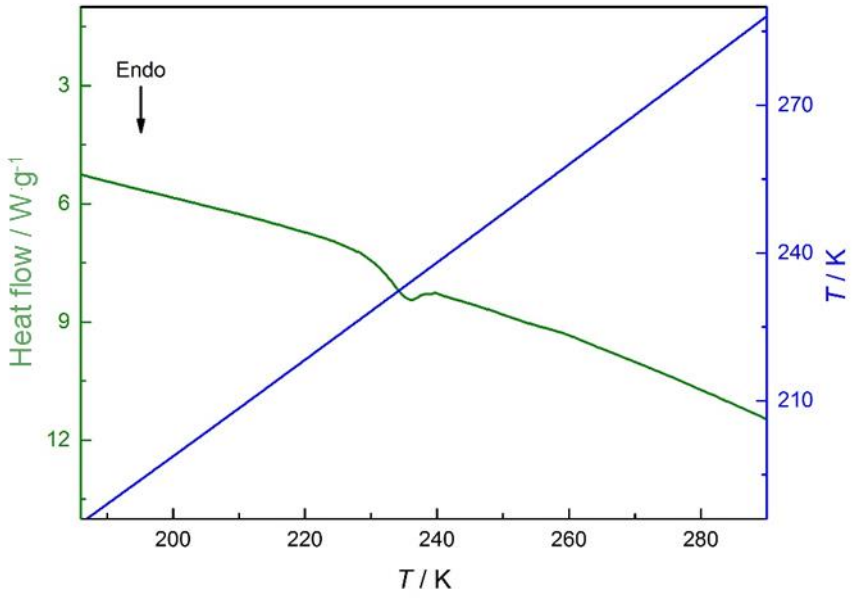

Figure C.10. Thermogram obtained for the protic ionic liquid [DBUH][EtCOO].

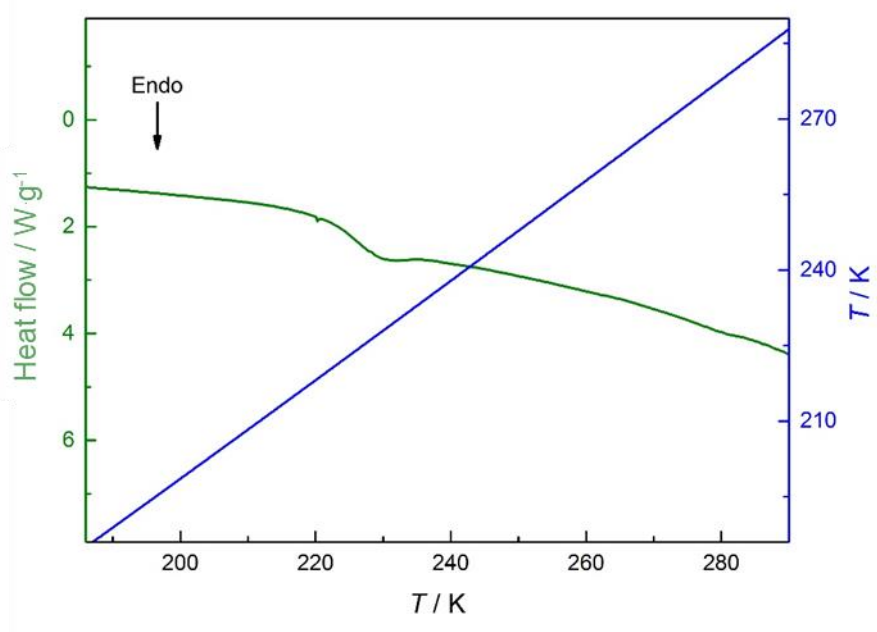

Figure C.11. Thermogram obtained for the protic ionic liquid [DBUH][nPrCOO].

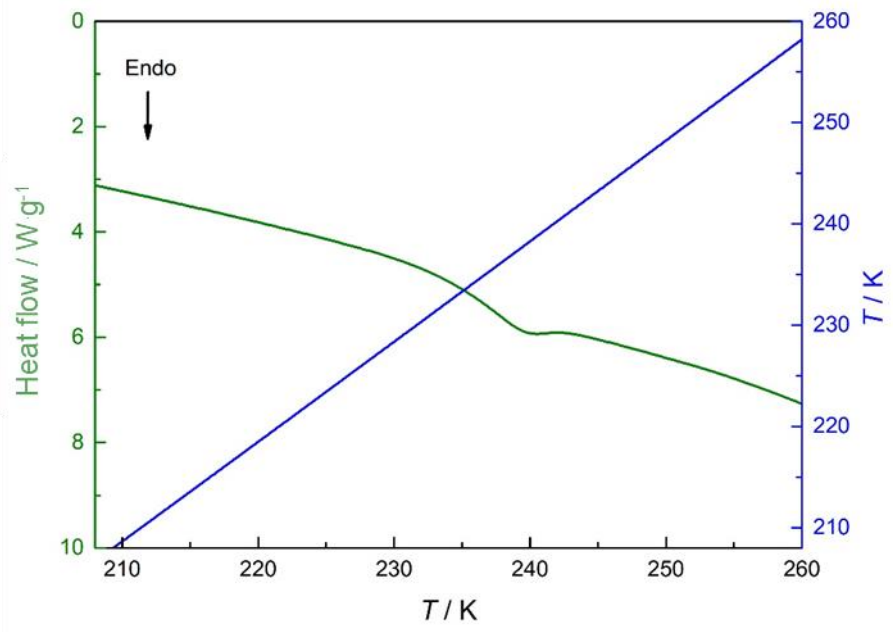

Figure C.12. Thermogram obtained for the protic ionic liquid [DBUH][iPrCOO].

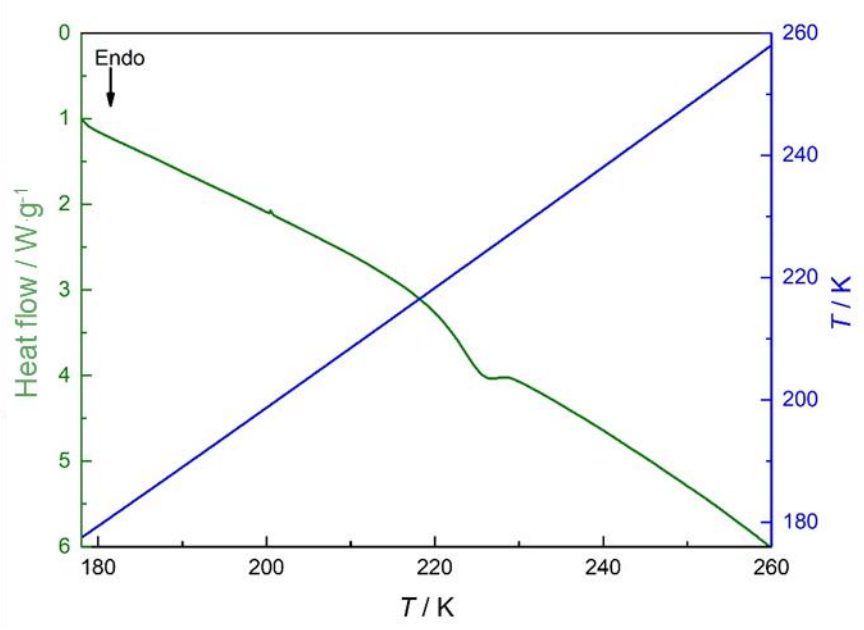

Figure C.13. Thermogram obtained for the protic ionic liquid [DBUH][nPentCOO].

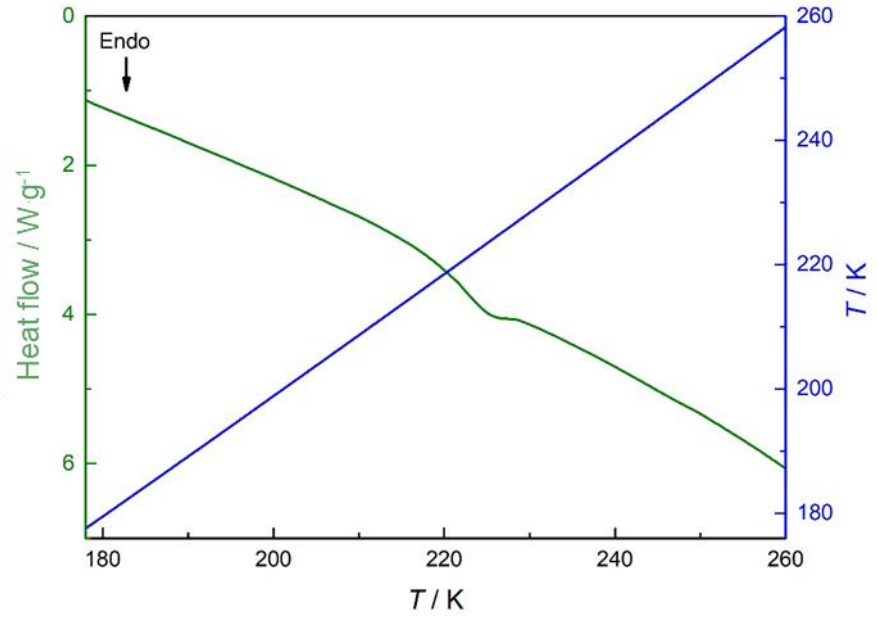

Figure C.14. Thermogram obtained for the protic ionic liquid [DBUH][nHeptCOO].

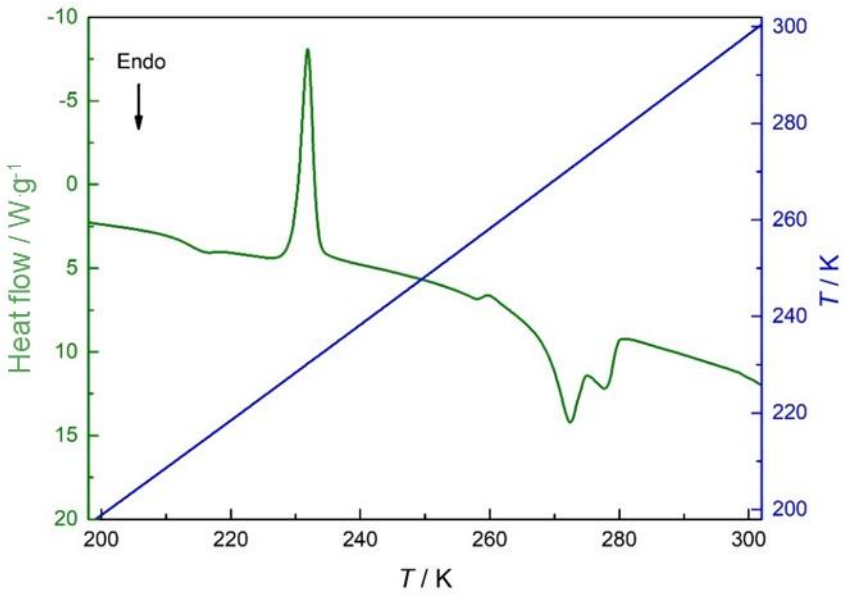

Figure C.15. Thermogram obtained for the protic ionic liquid [TBDH][nPentCOO]. For this protic ionic liquid, a T_c = 226.2 K was found.

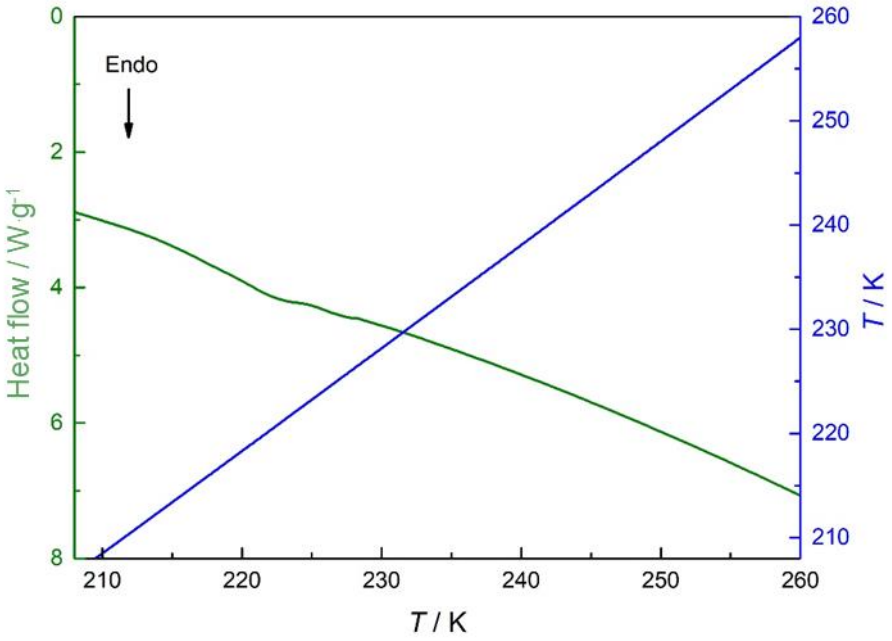

Figure C.16. Thermogram obtained for the protic ionic liquid [TMGH][EtCOO].

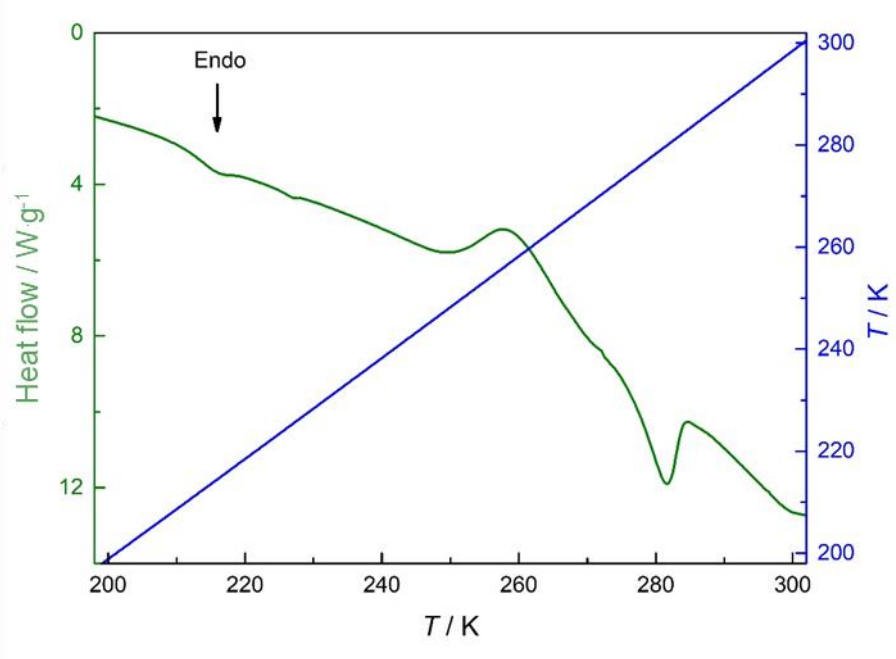

Figure C.17. Thermogram obtained for the protic ionic liquid [TMGH][nPentCOO]. For this protic ionic liquid, a T_c = 243.8 K was found.